A First Study of Multijet Dynamics in Hard Photoproduction at HERA

Esther Joanne Strickland

Department of Physics & Astronomy
University of Glasgow
Glasgow

Thesis submitted for the degree of
Doctor of Philosophy

September 1998

ProQuest LLC.
789 East Eisenhower Parkway
P.O. Box 1346
Ann Arbor, MI 48106 – 1346

Abstract

The cross section for the photoproduction of events containing three high transverse energy jets with a three-jet invariant mass of $M_{3J} > 50$ GeV has been measured with ZEUS at HERA. The data are compared with two different types of QCD prediction; $\mathcal{O}(\alpha\alpha_s^2)$ pQCD calculations which are leading order for the process under consideration and parton shower models which resum leading logarithms to produce multi-parton final states. The magnitude of the three-jet cross section is in good agreement with the $\mathcal{O}(\alpha\alpha_s^2)$ pQCD calculations; the parton shower models underestimate the cross section by 20 to 40%. The angular distribution of the three jets is inconsistent with a uniform population of the available phase space. In contrast, parton shower models and $\mathcal{O}(\alpha\alpha_s^2)$ pQCD calculations are able to describe the three-jet dynamics. Within the parton shower model the relative contribution to three-jet production from initial and final state radiation has been studied and the effect of colour coherence on the angular distribution is demonstrated for the first time.

Preface

The data collected at the HERA e^+p collider at DESY in Hamburg comprise a wealth of different interactions which have much to reveal on the structure of matter. In particular, the strong interaction between coloured partons, fundamental constituents of matter, can be investigated in detail. As an example, studies have been made of events where one or two high transverse energy jets of particles are observed in the final states of deep inelastic scattering and photoproduction interactions. These have allowed tests of QCD, and extracted information on, amongst other things, the structure of jets, the QCD evolution of the initial and final states, the structure of real and virtual photons and the gluon density of the proton.

These investigations have been taken further at the TEVATRON $p\overline{p}$ collider, where events containing three or more high transverse energy jets have enabled experimenters to go beyond the leading order two-jet final state and test current QCD calculations at higher order.

The data recorded by the ZEUS experiment at HERA has grown year-by-year since 1992. The 1995 and 1996 data samples have yielded a significant number of photoproduction events with three high transverse energy jets in the final state and a high three-jet invariant mass, $M_{3J} > 50$ GeV. As at the TEVATRON, the study of multijet final states provides important tests of perturbative QCD based calculations at and beyond leading order which are able to deepen our understanding of photon induced reactions at HERA and reveal universal factors which are important in determining the structure of the three-jet final state. A further motivation for this study is that this knowledge could be used to evaluate the type of QCD multijet background that might be expected in high energy hadronic interactions.

This thesis constitutes the first direct study of multijet events in photoproduction at HERA. The cross section for the production of three high transverse energy jets with a high three-jet invariant mass, $M_{3J} > 50$ GeV, is measured and the dynamics of three-jet production are investigated.

Chapter 1 describes briefly the underlying theory with particular emphasis on obtaining reliable QCD predictions. Also introduced are some of the physics processes studied at HERA and the contribution that they can make to the understanding of multijet final states. Details of the HERA accelerator itself are given in chapter 2 along with a description of the detector components and data selection procedures of the ZEUS experiment considered important for this study.

Chapter 3 describes in more detail the types of physics events recorded by the Jets and High E_T working group within the ZEUS Collaboration. The procedures employed to monitor the data quality after offline reconstruction, a task for which I was responsible during the 1996 and 1997 run periods, are also discussed.

The specific event selection used in this study is described in chapter 4; in particular the jet finding algorithm is presented and the criteria which define the three-jet event sample are motivated.

Monte Carlo event generators are used to provide simulated events which can yield information on the effects of the detector on the measured data such that they can be corrected for. The event generators used are discussed in chapter 5 and their ability to describe the raw ZEUS data is demonstrated. The event samples used are detailed in appendix A.

Chapter 6 describes the procedures carried out to correct the data for energy losses in the detector and for detector acceptance. The corrected data are shown in chapter 7 along with a study of the variation of the results when steps of the analysis were systematically changed. The corrected data with statistical and full systematic uncertainties are listed in tables in appendix B.

Chapter 8 compares the data to calculations from two groups of authors; Harris & Owens and Klasen. Also shown for comparison are the predictions of various Monte Carlo models. The conclusions drawn from these comparisons are summarised in chapter 9.

The main results of this study have been accepted for publication in Physics Letters B. Preliminary versions of these results have been presented at the Sixth International Workshop on Deep Inelastic Scattering and QCD (DIS '98) [1] and at the International Conference on High Energy Physics, Vancouver [2] by Dr L. E. Sinclair.

A previous study of colour coherence effects in multijet final states, in which I took part, was shown at the Future Physics at HERA Workshop [3]. The contribution to the proceedings is included as appendix C.

Another earlier study of multijet final states was presented at the Photon '97 conference [4]. My contribution to the proceedings constitutes appendix D.

Acknowledgements

Many people have contributed to the production of this thesis in many ways; to those not mentioned individually by name I apologise.

I am deeply grateful to Dr. Peter Bussey, my supervisor, and Dr. Laurel Sinclair for their continual help, guidance and support. Their dedication and enthusiasm for particle physics made as important a contribution to my studies as their expert advice.

My time working in the ZEUS Collaboration has been extrememely rewarding. I am very grateful to have had the opportunity to work on such an interesting project with so many talented individuals. The members of the Jets and High E_T working group, in particular, provided many interesting discussions and suggestions.

Laurel, Allan, Martin, Jane, Rob, Neil, Gavin and Sung-Won, who have had the dubious pleasure of sharing an office with me, have been great colleagues and friends. Thanks also to Nick, Tony and Ian for answering my many questions with such patience.

Catherine McIntyre and Susan Ketels also deserve a special mention for their outstanding support of staff and students at Glasgow and DESY.

I would also like to thank my friends in Glasgow, Hamburg and elsewhere, in

particular Laurel, Pat, Jane, Elizabeth, Marianne and Martin, for keeping my spirits up over the past three years and reminding me what fun is. My family are also a continual source of strength - thanks for being there for me.

Finally, thank you Gerard for encouraging and believing in me when I was close to giving up - with your love and support I can face anything.

Contents

List of Figures

List of Tables

Chapter 1

Introduction

1.1 Particle Physics and the Structure of Matter

The belief that the universe is structured in an orderly way and the desire to understand more about that order, have been prime motivators in scientific research for thousands of years. This century has seen dramatic scientific progress in both theoretical and experimental physics which has allowed us for the first time to see deep into the structure of matter.

At the turn of the century only two forces were recognised to play a part in the workings of the universe: gravitation and electromagnetism. Several major discoveries had just been made, such as X-rays, radioactivity and the electron, which greatly excited the scientific community. In 1911 Rutherford showed that the atom consisted of a small nucleus surrounded by clouds of electrons. He tested the structure of the atom by scattering alpha particles (the probe) off gold atoms (the target). He discovered that the pattern of the deflected alpha particles was consistent with scattering from a small, compact object within the atom, the nucleus. The principle of using particles to probe further into the structure of matter has been used ever since in particle physics experiments in search of deeper levels of substructure. The spatial resolution which can be studied is limited by the wavelength of the probe particles, $\lambda = h/p$, where p is the momentum of the particle and h is Planck's constant. Thus higher particle energies are required to see finer details of substructure, as illustrated in figure 1.1.

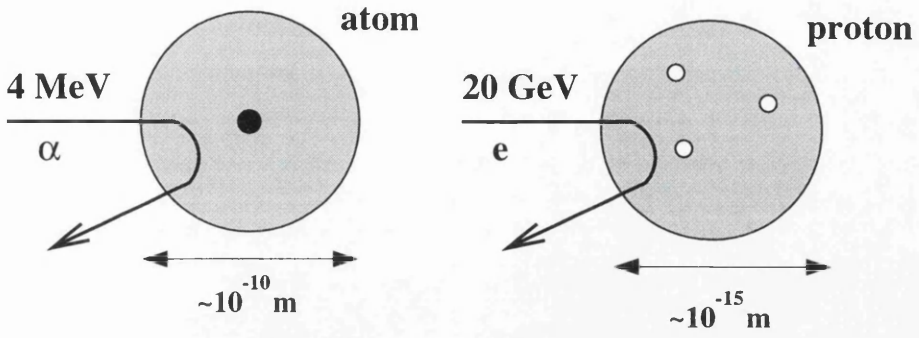

Figure 1.1: Testing the stucture of the atom and of the proton using particle probes. Here the α particles have energies of a few MeV but the electrons need to have energies of several GeV.

Today, the known elementary particles and their interactions make up the 'Standard Model' of particles physics, a description of which can be found in most textbooks, for example, 'Quarks and Leptons' by F. Halzen and A. Martin [5]. Of the four known fundamental forces only three are included in the Standard Model: electromagnetism, the weak force which governs radioactive decay, and the strong force which binds protons and neutrons together in the nucleus. Gravity is weaker by far even though it was the first force to be recognised. Its apparent strength lies in its cumulative effect and on the fact that we live in the vicinity of a very massive body, the Earth. The gravitational force acting between elementary particles at close distances is negligibly small in comparison to the other three forces.

Elementary particles can be grouped into three categories: leptons, quarks and gauge bosons. Leptons and quarks can be considered to consist of three 'generations' of particles. For leptons, the first generation consists of the familiar electron and the less familiar electron neutrino which is produced in β decay. Further generations contain the μ and τ particles, essentially heavy electrons, and their corresponding neutrinos.

Experiments at the Stanford Linear Accelerator (SLAC) in the late 1960's probed the structure of the proton with 20 GeV electron beams. They discovered that electrons scattered strongly off pointlike objects within the proton [6] in a process known as 'Deep Inelastic Scattering' (DIS) illustrated in figure 1.2(a). These constituents of the proton, or 'partons', turned out to be the 'quarks' that had been postulated by Gell-Mann[7] and Zweig[8] to describe the profusion of short lived baryons and mesons

which had been discovered in scattering experiments in the 1950's and 60's. Further experiments confirmed the existence of six quarks grouped, like the leptons, into three generations: up and down (the lightest quarks), charm and strange, and top and bottom (the heaviest).

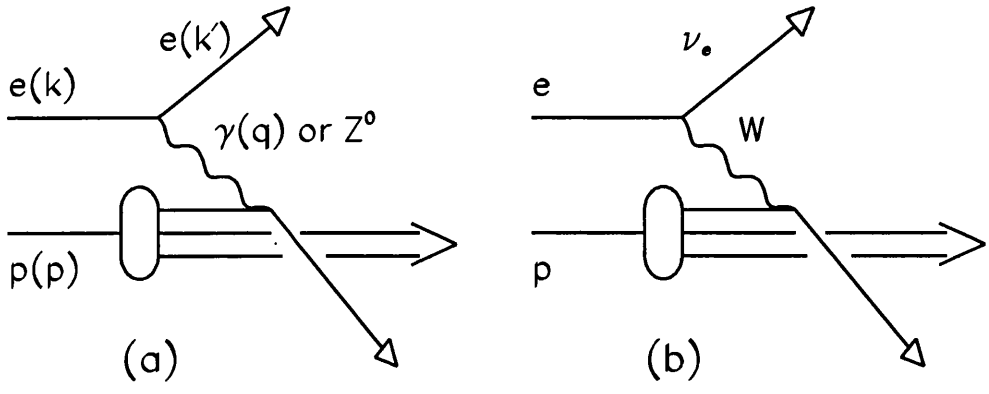

Figure 1.2: Leading order diagrams for DIS showing (a) neutral current where a photon or Z^0 is exchanged and (b) charge current where a W is exchanged and the incident electron changes to a neutrino. The normal nomenclature for the four-momentum is indicated.

Finally, the electromagnetic, weak and strong interactions between all of these particles can be described by the exchange of gauge bosons associated with the interaction. Momentum and energy are conserved at the vertices where bosons are emitted and absorbed. The exchanged particles can exist for a limited time (from the uncertainty principle of quantum mechanics) but without the well-defined mass of a real particle, and are said to be 'virtual'.

The electromagnetic force acts on all electrically charged particles, such as electrons and quarks, through the exchange of photons. Electromagnetic interactions are described by the theory of quantum electrodynamics (QED) which arose from the application of quantum and relativistic principles to the way in which charged particles interact with the electromagnetic field. The static potential has the form $-\alpha/r$ where r is the distance between particles and α ($\sim 1/137$) is the coupling constant. In order to calculate the behaviour of a given pair of interacting particles one must consider all possible processes, and the exchange, emission or absorption of more than one photon will be suppressed by further factors of α. QED cannot be solved with infinite precision

but since α is small any process can be described perturbatively by an expansion in terms of α, where higher orders are neglected. This approximation is so good that QED is the most precise and well-tested theory ever formulated, as discussed in [9].

The momentum transfer in an interaction due to the exchange of a boson is denoted q, see for example figure 1.2, and a kinematic variable $Q^2 \equiv -q^2$ can be defined. This can be thought of as the negative invariant mass squared of the exchanged boson and is also referred to as the 'virtuality'. As Q^2 increases the photon probes deeper through the e^+e^- pairs produced by the vacuum which shield the charge on the electron, an effect known as vacuum polarisation. The result is that the coupling α is not constant but varies with Q^2 and can be written as

$$\alpha(Q^2) \simeq \frac{\alpha}{1 - \frac{\alpha}{3\pi} \log \frac{Q^2}{m^2}} \tag{1.1}$$

for $Q^2 >> m^2$ where m is the mass of the electron. The extra term in the denominator which depends on Q^2 causes α to rise as Q^2 increases but for all presently attainable Q^2, α remains small enough that the perturbative approach is valid.

The weak force, which acts on all leptons and quarks, is mediated by the massive $W^{\pm}$ and Z^0 particles. The DIS diagrams in figure 1.2 show that electron-quark scattering can occur not only through exchange of a photon but also through exchange of a W or Z^0 boson. At small Q^2 the strength of the weak interaction ($\alpha_w \sim 10^{-6}$) is much lower than that of the electromagnetic interaction since the probability of producing virtual W or Z^0 particles is much less than of producing a photon of the same energy. However it has been shown that as the energy of the interaction increases the weak coupling strength increases. The result is that when the interaction energy is high enough for W or Z^0 exchange to be important the weak and electromagnetic couplings strengths are similar [10]. In fact, in the Standard Model the weak and electromagnetic interactions are manifestations of a common electroweak force [11].

The strong force arises through the exchange of gluons, the quanta of the colour field, between coloured partons such as quarks. The attribute of colour is analogous to the electric charge of the electromagnetic force and the theory of quantum chromodynamics (QCD) was developed to describe the way in which coloured particles interact.

QCD differs from QED in a crucial aspect; unlike photons, which are electrically

neutral, gluons carry colour charge and can couple to themselves. The contribution from the self-coupling of gluons in vacuum polarisation effects causes the behaviour of the strong coupling constant, α_s, to differ significantly from that of α. α_s is given by

$$\alpha_s(Q^2) \simeq \frac{12\pi}{(33-2N_f)\log\frac{Q^2}{\Lambda^2_{QCD}}} \tag{1.2}$$

where $N_f(=6)$ denotes the number of flavours and Λ_{QCD} is a fundamental parameter of QCD, the value of which is not predicted but has been determined experimentally to lie in the range 200-500 MeV.

The outcome of this form for α_s is that $\alpha_s \to 0$ as $Q^2 \to \infty$, a consequence known as 'asymptotic freedom' [12] since partons which are close together act as if no attraction exists between them. Another result is that $\alpha_s \to \infty$ as $Q^2 \to \Lambda^2_{QCD}$. In effect, this means that at small momentum transfers, or large distances, α_s is so large that the attractive force between partons keeps them confined inside hadrons. This is termed 'infrared slavery', as summarised in [13], and is thought to explain why free quarks have never been observed.

In practice the confrontation of QCD predictions with experimental observations is complicated. Since the coloured partons remain confined inside colourless hadrons a way must be found to isolate the behaviour of the asymptotically free quarks inside the hadrons from the confining mechanism. This can be achieved through scattering experiments between hadrons and a beam of probe particles. In DIS the resolution of the scatter has a $1/Q$ dependence; thus in high Q^2 (hard) scattering the exchanged particle becomes capable of resolving individual partons inside the hadron and interacting with them independently of the confinement mechanism. Lepton-hadron scattering tests electromagnetic and weak structure while hadron-hadron scattering provides information on the strong interaction. At $Q^2 \sim 3$ GeV^2 $\alpha_s \sim 0.2$ so perturbative QCD (pQCD) can predict the high Q^2 kinematic region.

To a good approximation, the cross section for any high Q^2 scattering process can be 'factorised' into a long distance, non-perturbative part describing the distribution of partons in the hadron and a short distance subprocess, perturbatively calculable from first principles, which describes the parton-parton or photon-parton scattering. The principle behind this factorisation is discussed in [14]. The distribution of partons in

the proton is a function of x, the fraction of the hadron's momentum carried by a given parton. The measured distributions have been shown to be 'universal'. For example, the proton structure is found to be the same whether calculated from ep, μp or νp scattering. The quark and gluon compositon of a particular hadron, once measured, can be used to describe any hard interaction experienced by that hadron.

As Q^2 increases, levels of structure within the hadron involving gluon emission and absorption and the creation of $q\overline{q}$ pairs can be identified. The evolution of the parton's observed structure with Q^2 is perturbatively calculable in QCD using the DGLAP evolution equations [15]. Any divergent contributions to the cross section can be absorbed into the definition of the parton distribution functions with the result that a dependence on Q^2 as well as x is acquired. This prediction has been experimentally verified by the ZEUS and H1 collaborations in measurements of the proton structure function, F_2 [16].

The final state of any hard scattering which produces quarks and gluons is also complicated by the confinement of quarks and gluons in colourless hadrons. Consider a high Q^2 process where a $q\overline{q}$ pair is produced. As the particles move away from the interaction point and, more importantly, from each other, the potential energy in the colour field between them increases. At a certain point the creation of an additional $q\overline{q}$ pair from the vacuum becomes energetically favourable. The new quarks interact with each other through gluon exchange. This process continues until the remaining energy is insufficient to create further partons and α_s is large enough that partons bind together into hadrons. The fragmentation of the original q and $\overline{q}$ thus forms jets of hadrons [17] which are collimated around the original direction of the partons. The summed momenta of the hadrons in the jets also bears a close resemblance to that of the original parton. This correspondence between partons and jets of hadrons forms the basis of the local parton-hadron duality principle [18].

The factorisation property discussed earlier can be expressed in the representation of the cross section for hard scattering processes. Figure 1.3 shows the interaction of partons a and b which carry respectively a fraction x_A and x_B of their parent hadron's momentum with a probability $f_{a/A}(x_A, Q^2)$ and $f_{b/B}(x_B, Q^2)$. The scattering between a and b produces partons c and d in the final state which manifest themselves as jets

of hadrons. The cross section for the process can be represented as

$$d\sigma(AB \rightarrow jets) = \sum \int \int dx_A dx_B f_{a/A}(x_A, Q^2) f_{b/B}(x_B, Q^2) d\hat{\sigma}(ab \rightarrow cd) \qquad (1.3)$$

where $d\hat{\sigma}(ab \rightarrow cd)$ is the perturbatively calculable cross section for the hard scattering partonic subprocess and the summation is over all possible subprocesses. The total cross section therefore consists of two parts; the structure functions of the hadrons in question, in which is included all the non-perturbative aspects of QCD and which are experimentally determined, and the perturbatively calculable hard QCD subprocess.

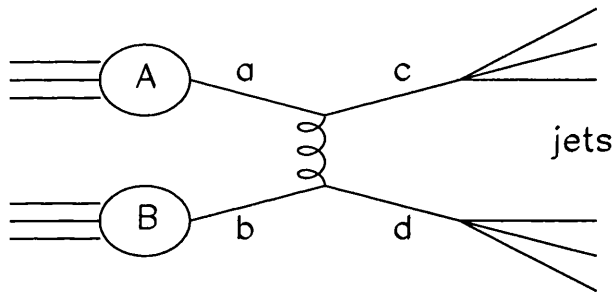

Figure 1.3: Schematic diagram of an interaction between two hadrons with jets produced in the final state.

1.2 γp Physics at HERA

The Hadron Elektron Ring Anlage (HERA) is the world's first ep collider and was built with the intention, amongst other things, of studying the structure of the proton through high Q^2 deep inelastic ep scattering, DIS, as shown above in figure 1.2. The range of available Q^2 values, from close to 0 GeV^2 up to 10^5 GeV^2, enables investigation of the proton structure at different scales. This section describes some of the wide range of physics processes which take place at HERA. HERA itself will be described in more detail in the following chapter.

The final state of a DIS event at leading order (LO), is indicated in figure 1.2. A scattered lepton (electron for neutral current or neutrino for charged current) with high transverse momentum (p_T) is accompanied by a quark which is struck out of the proton and fragments into a jet of hadrons which balance the lepton in p_T. The

spectator partons in the proton also form a jet of hadrons concentrated around the original proton direction, known as the proton 'remnant'. The Q^2 of the scatter can be calculated from the energy and angle of the scattered electron,

$$Q^2 = 2E_e E'_e(1 + \cos\theta'_e) \tag{1.4}$$

where E_e and E'_e are the energies of the initial and scattered electron and θ'_e is the angle of the scattered electron with respect to the proton beam direction.

The cross section for ep scattering has a $1/Q^4$ dependence hence low Q^2 processes dominate. The electron beam is therefore also the source of a large flux of almost real photons making HERA the ideal place to study photon-nucleon interactions, referred to as 'photoproduction'. HERA provides γp centre-of-mass energies of up to about 300 GeV, an order of magnitude greater than previous fixed target γp experiments.

Photoproduction processes occur in several different ways due to the complex nature of the photon. In the simplest case, the photon can interact directly with a parton in the proton as shown in figure 1.4(a). Here, although the virtuality of the photon is almost zero, a hard scale in the event can be provided by the invariant mass of the mediating quark propagator. Unlike DIS where the scattered electron and a single, p_T-balanced quark jet are found at LO, the final state in LO direct photoproduction consists of two high p_T quark or gluon jets balanced in p_T, the beam electron scattered through a small angle together with the proton remnant. The process is of order $\mathcal{O}(\alpha\alpha_s)$ due to the photon-quark and quark-gluon couplings.

At low photon virtuality the lifetime of a fluctuation into a $q\bar{q}$ pair is significant and the photon can acquire a hadronic structure. The first studies at photon-nucleon fixed target experiments revealed that the photon behaved essentially as a vector meson, such as a ρ, ω or ϕ meson, with the same quantum numbers as the photon. This behaviour inspired the Vector Meson Dominance model (VMD), reviewed in [19]. However, the existence of high transverse energy $q\bar{q}$ fluctuations without the formation of a bound state was predicted by QCD and was observed in measurements of the photon structure function in two photon reactions at e^+e^- collider experiments, reviewed in [20]. This perturbative component becomes increasingly dominant as the virtuality of the photon increases and the time available is insufficient to create a bound state. The photon

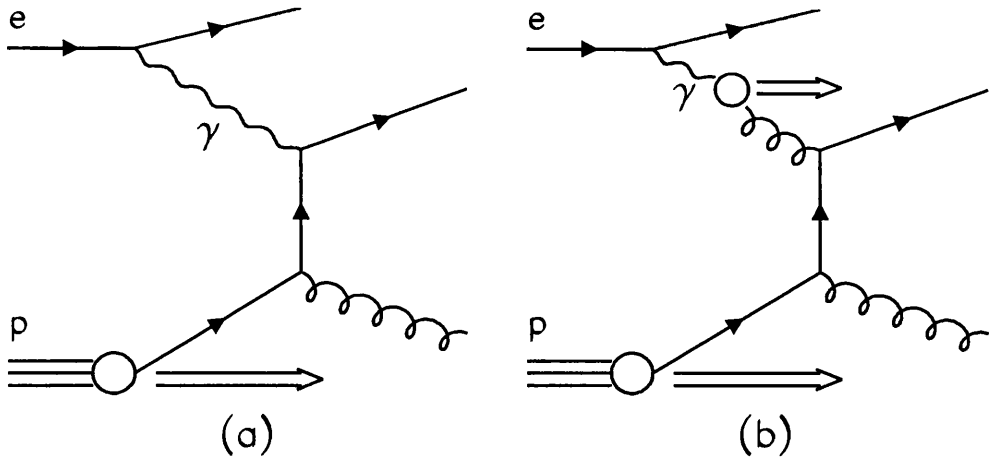

Figure 1.4: Leading order photoproduction diagrams showing examples of (a) direct (QCD Compton) and (b) resolved processes.

structure is thus modelled by a combination of two components, a perturbatively calculable 'anomalous' part and a non-perturbative VMD part which must be measured experimentally, and has an α/α_s dependence.

Photoproduction events where the photon acts as a source of partons are termed 'resolved'; an example of one such process is shown in figure 1.4(b). The final state differs from direct photoproduction in that a photon 'remnant' formed by the quarks and gluons not involved in the hard scatter is present. The resolved hard scatter has the same form as at hadron-hadron colliders and has order $\mathcal{O}(\alpha_s^2)$. The α/α_s factor from the photon structure function gives $\mathcal{O}(\alpha\alpha_s)$ overall with the result that resolved and direct processes are of the same order theoretically.

The separation between direct and resolved photoproduction, though well defined at leading order, is blurred at higher order. As an illustration, figure 1.5 presents a $2 \rightarrow 3$ scattering process in two slightly different ways. The first diagram, figure 1.5(a) could be considered a next-to-leading order (NLO) direct process. The second diagram shows the photon fluctuating into a $q\overline{q}$ pair where the high relative p_T of the q and $\overline{q}$ preclude the formation of a bound state. One of the partons then interacts with a parton from the proton. This would be considered a LO anomalous resolved process. The terms 'direct' and 'resolved' can thus only refer in a simple manner to LO diagrams.

The fraction of the photon's momentum taking part in the hard scatter, x_γ, is

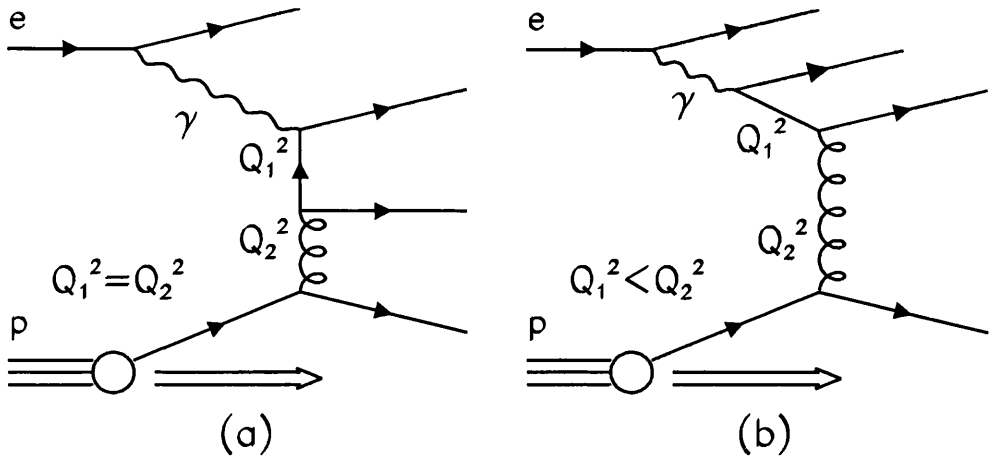

Figure 1.5: Photoproduction diagrams showing examples of (a) next-to-leading order direct and (b) leading order anomalous resolved processes.

naturally equal to 1 for LO direct and less than 1 for LO resolved events. An experimental observable x_γ^{obs} can be introduced which gives the fraction of the photon's momentum participating in the production of the final state jets,

$$x_\gamma^{obs} = \frac{\sum_{jets} E_T^{jet} \exp(-\eta^{jet})}{2E_\gamma} \tag{1.5}$$

E_T^{jet} and η^{jet} are the transverse energy and pseudorapidity[1] of the jets and E_γ is the energy of the photon. x_γ^{obs} is well defined and calculable at the parton level to all orders in perturbation theory. At LO replacing the sum over jets with the sum over the two final state partons reduces x_γ^{obs} to x_γ.

An operational separation of direct and resolved events can be made on the basis of x_γ^{obs}. Figure 1.6 shows the x_γ^{obs} distribution of ZEUS photoproduction data where two jets are identified in the final state [21]. The data show a clear peak at $x_\gamma^{obs} \sim 0.9$ and a tail to low values. The histograms represent the sum of the LO direct and LO resolved processes for a QCD based model. The shaded histogram indicates the contribution for the LO direct process only. It is evident that the peak at high x_γ^{obs} is associated with LO direct photoproduction while the events at low x_γ^{obs} come mainly from LO resolved processes. Applying a cut on x_γ^{obs} (at 0.75 in figure 1.6) provides a means for

[1]The pseudorapidity is defined as $\eta = -ln(tan\frac{\theta}{2})$, where the polar angle θ is taken with respect to the proton beam direction.

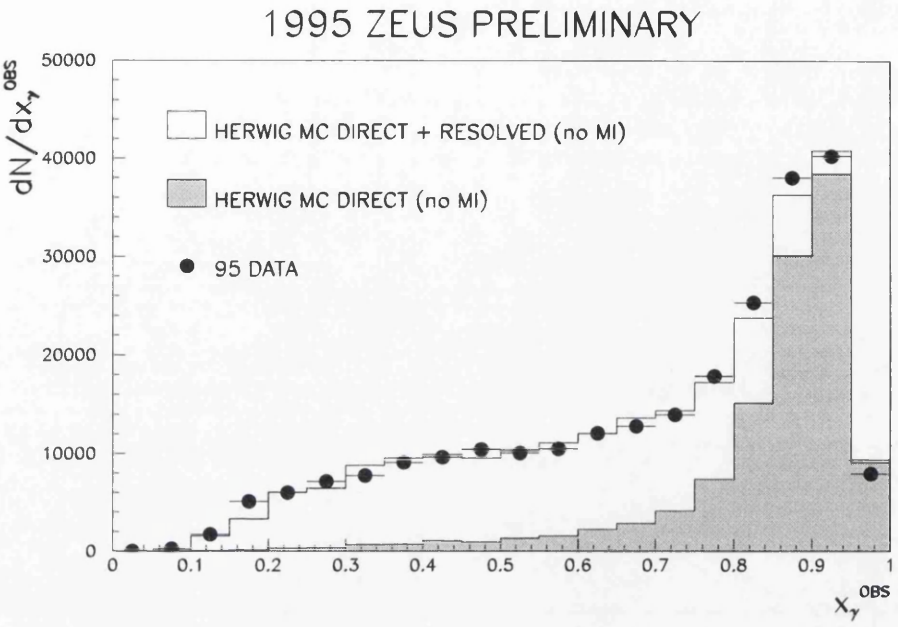

Figure 1.6: x_γ^{obs} distribution for 1995 ZEUS dijet photoproduction data. Shown for comparison are the predictions of the leading order Monte Carlo event generator HERWIG. The shaded histogram shows the contribution from LO direct processes only.

separating the data sample into direct and resolved enhanced subsamples. Resolved photoproduction is dominant in the low E_T^{jet} region while direct photoproduction, in which all the photon's energy contributes, dominates at high E_T^{jet}.

E_γ in equation 1.5 can be obtained from $E_\gamma = E_e - E_e' = yE_e$ where y is the fraction of the electron's momentum taken by the photon. y can be determined from the scattered electron

$$y_e \equiv 1 - (\frac{E_e'}{2E_e})(1 - \cos\theta_e') \tag{1.6}$$

where the mass of the electron is neglected. In most photoproduction events, however, the scattered electron is not observed. In this case y can be reconstructed from the hadronic energy flow in the final state using the 'Jacquet-Blondel' method [22].

$$y_{JB} \equiv \frac{\sum_i (E_i - p_{zi})}{2E_e} \simeq \frac{E_\gamma}{E_e} = y \tag{1.7}$$

where E_i is the energy of a particle or detector cell, p_{zi} is the longitudinal momentum and the sum runs over all particles or cells in the final state.

Finally, the multiparton nature of the proton and of the photon in resolved photoproduction leads to the possibility that secondary interactions may take place between the partons from the proton and photon, as illustrated in figure 1.7 [23]. Multiparton interactions are not included in any LO or NLO pQCD photoproduction calculations but can be modelled in the LO Monte Carlo event generators described in section 5.1. Their effect, if present, is that a QCD subprocess may be accompanied by a secondary or 'underlying' process whose energy flow is mainly at low E_T but which may also have a high E_T component.

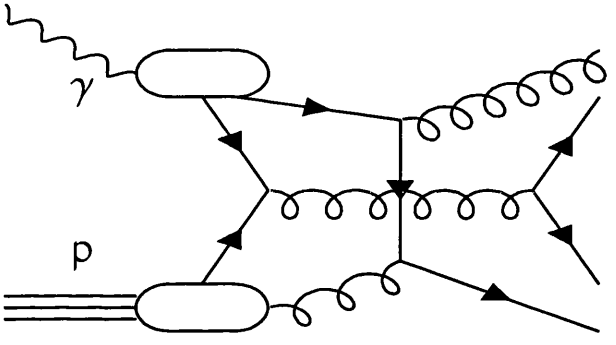

Figure 1.7: Schematic diagram of a resolved photoproduction interaction where two independent hard scatters take place between the constituents of the photon and proton.

1.3 QCD Coherence

QCD colour coherence describes phenomena arising from the interference of soft gluon radiation emitted between colour connected partons. Colour coherence is implemented in the parton shower in the Monte Carlo event generators discussed in section 5.1. For more detailed reviews see [24].

Physically, the main consequences can be separated into 'intrajet' and 'interjet' coherence. The term 'intrajet' refers to the way in which a jet evolves from an initial parton. The complex multiparton system that develops can be viewed as a sequence of parton branchings as shown in figure 1.8. For illustrative purposes, a q and $\overline{q}$ are produced with high transverse energy in the final state with an opening angle of θ_1. A gluon is then radiated from the quark with an angle θ_2 relative to the quark. In the case

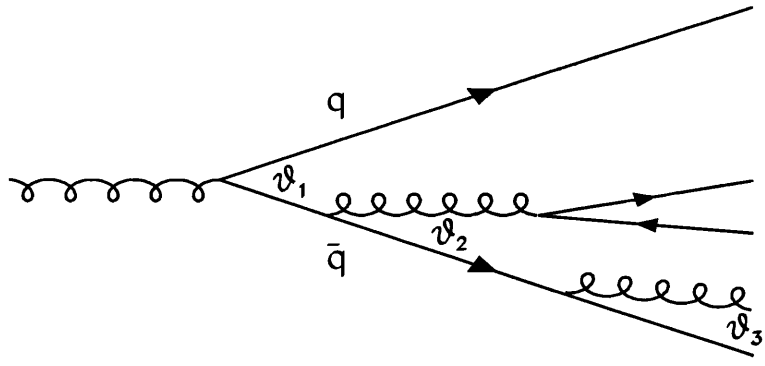

Figure 1.8: Schematic diagram showing the development of a shower of coloured partons and the angular ordering effect.

where $\theta_2 > \theta_1$ the gluon cannot resolve the q and $\overline{q}$ as separate particles and behaves instead as if it were radiated from the parent gluon (which produced the $q\overline{q}$ pair), assumed to be on shell. In general, this means that the description of the evolution of a jet in terms of successive parton splittings requires an angular ordering condition, $\theta_1 > \theta_2 > \theta_3 \ldots$, in order that each quark or gluon can resolve the parton from which it was emitted.

Interjet coherence refers to the manner in which the angular distribution of gluon radiation is affected by the colour flow in an event. In a high p_T hadronic interaction there is a background of soft particles, in addition to the gluon radiation involved in the evolution of the final state jets, whose behaviour depends on the colour topology of the whole event. A good example of this type of coherence is the string (or drag) effect observed in $e^+e^- \rightarrow 3$ jets interactions [25, 26].

Figure 1.9(a) shows the final state of the reaction $e^+e^- \rightarrow q\overline{q}\gamma$. The q and $\overline{q}$ carry colour charge and a 'string' can be drawn between them representing the colour field. The event is further illustrated in figure 1.9(b) with a gluon replacing the photon. Now the strings connecting the colour partners must be drawn between $q - g$ and $\overline{q} - g$; there is no colour connection between the $q\overline{q}$ pair. In the three-body plane the particle multiplicity in the region between the $q\overline{q}$ pair is lower in $q\overline{q}g$ final states than in the corresponding $q\overline{q}\gamma$ events. This suppression of gluon radiation, which can be visualised by way of strings indicating the colour fields, is due to quantum mechanical interference

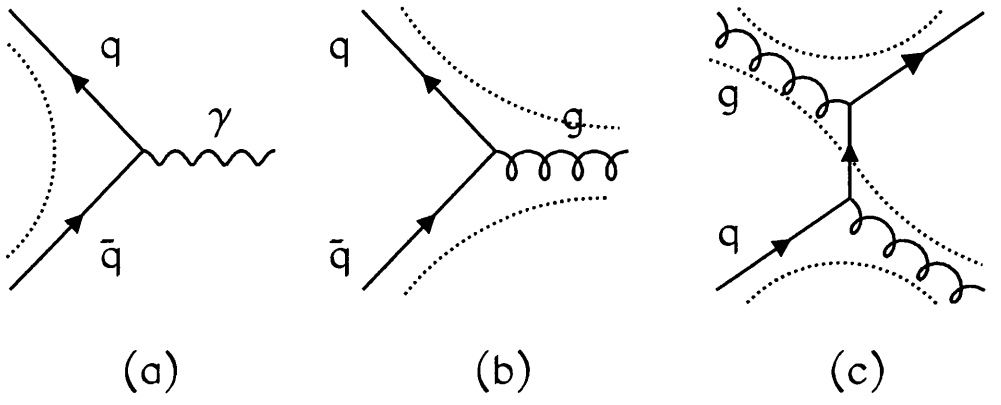

Figure 1.9: Schematic diagram showing the colour flows in (a) the final state of $e^+e^- \rightarrow q\bar{q}\gamma$, (b) the final state of $e^+e^- \rightarrow q\bar{q}g$ and (c) in a resolved photoproduction event.

effects. The predictions of particle distributions obtained from QCD taking into account colour flow are qualitatively similar to the predictions of the Lund string model [27] discussed further in section 5.1.

The signal of interjet colour coherence effects in particle distributions obtained from the final state in $e^+e^- \rightarrow$ 3 jets interactions is particularly clear due to the simple colour flows involved. An example of a hard scatter in resolved photoproduction, essentially the same as in hadron-hadron collisions, is shown in figure 1.9(c). Here the colour flow is more complicated and the strings connecting colour partners are shown linking initial and final state partons. Many processes with very different colour flows make up the total hard photoproduction cross section thus obscuring specific effects arising from the colour flow in an event.

In an attempt to overcome these difficulties the CDF and DØ experiments at the TEVATRON $p\bar{p}$ collider studied events containing high E_T jets where the soft radiation was itself hard enough to form secondary jets [28, 29]. Studying the spatial correlations between the softest jet in the event and the leading jets is similar to studying patterns of hadron multiplicity as was done in the final states of e^+e^- collisions. It was found that coherence was required in models to describe the data satisfactorily. A Monte Carlo study was carried out to investigate the sensitivity of such a study in hard photoproduction at HERA to colour coherence effects [3] and is included as appendix C.

1.4 Multijet Final States

Inclusive jet and dijet studies of hard photoproduction at HERA have established the existence of direct and resolved processes [30], tested QCD predictions [31, 32, 33, 34, 35, 36] and extracted information on the structure of real and virtual photons [37, 38, 39], the underlying event [40] and the structure of jets [41]. The study of multijet final states provides tests of pQCD at and beyond leading order, in particular providing a direct test of $\mathcal{O}(\alpha\alpha_s^2)$ pQCD calculations. It should also increase the knowledge of the type of multijet production mechanisms dominant in photoproduction.

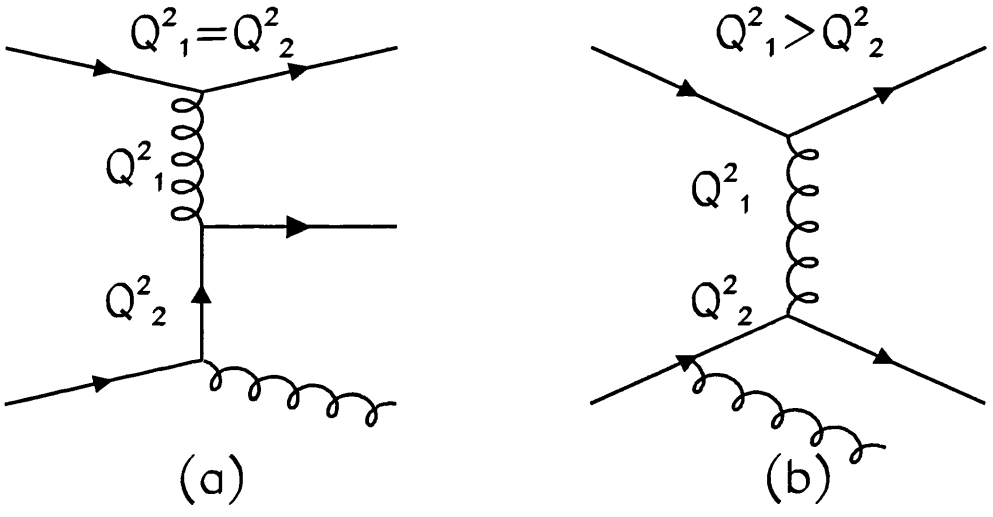

Figure 1.10: Two different ways of producing a three-jet final state in hard photoproduction.

A three-jet event of the type shown in figure 1.10(a) contains two hard scales, Q_1 and Q_2 which are similar in magnitude. A $2 \rightarrow 3$ $\mathcal{O}(\alpha\alpha_s^2)$ calculation, while next-to-leading order (NLO) for dijet photoproduction, is the lowest order of QCD calculation which could be used to describe this process. Figure 1.10(b) shows a three-jet event where the hard scatter is essentially a $2 \rightarrow 2$ process and the third jet is formed by gluon radiation from one of the partons involved in the hard scatter. Provided that the scale of the gluon radiation is much less than that of the hard scatter the gluon radiation from a parton can be described by DGLAP evolution. This approach for approximating higher order matrix elements using a $2 \rightarrow 2$ matrix element and an evolved 'parton shower' mechanism can be implemented using Monte Carlo techniques as detailed in

section 5.1. Confronting the predictions of these two methods with experimental data should shed light on the multijet production mechanisms which are important in hard photoproduction.

Multijet final states can be characterised by a set of kinematic parameters which span the multijet parameter space, facilitate the interpretation of the data within pQCD and simplify comparisons of events with different numbers of jets in the final state [42]. Measurements of such parameters have already been made for two-jet production at HERA [43] and for events containing three or more jets at the TEVATRON [44]. Here they are presented for inclusive three-jet photoproduction for the first time.

The variables chosen to describe the three-jet final state are the three-jet invariant mass, M_{345}, and four dimensionless variables, $\cos\theta_3$, ψ_3, X_3 and X_4 which are defined in the three-jet rest frame as :

$$\cos\theta_3 \equiv \frac{\vec{p}_{beam} \cdot \vec{p}_3}{|\vec{p}_{beam}||\vec{p}_3|} \tag{1.8}$$

$$\cos\psi_3 \equiv \frac{(\vec{p}_3 \times \vec{p}_{beam}) \cdot (\vec{p}_4 \times \vec{p}_5)}{|\vec{p}_3 \times \vec{p}_{beam}||\vec{p}_4 \times \vec{p}_5|} \tag{1.9}$$

$$X_3 \equiv \frac{2E_3}{E_3 + E_4 + E_5} = \frac{2E_3}{M_{345}} \tag{1.10}$$

$$X_4 \equiv \frac{2E_4}{E_3 + E_4 + E_5} = \frac{2E_4}{M_{345}} \tag{1.11}$$

where E and $\vec{p}$ are the energies and three-vectors of the jets in the three-jet rest frame. The jets are labeled 3, 4 and 5 in order of descending energy, ie the highest energy jet in the three-jet rest frame is labeled '3' and so on. $\vec{p}_{beam}$ is the three vector of the resultant beam direction, here $(0,0,E_p - E_e)$, where E_p and E_e are the proton and electron beam energies.

Figure 1.11 shows a schematic definition of the angular variables $\cos\theta_3$ and ψ_3. In the three-jet rest frame θ_3 is the angle between the highest energy jet and the average beam direction. This is similar to the angle θ^* used in dijet studies [43] which represents the angle between the jets and the beam direction in the dijet centre-of-mass. Since $\cos\theta_3$ depends on the highest energy jet only it should not be very sensitive to the

third jet in the event. The distribution is therefore expected to resemble the shape of the $\cos\theta^*$ distribution in dijet events and follow the Rutherford scattering form $\sim (1 - \cos\theta_3)^{-2}$ when the exchanged parton has spin 1.

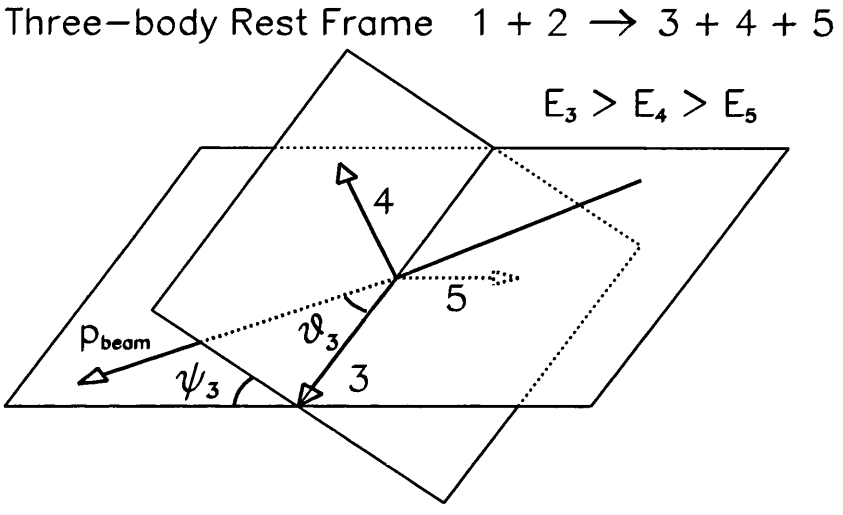

Figure 1.11: Schematic definition of angles used to describe the three-jet system in the three-jet rest frame.

ψ_3 is defined as the angle between the three-jet plane and the plane containing the highest energy jet and the average beam direction. It is undefined for dijet events and its shape may be considered as driven mainly by the properties of the third jet. In the case where the third highest E_T^{jet} jet comes from QCD radiation from one of the initial state partons involved in the hard scatter, the coherence property of QCD will tend to orient the third jet close to the plane containing the beam and the highest energy jet. The two planes will therefore tend to coincide leading to a ψ_3 distribution which peaks at 0 and π.

X_3 and X_4 are energy-sharing variables which show the fraction of the available three-jet centre-of-mass energy taken by the highest and second highest energy jet respectively. They are normalised so that $X_3 + X_4 + X_5 = 2$ and energy conservation restricts their range to $\frac{2}{3} < X_3 < 1$, $\frac{1}{2} < X_4 < 1$ and $0 < X_5 < \frac{2}{3}$.

The study of these multijet observables directly enhances our understanding of the strong force by providing a valuable test of QCD beyond leading order. It also extends our insight into the multijet production mechanisms important in photon-induced reactions.

Chapter 2

HERA and the ZEUS Detector

2.1 HERA

HERA (Hadron Elektron Ring Anlage) is situated at the Deutsches Elektron Synchrotron (DESY) in Hamburg, Germany and, as mentioned previously, is the world's first lepton-nucleon collider. Protons and electrons or positrons[1] are accelerated to 820 GeV and 27.5 GeV respectively in two independent rings. These rings are approximately circular and are 6.3 km in circumference. Experimental halls are situated at four equidistant points along the circumference of the ring as shown in figure 2.1. The general purpose experiments H1 and ZEUS are located in the north and south halls respectively. At these points the two beam pipes merge and the counterrotating beams are brought to collide. Resulting centre-of-mass energies of around 300 GeV are obtainable. There are also two beam-target experiments HERMES and HERA-B which are situated in the east and west halls respectively. HERA-B uses an internal target in the proton beam to study CP violation in the B system. HERMES measures the spin distributions of the quarks and gluons in the proton and neutron with an internal target in the HERA electron beam. Both ZEUS and H1 have been operational since 1992. Data-taking in HERMES started in 1995 and HERA-B is due to start taking data in 1998.

Electron energies of 27.5 GeV can be obtained by an acceleration complex which

[1] From 1994 - 1997 HERA operated with positrons only. For the rest of the study, unless stated otherwise, the term electron is taken to refer also to positrons.

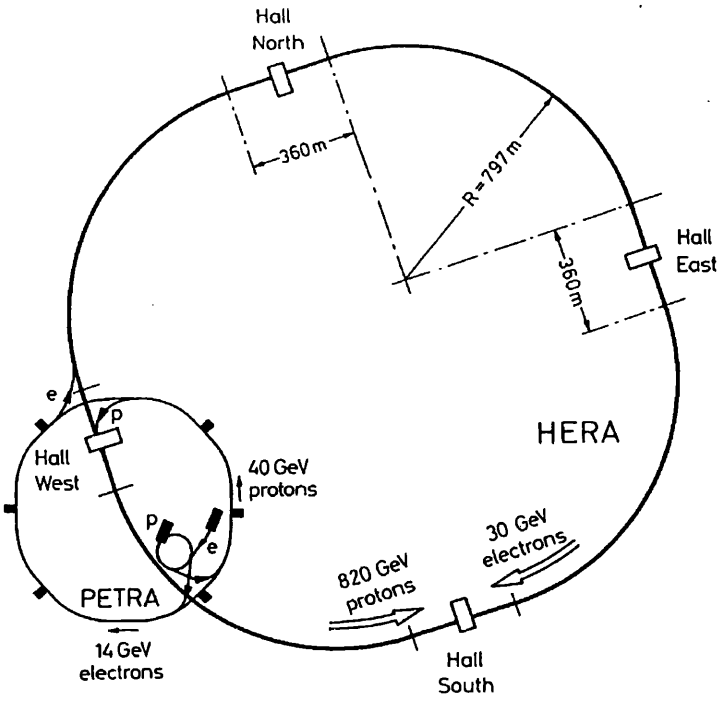

Figure 2.1: A schematic diagram showing the layout of the HERA accelerator complex.

consists of a combination of new and previously existing machines. Firstly 500 MeV electrons from a linear accelerator are injected into a small storage ring. They are then accelerated to 7 GeV in DESY II, an electron synchrotron, and transferred to PETRA II, the former PETRA e^+e^- storage ring rebuilt to act as a preaccelerator for electrons and protons. The process is repeated until PETRA is filled with 70 bunches of electrons. The bunches are spaced 28.8 m apart, the spacing they will have in the HERA ring. From PETRA the electrons are injected into the HERA ring and the process repeats until HERA contains 210 electron bunches.

The proton acceleration starts with a 50 MeV linear accelerator which accelerates negatively charged hydrogen ions. The electrons are stripped from the ions upon injection into DESY III, a proton synchrotron, and the protons are captured into 11 buckets, again 28.8 m apart. After being accelerated to 7.5 GeV the protons are injected into PETRA II and accelerated to 40 GeV. Up to 70 bunches are accumulated before transfer to the HERA ring.

Position monitors located ± 7 m from the interaction point are used to centre the beam. Timing information from the interaction point, IP, in the east hall is used to collide the beams accurately at the interaction point in the north and south halls with a time interval between bunch crossings of 96 ns.

Some bunches are left unpaired to study non-ep background processes which include the interactions of electrons and protons with the residual gas molecules in the beampipe and cosmic ray events. In 1995 there were 174 paired ep bunches, 15 e and 6 p unpaired bunches. The remaining bunches were left empty.

2.2 ZEUS Detector

The detection and study of the wide variety of physical processes which are produced at HERA provides many complex challenges. An experiment flexible enough to study known ep interactions, such as those described in chapter 1, and also to search for unknown processes must be able to detect and identify the products of these reactions. This places many different requirements on the experiment. The position, momentum and identity of charged particles must be known accurately. The energies of particles should be measured with excellent resolution over a wide range of energies for hadrons as well as electrons and photons. Fine segmentation is needed to provide good angular resolution. There should be full solid angle coverage such that few particles of interest escape undetected. The detector should also be capable of dealing with large fluxes of particles in the proton direction due to the large momentum imbalance between the incoming proton and electron beams. A number of different detector components are necessary to satisfy all these requirements.

A view of the longitudinal cross section through the ZEUS detector is shown in figure 2.2. In the ZEUS coordinate system the z axis follows the line of the beam direction. The nominal interaction point is taken as the origin and z is positive in the proton direction. The polar angle, θ, is measured with respect to the proton direction. The x and y axes point to the centre of the HERA ring (x) and directly upwards (y). The azimuthal angle, ϕ, is measured with respect to the x axis in the $x - y$ plane.

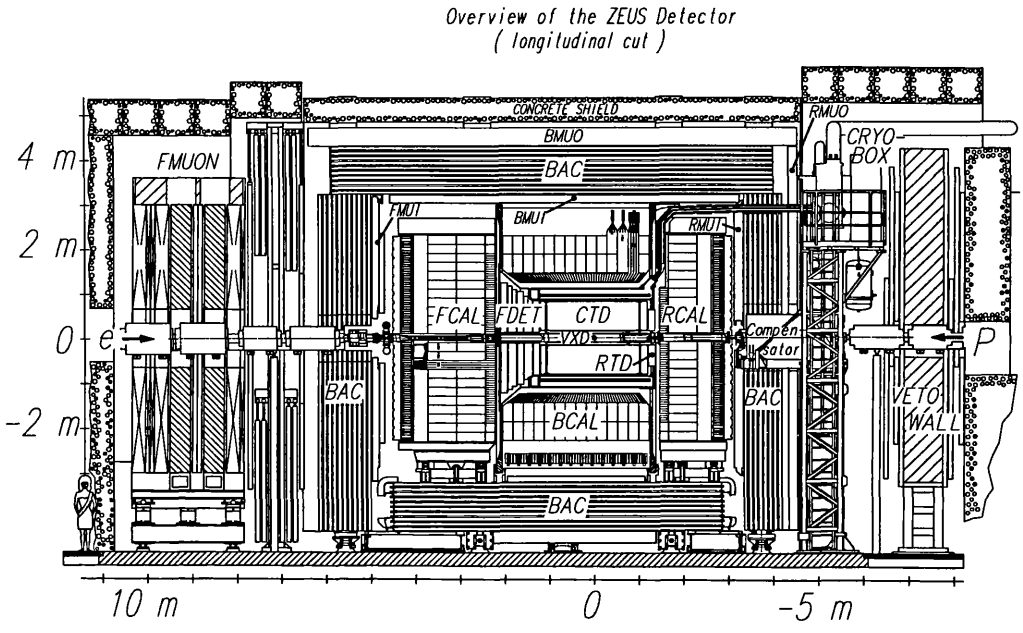

Figure 2.2: A schematic diagram showing a longitudinal section through the components which make up the ZEUS Detector.

The innermost detectors are the vertex detector, VXD [2], and the tracking detectors CTD and FDET. The CTD tracks charged particles in the central region while the FDET encompasses a range of tracking detectors in the forward and rear regions. A solenoid surrounds the tracking detectors providing the magnetic field required for their operation. The main calorimeter, which measures particle energies, encircles the solenoid and is divided into forward, central and rear components, FCAL, BCAL and RCAL. This in turn is enclosed in the backing calorimeter, BAC. Finally muon chambers, FMUON, BMUO and RMUO, surround the detector. Much of the instrumentation is situated in the proton direction due to the high concentration of particles resulting from the asymmetry in the beam energies.

Additional detectors not shown in figure 2.2 are located downstream of the electron and proton beams to tag particles produced at small angles to the beam direction and help reject background. The luminosity monitor (LUMI) and beam pipe calorimeter (BPC) are situated downstream of the electron beam and measure small angle electrons.

[2]The VXD was removed at the end of the 1995 data-taking period.

The LUMI also measures photons. The leading proton spectrometer (LPS) and the forward neutron calorimeter (FNC) are located downstream of the proton beam and measure high energy protons and neutrons. The C5 counter and the vetowall are situated respectively 3.2 m and 7.3 m from the interaction point upstream of the proton beam and are used to reject background interactions. The C5 counter measures the timing of the positron and proton bunches and detects proton beam interactions upstream of the IP. The vetowall protects the main detector from particles from the beam halo which accompanies the proton beam.

The main components used for this study were the calorimeter, the central tracking detector and the luminosity monitor (not shown). These will be detailed in the following sections. A full description of the ZEUS detector is given in [45].

2.2.1 Calorimeter

The ZEUS calorimeter [46] is designed to measure the energy of particles with an excellent resolution over a wide range of energies. It provides full angular coverage, fine segmentation for good position determination and has a fast reponse time.

Particles entering a calorimeter interact with the detector medium producing secondary particles. These in turn generate more particles until all, or nearly all, of the incident particle energy is used up to give ionisation or excitation of the detector medium. A sampling of this ionisation or other excitation energy can then be used as a measure of the initial particle energy; this is the principle behind a sampling calorimeter. For example, layers of scintillating material placed alternating with the absorbing material emit light due to the interaction with the ionising particles. This light signal can be used to measure the energy of the incident particles.

Different incident particles, however, interact with the detector medium in different ways. An electron, upon contact with a dense material, experiences deceleration due to the electric field of the atomic nuclei and radiates high energy photons by bremsstrahlung. The photons in turn produce e^+e^- pairs which also undergo bremsstrahlung, and so a shower develops. After travelling a distance of X_o, the radiation length of the medium, the energy of the electron is reduced on average by a factor of e. The shower of particles continues to grow until the loss of energy through

ionisation dominates and no further radiation occurs. Eventually almost all of the energy of the shower is used up to produce ionisation in the medium. The shower from an electromagnetic particle can be contained in a small volume by use of a material with small X_o as the absorbing medium.

The interaction of hadrons with the detecting medium is somewhat different. An incident hadron collides inelastically with the nuclei of the medium with the production of secondary hadrons. These in turn undergo inelastic collisions and a hadronic shower develops. This type of shower differs from an electromagnetic shower in several ways.

Firstly, the longitudinal development of the shower is determined not by X_o but by the nuclear absorption length, λ. The differences between electromagnetic and hadronic showers can be used for particle identification; the best results are obtained when the absorbing medium is made from a heavy element. In this case λ is large compared to X_o ($\lambda \sim 25X_o$) so much more material is required to contain a hadronic shower than for an electromagnetic shower.

Secondly, ~30% of the energy of the incident hadron is taken up by the break-up of nuclei and nuclear excitation [47]. This means that the output signal obtained for a hadron is typically lower than that of an electromagnetic particle of the same energy. The situation is further complicated in that π^0's produced in hadronic showers decay electromagnetically to two photons which give rise to electromagnetic showers. The response of the calorimeter to hadrons will therefore vary as a function of the number of π^0's produced.

One way of overcoming these problems is to find a mechanism which 'compensates' the energy losses in hadronic showers. This is achieved in the ZEUS calorimeter by the use of depleted U^{238} as the absorbing medium. Plates of uranium are interleaved with a hydrogenous scintillating material (SCSN-38) which samples the shower development. The extra energy released by the fast neutron fission of the U^{238} and neutron-proton scatters in the hydrogenous detector make up for energy losses due to nuclear break-up. The relative thickness of the absorber and scintillator plates is adjusted to obtain equal energy response to both electromagnetic and hadronic showers to within 1-2%.

The calorimeter (CAL) is divided into three overlapping sections which cover the forward (FCAL), barrel (BCAL) and rear (RCAL) regions. These components cover the

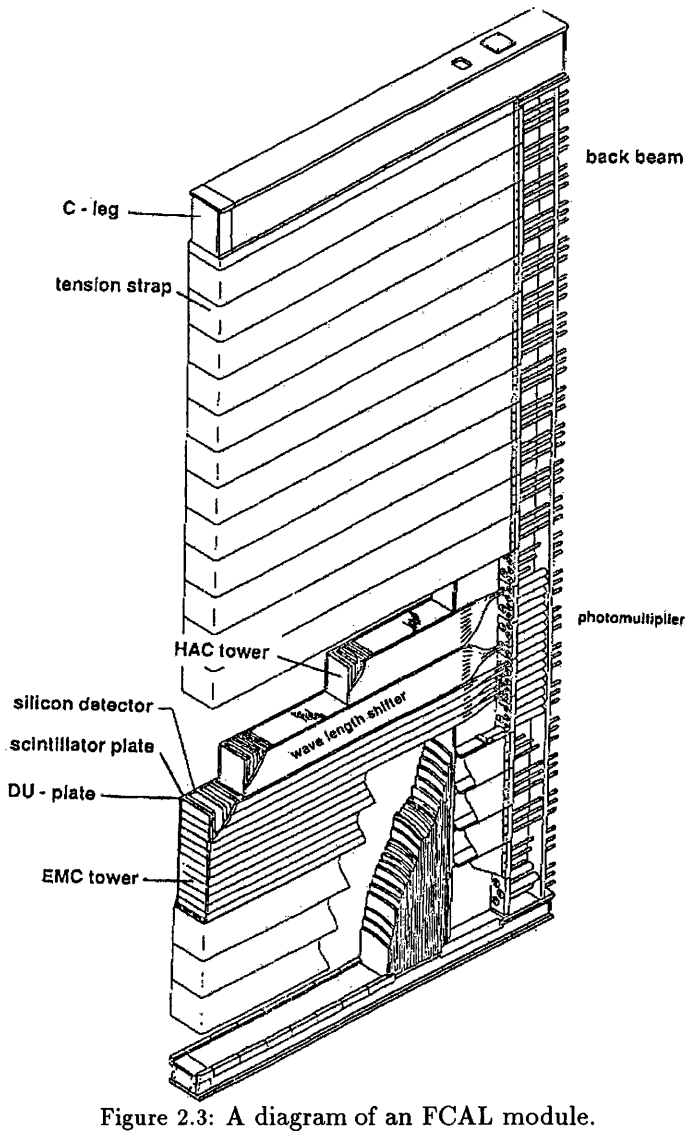

Figure 2.3: A diagram of an FCAL module.

polar angles (pseudorapidity) $2.2^o < \theta < 39.9^o$ ($3.95 > \eta > 1.01$), $36.7^o < \theta < 129.1^o$ ($1.10 > \eta > -0.74$) and $128.1^o < \theta < 178.4^o$ ($-0.72 > \eta > -4.27$) respectively and provide a solid angle coverage of 99.8% in the forward hemisphere and 99.5% in the backward hemisphere. The resolution achieved has been measured in test beams to be

$$\frac{\sigma_E}{E} = \frac{0.18}{\sqrt{E}} \oplus 0.01 \text{ for electrons}^3 \tag{2.1}$$

$$\frac{\sigma_E}{E} = \frac{0.35}{\sqrt{E}} \oplus 0.02 \text{ for hadrons} \tag{2.2}$$

where E is measured in GeV.

[3] $\oplus$ denotes addition in quadrature

Each of the CAL components has a modular structure to obtain good spatial resolution. One such module, from the FCAL, is illustrated in figure 2.3. The module is constructed of towers which are divided longitudinally into electromagnetic (EMC) and hadronic (HAC) sections which are read out separately. Uranium and scintillator plates are interleaved to a total depth of 1λ in EMC sections and 6-3λ in HAC sections depending on the position of the module. Thicker calorimetry is required in areas where a large flux of very energetic particles are produced, such as around the FCAL beampipe. The HAC is therefore thickest in the FCAL (6λ) and in the BCAL (4λ) and is read out in two separate sections in these components.

The position resolution is governed by the dimensions of the scintillator tiles used. Electromagnetic showers are well collimated so the granularity is finest in the EMC where the typical cell size is 5×20 cm^2. Since hadronic showers are broader than electromagnetic showers HAC cells can be larger; the typical size is 20×20 cm^2. In total there are almost 6000 cells to read out. Wavelength shifters placed along both sides of the cell engineer the transmission of light out of the system. The light travels along the shifters by internal reflection and is converted into an electronic signal by photomultiplier tubes. Photomultiplier tubes generate random noise; therefore to obtain a reliable signal each cell is read out by a photomultiplier at each end and coincidence of both is required. Accidental coincidence rates are small due to excellent timing resolution. The rapid rise time of pulses from the scintillator allows the time to be measured to better than 1 ns for incident particle energies above 4.5 GeV.

The natural radioactivity from U^{238} also gives rise to a signal from the photomultipliers. The uranium plates are encased in steel as a safety measure and to reduce this signal to a level where it does not interfere with the measurement. The residual signal from the uranium is known to better than 0.2% and enables a continuous calibration of the gain of the photomultiplier tubes at a 1% precision.

2.2.2 Central Tracking Detector

Charged particle trajectories and momenta are measured by the Central Tracking Detector (CTD) [48]. This is a cylindrical drift chamber covering the polar angles from 15^o to 164^o. Charged particles pass through a gas-filled chamber ionising the

gas molecules to produce electrons. The composition of the gas is 90% argon, 8% carbon dioxide and 2% ethane. The ionisation electrons drift according to the electric and magnetic fields acting upon them giving rise to pulses on sense wires that they come into contact with. A pulse is considered to be a 'hit' if its amplitude exceeds a particular threshold. The sense wires are arranged into nine superlayers consisting of eight wire layers. Five superlayers ('axial') have their wires parallel to the axis while the other four have wires positioned at a small angle (5^o) to the axis ('stereo'). Layers are alternately axial and stereo. The stereo wires allow the z coordinate of a particle to be measured with a resolution of 1 mm. Wires in superlayers one, three and five are read out at each end of the chamber. The difference in time of the arrival signals at both ends of the chamber can be compared to obtain a fast measurement of the z position of the original hit. Hits in a superlayer and their associated drift times are used to construct track vectors. Track vectors from different superlayers are then linked together to reconstruct the charged particle's trajectory.

The momentum of a charged particle can be calculated from the curvature of its motion in a magnetic field. Since charged particles produced in ep collisions at HERA can have high transverse momenta a large magnetic field is required to produce a useful degree of curvature. A magnetic field of 1.4 T is applied and the resulting curvature gives a transverse momentum measurement with a resolution of

$$\frac{\sigma_{p_T}}{p_T} = 0.005 p_T \oplus 0.016 \tag{2.3}$$

for p_T in GeV, for particle momenta of greater than 150 MeV where the track passes through all nine superlayers. The first term is due to the spatial resolution of hits while the second arises from multiple Coulomb scattering.

2.2.3 Luminosity Measurement

The luminosity at HERA is measured via the rate of the bremsstrahlung process $ep \rightarrow ep\gamma$. The luminosity monitor (LUMI) consists of two separate detectors - one of which measures the scattered electron and the other the photon [49].

A lead-scintillator sampling electron calorimeter, situated 35 m from the interaction point in the electron direction, measures the energy of electrons scattered at small angle

to the beam direction. It detects electrons with $\theta_e' < 6$ mrad with an efficiency greater than 70% for $0.35E_e < E_e' < 0.65E_e$. A sample of photoproduction events can be isolated where the electron has been scattered with $\theta_e' < 6$ mrad and is detected in the LUMI. An upper limit of $Q^2 < 0.002$ GeV^2 is set on the virtuality of the photon for these events from the maximum angle an electron can have while still escaping along the beam pipe, i.e., 6 mrad. The LUMI tagged photoproduction events provide a well characterised sample which can be used to find ways of reducing background in photoproduction events where the electron is not detected.

A photon detector is located close to the proton beam 107 m downstream of the interaction point in the direction of the electron beam. A carbon filter is used to absorb synchrotron radiation, a Cerenkov counter vetos charged particles and finally a lead-scintillator sampling calorimeter measures the energy of the photon. The geometrical acceptance is 98% for the process $ep \rightarrow ep\gamma$ and is independent of the energy of the photon. The luminosity measurement is obtained from the rate of photon events measured in this calorimeter corrected as follows :

$$R_{ep} = R_{tot} - R_{unp}\frac{I_{tot}}{I_{unp}} \tag{2.4}$$

where R_{tot} is the total rate, R_{unp} is the rate in unpaired electron bunches, I_{tot} is the total current and I_{unp} is the current in unpaired electron bunches. This corrects for beam gas backgrounds. The value of the integrated luminosity in 1995 and 1996 was measured to an accuracy of $\pm$ 1.5%.

2.3 Online Data Selection

An experiment must be able to select good physics events while rejecting the background events which may dominate the desired signals by a factor of 10^3-10^5 [50]. At HERA, the bunch crossing time of 96 ns is much less than the time taken for the detector to come to a decision on a particular event. Crossings occur at a rate of 10.4 MHz yet only a few events per second can be written out and stored. In this situation every bunch crossing must be analysed and the detector must be able to discriminate quickly, and without dead-time, between background and events containing useful information. Several types of background are present:

non-*ep* background The main contributions occur from the interaction of beam particles with the molecules of gas remaining in the beam pipe. Cosmic rays also give rise to background.

unwanted *ep* processes At the design luminosity of 1.5×10^{31} cm^{-2}s^{-1} the rate of *ep* collisions is around 200 Hz [51] and is dominated by soft photoproduction. Not all of these events are of interest and only a fraction can be written to tape. Decisions must be taken online to ensure that rare interactions of interest for study are saved. Interesting processes whose analysis is not statistically limited are prescaled, i.e. only a fraction of the accepted events are written out. The remaining *ep* processes must be rejected.

The data selection process is organised into three stages with more time and information available at each successive stage to make a decision. A schematic overview of this process is shown in figure 2.4.

First Level Trigger (FLT) The time between bunch crossings, 96 ns, is much less than the time needed even to read out all the components of the detector. A pipeline 52 bunch crossings in length is set up to store data while the decision to continue to process or to reject the event is made. Data from each component are processed in parallel and then brought together for a global FLT decision (GFLT). Quantities available at this stage of processing are necessarily roughly measured due to the time constraints - only 5 μs are available from the bunch crossing to the decision arriving at the front end electronics. Nevertheless, the FLT manages to define an event rate at $\sim$ 1 kHz with strong background rejection applied through timing cuts (see section 4.1).

Second Level Trigger (SLT) The SLT accepts data at a rate of 1 kHz. Again the detector components process the data in parallel before a global decision is made (GSLT). The data are pipelined (16 bunch crossings long) and 10 ms, taking into account the lower event rate and the data pipeline, are available to analyse the event. This enables more detailed processing and reduces the rate by a further factor of 10.

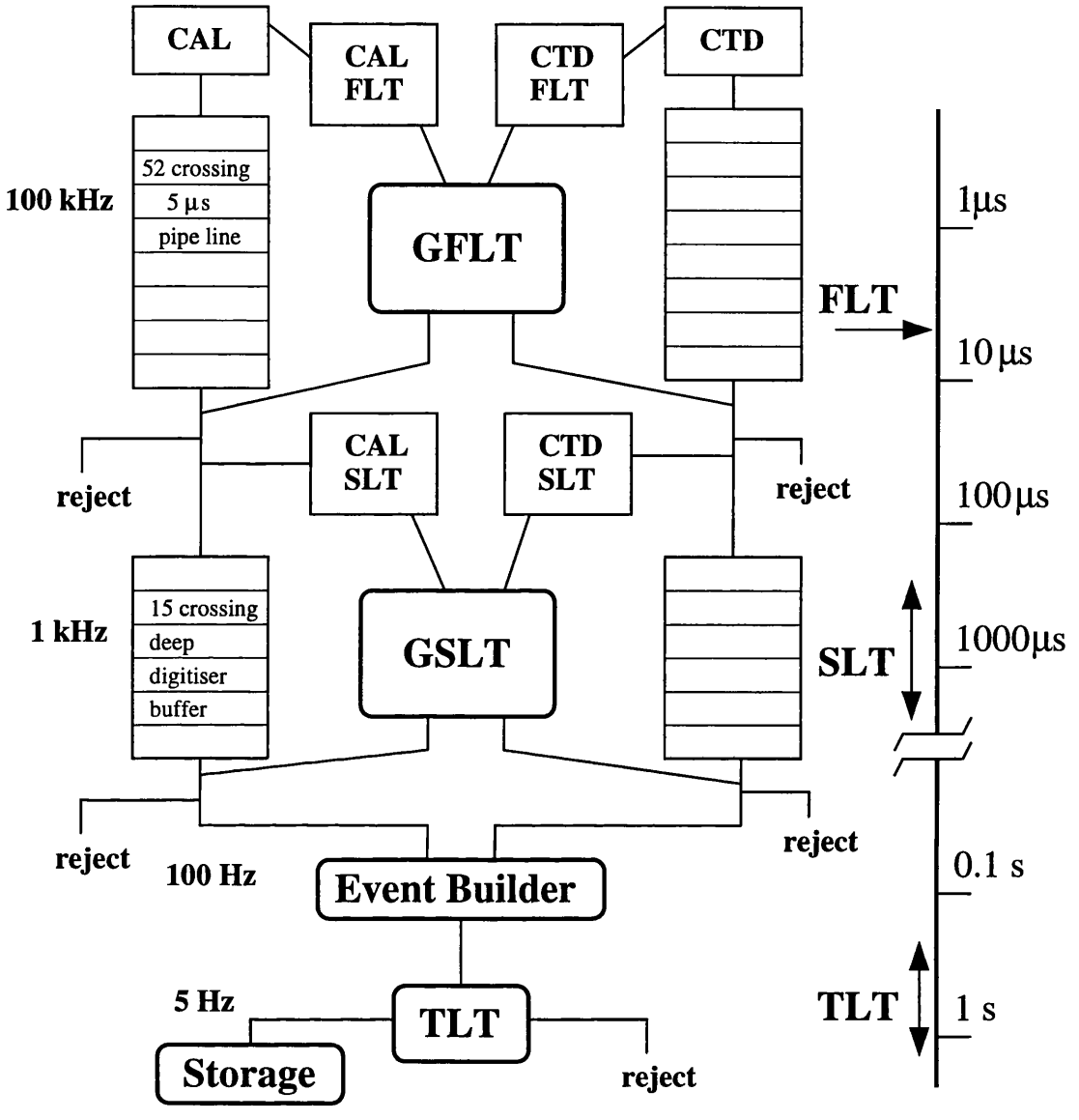

Figure 2.4: A schematic diagram of the processes which make up the ZEUS three-level trigger system.

Third Level Trigger (TLT) Events satisfying the SLT are reconstructed by the Event Builder, which has access to the full event record, and are then passed to the TLT. Selection algorithms similar to those used in offline analysis can be implemented at the TLT, for example, jet finding and electron finding algorithms are applied. Events are written to offline storage at a rate of less than 10 Hz which is imposed by the DESY data transfer and storage limitations.

The online selection used to obtain the data presented in this study is shown in detail in section 4.1.

The criteria used to select events have become more sophisticated through experience gathered over the past years of data-taking. Increases in the delivered luminosity since data-taking began have led to a higher rate of ep interactions. It is therefore essential to review continually the priorities of the data selection to ensure that the most important events are available for analysis. Figure 2.5 shows the FLT, SLT and TLT rates for 1993, 94, 96 and 97 as a function of luminosity. Although the luminosity has increased by a factor of 20 the TLT rate was only slightly higher in 1997 than it was in 1993.

2.4 Summary

The ZEUS experiment consists of a sophisticated, highly complex group of detector components. These provide information on particle energies, momenta and identity which are necessary to obtain insight into the physical processes which produced them.

Several components are particularly important for the analysis presented here. The calorimeter enables high transverse energy jets to be constructed with excellent position and energy resolution. The CTD provides a measurement of the position in space at which the interaction occured and helps reduce background. The LUMI photon and electron calorimeters provide an accurate determination of the luminosity delivered and tag a sample of pure photoproduction events.

The online data selection consists of a three-level trigger system which rejects background and selects particular types of physics processes reducing the rate from 100 kHz to less than 10 Hz.

The following chapter will deal with further offline data selection procedures and monitoring the quality of the data selected by the TLT.

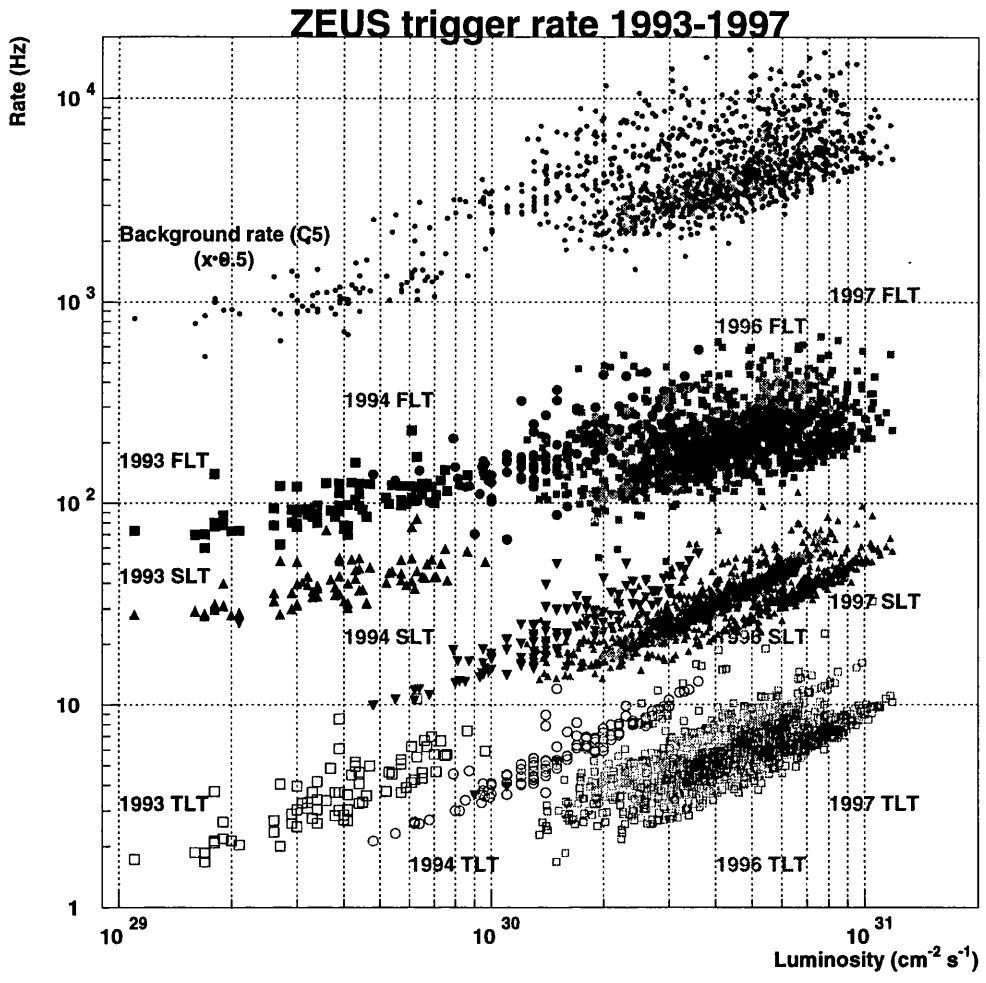

Figure 2.5: Trigger rates from the first, second and third level triggers as a function of luminosity and data-taking period. The different symbols used indicate different trigger levels and different data-taking periods.

Chapter 3

Data Selection and Data Quality Monitoring

3.1 Offline Data Processing

Chapter 2 described the three-level online data selection procedure employed by the ZEUS Experiment. A further stage of data selection is applied offline to facilitate data analysis. Events passing the TLT are fully reconstructed here. Complex and time-consuming algorithms, such as track-fitting, are applied to the data at this stage when up-to-date calibration constants are available. During the reconstruction it is also possible to flag events which have passed a particular selection at the TLT. The flag given is known as a Data Summary Tape (DST) bit and information summarising the DST bits set is available for each event. An analysis can look then at the subsample of the data corresponding to a particular DST bit rather than examining the complete data set, thus saving computer time. There is also the opportunity to apply additional cuts to the data when setting the DST bit rather than changing the TLT selection. A subsample of the data containing events which are considered particularly important and interesting can also be selected during the offline reconstruction. These 'hotline' events are written immediately to disk enabling rapid analysis.

Responsibility for the recording and analysis of particular types of physics within the ZEUS Collaboration was divided between four working groups. This work was carried

out in the Jets and High E_T Phenomena (JHET) working group which encompasses a wide range of studies of jets in deep inelastic scattering and photoproduction and of particle distributions in hadronic final states. These analyses seek to test QCD and extract information on, amongst other things, jet structure, QCD evolution of the initial and final state, the structure of real and virtual photons and the gluon density of the proton.

During the 1996 run period 23 different physics filters, also referred to in the following as TLT branches, were applied by the JHET group at the TLT. In addition to general cleaning cuts each filter involved specific requirements aimed at selecting the variety of physics events requested for the analyses tackled by the group. The most widely used quantities for triggering are energy deposits in the CAL and the transverse energy (E_T^{jet}) and pseudorapidity (η^{jet}) of jets. Hits in BPC, FNC and LPS tagging detectors are also used. A brief description of the more important selection criteria of these filters follows:

Very High E_T: $E_T^{cone} > 25$ GeV, where E_T^{cone} is the transverse energy deposited in the CAL outwith a cone of 10^o around the FCAL beam pipe.

Inclusive Jet: At least one jet with $E_T^{jet} > 10$ GeV and $\eta^{jet} < 2.5$.

These two branches are particularly useful for the measurement of inclusive high E_T jet quantities.

High p_T Track I: At least one vertex fitted track.

High p_T Track II: At least one vertex fitted track with $p_T > 2$ GeV and an electron tagged in the LUMI detector with $E_e > 5$ GeV.

High p_T Track III: At least one vertex fitted track with $p_T > 4$ GeV.

High p_T Track IV: At least one vertex fitted track with $p_T > 5$ GeV - disabled for most of the run period.

High p_T Track V: At least one vertex fitted track and strangeness enhancement.

The branches requiring high p_T tracks are aimed at studying heavy flavour production.

FNC Inclusive Jet: A hit in the FNC and at least one jet with $E_T^{jet} > 4$ GeV and $\eta^{jet} < 2.5$.

FNC Dijet: A hit in the FNC and at least two jets with $E_T^{jet} > 4$ GeV and $\eta^{jet} < 2.5$.

These branches study jet production in events containing a leading neutron.

BPC Inclusive Jet: A hit in the BPC and at least one jet with $E_T^{jet} > 4$ GeV and $\eta^{jet} < 2.5$.

BPC Dijet: A hit in the BPC and at least two jets with $E_T^{jet} > 4$ GeV and $\eta^{jet} < 2.5$.

The requirement that the scattered electron be tagged in the BPC enables the study of intermediate Q^2 processes which should extend our understanding of the transition region between DIS and photoproduction.

Very High LRG: $E_T^{cone} > 11$ GeV and no energy in the region around the FCAL beampipe.

Dijet LRG: At least two jets with $E_T^{jet} > 4$ GeV and $\eta^{jet} < 2.5$ and no energy in the region around the FCAL beampipe.

LRI: At least two jets with $E_T^{jet} > 4$ GeV and $\eta^{jet} < 2.5$ and $\eta_1^{jet} - \eta_2^{jet} > 3$.

These three branches select events containing rapidity gaps to enable the study of diffractive processes.

Very High LPS: A hit in the LPS and $E_T^{cone} > 8$ GeV.

Dijet LPS: A hit in the LPS and at least two jets with $E_T^{jet} > 4$ GeV and $\eta^{jet} < 2.5$.

Jet production can be studied in events where the proton does not dissociate and is tagged in the LPS.

Low E_T Dijet: At least two jets with $E_T^{jet} > 4$ GeV and $\eta^{jet} < 2.5$.

High E_T Dijet: At least two jets with $E_T^{jet} > 6$ GeV and $\eta^{jet} < 2.5$ or $E_T^{jet} > 4$ GeV and $\eta^{jet} < 1.5$.

General purpose jet triggers for the study of low and high E_T dijet cross sections.

Prompt Photon: $E_T^{cone} > 8$ GeV and an electron with $E_T^{elec} > 4$ GeV.

Triggers events where the found 'electron' indicates the presence of large deposit of energy in the electromagnetic calorimeter (EMC) which could prove to be a high E_T photon.

DIS Inclusive Jet: An electron with $E_T^{elec} > 6$ GeV and at least one jet with $E_T^{jet} > 3$ GeV and $1.5 < \eta^{jet} < 3.5$.

DIS Gluons I: An electron with $E_T^{elec} > 6$ GeV and at least two jets with $E_T^{jet} > 3$ GeV and -3.5 $< \eta^{jet} <$ 3.0.

DIS Gluons II: An electron with $E_T^{elec} > 6$ GeV and at least two jets with $E_T^{jet} > 4$ GeV and -3.5 $< \eta^{jet} <$ 3.0.

DIS α_s: An electron with $E_T^{elec} > 8$ GeV and at least two jets with $E_T^{jet} > 3$ GeV and -3.5 $< \eta^{jet} <$ 3.5.

These four branches are aimed at studying jet production in DIS.

25 DST bits were available to the JHET group, 21 of which were used to flag events passing the above TLT branches. Since there were 23 TLT filters in total the High p_T Track branches I and II were combined as were DIS Gluons I and II. No further cuts were applied giving direct correspondence between the TLT and DST levels of selection.

The rate at which each type of DST event is recorded is shown in figure 3.1. It should be noted that the High p_T Track branches I, III and V were prescaled by 100, 25 and 125 respectively and would have dominated the event rate were they not prescaled. It can be seen from figure 3.1 that the largest selection of events written out by the JHET group contain two low E_T jets. Raising the E_T^{jet} cut or requiring an electron in the CAL or a rapidity interval between the jets reduces the rate further. Events with hits in one of the taggers close to the beam are relatively rare, as are events with no energy around the FCAL beampipe. It is clear that the rate from the LPS High E_T branch is quite high. The LPS TLT was in fact disabled for much of the 96 run period due to problems with high rates.

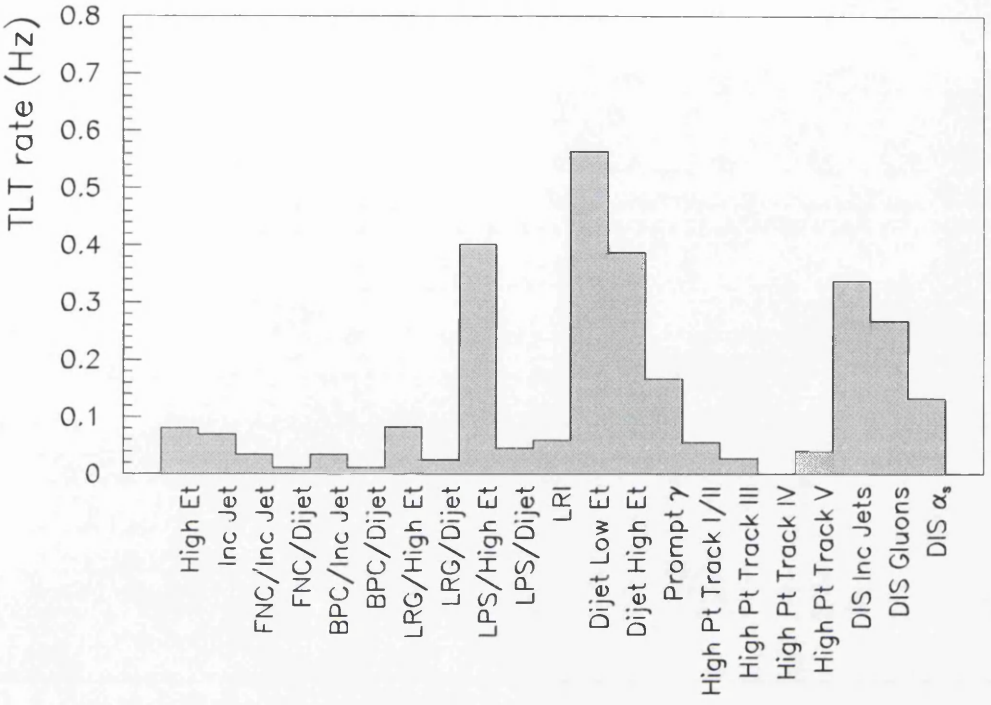

Figure 3.1: The event rate for events passing each Jets and High E_T TLT branch.

The remaining four DST bits were used to flag hotline events with three bits assigned to photoproduction and one to DIS. The following types of events were chosen:

Hotline I: Very High E_T with $E_T^{cone} > 50$ GeV.

Hotline II: An .OR. of High E_T Dijets prescaled by 100 and LRI.

Hotline III: An .OR. of BPC Dijets, FNC Dijets, LPS Dijets, Prompt Photon and High p_T Track III.

Hotline IV: An .OR. of DIS Inclusive Jets, DIS Gluons I, DIS Gluons II and DIS α_s.

The photoproduction hotline events were also required to pass an additional series of cleaning cuts to reduce contamination from beam gas events and from DIS.

3.2 Data Quality Monitoring

An important role of the reconstruction procedure is the data quality monitoring (DQM) which is carried out on events passing the DST selection. The DQM tests

the functioning of the detector components and the online three-level trigger. It also checks that the data have been written out properly and that the non-*ep* background is low. DQM histograms are produced during the offline reconstruction and are checked for each run. In this way problems can be spotted quickly and resolved without wasting months of data-taking. By checking the data quality run-by-run it is also possible to identify problematic runs which can then be eliminated from the list of 'good' runs for analysis.

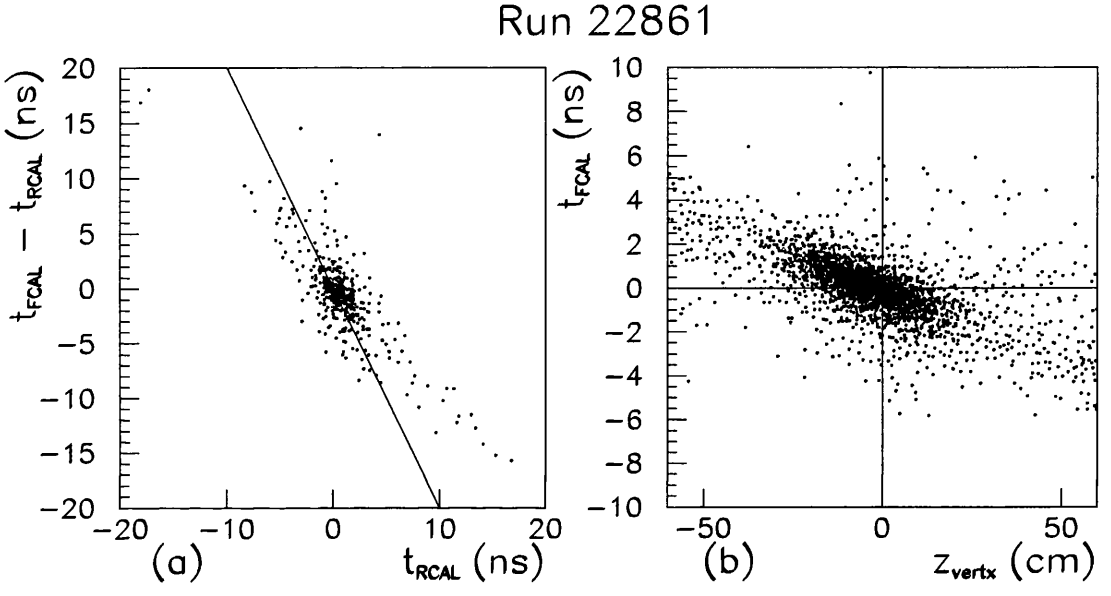

Figure 3.2: General data quality histograms: (a) $t_{FCAL} - t_{RCAL}$ versus t_{RCAL} and (b) t_{FCAL} versus z_{vertx}.

Several quantities are used to check the general quality of the data taken. Figure 3.2(a) shows the difference in the timing measured in the FCAL and the RCAL, $t_{FCAL} - t_{RCAL}$, plotted versus the time measured in the RCAL. The timing in the FCAL and RCAL is calibrated such that particles produced from an *ep* collision at the interaction point (IP) hit the FCAL and the RCAL at 0 ns. Particles from an interaction which took place upstream of the IP, $z < 0$ cm, would arrive at the RCAL(FCAL) before(after) particles from an interaction at the IP and would thus have a negative(positive) time in the RCAL(FCAL). This gives the correlation shown by the diagonal line. The dots show that the data are clustered round zero, indicating

that the timing is well calibrated. Proton beam gas interactions which generally take place upstream of the IP would be expected to have large negative t_{RCAL} and lie in the top left-hand corner of the plot. It is clear from figure 3.2(a) that the proton beam gas contamination is small.

Figure 3.2(b) shows the FCAL timing versus the z coordinate of the vertex position, z_{vertx}. The intersection between the lines show where an event would lie if produced at the IP. The data are slightly shifted in the negative z direction indicating that the e and p beams do not collide at the nominal vertex. The data are equally distributed between positive and negative t_{FCAL} showing that the calorimeter timing is correctly calibrated. This is an important check as the timing is used during the event selection to cut out background whose timing is not consistent with that of an ep event.

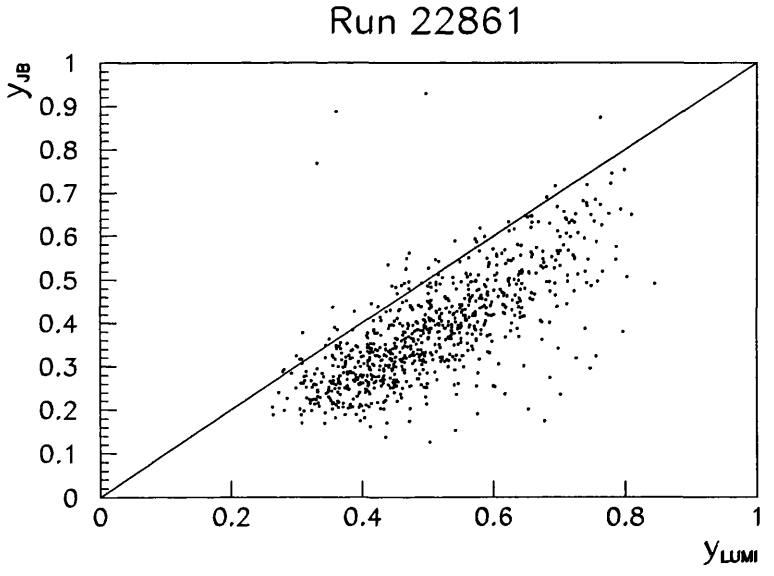

Figure 3.3: y_{JB} versus y_{LUMI} for events with an electron tagged in the LUMI detector.

The correlation between y calculated using the energy of electrons tagged in the LUMI electron calorimeter and y_{JB} calculated from energy deposits in the calorimeter is shown in figure 3.3 for those events with a LUMI tag. If the energy of the particles were reproduced perfectly by the CAL, y_{LUMI} would equal y_{JB}, indicated by the line. The data indeed show a linear correlation. However the correlation is slightly shifted due to energy losses in inactive material in front of the CAL, a problem which must be

corrected for in the subsequent analysis and is discussed in chapter 6.

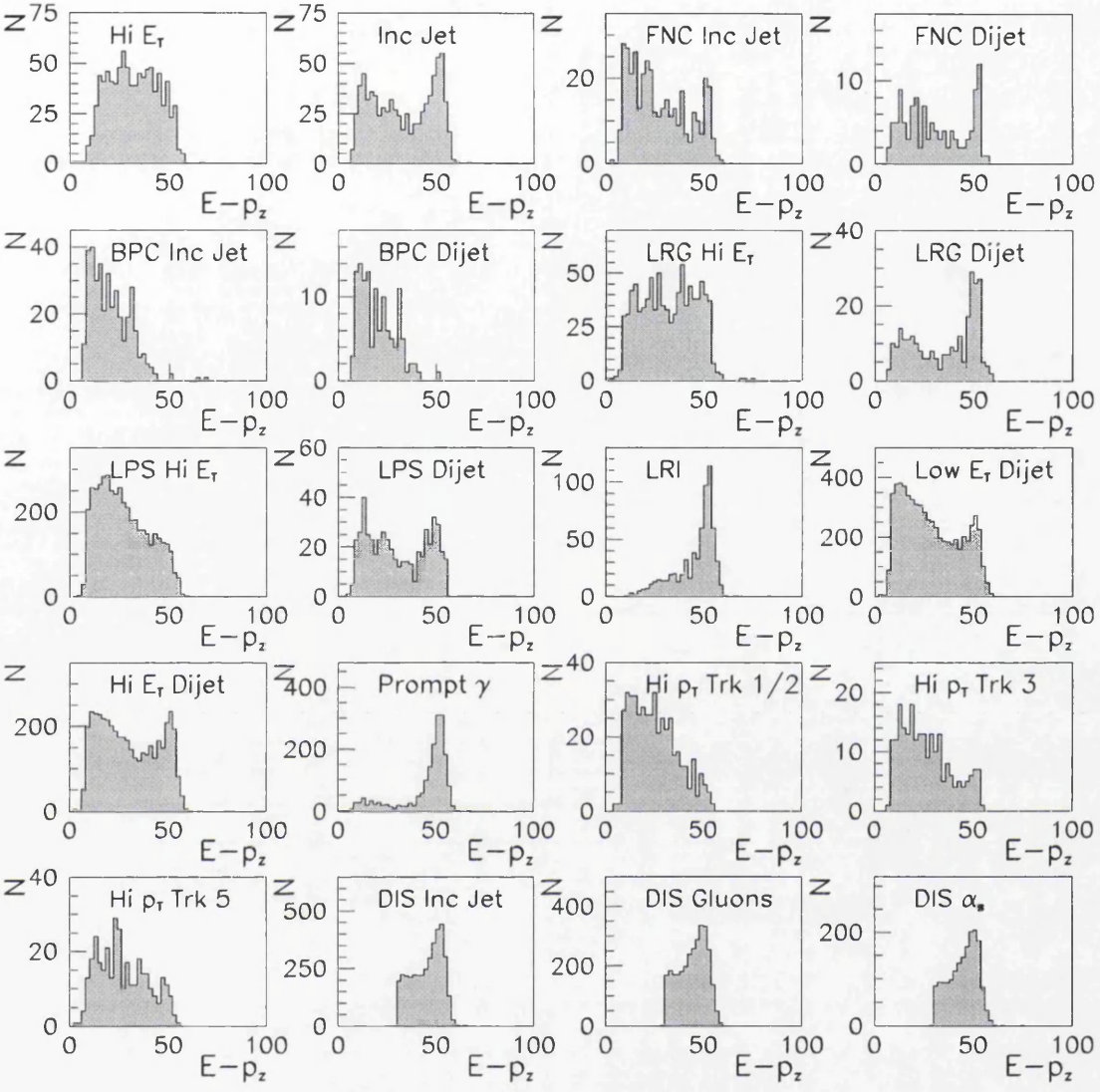

Figure 3.4: $E - p_z$ distributions calculated offline for each DST bit.

Proton beam gas events typically have a large amount of track activity parallel to the beam direction and only a small amount of transverse track activity. Summing over all the cells in the CAL, the observable $E - p_z$, where E is the energy and p_z the longitudinal momentum, tends to be of the order of a few GeV for beam gas events since $E \sim p_z >> p_x, p_y$.

A cut of $E - p_z > 8$ GeV is applied at the SLT and the $E - p_z$ distributions

are checked offline to ensure that the trigger is functioning correctly and the offline quantities bear close resemblance to those applied online at the SLT. The $E - p_z$ distributions of each DST bit are shown in figure 3.4. The High p_T Track IV branch was disabled and is not shown. There are very few events with $E - p_z \sim 0$ in any of the plots in figure 3.4 indicating that the cuts applied to the $E - p_z$ calculated at the SLT succeed in suppressing the beam gas background.

The $E - p_z$ distributions can also provide insight into the different types of event selected by each TLT branch. In DIS the scattered electron is detected in the CAL giving rise to a peak in the $E - p_z$ distribution at around 55 GeV, i.e. twice the electron energy. This peak is clearly shown in the plots in figure 3.4 corresponding to the three DIS DST bits. A lower cut on $E - p_z$ is implemented in these branches to minimise contamination from photoproduction events. The photoproduction filters which require a large transverse energy deposit in the CAL have an approximately uniform $E - p_z$ distribution. Requiring a jet introduces a peak at $E - p_z \sim 55$ GeV due to the acceptance of DIS events, as can be seen in all 'Inclusive Jet' and 'Dijet' triggers. Exceptions are the BPC jet branches where the scattered electron is detected in the BPC rather than the CAL. Further work must therefore be done in an analysis of jets in photoproduction to remove the DIS background. The 'Prompt Photon' branch also has a large peak at $E - p_z \sim 55$ GeV. The 'Prompt Photon' filter at the TLT is aimed at detecting events containing a large isolated deposit of energy in the EMC. In many cases this energy has come from an electron thus the trigger accepts many DIS events. Much work is required to extract the prompt photon signal from this background [35].

Several other quantities are checked to monitor the data quality of each DST bit individually. Four of these are presented in figure 3.5 for the 'Dijet Low E_T' branch which contains the data used in this study. The bunch crossing number (BCN) is shown in figure 3.5(a). As mentioned in section 2.1 a number of electron and proton bunches are left unpaired or empty to estimate the contribution from non-ep background processes. The structure in the BCN demonstrates that very few events are produced from unpaired or empty bunch crossings. The fact that these bins are not completely empty means however that some background is present. Figures 3.5(b) and (c) show two quantities used during the TLT event selection, the transverse energy in the CAL

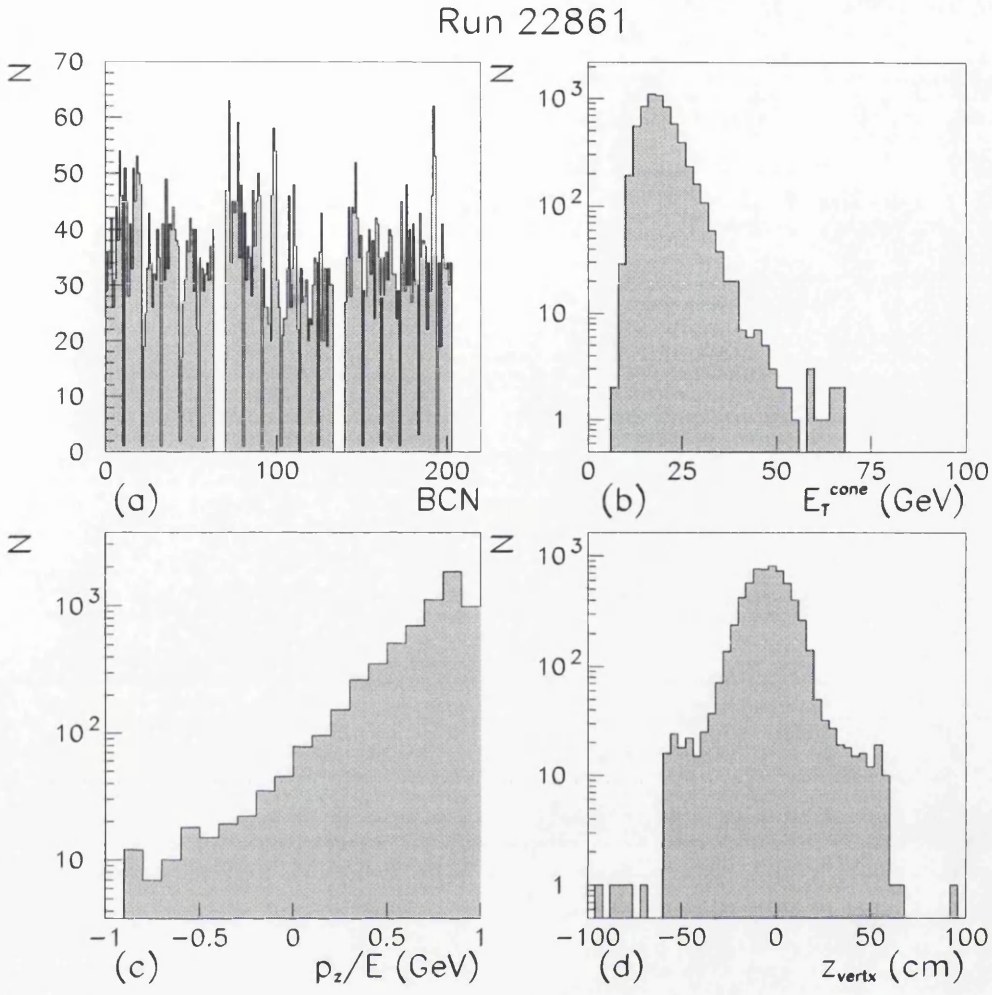

Figure 3.5: Several quantities used in the data quality monitoring shown for the 'Dijet Low E_T' branch: (a) bunch crossing number, (b) E_T outwith a cone of 10^o around the FCAL beampipe, (c) p_z/E and (d) z position of vertex.

outwith a cone of 10^o around the FCAL beampipe, E_T^{cone}, and p_z/E. The shape of the distributions of these quantities is checked to ensure that the information on which the trigger decision is based in that that run is sensible. Figure 3.5(d) shows the vertex position, z_{vertx}. A cut of $|z_{vertx}| < 60$ cm is applied at the TLT in all photoproduction filters and the few events with $|z_{vertx}| > 60$ cm illustrate the slight differences between quantities calculated on- and offline.

The vertex distribution also provides information on satellite bunches, secondary clusters of particles which precede and follow the main bunch of particles. Interactions

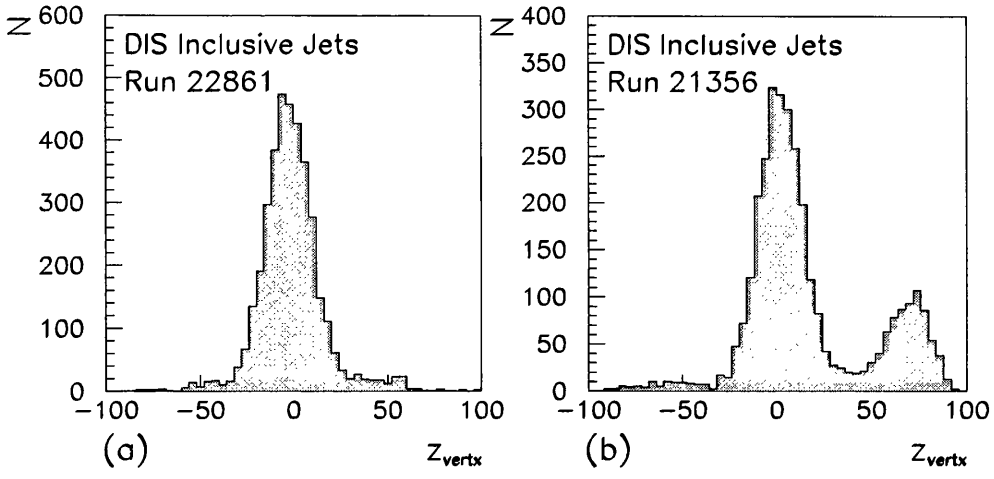

Figure 3.6: z position of vertex for the 'DIS Inclusive Jets' branch for runs 22861 and 21356.

between these secondary bunches give rise to events whose z_{vertx} is offset from zero. This effect cannot be observed in events selected with photoproduction triggers due to the $|z_{vertx}| < 60$ cm cut. No such cut is applied to the four DIS branches and figure 3.6 shows the vertex distribution for the 'DIS Inclusive Jets' branch for two different runs. In a typical run, figure 3.6(a), the vertex distribution has a central peak at $z_{vertx} = 0$ associated with ep interactions from the main bunches. The satellite bunches give rise to events with $|z_{vertx}| > 40$ cm. The number of particles in the satellite bunches is generally small compared to the main bunch as can be inferred from the scarcity of events with $|z_{vertx}| > 40$ cm. However, some runs in 1996 had large proton satellite bunches. For example, figure 3.6(b) demonstrates that the satellite bunch preceding the main proton bunch in run 21356 contained large number of protons. The satellite protons collided with the electron bunch at $\sim$70 cm downstream of the IP causing a secondary peak. It is important that the effect on the vertex distribution from collisions involving the satellite bunches is understood and is properly accounted for in the detector simulation which is applied to Monte Carlo events, discussed in section 5.1.

Offline, jet and electron quantities calculated at the TLT are reexamined to check that the TLT accepts only events which pass the selection criteria. Events which fail the selection are flagged and indicated in the DQM plots as entries in a designated bin. In addition to checking the TLT operation this procedure also checks that data tables

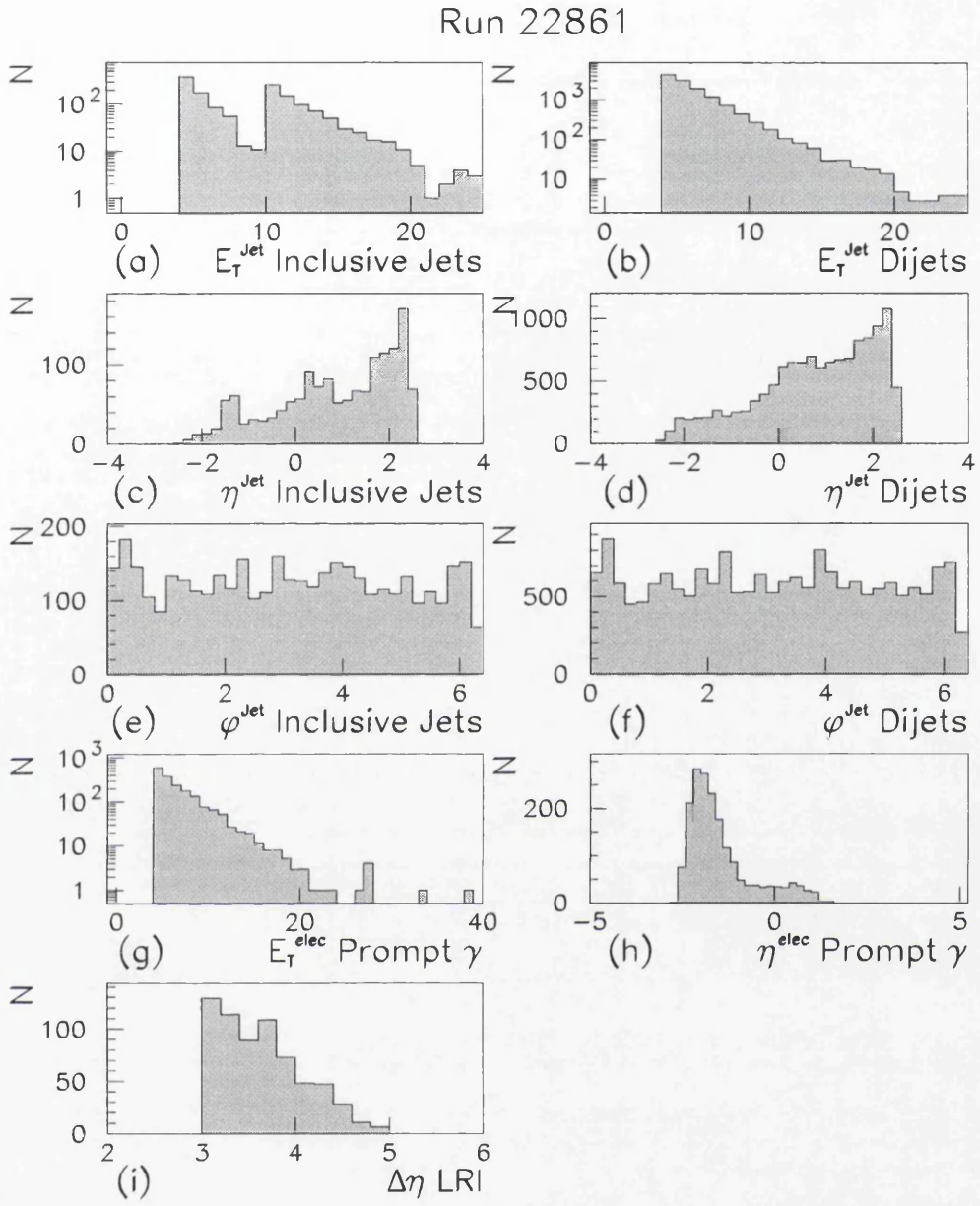

Figure 3.7: Quantities used to select different types of photoproduction events at the TLT.

filled online have been written out to disk correctly.

The E_T^{jet} and η^{jet} distributions for 'Inclusive Jet' and 'Dijet' photoproduction branches, shown in figure 3.7(a),(b),(c) and (d), illustrate the E_T^{jet} cut-offs applied at 4 and 10 GeV for 'Inclusive Jets' and at 4 GeV for 'Dijets' and the $\eta^{jet} < 2.5$ requirement. The φ^{jet} distributions presented in figure 3.7(e) and (f) should be flat in

φ^{jet}; any structure is a sign of problems elsewhere. The transverse energy of the electron candidate from the Prompt Photon branch is shown in figure 3.7(g) and indicates the cut-off applied at 4 GeV. The pseudorapidity distribution of the electron candidate, figure3.7(h), shows a large peak at negative values, indicative of DIS processes, and a flat region extending to $\eta^{elec} \sim 1$ which is more likely to arise from prompt photon production. Lastly, the pseudorapidity interval employed to select 'LRI' events is shown. The TLT requires $\Delta\eta \equiv \eta_1^{jet} - \eta_2^{jet} \geq 3$ as illustrated in figure 3.7(i).

3.3 Summary

The Jets and High E_T group is responsible for a wide range of DIS and photoproduction analyses. Twenty-three different selection algorithms are used at the TLT. During the 1996 and 1997 data-taking periods I was responsible for the offline DST selection and for monitoring the quality of the data selected. Offline the data are reconstructed fully, having access to the complete event record, and are subject to further data selection procedures. Each event is given a flag denoting which TLT branches it passed which speeds up and simplifies offline data analysis. In addition, rare, interesting events which are required for immediate analysis are written out to disk as 'hotline' events.

Data quality monitoring histograms for each run are also produced during the reconstruction. The DQM histograms check that the components and data-taking procedures are functioning accurately, the data written out correctly and the beam conditions good. This is vital to avoid errors which could result in months of wasted data-taking. The level of background events present can also be checked. Problem runs can be identified and eliminated from further analysis.

In general, the DQM confirms that the online data selection reduces the amount of non-*ep* background to a low level. It also demonstrates that there is a considerable degree of overlap between events selected by the photoproduction and DIS jets TLT branches. An analysis of jets in photoproduction must therefore take steps to remove the DIS events and the small amount of non-*ep* background events present in the data sample. The data selection criteria applied in this study are discussed in detail in the following chapter.

Chapter 4

Three-jet Selection

The general data taking procedures of the ZEUS Experiment are described in chapters 2 and 3. This chapter discusses the online and offline data selection criteria specific to this study.

At HERA, in addition to interactions from ep collisions there is a significant background from beam gas events, where the beam particles interact with residual gas molecules in the beam pipe, and also from cosmic rays. Photoproduction processes also have to be separated from other ep processes such as Deep Inelastic Scattering.

Section 4.1 describes the quantities available at each stage of the three-level online trigger and how these can be used to reduce the background. More time and information is available to make decisions offline and therefore more detailed cuts can be applied as shown in section 4.2. The algorithm used to find jets is discussed in section 4.3. Finally, the three-jet event selection is motivated in section 4.4.

4.1 Online Data Selection

4.1.1 First Level Trigger

The time available for decision making at first level trigger, as discussed in section 2.3, is limited to $< 5\ \mu s$. Events containing jets would have sizeable energy deposits in the CAL and this characteristic is used to select events rather than running a time consuming jet finding algorithm. The energy deposit required is

- total energy in the CAL > 15.0 GeV
- or total energy in electromagnetic CAL > 10.0 GeV
- or total energy in the BCAL > 3.4 GeV
- or total energy in the RCAL > 2.0 GeV
- or total transverse energy in the CAL excluding the two innermost rings around the FCAL beampipe > 11.6 GeV

There is also a requirement that $\geq 42\%$ of tracks in the event come from the nominal vertex. Timing information from detectors upstream of the proton beam, i.e. the C5 counter and the vetowall, is used to reject events where the timing is not consistent with the signals having come from an *ep* interaction.

4.1.2 Second Level Trigger

Events which pass the FLT selection proceed to the second level trigger. At this stage a vertex from the CTD is required, unless there is no CTD SLT information. The nominal vertex of $(x, y, z) = (0, 0, 0)$ is used to calculate quantities such as longitudinal and transverse momenta. Further selection criteria select events where a hard scatter has occurred

- the sum of the transverse energy on the calorimeter cells, excluding the first ring round the FCAL beampipe, > 8 GeV

and reduce proton beam gas background

- the total energy minus the total longitudinal momentum summed over all CAL cells, $E - p_z$, > 8 GeV
- if $E - p_z < 12$ GeV then $p_z/E < 0.95$

4.1.3 Third Level Trigger

At the third level trigger there is enough time to apply a jet finding algorithm. A cone based algorithm is used which looks for jets with transverse energy, E_T^{jet}, greater than

3 GeV, pseudorapidity, η^{jet}, less than 2.5 and a cone radius of 1.0. In the trigger used for this analysis, an event is selected if it has

- two jets with $E_T^{jet} > 4$ GeV and $\eta^{jet} < 2.5$
- $E - p_z < 75$ GeV
- less than 6 bad tracks[1]
- a vertex with a z position of $|z_{vertx}| < 60$ cm

The vertex position as measured by the CTD is used by the jet finding algorithm and in calculating longitundinal and transverse momenta. This TLT jet selection is shown in section 6.2.1 to be very efficient. Events passing all three levels of online data selection are then analysed offline in more detail.

4.2 Offline Data Selection

The TLT cuts the event rate from 100 kHz to $\sim$ 3-5 Hz using quantities which can be calculated in the time available to make a decision online. Offline, more time is available and complete information from all data-taking components is accessible.

Photoproduction events where the electron is scattered at small angles to the beam pipe are tagged by the LUMI detector. These comprise a sample of pure and background-free photoproduction events events which can be studied to enable the background from beam gas interactions, cosmic rays and also from other ep processes such as DIS to be further reduced.

The contribution from DIS was estimated using events generated with the Monte Carlo event generator DJANGO [52]. The number of events is normalised to the integrated luminosity represented by the data.

Dijet events with $E_T^{jet} > 5$ GeV and $\eta^{jet} < 2.5$ are selected from those passing the TLT. The subsample of the dijet events tagged by the LUMI detector or established as

[1] A bad track is defined as one which has $5^0 \leq \theta \leq 70^0$, $p_T > 200$ MeV, enough measured points to give more than 20 degrees of freedom in the fit, more than 5 axial or stereo hits and distance of closest approach along the z-axis < -75 cm.

beam gas or cosmic ray events from the bunch crossing information are also identified. Comparisons between the data and the DIS Monte Carlo events are shown in this section to motivate the cleaning cuts used to reduce background. The effect of applying each cut is studied individually.

The distribution of y_{JB}, defined in 1.7, is shown in figure 4.1 for the inclusive dijet data sample. Also shown are the LUMI tagged and proton beam gas subsamples and the DIS events. The dijet sample shows two peaks at ~ 0.2 and ~ 0.9. It is evident that the dominant contribution at high y_{JB} comes from DIS background. Requiring $0.15 < y_{JB} < 0.65$ removes most of the background while retaining most of the good photoproduction events.

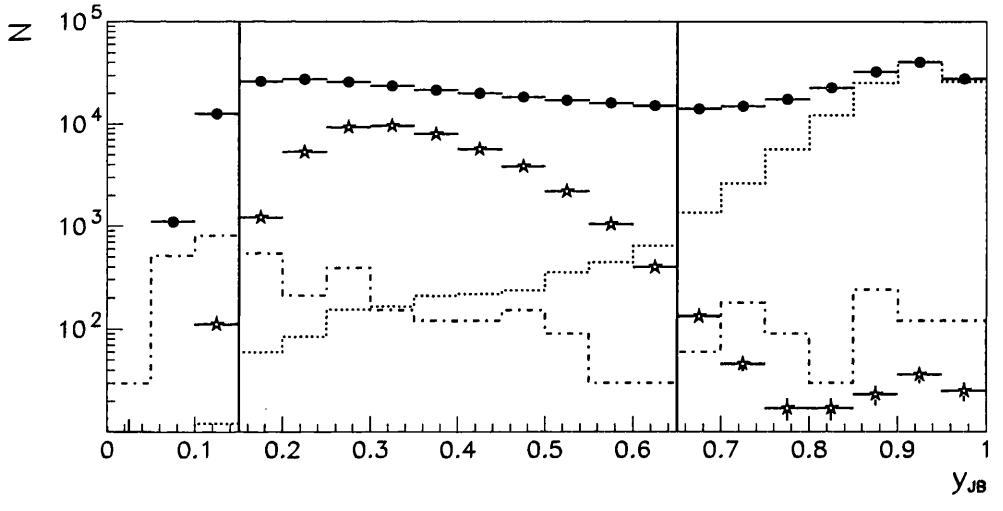

Figure 4.1: y_{JB} distribution for the dijet data sample (dots), LUMI tagged (stars) and proton beam gas (dot-dashed histogram) subsamples and DIS Monte Carlo events (dotted histogram).

The electron in photoproduction is scattered at low angles to the beam pipe and is not detected in the CAL. Nevertheless, some highly collimated jets consisting, for example, of mainly π^o's may give rise to large deposits of energy in the EMC and none in the HAC and could be mis-identified as electrons by the electron finding algorithm. The number of electrons in an event is shown in figure 4.2(a) for the dijet events, LUMI tagged subsample and the DIS Monte Carlo prediction. The data show that a large fraction of dijet events contain one or more electrons and that this is not entirely due to contamination by DIS events. For events containing at least one electron, y_e as

defined in 1.6 is shown in figure 4.2(b). It is clear that the peak in the dijet data at low y_e comes predominantly from DIS contamination. The dijet data also peak at high y_e, as do the LUMI tagged data, while the contribution from DIS has died away. High y_e values arising from scattered electrons are very rare since the cross section varies as $1/y^2$. The conclusion that the 'electrons' with high y_e are in fact mis-indentified π^o's or other mesons that decay electromagnetically to two photons is supported by the DIS and LUMI tagged photoproduction events. A cut of $y_e > 0.7$ for events containing an 'electron' selects almost pure photoproduction events with a minimum of DIS background.

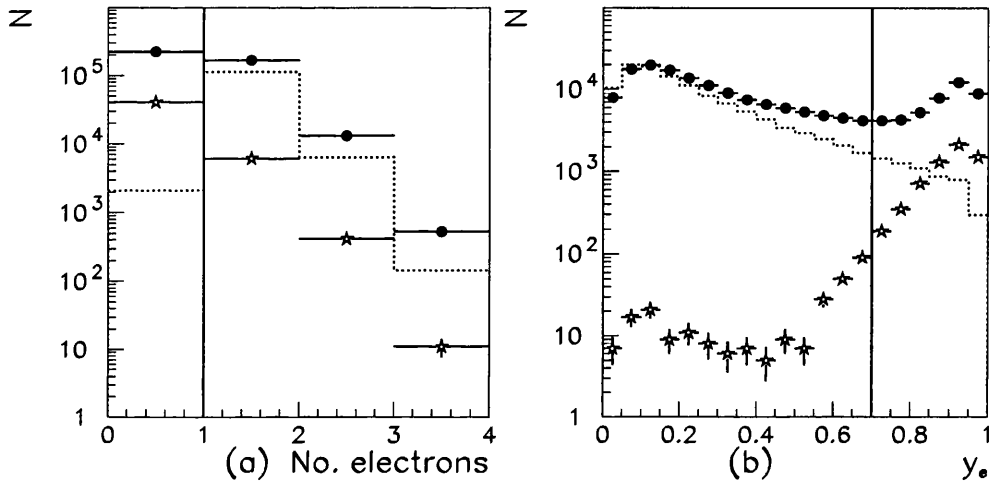

Figure 4.2: The number of electrons found (a) and y_e for events containing an electron (b). The inclusive dijet data are shown by dots, the LUMI tagged data by stars and the DIS Monte Carlo events by the dotted histogram. The total number of events in each sample is shown.

Figure 4.3(a) shows the number of events which have a well-defined vertex. As expected, beam gas or cosmic ray events are less likely to have a well-defined vertex since they do not come from ep interactions. Therefore, requiring a vertex in an event reduces the background. Figure 4.3(b) shows the z position of the vertex for dijet and beam gas events. The data are peaked near zero and are concentrated in a region of $\pm$ 30 cm. A cut of $\pm$ 60 cm is applied at the TLT. Events shown here with $|z| > 60$ cm are caused by slight differences in offline and online quantities. Applying a cut of $|z| < 50$ cm reduces the background from beam gas events.

The number of bad tracks, $N_{bad\,track}$, in the event is shown in figure 4.4(a)

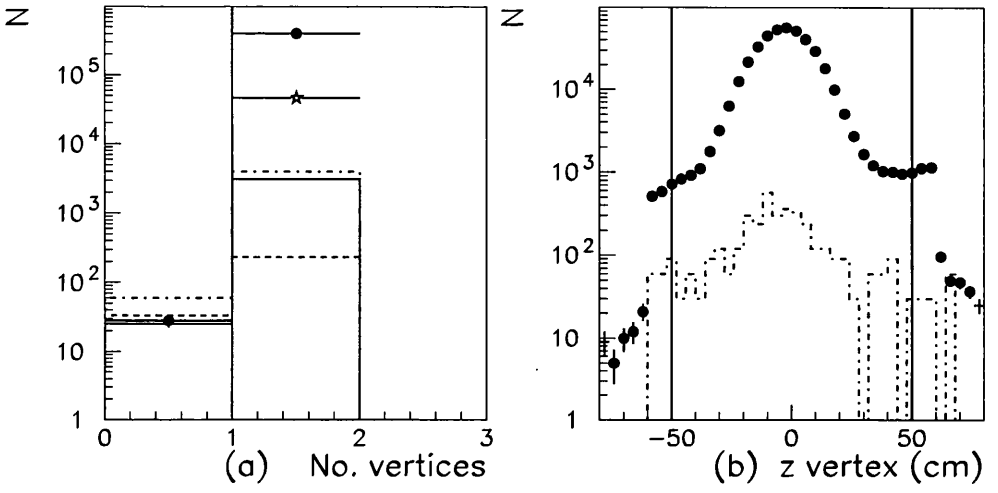

Figure 4.3: The number of vertices found (a) and the z position of the vertex (b). The inclusive dijet data are shown by dots, the LUMI tagged data by stars, proton beam gas by the dot-dashed histogram, electron beam gas by the solid histogram and cosmic rays by the dashed histogram.

for the dijet sample and LUMI tagged and proton beam gas subsamples of events. The data are peaked at zero and decrease sharply with increasing $N^{bad\,track}$. The tail at $N^{bad\,track} > 3$ can be accounted for by proton beam gas events. Requiring $N^{bad\,track} < 3$ reduces the background with the loss of few real physics events.

The missing transverse momentum normalised to the square root of the total E_T in the event, $\not{p}/\sqrt{E_T}$, is shown in figure 4.4(b) for the dijet and LUMI tagged events. The data are peaked at zero with a tail extending to 6. The pure photoproduction events lie almost exclusively in the $\not{p}/\sqrt{E_T} < 2$ region while the tail of the distribution is likely to come from charged current DIS events where a neutrino rather than an electron is produced in the final state giving rise to a large amount of missing p_T.

In summary, the additional offline cuts which are applied to the data are:

- $y_{JB} < 0.65$
- no electron found or $y_e > 0.7$
- $\not{p}/\sqrt{E_T} < 2$

to reduce DIS background and

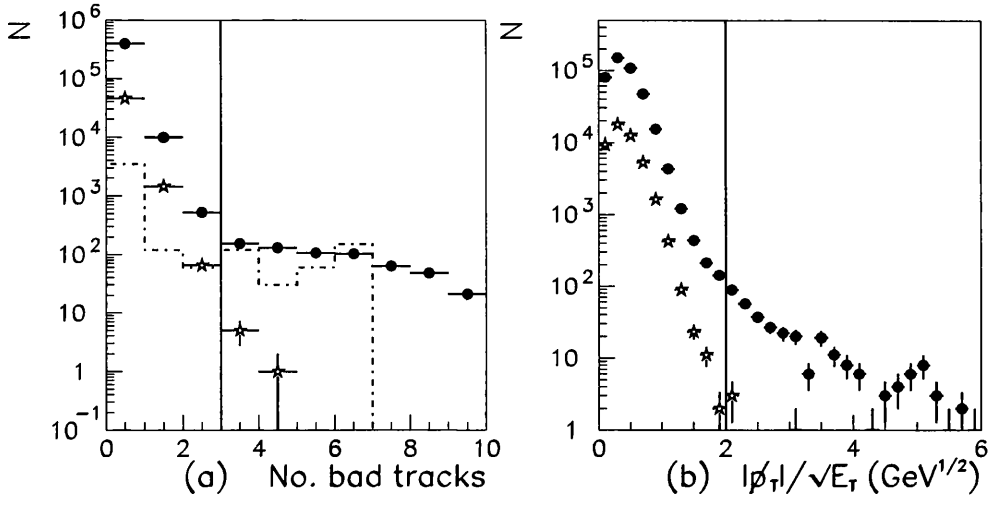

Figure 4.4: The number of bad tracks found in an event (a) and the missing p_t normalised to the total transverse energy in the event (b). The inclusive dijet data are shown by dots, the LUMI tagged data by stars and proton beam gas by the dot-dashed histogram.

- $0.15 < y_{JB}$
- a vertex found and $|z_{vertex}| < 50$ cm
- number of bad tracks < 3

to reduce contamination from beam gas and cosmic ray events. A Monte Carlo study given in section 6.2.1 shows that only 2% of good photoproduction events are rejected by these cleaning cuts.

4.3 Jet Finding Algorithms

Jets observed in hadronic final states are features of the event which, although closely related to the final state partons which create them by hadronisation, require an operational definition. When studying jet quantites, what is measured depends on the jet definition used.

To enable comparison of results between experiments and between experiment and theory it is important to use standard jet finding algorithms. The 1990 Snowmass Workshop [53] stated that any jet definition should be simple to implement in an

experimental analysis and in theoretical calculations, should be defined at any order of perturbation theory, and should yield a finite cross section at any order of perturbation theory that is also relatively insensitive to hadronisation.

Energy deposits in calorimeter (CAL) cells or tracks in the central tracking detector (CTD) can be used to find jets in ZEUS data (*detector level*). In theoretical calculations, jets can be found from partons from the hard scatter (*parton level*) (at LO each parton is identified with one jet) or, using events from QCD Monte Carlo events generators, from partons from the parton shower (*parton shower level*) or final state hadrons (*hadron level*). In order to compare experimental data meaningfully with theoretical predictions it is essential to have a good correspondence between jets at all levels. An important aspect of this is that the chosen jet definition should be applied to experimental and theoretical quantities in a consistent way.

Two types of algorithm are in general use at present: a cone-type algorithm related to the Sterman-Weinberg treatment of QCD radiation [54] and a clustering algorithm of the type first used by the JADE Collaboration [55].

4.3.1 Cone Algorithms

Cone algorithms search for jets by trying to maximize the amount of transverse energy inside a cone of fixed radius, R_0, in the $\eta - \varphi$ plane. The choice of variables ensures invariance under boosts along the beam direction, an essential property of any algorithm used in hadron-hadron collisions.

In general, the algorithm proceeds by choosing any particle or cell, i, and summing over all particles/cells with $R_{ij} = \sqrt{(\eta_i - \eta_j)^2 + (\varphi_i - \varphi_j)^2} \leq R_0$, evaluates the total E_T in the cone and the η and ϕ coordinates of the jet axis according to

$$E_T^{jet} = \sum_{i \in jet} E_{Ti}$$

$$\eta^{jet} = \frac{1}{E_T^{jet}} \sum_{i \in jet} E_{Ti}\eta_i$$

$$\varphi^{jet} = \frac{1}{E_T^{jet}} \sum_{i \in jet} E_{Ti}\varphi_i$$

The jet axis is now taken as the centre of a new cone and the process iterated until a stable jet axis is obtained. Cones with E_T above a given threshold are selected as

jets. A new seed direction is then chosen and the process repeats. Not every particle is assigned to a jet but some can be assigned to two or more when the cone of one jet overlaps with that of another.

Experimentally, the issue of overlapping cones is dealt in different ways. At the CDF experiment [56], two cones are merged if they share 75% (50% at DØ[57]) of their energy. Otherwise they are split with the particle/cell energy being assigned to the nearest jet. However the same criteria cannot be applied to final state partons from QCD calculations. This can lead to big differences between parton, hadron and detector level jets and has been the subject of much discussion [58, 59, 60].

4.3.2 Clustering Algorithms

Clustering algorithms have been widely used for many years in e^+e^- collisions [55] and differ significantly from cone-type algorithms. Several changes have been incorporated to allow this type of algorithm to be used in hadron-hadron collisions [61, 62].

Generally, groups of particles close together in phase space are sought and merged. For each particle in the final state, i, the variable d_{ib} is defined as the transverse energy squared,

$$d_{ib} = E_{Ti}^2$$

For all pairs of particles, i and j, a closeness, d_{ij} is calculated.

$$d_{ij} = min(E_{Ti}^2, E_{Tj}^2)\frac{R_{ij}^2}{R}$$

where $R_{ij}^2 = (\eta_j - \eta_i)^2 + (\varphi_j - \varphi_i)^2$ and R is a parameter of order 1. This d_{ij} reduces to k_T^2, for small opening angles between particles, where k_T is the relative transverse momentum of one particle with respect to another. The expressions for d_{ib} and d_{ij} are longitudinally boost invariant, an important property when the centre-of-mass of the hard scatter is not the same as the lab frame.

The minimum value of all the calculated d_{ij} and d_{ib} is found and labeled as d_{min}. If this minimum value refers to the relative k_T of two particles then the particles are merged into a single cluster, or 'protojet', according to a particular recombination scheme. If on the other hand d_{min} is the p_T of a particle then that particle is removed

from the sample and is included in a list of complete jets. This process is repeated for all particles/protojets not included in the list of jets until all objects are associated with a complete jet. In effect, the softest particle in the event is repeatedly merged with its nearest neighbour in angle. The recombination scheme used in this analysis is

$$E_{Tij} = E_{Ti} + E_{Tj}$$

$$\eta_{ij} = \frac{E_{Ti}\eta_i + E_{Tj}\eta_j}{E_{Tij}}$$

$$\varphi_{ij} = \frac{E_{Ti}\varphi_i + E_{Tj}\varphi_j}{E_{Tij}}$$

The variables used in the resolution and recombination steps are chosen to ensure invariance under boosts along the beam direction. The algorithm satisfies the requirements of infra-red and collinear safety. For vanishingly small energies and angles $d_{ij} \rightarrow 0$; adding extra soft particles or replacing one particle with two or more collinear ones does not affect the jets that emerge from the algorithm.

4.3.3 Algorithm used in this study

The k_T algorithm described above is well defined to all orders in perturbation theory and can be applied in exactly the same way at parton, parton-shower, hadron and detector levels. It has several advantages over a cone algorithm for a study of multijet events in photoproduction. Particles are merged in a strictly defined way if they are close enough together, in contrast with the cone algorithm which seeks only to maximise the energy in a cone of fixed radius. The use of the k_T resolution variable means that the algorithm is sensitive to the shape and size of the jet; characteristics that can be affected by the hardness of a jet and the colour flow of the hard subprocess. The algorithm is however insensitive to soft particles on the edges of jets, which cone algorithms tend to have a problem dealing with unambiguously. This should lead to smaller hadronisation and detector corrections and less model dependence. In addition, there are none of the splitting-merging uncertainties evident with overlapping cones in cone algorithms since each particle is assigned unambiguously to one jet.

The results of applying this algorithm to data are illustrated in figures 4.5 and 4.6 for 180 nb^{-1} of ZEUS data where the online data selection described in section 4.1 was

applied. Only jets with tranverse energy, E_T^{cal}, of more than 3 GeV and pseudorapidity, η^{cal}, between $\pm$ 3 are considered. The superscript ^{cal} denotes that the energies and positions of calorimeter cells were used by the algorithm to find jets.

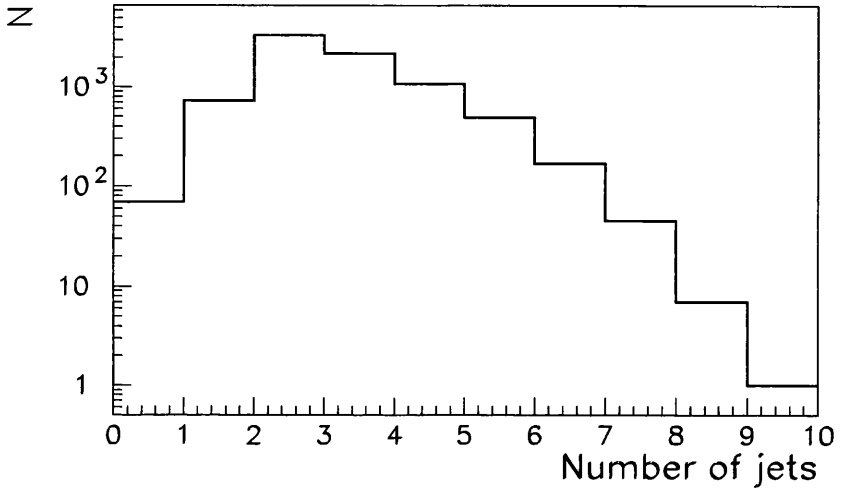

Figure 4.5: The number of jets per event with $E_T^{cal} > 3$ GeV and $\eta^{cal} < 3.0$. The k_T algorithm is applied to the data passing the online and offline selection cuts.

Figure 4.5 shows that the majority of events have two or more jets. The E_T^{cal} distribution, figure 4.6(a), peaks at the threshold value of 3 GeV, falls steeply with increasing E_T^{cal} and reaches out to 40 GeV. Figure 4.6(b) shows that the jets are concentrated in the region where $\eta^{cal} > 0$, as would be expected from the strong boost in the proton direction due to the asymmetry in the proton and electron beam energies. The dip in the distribution at $\eta^{cal} \sim 1$ is due to the limited acceptance of the detector in the join between the BCAL and FCAL. The TLT requires two jets with $E_T^{cal} > 4$ GeV and $\eta^{cal} < 2.5$; thus jets with $\eta^{jet} > 2.5$ will only occur in events with three or more jets. This appears as a depletion rather than an abrupt drop at $\eta^{jet} = 2.5$ since the jet algorithms used on- and offline are different; a cone algorithm was used at the TLT and a clustering algorithm offline.

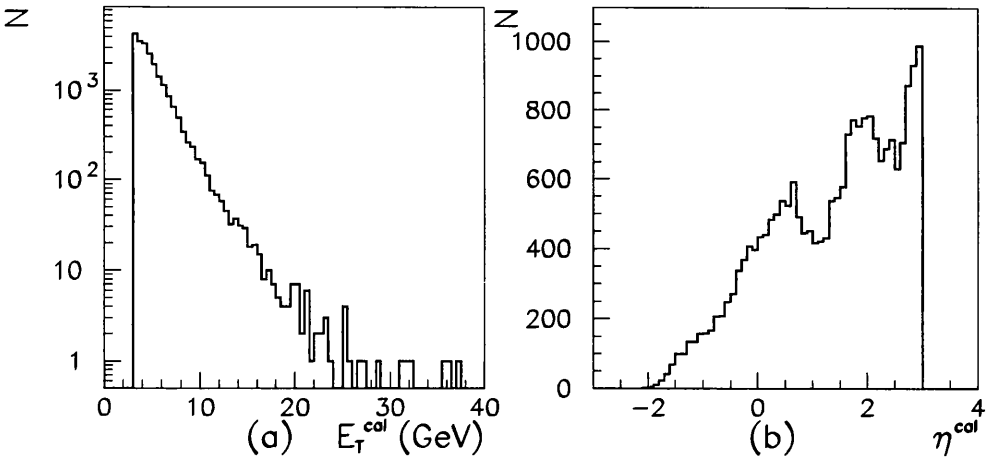

Figure 4.6: (a) E_T^{cal} and (b) η^{cal} for jets found by applying the k_T algorithm to the data after online and offline selection cuts.

4.4 Three-jet Event Selection

After application of all online and offline selection cuts, two jets are selected with $E_T^{cal} > 5$ GeV and $\eta^{cal} < 2.4$, and a third jet with $E_T^{cal} > 4$ GeV and $\eta^{cal} < 2.4$ is also required. These E_T^{cal} cuts for the three-jet selection are designed to obtain a cross section which is perturbatively calculable while maximising the available statistics. As shown in figure 4.6, with these cuts the E_T^{cal} distribution of jets falls off rapidly with increasing E_T^{cal}. The three-jet observables of interest in this study were introduced in section 1.4. The effect of the jet selection cuts should be investigated to ensure that the observables are sensitive to the dynamics of the processes studied and are not determined predominantly by the jet selection criteria.

As stated above, requiring a high tranverse energy tends to reject jets produced at small angles to the beam line, i.e. events with high $\cos\theta_3$. Setting a minimum E_T^{cal} can therefore bias the $\cos\theta_3$ distribution at high $|\cos\theta_3|$. The variation in this effect with the three-jet invariant mass, M_{3J}^{cal}, is shown in figure 4.7 for three-jet events with the above selection cuts. At low M_{3J}^{cal} the $\cos\theta_3$ distribution is clearly biased; at $M_{3J}^{cal} < 25$ GeV part of the $\cos\theta_3$ range is completely excluded. As M_{3J}^{cal} increases the proportion of events passing the E_T^{cal} cuts with high $|\cos\theta_3|$ increases. This suggests that applying a cut on the three-jet invariant mass may allow $\cos\theta_3$ to be measured

without serious suppression at high $|\cos\theta_3|$ arising from the E_T^{cal} threshold.

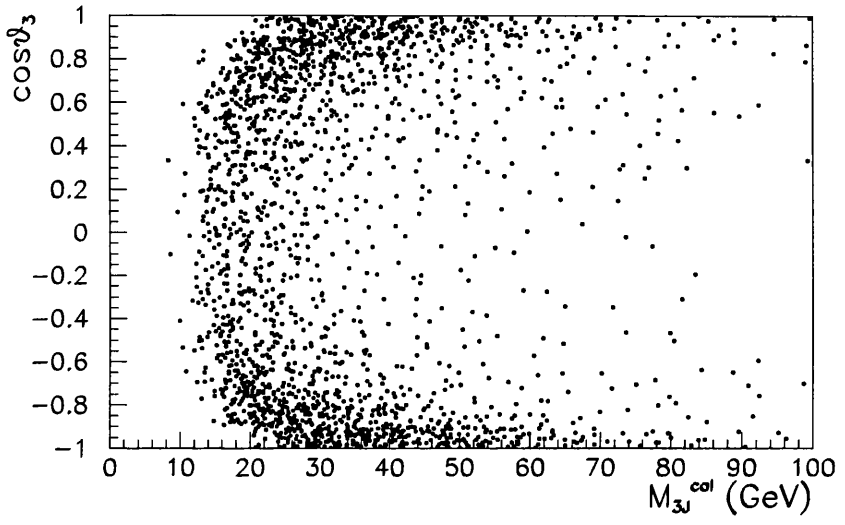

Figure 4.7: $\cos\theta_3$ vs M_{3J}^{cal} for three-jet events passing the above E_T^{cal} and η^{cal} cuts.

Studying the M_{3J}^{cal} distribution in bins of $|\cos\theta_3|$ shows the effectiveness of a cut on M_{3J}^{cal} at reducing the effect of the jet E_T^{cal} thresholds. Figure 4.8 shows the M_{3J}^{cal} distributions of two different three-jet data samples, one using the above selection cuts and the other requiring three jets each with $E_T^{cal} > 3$ GeV and $\eta^{cal} < 2.4$. At low M_{3J}^{cal} the distributions are very different showing the sensitivity to the E_T^{cal} threshold. However, at high M_{3J}^{cal} the distributions begin to merge indicating that the E_T^{cal} threshold no longer has any effect. The value of M_{3J}^{cal} at which the distributions coincide rises as $|\cos\theta_3|$ increases until for $0.8 < |\cos\theta_3| < 1.0$ the two never fully merge. Restricting the measured region to $M_{3J}^{cal} > 42$ GeV and $|\cos\theta_3| < 0.8$ maximises the number of events available while reducing the effect of the E_T^{cal} cut on the $\cos\theta_3$ measurement.

As mentioned in chapter 1, X_3 is defined as twice the fraction of the total three-jet centre-of-mass energy taken by the highest energy jet in the centre-of-mass. It is allowed to range between $\frac{2}{3}$, where all three jets have an equal share of the energy, and 1, where the highest energy jet takes all the energy available to it, i.e. fully half of the total energy. In this analysis X_3 is required to be less than 0.95 to limit the fraction of the energy taken by the highest two energy jets and make more available to the third jet.

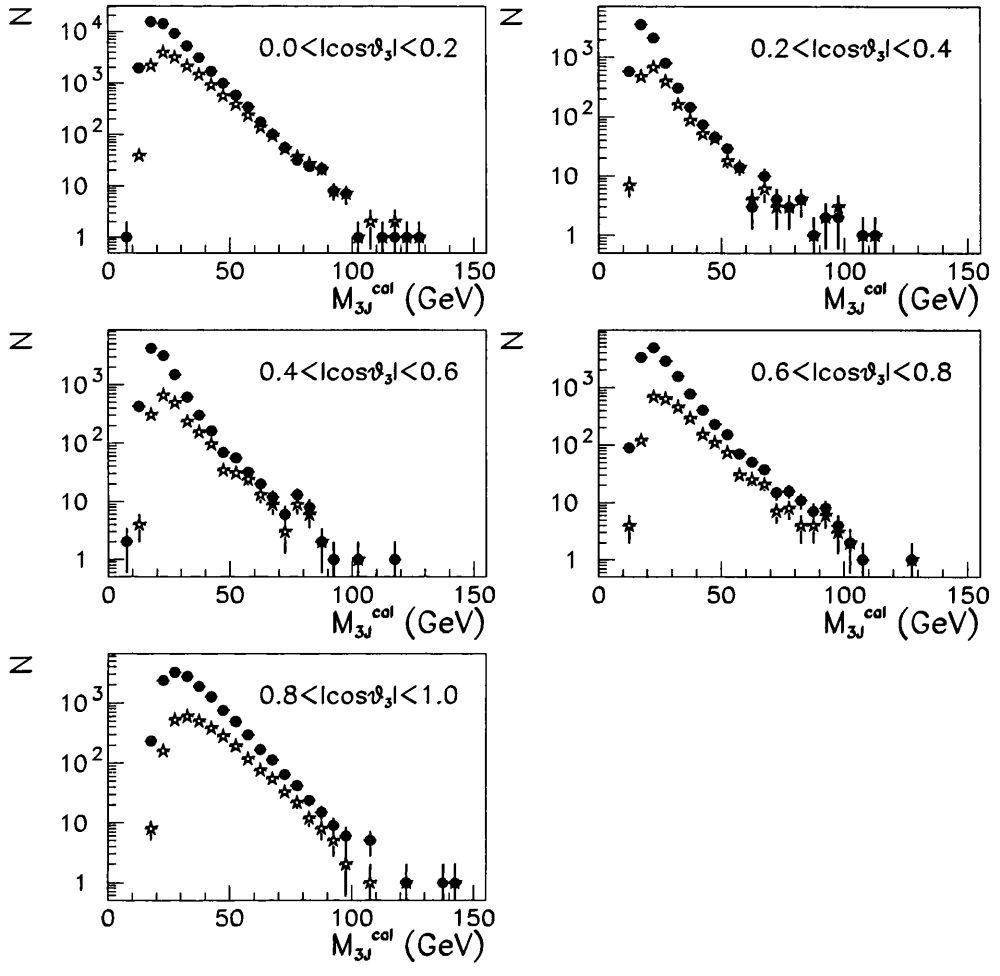

Figure 4.8: M_{3J}^{cal} distribution in bins of $|\cos\theta_3|$ for three-jet events with three jets with $E_T^{cal} >$ 3 GeV and $\eta < 2.5$, dots, and with three jets with $E_T^{cal} > 5$ GeV and $\eta < 2.5$, stars.

In summary, at detector level after all online and offline selection criteria described in sections 4.1 and 4.2, three-jet events are defined by

- two jets with $E_T^{cal} > 5$ GeV and $\eta^{cal} < 2.4$
- a third jet with $E_T^{cal} > 4$ GeV and $\eta^{cal} < 2.4$
- $M_{3J}^{cal} > 42$ GeV, $|\cos\theta_3| < 0.8$ and $X_3 < 0.95$

This selection will be used in chapter 5 to study the characteristics of three-jet events. Details of the number of events obtained after correction for energy losses in inactive material in the detector are given in chapter 7.

Chapter 5

Data Description by Monte Carlo Models

Computer calculations can be used to simulate 'events' from ep collisions. In general, event generators build the events from the parton distribution functions, matrix elements for particular processes, a mechanism for QED and QCD radiation from partons and a hadronisation scheme. A probabilistic approach is used with random number generators deciding the nature of each event based on the probability of a particular process or subprocess occurring. These events can be passed through a simulation of the ZEUS detector and data selection process. Knowing the 'true' hadron level and 'detector' level properties of these events a correction can be made for the effect of the detector on the measured ZEUS data.

This approach relies on a good description of the data by the models. Ideally, the correction should be independent of the model used to obtain it in order that it can be applied meaningfully to the data. To check the model-dependence, two different event generators, PYTHIA 5.7 [63] and HERWIG 5.9 [64], are used and compared.

In section 5.1 the event generators used in this study are discussed. The following sections 5.2, 5.3, 5.4 and 5.5 test the ability of the Monte Carlo events to describe the raw ZEUS data.

5.1 Event Generators

The aim of an event generator such as PYTHIA and HERWIG, as mentioned earlier, is to produce physics 'events' which resemble as closely as possible those created in experiments. To do this they make use of the factorisation property of QCD; any hard QCD process can be broken down into a series of elements which can be dealt with individually and brought together to complete the description of the event.

Hard Subprocess: This is computed exactly in perturbation theory to fixed order. At present, matrix elements for leading order $2 \rightarrow 2$ direct and resolved photoproduction processes are available. The hard scale of the interaction also acts as a boundary condition for the initial and final state parton showers as discussed in [63, 64].

Perturbative Initial and Final State Showers: Gluon and photon radiation from the partons involved in the hard scatter could give rise to potentially large corrections to the leading order matrix element. These corrections become increasingly important as the available energy rises. The analytical calculation of these corrections is not practicable due to the large numbers of gluons involved. Instead the effect is approximated by a parton shower where partons involved in the hard scatter radiate gluons by the splitting of one parton into two according to DGLAP evolution. An initial state parton with low space-like virtuality, Q^2, radiates time-like partons thus increasing its virtuality. The upper Q^2 limit on the parton shower is given by the Q^2 of the hard scatter. A virtual parton in the final state radiates partons with lower virtuality thereby decreasing Q^2 with each successive emission. The shower evolution is terminated at a lower cut-off, Q_0, which is typically $\sim$1 GeV^2 for QCD radiation.

Hadronisation: Partons are not observed individually due to the confinement property of QCD which keeps them confined in colourless hadrons. For the prediction of an event generator to be useful the coloured partons produced by the hard scatter and the parton shower must be turned into colourless hadrons. The hadronisation process takes place with low momentum transfer, and pQCD does

not apply due to the large value of α_s at this scale. Instead a phenomenological model must be used to associate partons with hadrons.

Two event generators, PYTHIA and HERWIG, were used in this study. Both are general purpose QCD event generators which contain a wide range of hard subprocesses at LO and use parton showers to approximate higher order matrix elements. The main differences between the two lie in the evolution of the parton shower and the hadronisation model used.

The parton shower algorithm implemented in HERWIG takes into account interference between soft gluons which gives rise to colour coherence in the parton shower. The choice of suitable evolution variables leads naturally to the restriction of the phase space available for further branching to an angular ordered region, a consequence of colour coherence. In PYTHIA, by contrast, the evolution of the parton shower is governed by the virtuality, Q^2. The angular ordering property of colour coherence is simulated by prohibiting non-ordered emission.

The Lund string model [27] as implemented in JETSET [65] was used by PYTHIA to fragment partons into hadrons. The string model is motivated by the physical picture of confinement. Take, for instance, the case where a $q\bar{q}$ pair is produced in an e^+e^- collision. As the partons move away from the interaction point the potential energy in the colour field between them increases. This can be modelled as a string which is stretched between the partons. Once the potential energy reaches a certain level a $q\bar{q}$ can be produced by the field. The system then splits into two new colour singlet systems. A radiated gluon can be regarded as a kink in the string. One can consider two strings, one stretched between the q and g and the other between the g and $\bar{q}$, which fragment in the same way as a $q\bar{q}$ string. In hadron collisions colour strings can also connect the final state partons with the hadron remnants. The string model has been generally successful in describing the data. There are however many free parameters which have had to be constrained from e^+e^- data.

HERWIG uses a cluster hadronisation model which is much less sophisticated than the Lund string model. It is local in colour and independent of the hard process and the energy. The model takes the partons produced by the parton shower and splits

the gluons into $q\bar{q}$ or diquark-antidiquark pairs. Clusters are then constructed by connecting a quark to the nearest neighbouring $\bar{q}$ or diquark that will form a colour singlet. Light clusters are simply taken to be hadrons while heavier clusters decay isotropically into lighter hadrons. A small fraction of clusters, usually those containing the partons from the hard scatter, are so heavy that isotropic decay is not a reasonable assumption. In this case the cluster fragments into two smaller clusters according to a 'fission' model whereby the products of the splitting move in the direction of the original cluster in its centre-of-mass system. In this respect the 'fission' model is not unlike string fragmentation. The smaller clusters are then free to decay isotropically into lighter hadrons.

In addition to generating physics events, Monte Carlo techniques can be used to simulate the behaviour of particles in a detector, for example, how they shower in the calorimeter, spiral in magnetic fields or even if they end up in inactive material and are not detected. At ZEUS the detector simulation is carried out by MOZART (Monte Carlo for ZEUS analysis, reconstruction and trigger) which is based on the GEANT program [66]. The output from MOZART is presented as tables of data which have the same format as the data recorded by the ZEUS experiment. In this way ZEUS data and PYTHIA and HERWIG events which have been subjected to the ZEUS detector simulation can be reconstructed and analysed using identical procedures. The Monte Carlo events contain additional information on the 'true' particles produced by the events. In the following, quantities based on information from particles produced by a generator are referred to as 'hadron level' while quantities reconstructed from simulated detector information are denoted 'detector level'. Hadron and detector level quantities can then be compared to extract information on the effects of the detector on the data and correct for these effects.

In this study PYTHIA and HERWIG events were generated and passed through the ZEUS detector simulation, MOZART. The GRV [67] and CTEQ [68] parametrisations were used for the photon and proton structure functions respectively. Secondary interactions between the photon and proton remnants, as discussed in section 1.2, were simulated in the HERWIG events. Direct and resolved events were generated separately and combined according to their cross sections. Details of the event samples

used in this study are given in appendix A. The following sections show the raw ZEUS data compared with detector level Monte Carlo predictions. The event selection used is as described in section 4.4 for both data and Monte Carlo events.

5.2 Initial Selection Variables

Global energy quantities are shown in figure 5.1. The total energy deposit in the CAL, (a), and the total energy deposited in the FCAL, (b), show the data systematically shifted to energies higher than the PYTHIA and HERWIG predictions. This feature of the data has previously been seen by both the H1 [37] and ZEUS [69] collaborations and is not yet fully understood. The BCAL and RCAL energies are shown in figure 5.1(c) and (d) respectively. The BCAL energy is peaked at around 20 GeV with a tail extending to 80 GeV. The PYTHIA and HERWIG predictions agree reasonably well with the data. The RCAL energy is peaked at zero as the events are strongly boosted in the proton direction. Energy deposits in the RCAL are likely to come from the photon remnant only. The agreement between the data and Monte Carlo in the lowest bin suggests that the relative proportions of LO direct to LO resolved processes in the Monte Carlo is similar to that in the data.

Figure 5.2(a) shows the transverse energy deposits outwith a cone of 10^o ($\eta = 2.44$) around the forward beam pipe. The data range between 20 and 100 GeV and are peaked at 40 GeV. In contrast to the total energy in the CAL the data here are well described by PYTHIA and are reasonably well described by HERWIG prediction. This illustrates that the forward energy discrepancy is confined to a small area around the beam pipe and will not affect this analysis in an important way. The reasonable description of the global energy distributions by PYTHIA and HERWIG supports the understanding on the online trigger efficiencies using Monte Carlo events, section 6.2.1.

A quantity used in the SLT is p_z/E, shown in figure 5.2(b) for events with $8 < E - p_z < 12$ GeV. The data are peaked at 0.9 and are well described by both Monte Carlo models.

y_{JB}, shown in figure 5.3(a) is an important quantity for defining the event sample and cutting out contamination from non-photoproduction events. The Monte Carlo

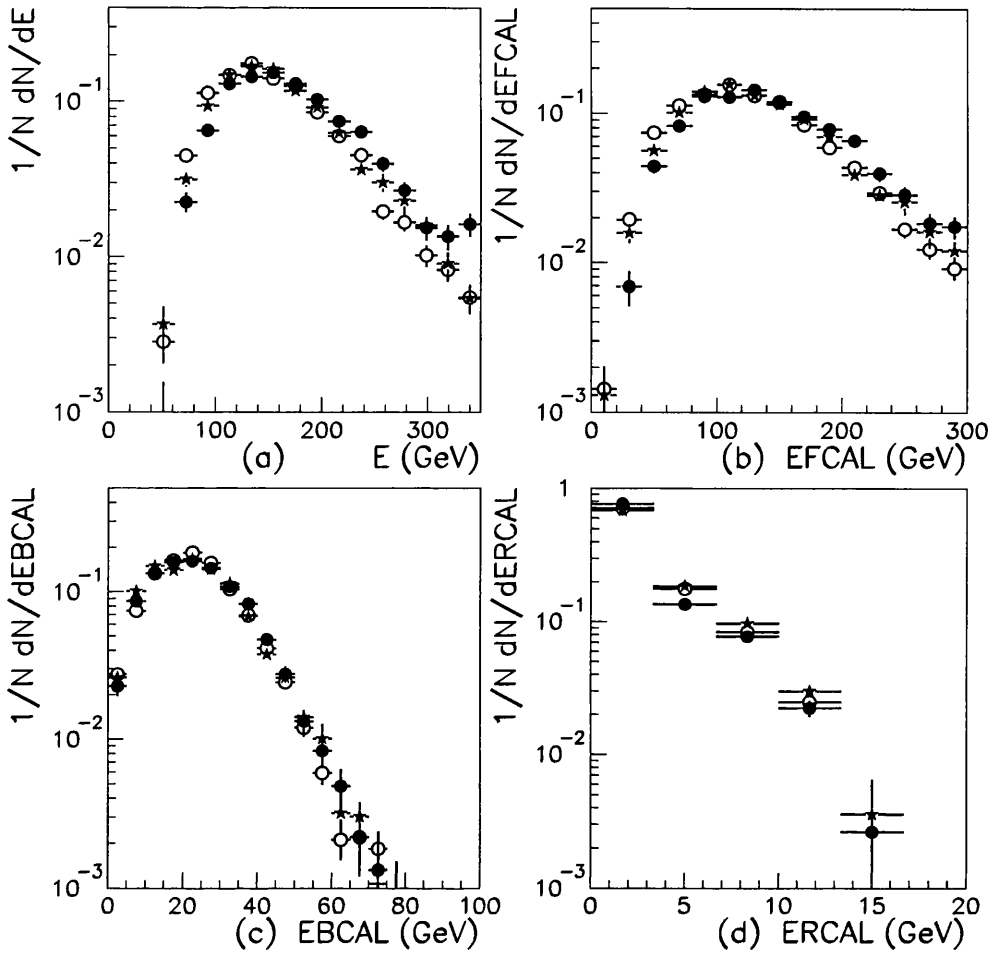

Figure 5.1: Comparison between data and Monte Carlo for some global energy variables normalised to the area. ZEUS data are shown by black dots, PYTHIA by open circles and HERWIG by stars. Only statistical errors are shown.

reproduces the general shape of the distribution. y_e is shown in figure 5.3(b) for events containing an electron which may be a π^0 or η meson which decayed electromagnetically to two photons, producing a narrow electromagnetic shower which led to its misidentification as an electron. As dicussed in section 4.2, DIS events generally have low values of y_e and it is clear that the events selected here with $y_e > 0.7$ are not DIS background. The good description of the data by the photoproduction Monte Carlo events shows it is possible that photoproduction events contain π^0 or η mesons which are reconstructed at detector level as electrons. It is to avoid losing these events that the $y_e > 0.7$ cut is applied.

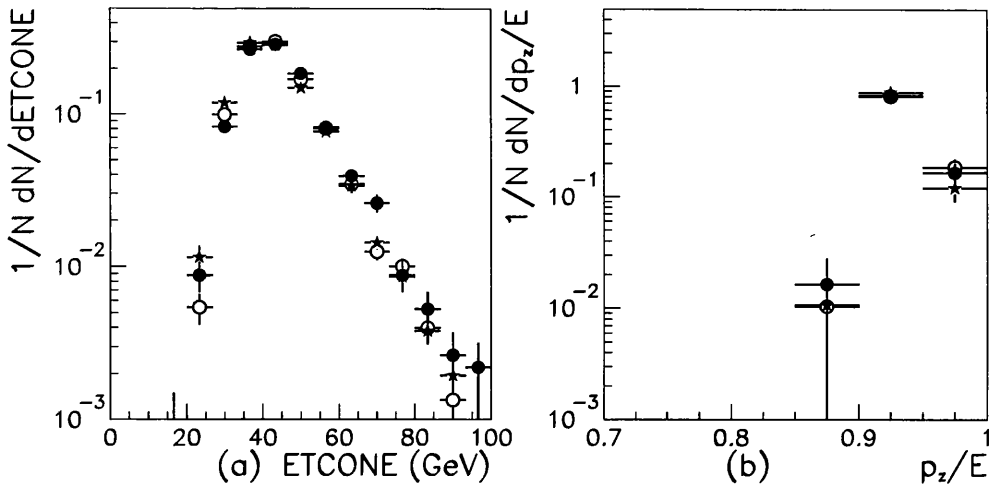

Figure 5.2: Comparison between data and Monte Carlo for some global energy variables normalised to the area. ZEUS data are shown by black dots, PYTHIA by open circles and HERWIG by stars. Only statistical errors are shown.

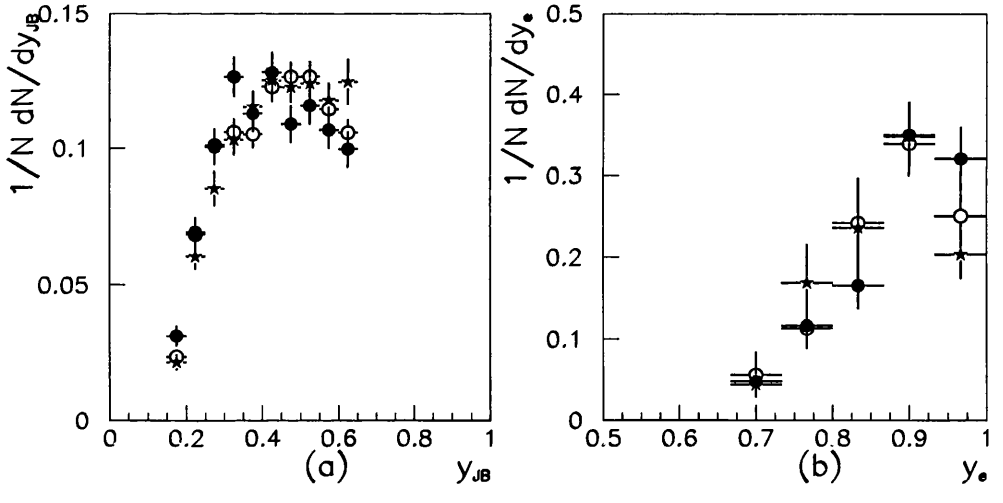

Figure 5.3: Comparison between data and Monte Carlo for y_{JB} (all events) and y_e (only events containing an electron) normalised to the area. ZEUS data are shown by black dots, PYTHIA by open circles and HERWIG by stars. Only statistical errors are shown.

Other quantities used in the initial selection cuts are the z position of the vertex (figure 5.4), the missing p_T in the events normalised by the square root of the total transverse energy (figure 5.5(a)) and the number of bad tracks (figure 5.5(b)) which are also well described by both Monte Carlos.

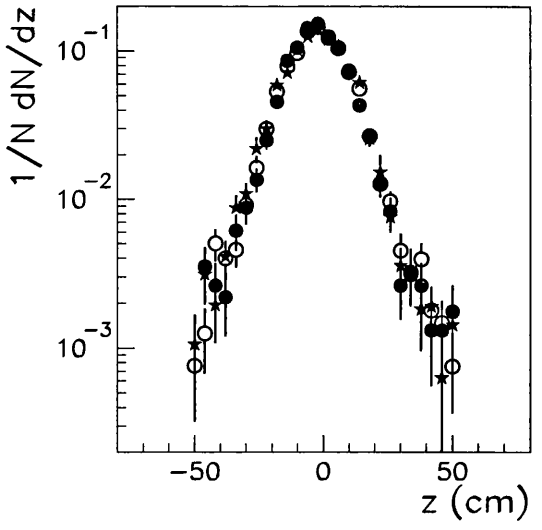

Figure 5.4: Comparison between data and Monte Carlo for the vertex distribution shown normalised to the area. ZEUS data are shown by black dots, PYTHIA by open circles and HERWIG by stars. Only statistical errors are shown.

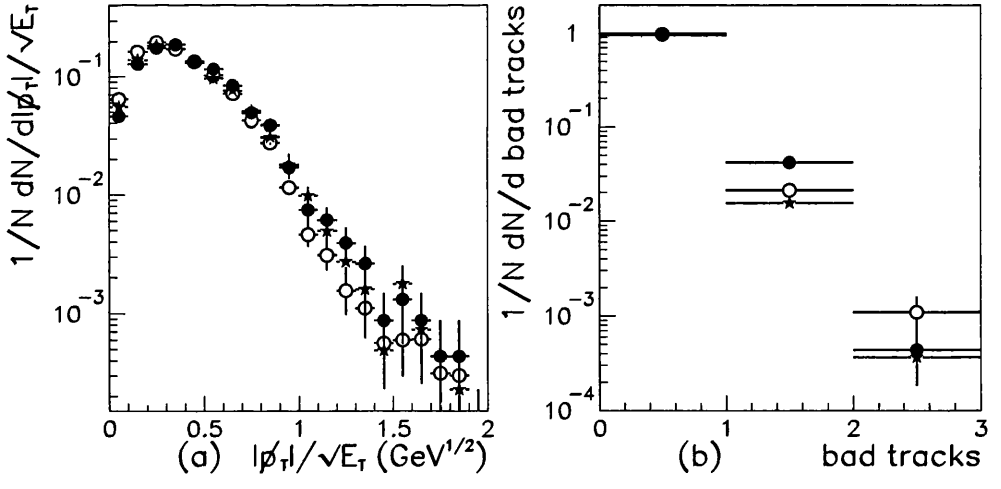

Figure 5.5: Comparison between data and Monte Carlo for the the missing p_T in the events normalised by the transverse energy and the number of bad tracks. ZEUS data are shown by black dots, PYTHIA by open circles and HERWIG by stars. Only statistical errors are shown.

5.3 Jet Characteristics

Figure 5.6(a),(c) and (e) shows the transverse energies of the three highest E_T^{cal} jets in the lab frame labeled 1, 2 and 3 in order of decreasing E_T^{cal}. The selection criteria

stated in 4.4 require that $E_T^{cal} > 5$ GeV for the highest two E_T^{cal} jets and $E_T^{cal} > 4$ GeV for the third jet and the E_T^{cal} distributions would be expected to fall steeply from these thresholds. In practice the selected data peak at 17 GeV for the highest E_T^{cal} jet, at 13 GeV for the second highest and although the E_T^{cal} distribution of the third highest E_T^{cal} jet does peak at the threshold it does not fall off exponentially as might be expected. A combination of the $M_{3J}^{cal} > 42$ GeV and the $|\cos\theta_3| < 0.8$ cuts, designed to reduce the bias on the angular distributions as shown in section 4.4, restrict the phase space for low E_T jet production. Since the resulting E_T^{cal} distributions do not peak at threshold the angular distributions should be fairly insensitive to the E_T selection criteria. The pseudorapidity distributions of the three highest E_T^{cal} jet are shown in figure 5.6(b),(d) and (f). The data are concentrated in the $\eta > 0$ region due to the large boost of most of the QCD subprocesses in the proton direction; the dip at $\eta \approx 1$ arises partly from the detector and partly from the event selection. Both the jet transverse energies and pseudorapidities are well described by the Monte Carlos. The PYTHIA description of the data is generally better than the HERWIG for $\eta^{cal\,3}$ while HERWIG is better than PYTHIA at reproducing $E_T^{cal\,3}$.

Photon remnants in dijet events with two jets with $E_T > 6$ GeV and $\eta < 1.6$ have been studied at ZEUS [70]. A third cluster, associated with the photon remnant, was found to have a mean E_T of 2 GeV and an η distribution peaked at -2. In the present study the third highest E_T^{cal} jet has a mean E_T^{cal} of 8 GeV with a tail extending to 20 GeV. The jets are concentrated in the forward direction and the η distribution extends back to only $\sim$ -1.5. It would therefore be unreasonable to associate the third highest E_T^{cal} jet in this analysis with the photon remnant.

$x_{\gamma\,3J}^{obs}$, shown in figure 5.7, is obtained from

$$x_{\gamma\,3J}^{obs} \equiv \sum_{3\ jets} \frac{E_T^{cal} \exp(-\eta^{cal})}{2 y_{JB} E_e} \tag{5.1}$$

where the sum runs over the three highest E_T^{cal} jets in the event. The data are peaked at $x_{\gamma\,3J}^{obs} = 0.9$ with a tail extending down to 0.2 and are in general agreement with PYTHIA and HERWIG. The PYTHIA prediction for the LO direct process only is shown as the shaded histogram and is concentrated at $x_{\gamma 3J}^{obs} > 0.8$. At LO, resolved processes are therefore required to describe the low $x_{\gamma\,3J}^{obs}$ part of the distribution. Note

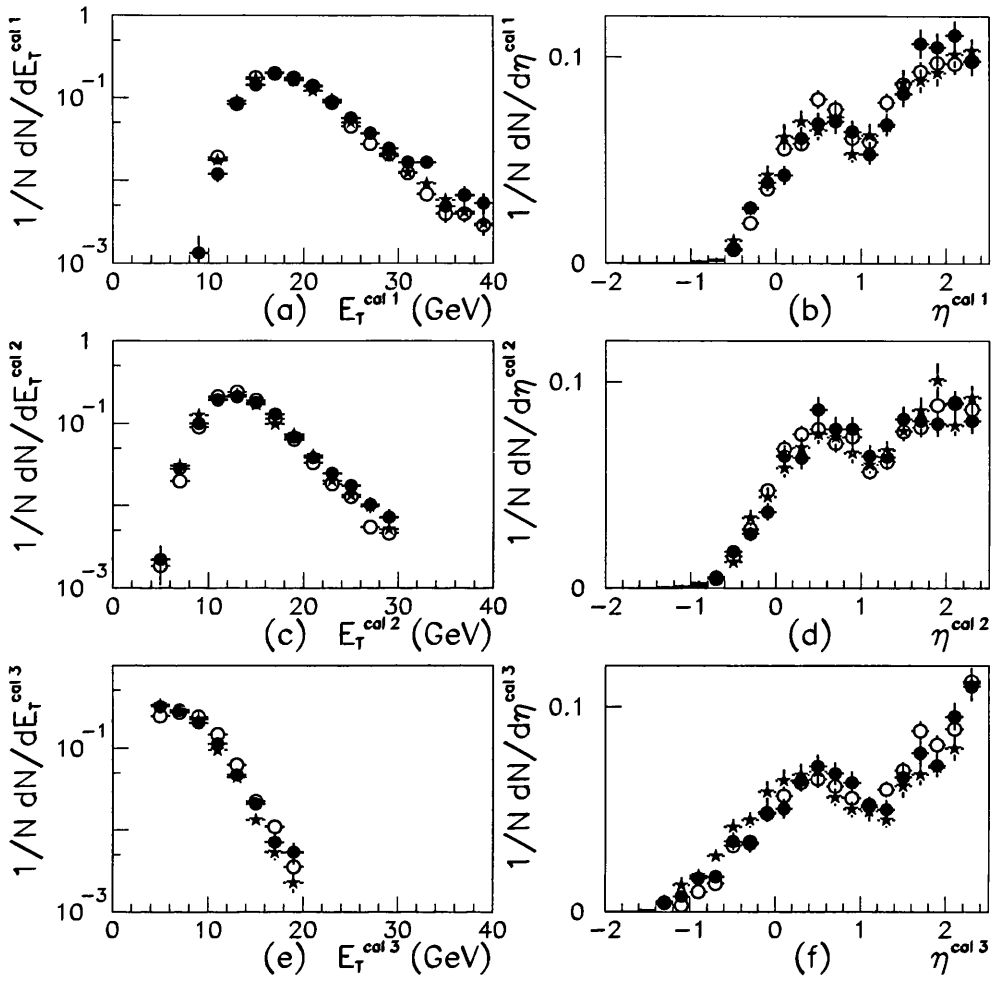

Figure 5.6: Comparison between data and Monte Carlo for the transverse energies and pseudo-rapidities of the three highest E_T^{cal} jets in the lab frame. The jets are ordered 1, 2 and 3 in order of decreasing E_T^{cal}. ZEUS data are shown by black dots, PYTHIA by open circles and HERWIG by stars. Distributions are shown normalised to the area and only statistical errors are shown.

that LO resolved processes also make a non-negligible contribution to the $x_{\gamma 3J}^{obs} > 0.8$ region.

The invariant mass of the three-jet events is shown in figure 5.8. The data are peaked at the threshold, 42 GeV, and fall off exponentially with increasing M_{3J}^{cal}. The distribution extends to 140 GeV and the shape is well described by PYTHIA and HERWIG.

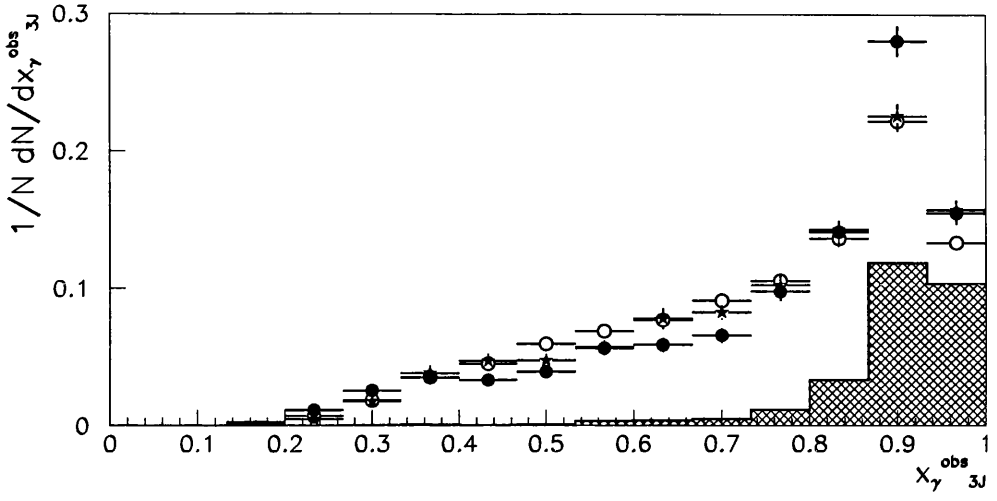

Figure 5.7: Comparison between data and Monte Carlo for $x_{\gamma\,3J}^{obs}$. ZEUS data are shown by black dots, PYTHIA by open circles and HERWIG by stars. The PYTHIA prediction for the direct process only is indicated by the shaded histogram. Distributions are shown normalised to the area except for the PYTHIA direct only which is normalised to show the correct fraction of PYTHIA events which come from the direct process. Only statistical errors are shown.

5.4 Jet Profiles

Jet profiles provide a means to study the distribution of transverse energy in and around a jet as a function of pseudorapidity and azimuth, as illustrated in figure 5.9. The distance in η or φ between each cell in the calorimeter and the centre of the jet is calculated, $\Delta\eta \equiv \eta^{cell} - \eta^{cal}$, $\Delta\varphi \equiv \varphi^{cell} - \varphi^{cal}$. The E_T profile as a function of $\Delta\eta$ is obtained by plotting $\Delta\eta$, weighted by E_T^{cell}, divided by the bin width, for each cell in a band of $\Delta\varphi < 1$ around the jet centre, as shown in figure 5.9(a). Similarly, the $\Delta\varphi$ profile is obtained by plotting $\Delta\varphi$, weighted by E_T^{cell}, divided by the bin width, for each cell in a band of $\Delta\eta < 1$ around the jet centre, figure 5.9(b).

Figure 5.10 shows the $\Delta\eta$ and $\Delta\varphi$ profiles of the highest E_T^{cal} jet in three different bins of η, $\eta < 0.5$, $0.5 < \eta < 1.5$ and $1.5 < \eta < 2.5$. The $\Delta\varphi$ profiles show the data concentrated around zero, the core of the jet, with two secondary peaks at $\pm\pi$ corresponding to the other jets in the event. The data are well described by the Monte Carlo. The η profiles of the highest E_T^{cal} jet, (b), (d) and (f), again show the energy deposits concentrated around the core of the jet with a pedestal of lower energy deposits

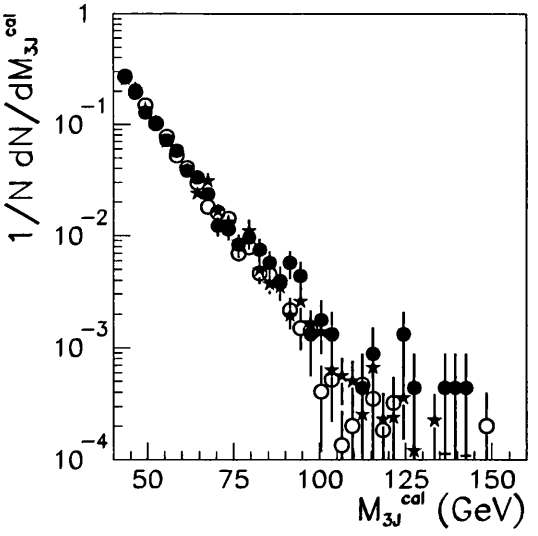

Figure 5.8: Comparison between data and Monte Carlo for the invariant mass of the three jets. ZEUS data are shown by black dots, PYTHIA by open circles and HERWIG by stars. Distributions are shown normalised to the area and only statistical errors are shown.

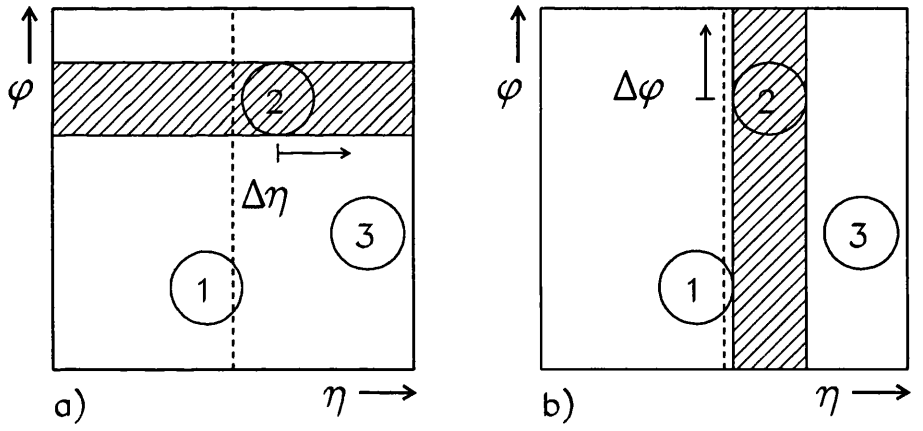

Figure 5.9: An illustration of the method employed to make jet profiles.

in the forward direction. There is good agreement between the data and the Monte Carlo.

The φ profiles, figures 5.11(a), (c) and (e), and η profiles, figures 5.11(b), (d) and (f), of the second highest E_T^{cal} jet are similar to those of the highest E_T^{cal} jet. They are well described by the Monte Carlo except perhaps for the most forward jets, figure 5.11(e), where HERWIG appears to underestimate the amount of transverse energy in

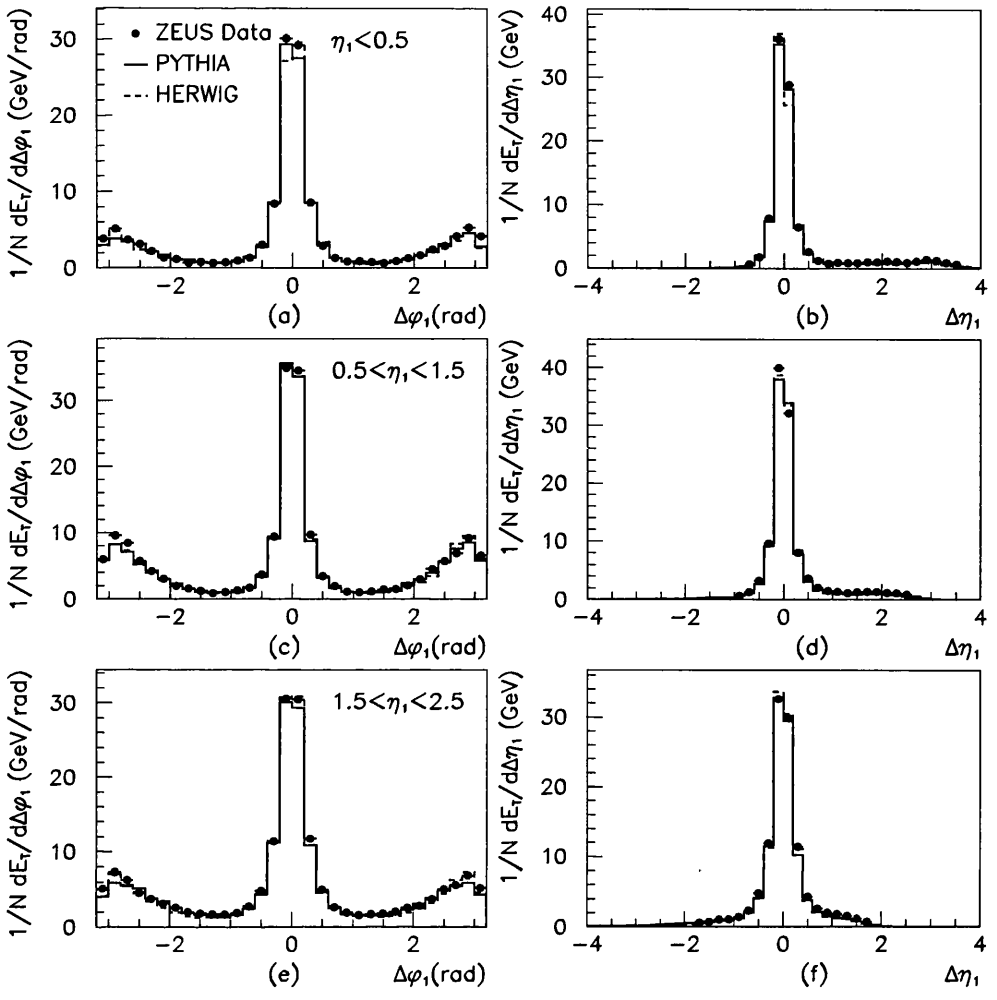

Figure 5.10: Comparison between data and Monte Carlo for the transverse energy jet profiles of the highest E_T^{cal} jet as a function of $\Delta\eta$ and $\Delta\varphi$. ZEUS data are shown by black dots, PYTHIA by the solid histogram and HERWIG by the dashed histogram.

the region between the jets.

Figure 5.12 shows the φ and η profiles of the third highest E_T^{cal} jet. The φ profiles, (a), (c) and (e), show the secondary peaks have moved closer to the jet core. Moving from the highest E_T^{cal} jet to the third highest, the secondary peaks just within $\pm\pi$ move to much smaller $\Delta\phi$ values. This indicates that the highest and second highest E_T^{cal} jets tend to have a roughly opposite balancing jet but that the third highest E_T^{cal} jet is much more randomly oriented in ϕ with respect to the other two. The η profiles, (b), (d) and (f), also show secondary peaks where another jet tends to lie close to the

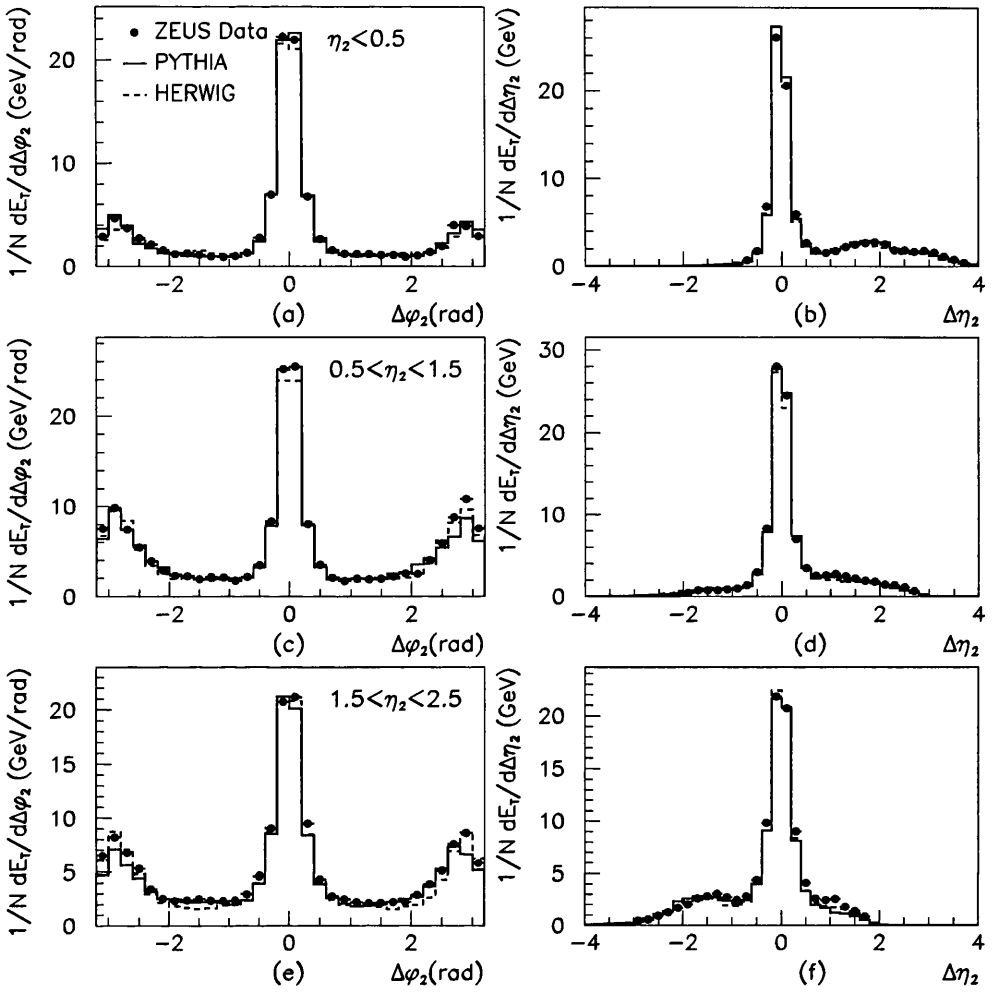

Figure 5.11: Comparison between data and Monte Carlo for the transverse energy jet profiles of the second highest E_T^{cal} jet as a function of $\Delta\eta$ and $\Delta\varphi$. ZEUS data are shown by black dots, PYTHIA by the solid histogram and HERWIG by the dashed histogram.

third jet in azimuth. Again the data are reasonably well described by PYTHIA and HERWIG.

The good agreement between the data and the Monte Carlos for all three jets confirms that the three-jet events in the Monte Carlo have similar jets and energy flows to those in the data. The Monte Carlo thus models the data well and is suitable for correcting the data to hadron level.

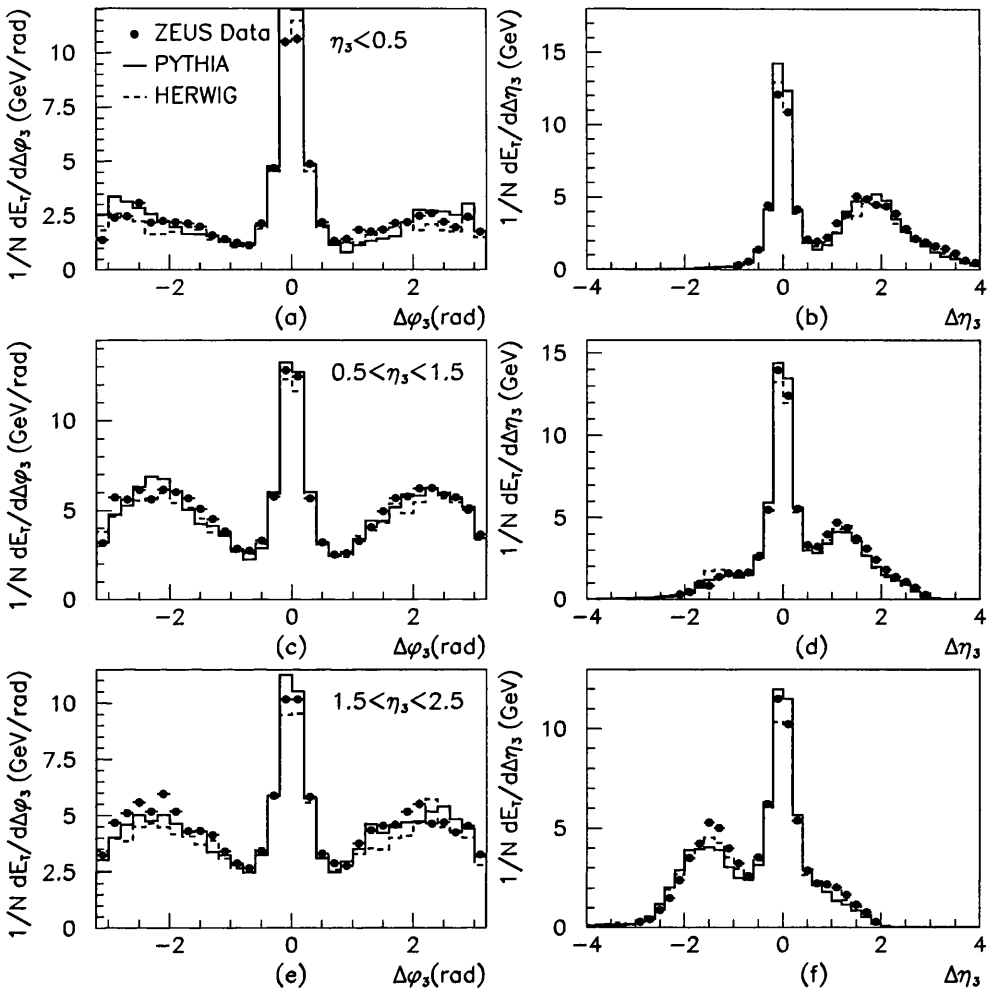

Figure 5.12: Comparison between data and Monte Carlo for the transverse energy jet profiles of the third highest E_T^{cal} jet as a function of $\Delta\eta$ and $\Delta\varphi$. ZEUS data are shown by black dots, PYTHIA by the solid histogram and HERWIG by the dashed histogram.

5.5 Centre-of-Mass Observables

In order to calculate the three-jet angular variables, $\cos\theta_3$ and ψ, and the energy-sharing variables, X_3 and X_4, it is necessary to boost the three-jet system to the centre-of-mass of the three jets on an event-by-event basis. The distribution of the x, y and z components of this boost are shown in figure 5.13. The boost is given by $tanh^{-1}\beta_{x,y,z}$, where β is the velocity of the centre-of-mass frame with respect to the lab frame, reflecting that the centre-of-mass and lab frames in photoproduction analyses

are related by a simple shift in pseudorapidity. As expected the main contribution to the boost is in the positive z direction, since the incoming partons are approximately collinear to the beam axis and the parton from the proton generally has more energy than the parton from the photon. The z component of the boost, figure 5.13(c) is peaked around 1.2 and ranges from 0.2-2.2. However, there is also a small transverse boost shown by the x and y components in figure 5.13(a) and (b). These range between $\pm$ 0.1 and are peaked at zero. The Monte Carlo reproduces the data distributions well.

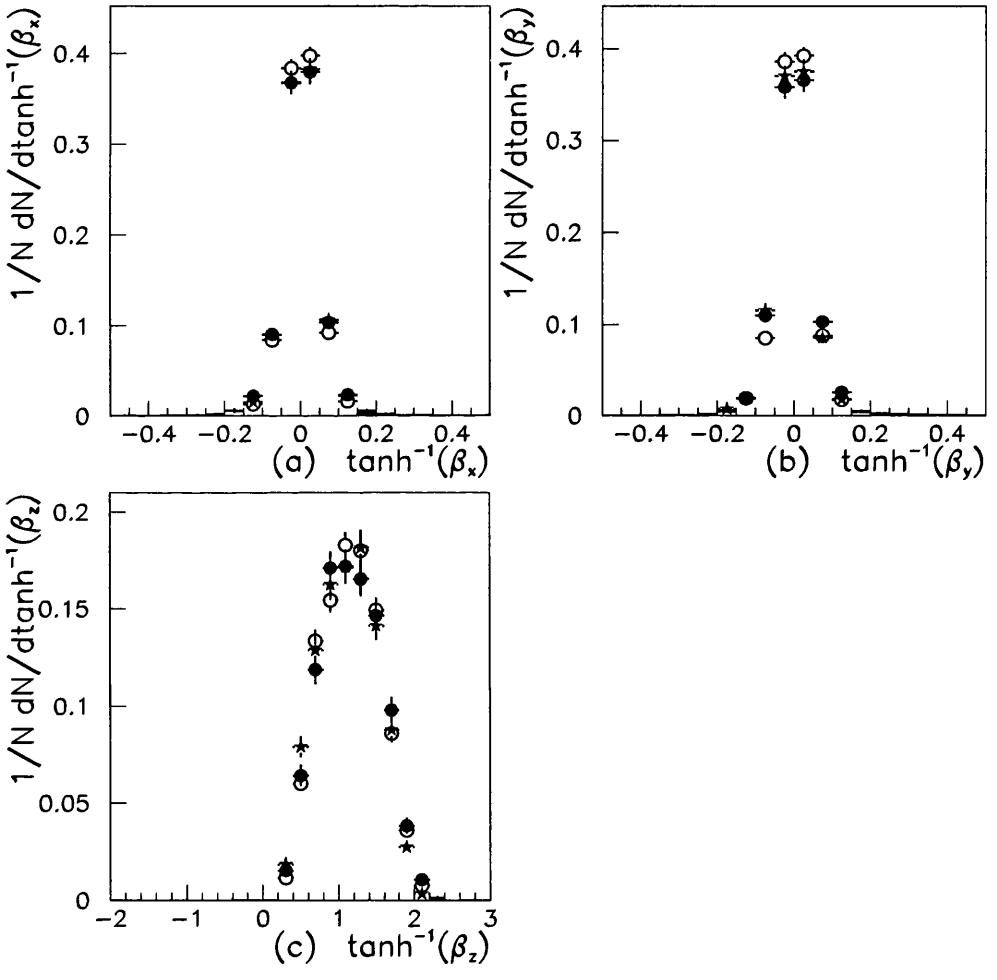

Figure 5.13: Comparison between data and Monte Carlo for the components of the boost to the three-jet centre-of-mass. ZEUS data are shown by black dots, PYTHIA by open circles and HERWIG by stars. Distributions are shown normalised to the area and only statistical errors are shown.

Figure 5.14 shows the angular variables $\cos\theta_3$ and ψ_3 , and the energy-sharing variables, X_3 and X_4. The $\cos\theta_3$ distribution is peaked at $\pm$ 0.8 with the data favouring small scattering angles as, for example, in Rutherford scattering. The data are generally well described by PYTHIA and HERWIG, with the exception of the lowest and highest HERWIG bins. There is a slight asymmetry in the distribution which could be due to some residual bias from the E_T^{cal} or η^{cal} cuts.

As pointed out in chapter 1, ψ_3 is undefined for two-jet events and its shape may be considered as driven mainly by the properties of the third jet. The ψ_3 distribution shows the data having a minimum around $\psi_3 = 1.6$ radians, peaking at $\sim$ 0.4 and 2.8 radians and dropping down again in the lowest and highest bins. The dip at 0 and π radians is due to the residual bias from the E_T^{cal} and η^{cal} cuts and also in part to the restrictions imposed on the angular separation of jets by the jet finder. The peaks in the distribution at low and high values of ψ_3 show that the third highest E_T^{cal} jet lies close to the beam direction suggesting that it comes from initial state radiation. The data are reasonably well described by PYTHIA. HERWIG seems to have more pronounced peaks than the data at high and low ψ_3 but the description of the data is also reasonable.

The X_3 distribution is shown in figure 5.14(c). As mentioned in section 1.4 this is constrained to lie between $\frac{2}{3}$ and 1 due to energy conservation. The data are peaked at the cut-off of 0.95 indicating that the highest energy jet has a tendency to take close to the maximum amount of energy available to it. HERWIG describes the data well while PYTHIA underestimates the number of jets taking large fractions of energy.

The X_4 distribution, figure 5.14(d) is constrained to lie between $\frac{1}{2}$ and 0.95. The data are peaked at $\sim$ 0.7 and have quite a broad distribution. PYTHIA and HERWIG, while in general agreement with the data, seem to have a slightly narrower, more peaked distribution.

5.6 Summary

In summary, it has been shown that the simulation of the ZEUS detector works well and that events from the LO matrix element plus parton shower Monte Carlo event

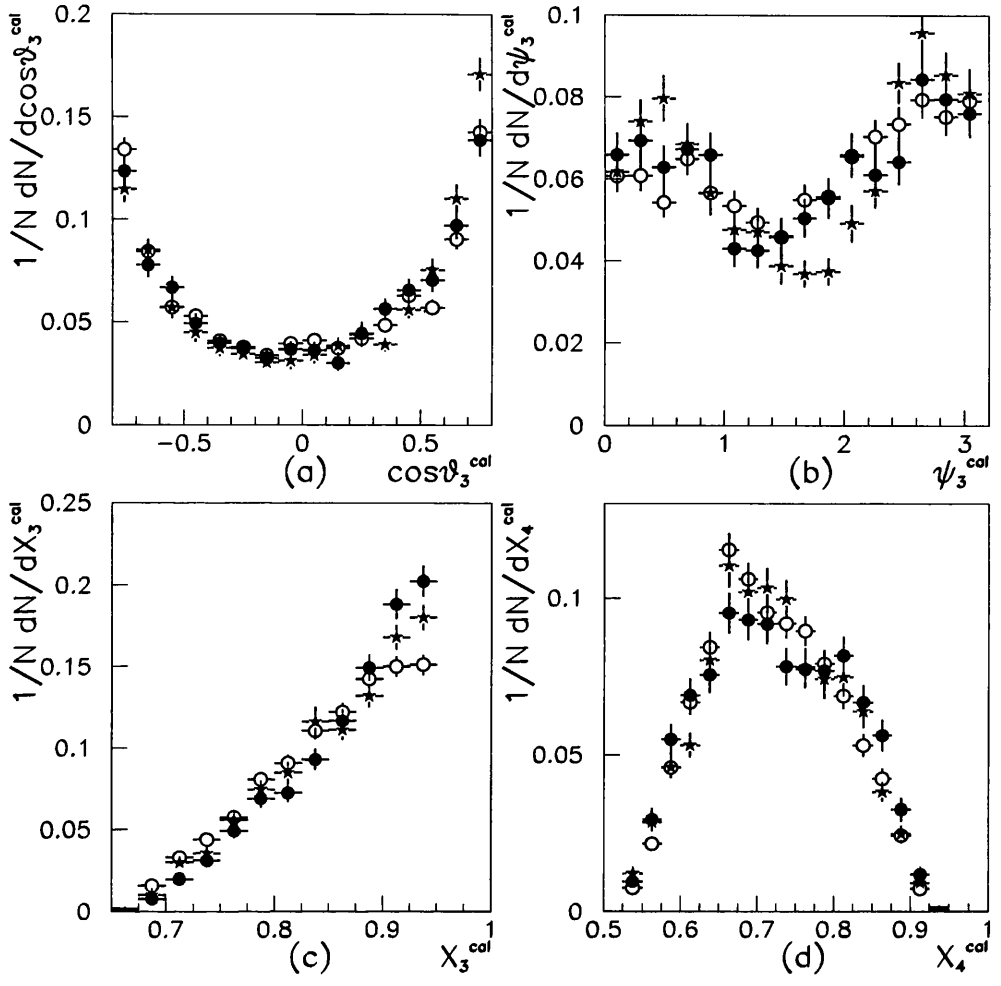

Figure 5.14: Comparison between data and Monte Carlo for the angular variables $\cos\theta_3$ and ψ_3 and the energy-sharing variables X_3 and X_4. ZEUS data are shown by black dots, PYTHIA by open circles and HERWIG by stars. Distributions are shown normalised to the area and only statistical errors are shown.

generators PYTHIA and HERWIG provide a reasonable description of the raw three-jet ZEUS data. General event features used to select good photoproduction events are well described. The properties of jets such as transverse energy, pseudorapidity, transverse energy flow and three-jet invariant mass are also reproduced satisfactorily by PYTHIA and HERWIG. Finally, the three-jet dimensionless quantities $\cos\theta_3$, ψ_3, X_3 and X_4 are all well described by at least one model.

The good agreement between the shapes of the data and Monte Carlo distributions

demonstrates the suitability of the Monte Carlo events for correcting the data for detector effects. Since PYTHIA gives a better description of the angular distributions it will be used for the basic correction. The correction procedure will be discussed in the following chapter.

Chapter 6

Correcting for Detector Effects

The aim of this chapter is to give an account of a procedure based on Monte Carlo events which can correct measured ZEUS data to the hadron level, thus facilitating comparison with theory. Chapter 5 showed that after simulation of the ZEUS detector the Monte Carlo event generators PYTHIA and HERWIG described the ZEUS data satisfactorily. This demonstrates that a Monte Carlo based method can be used to correct the data from detector to hadron level. The PYTHIA and HERWIG event samples described in appendix A were used in the following analysis.

For any distribution a bin-by-bin correction method can be employed such that

$$Data^{corrected}\ bin(i) = Data^{detector}\ bin(i) \cdot \frac{Monte\ Carlo^{hadron}\ bin(i)}{Monte\ Carlo^{detector}\ bin(i)} \qquad (6.1)$$

provided that the shape of the measured distribution is well described by the Monte Carlo detector level distribution and that each bin at detector level corresponds closely to the same bin at hadron level to minimise bin-by-bin migrations. Section 6.1 examines the agreement between hadron and detector level quantities while section 6.2 shows the correction factors obtained using the above bin-by-bin method.

6.1 Jet Energy Corrections

Ideally, a detector would be able to measure particle positions and energies exactly. However detectors have finite angular and energy resolutions and other factors such

as energy losses due to dead material in the detector, loss of low p_T hadrons and detector response varying with the energy of the incident particles also impair the correspondence between detector and hadron level quantities. This can be improved by studying, and correcting for, the differences between detector level and hadron level jets obtained by applying the k_T jet finder described in section 4.3 to both CAL cells and final state hadrons of Monte Carlo events which have been subjected to a full simulation of the ZEUS detector.

6.1.1 Transverse Energy Correction

Events are selected which pass a three jet selection at both detector and hadron level of

- 2 detector level jets with $E_T^{cal} > 5$ GeV, a third jet with $E_T^{cal} > 4$ GeV and $\eta^{cal} < 2.5$ for all jets.
- 2 hadron level jets with $E_T^{had} > 6$ GeV, a third jet with $E_T^{had} > 5$ GeV and $\eta^{cal} < 3.0$ for all jets.
- $M_{3J}^{cal} > 42$ GeV and $M_{3J}^{had} > 50$ GeV.

In this way the E_T correction is obtained from events which are representative of the final analysis selection. Detector level jets with $E_T^{cal} > 5$ GeV and $\eta^{cal} < 2.5$ are selected and a matching hadron level jet sought with $E_T^{had} > 4$ GeV and $\eta^{had} < 3.0$. Jets are considered to match if the distance between them in the $\eta - \varphi$ plane, $R \equiv \sqrt{(\eta^{cal} - \eta^{had})^2 + (\varphi^{cal} - \varphi^{had})^2} < 1$. The distance separating matching jets is shown in figure 6.1(a), the peak near zero showing that in most cases a good match been detector and hadron level is achieved. If more than one jet satisfies these criteria the closest is chosen. The fraction of detector level jets matching zero or two hadron level jets is shown in figure 6.1(b) and is of the order of 2%.

Once pairs of matched detector and hadron level jets have been found the differences in the angular and energy variables can be studied. Figures 6.2(b),(d) and (f) show scatter plots indicating how the energy and angles of matched jets are distributed. The resolutions shown in figures 6.2(a),(c),and (e), fitted by Gaussian functions, show how

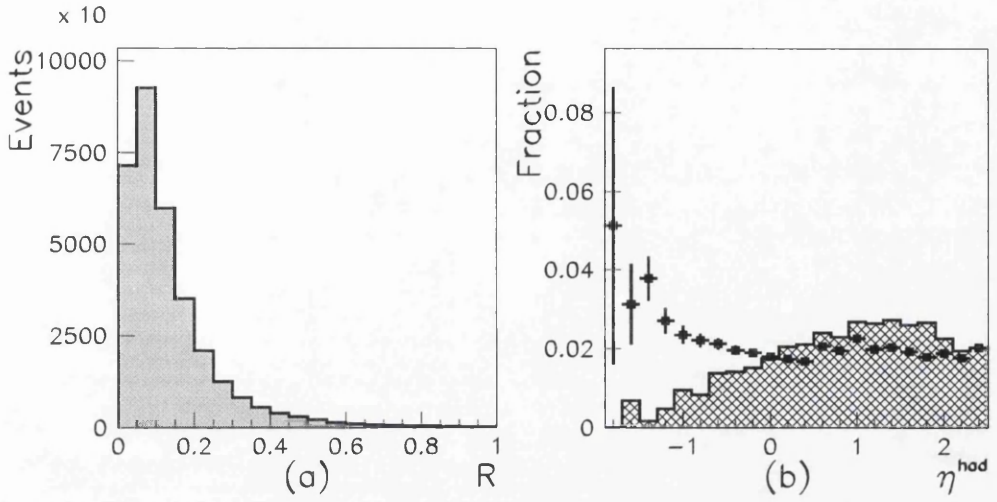

Figure 6.1: (a) The distance in the $\eta - \varphi$ plane between matching detector and hadron level jets and (b) the fraction of detector level jets which are matched with zero (points) or two (histogram) hadron level jets for PYTHIA events.

well the quantities for hadron level jets are reproduced by the detector variables. It can be seen that the angular variables η and φ are well correlated between detector and hadron level with no systematic shift and good resolution. The jet transverse energy, on the other hand, shows a systematic shift which must be corrected for with E_T^{cal} being on average 15% less than E_T^{had}.

The dependence of the difference in η, φ and E_T between detector and hadron level jets on η^{cal}, φ^{cal} and E_T^{cal} is shown in figure 6.3. $\Delta\varphi \equiv \varphi^{had} - \varphi^{cal}$, is flat in η^{cal}, φ^{cal} and E_T^{cal} and is centred on zero. $\Delta\eta \equiv \eta^{had} - \eta^{cal}$, is also flat in φ^{cal} and E_T^{cal} and is centred on zero but shows some dependence on η^{cal}. However, as the variation with η^{cal} of about $\pm$ 0.02 is much less than the width of the η resolution, 0.08, it can in effect be considered independent of η^{cal}. No corrections are required for η^{cal} or φ^{cal} and in future $\eta^{cal} = \eta^{cor} \equiv \eta$ and $\varphi^{cal} = \varphi^{cor} \equiv \varphi$, where ^{cor} indicates the value of a variable after correcting for detector shifts.

$\Delta E_T \equiv E_T^{had} - E_T^{cal}$, becomes larger as E_T^{cal} increases and also varies with η so a correction procedure is employed which varies with E_T^{cal} and η. Two different correction procedures have been studied, one to be used in the main analysis and the other as a systematic check of the E_T correction method.

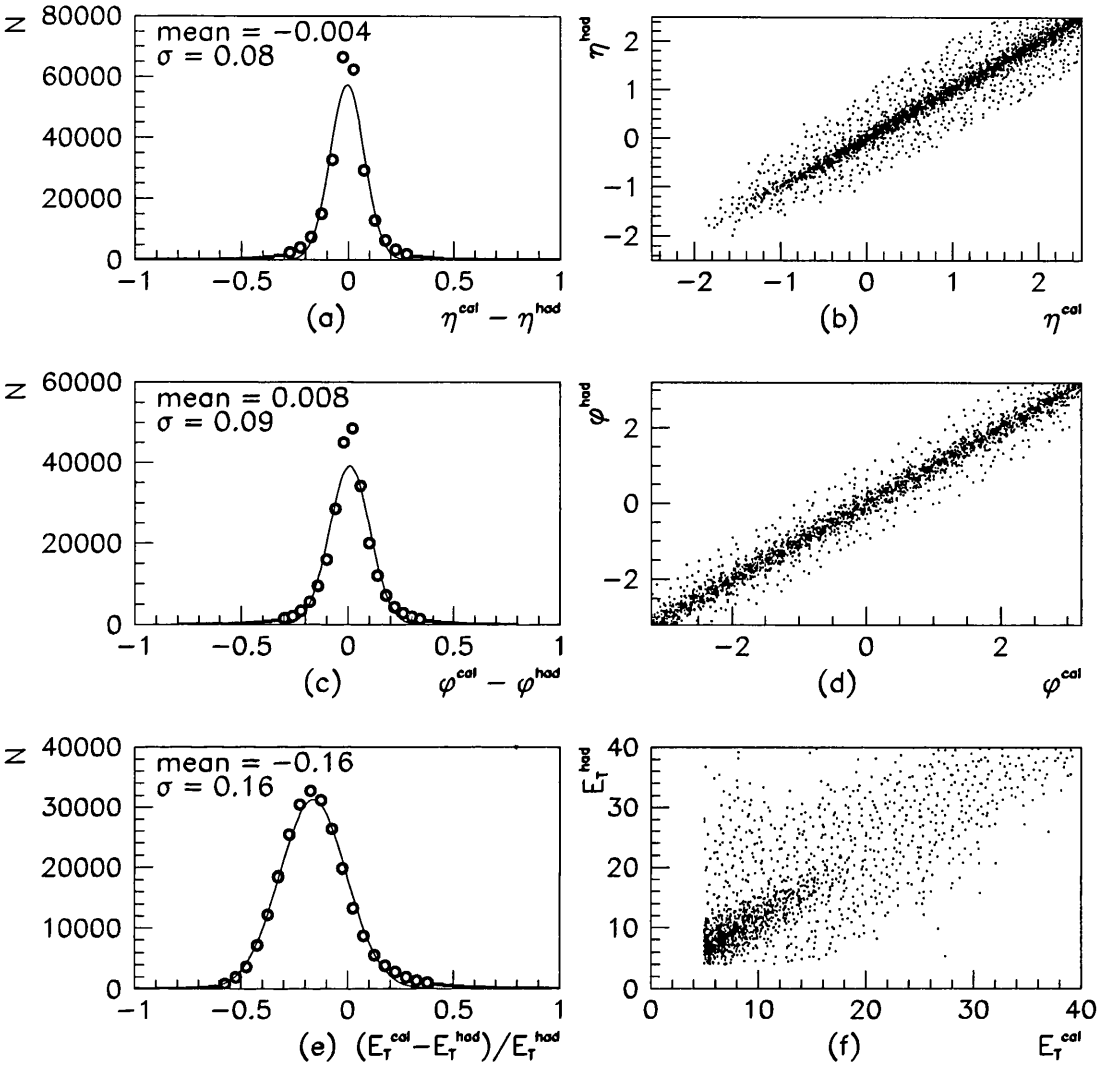

Figure 6.2: Resolutions for (a) η, (c) φ and (e) E_T for PYTHIA events and correlations between (b) η, (d) φ and (f) E_T for matching pairs of detector and hadron level jets.

The event sample is divided into 12 bins of η and 5 bins of transverse energy according to the resolution and the available statistics. The first procedure studied, in future referred to as *correction method 1*, involves plotting $\langle E_T^{had}/E_T^{cal}\rangle$ of a matched pair of jets as a function of E_T^{cal}. These distributions are fitted by a function of the form $F(E_T^{cal}) \equiv A + exp(B + C \cdot E_T^{cal})$ to give a multiplicative correction factor which can be applied on a jet-by-jet basis to give the corrected transverse energy of a jet, $E_T^{cor}(E_T^{cal}, \eta) = F \cdot E_T^{cal}$. The correction functions obtained by fitting PYTHIA

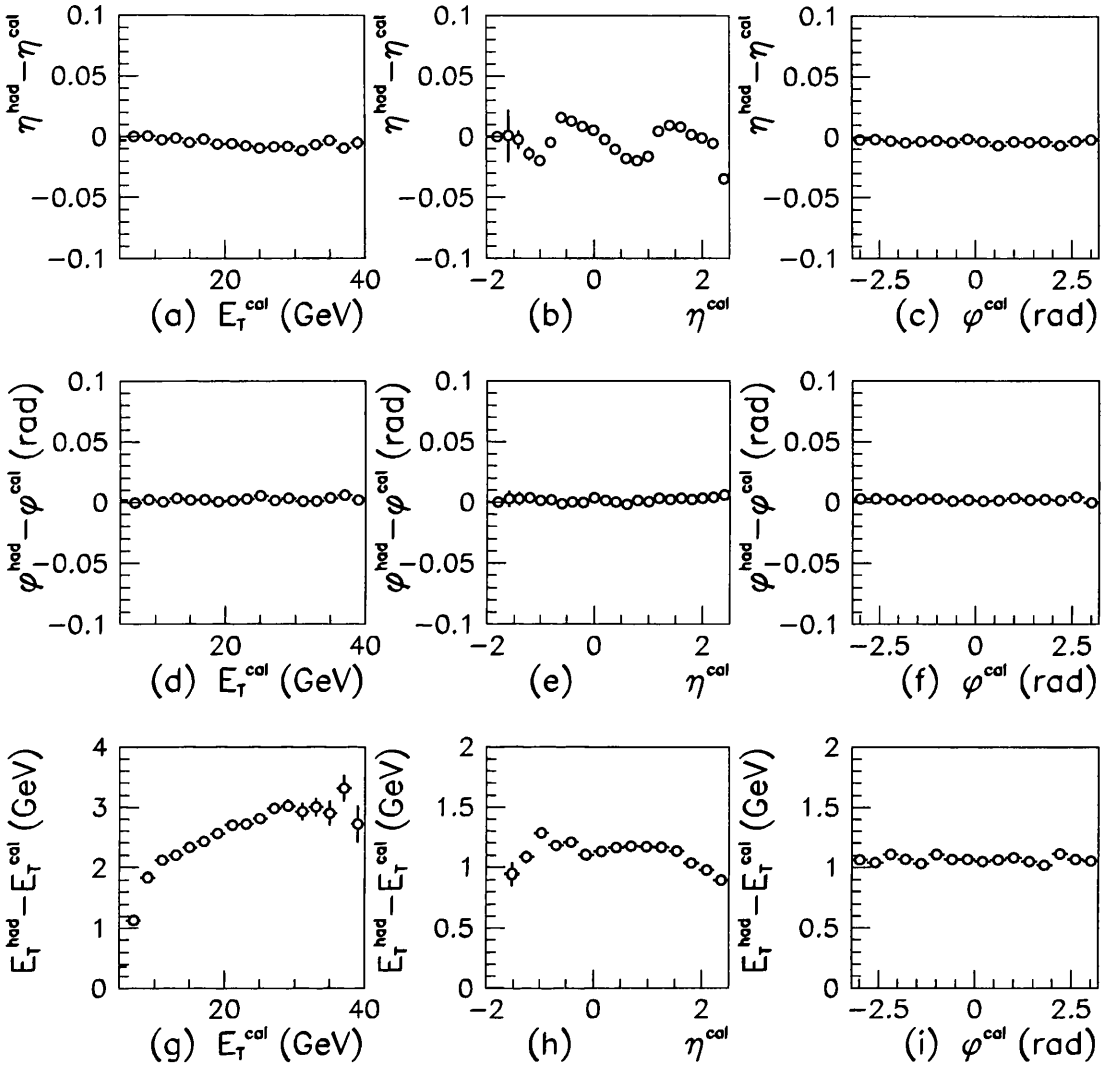

Figure 6.3: The correlation of the difference between detector and hadron level quantities with η, φ and E_T^{cal} shown for PYTHIA events. (a), (b), (c) $\Delta\eta$ vs E_T^{cal}, η, φ; (d), (e), (f) $\Delta\varphi$ vs E_T^{cal}, η, φ; (g), (h), (i) ΔE_T vs E_T^{cal}, η, φ. The points show the mean of the distributions and the error on the mean.

distributions are shown in figure 6.4. A reasonably good fit is obtained.

In the second E_T correction procedure, in future referred to as *correction method 2*, E_T^{cal} is plotted as a function of E_T^{had} for pairs of matched jets. The distributions are fitted with a function of the form $E_T^{cal} = A + B \cdot E_T^{had}$ from which the corrected E_T of the jet is obtained, $E_T^{cor} = \frac{E_T^{cal}-A}{B}$. Figure 6.5 shows that good fits to the PYTHIA distributions are obtained neglecting the lowest E_T point which is affected by the E_T

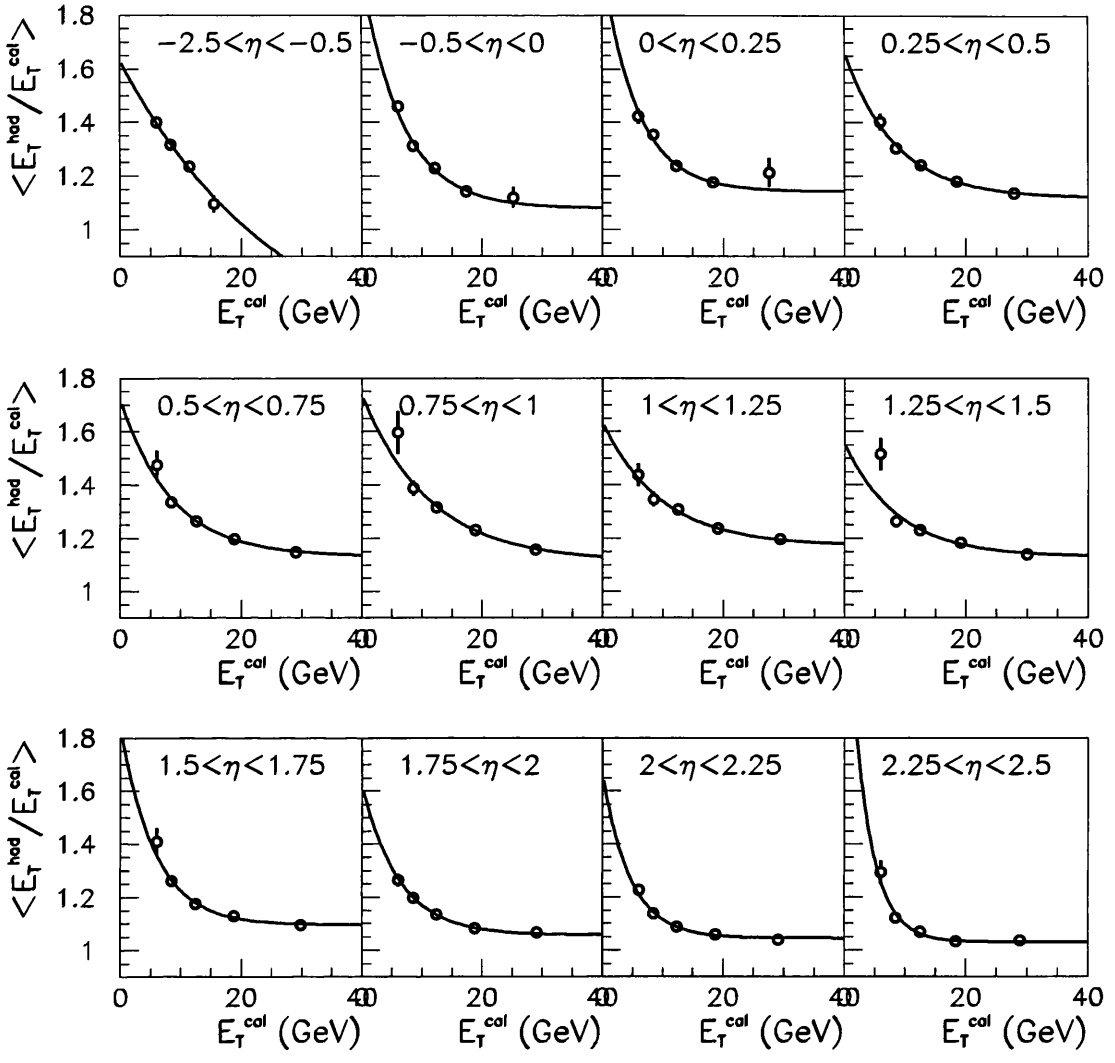

Figure 6.4: E_T^{had}/E_T^{cal} in bins of E_T^{cal} fitted by a function $F(E_T^{cal}, \eta) \equiv A + exp(B + C\dot{E}_T^{cal})$ to obtain the jet energy correction functions from PYTHIA events. Points are plotted at the mean of the bin.

thresholds applied when selecting the jets. The linear fit neglects any change in the amount of E_T correction as a function of E_T, only the change with η is taken into consideration.

As this correction method relies heavily on simulated Monte Carlo events it is important to check whether it is sensitive to model-dependent effects. Since the correction depends mainly on the energy and position of the jets and not on the internal structure the model dependence involved in correcting for detector effects to hadron

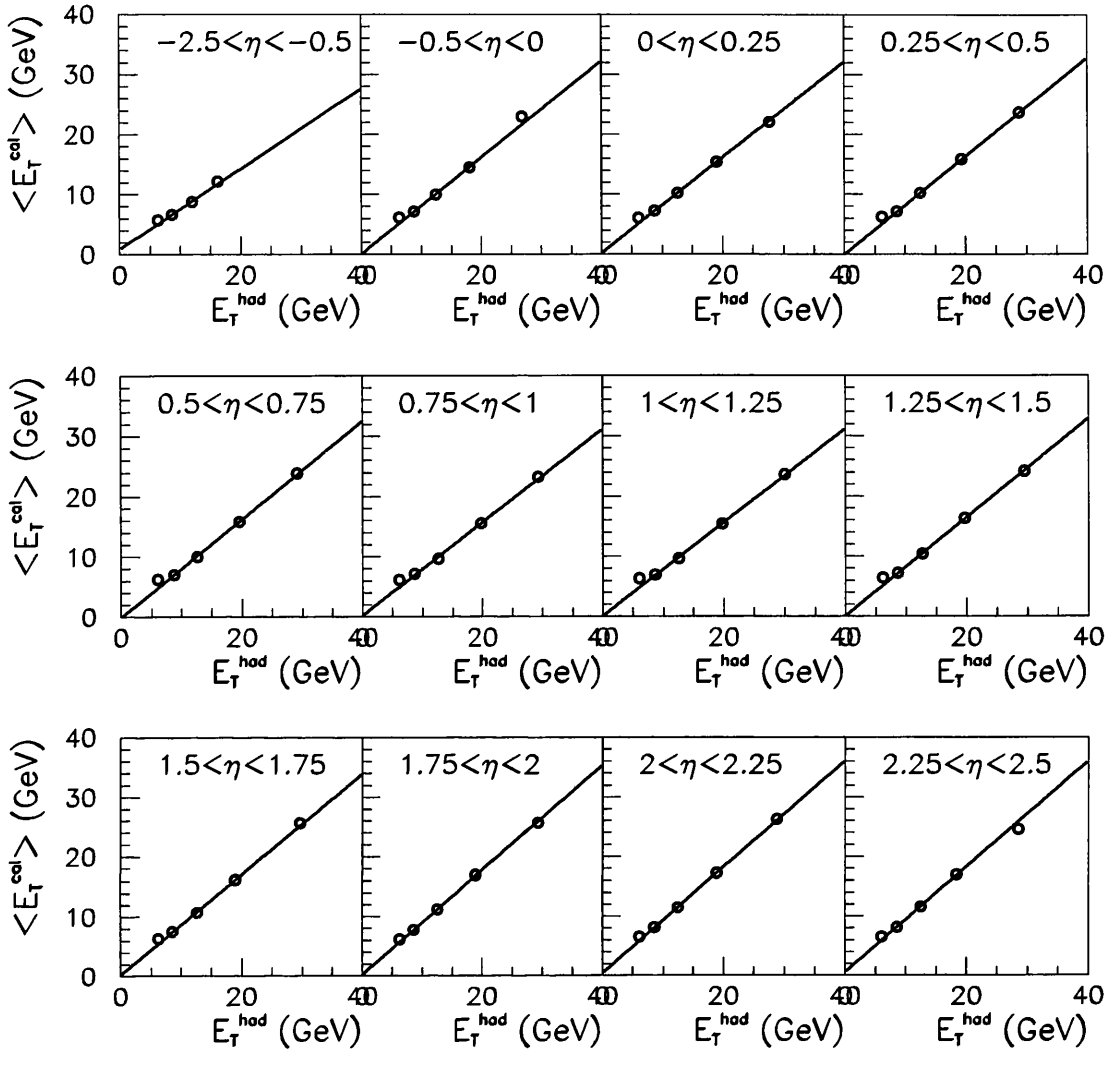

Figure 6.5: E_T^{cal} vs E_T^{had} fitted by a function $E_T^{cal} = A + B\dot{E}_T^{had}$ to obtain the jet energy correction functions using PYTHIA events.

level is not expected to be large. The correction functions obtained from PYTHIA and HERWIG events, which differ mainly in the treatment of the parton shower and the hadronisation process as discussed in section 5.1, are shown in figure 6.6 for correction method 1 and in figure 6.7 for correction method 2, in order to illustrate their functional form. The correction functions are very similar with the differences between them less than 5%.

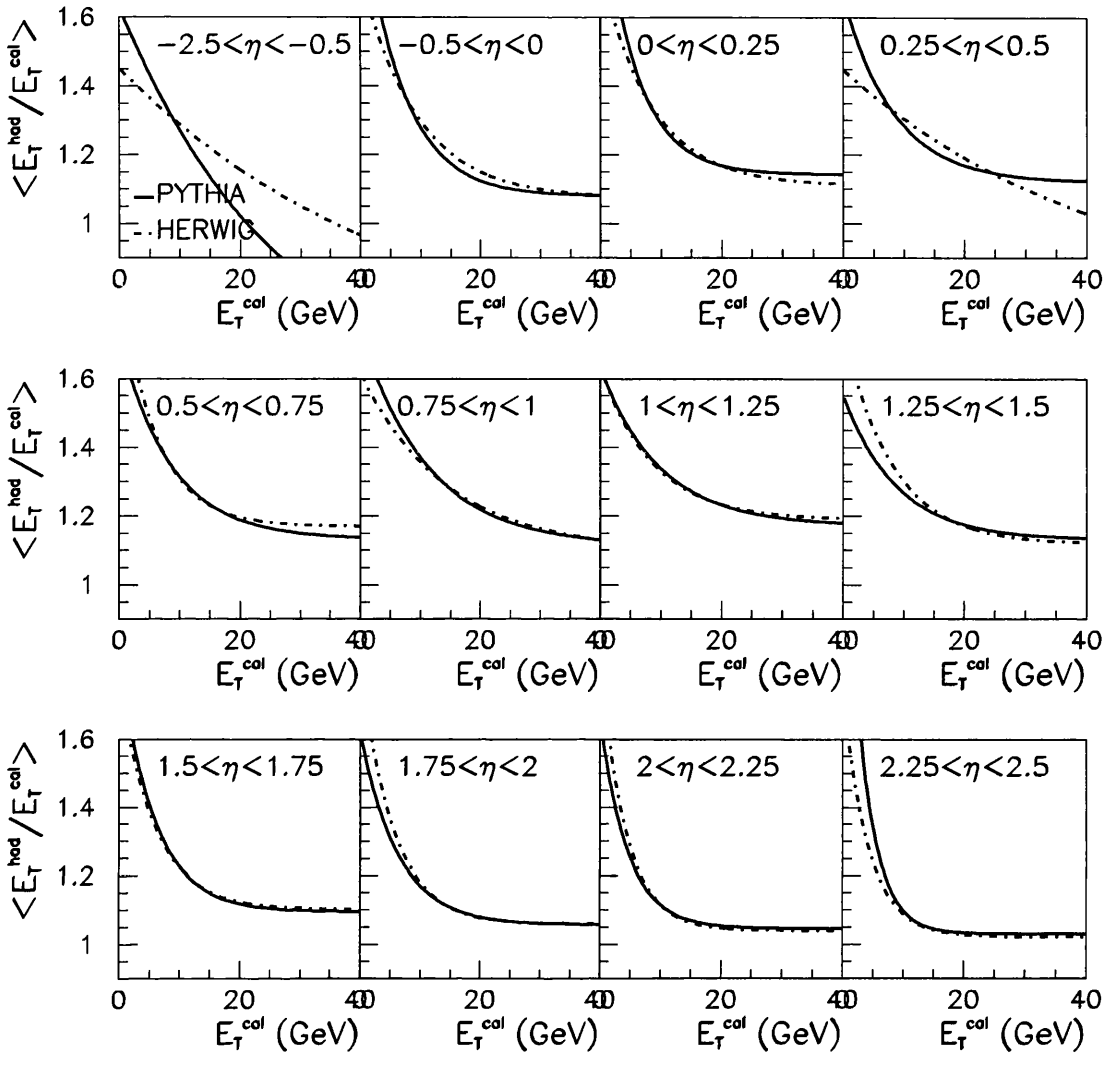

Figure 6.6: Jet E_T^{cal} correction functions obtained from HERWIG (solid line) and PYTHIA (dashed line) by method 1.

The ability of the correction functions to correct from detector to hadron level can be checked by correcting PYTHIA detector level jets with correction functions obtained from HERWIG, and vice versa, and plotting $\langle E_T^{had}/E_T^{cor}\rangle$ against E_T^{cor}, as shown in figures 6.8 and 6.9. This confirms that the corrected jet energy can be obtained to within $\pm$ 5% of the true hadron level jet energy using correction functions obtained from either event generator.

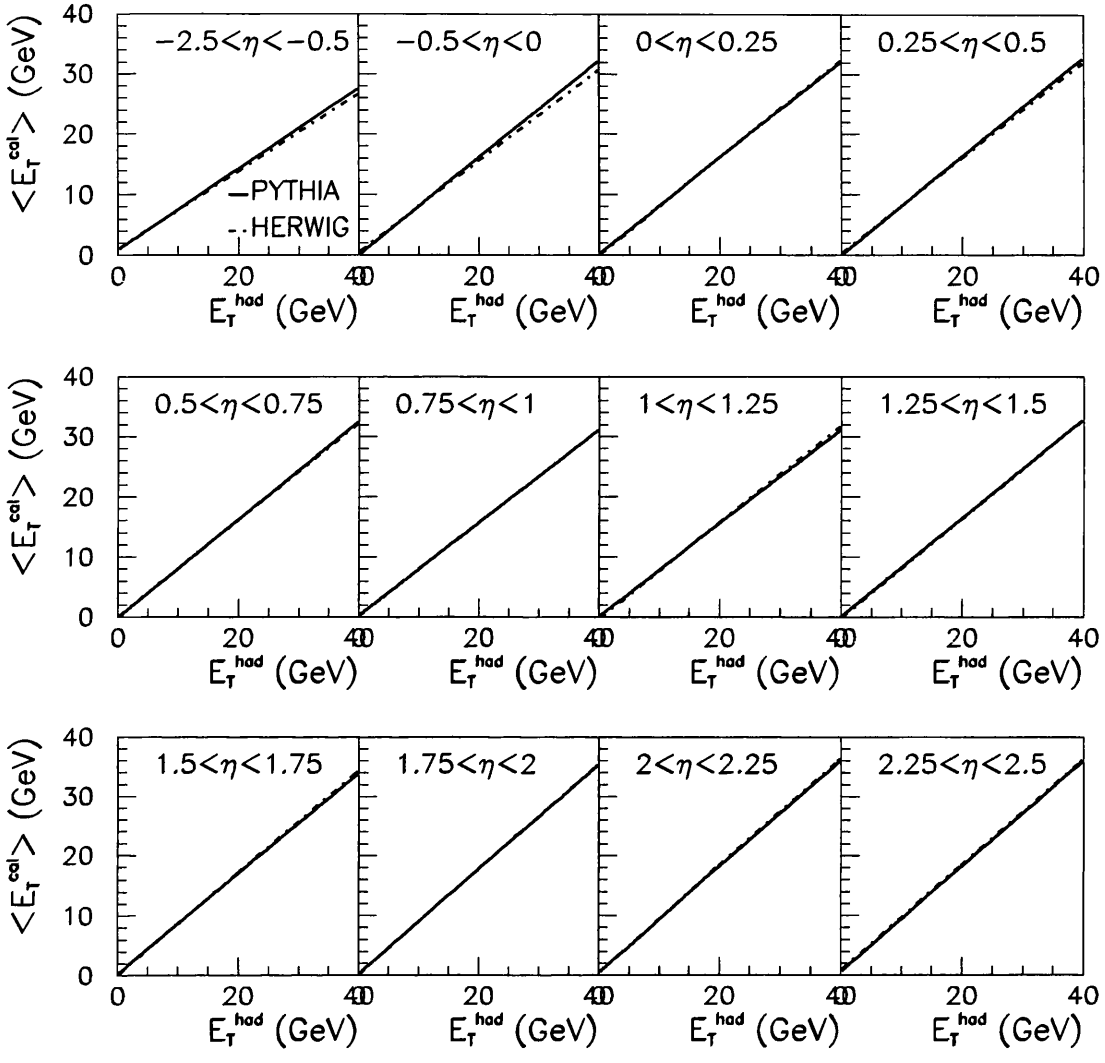

Figure 6.7: Jet E_T^{cal} correction functions obtained from HERWIG (solid line) and PYTHIA (dashed line) by method 2.

6.1.2 Resolutions

The primary objective when applying a correction to the transverse energy of a jet is to reproduce the hadron level E_T from the detector level jet. Figure 6.10 shows the E_T resolution before, (a), and after, (b) and (c), application of the two E_T corrections obtained in section 6.1.1. The correction succeeds in shifting the mean difference between the detector and hadron level transverse energies from 15% to within 2% without reducing the resolution with the result that there is now a good correspondence

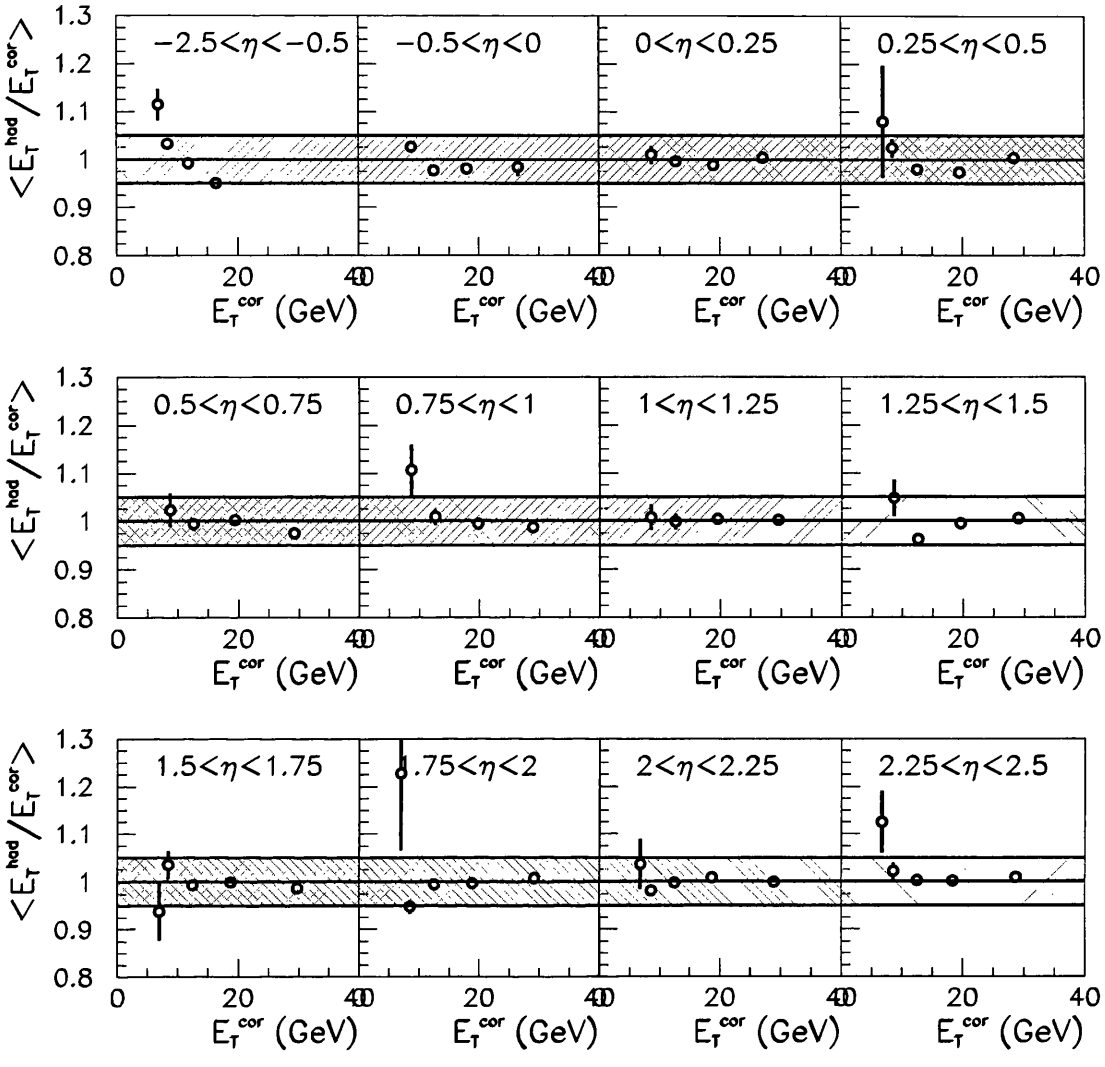

Figure 6.8: E_T^{had}/E_T^{cor} in bins of E_T^{cor} for pairs of matched PYTHIA jets where E_T^{cal} has been corrected with HERWIG correction functions.

between detector and hadron level.

Another quantity which is likely to be affected by the shift in the tranverse energy is the three-jet invariant mass, i.e. the centre of mass energy of the three-jet system. The invariant mass resolution is shown in figure 6.11 before, (a), and after, (b) and (c), the two E_T corrections. The E_T correction shifts the mean difference between detector and hadron level from 16% to less than 1% without significantly reducing the resolution. This is particularly important since the invariant mass distribution of the three-jet events, shown in figure 5.8, falls steeply from the threshold value used in the

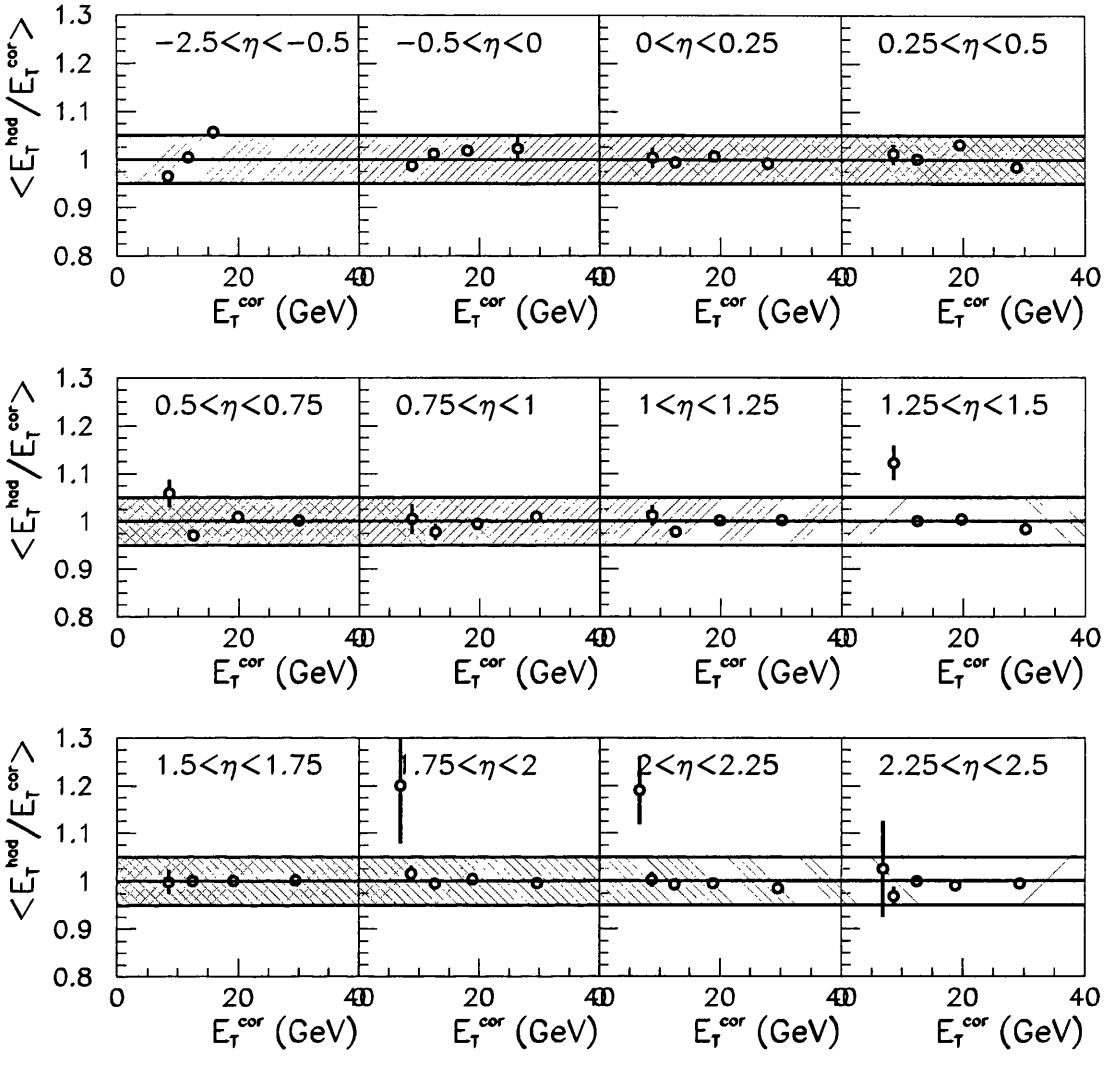

Figure 6.9: E_T^{had}/E_T^{cor} in bins of E_T^{cor} for pairs of matched HERWIG jets where E_T^{cal} has been corrected with PYTHIA correction functions.

event selection and is therefore particularly sensitive to migrations between hadron and detector level bins.

It is also important to check the correspondence between detector and hadron level of the angular variables, $\cos\theta_3$ and ψ_3, and the energy-sharing variables, X_3 and X_4. The resolutions of these quantities before the E_T correction are shown in figure 6.12. Since $\cos\theta_3$ and ψ_3 are angular variables to a good approximation they are unaffected by the difference in the E_T at hadron and detector level, giving resolutions which are centred on zero. Likewise, since X_3 and X_4 are energy ratios, the correspondence

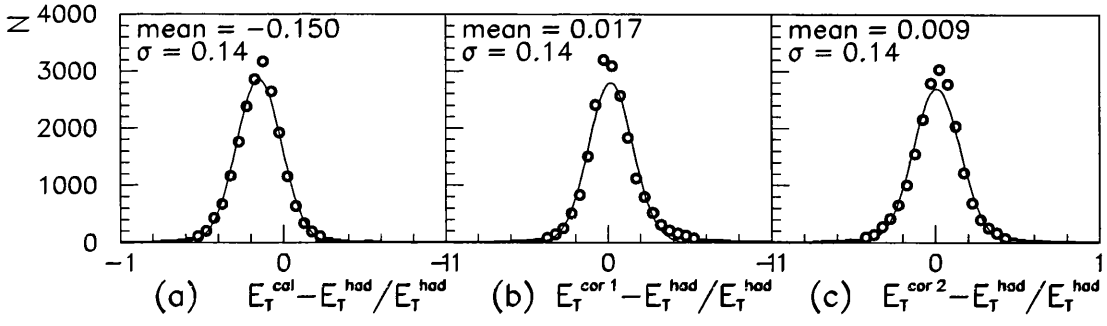

Figure 6.10: E_T resolution (a) before, (b) after E_T correction method 1 and (c) after E_T correction method 2.

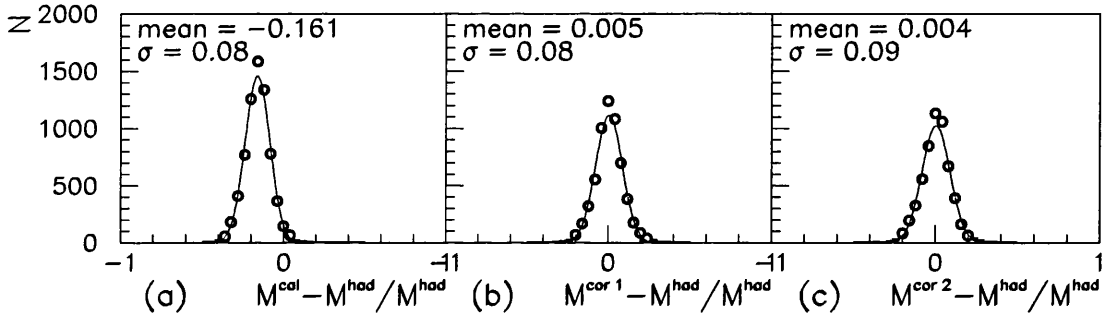

Figure 6.11: M_3J resolution (a) before, (b) after E_T correction method 1 and (c) after E_T correction method 2.

between detector and hadron level is good and the resolutions are centred on zero. The M_{3J}, $\cos\theta_3$, ψ_3, X_3 and X_4 resolutions sets a limit on the minimum useful bin size for future measurement.

6.1.3 Three-jet Selection Cuts

After applying corrections to the transverse energy of the jets the full three-jet data selection is changed to take into account the shift between E_T^{cal} and E_T^{cor} and M_{3J}^{cal} and M_{3J}^{cor}. The following three-jet selection criteria replace those stated in section 4.4 for any data to which a jet transverse energy correction has been applied.

- $0.15 < y_{JB} < 0.65$
- two jets with $E_T^{cor} > 6$ GeV, a third with $E_T^{cor} > 5$ GeV and $\eta < 2.4$ for all three jets
- $M_{3J}^{cor} > 50$ GeV, $|\cos\theta_3|^{cor} < 0.8$ and $X_3^{cor} < 0.95$

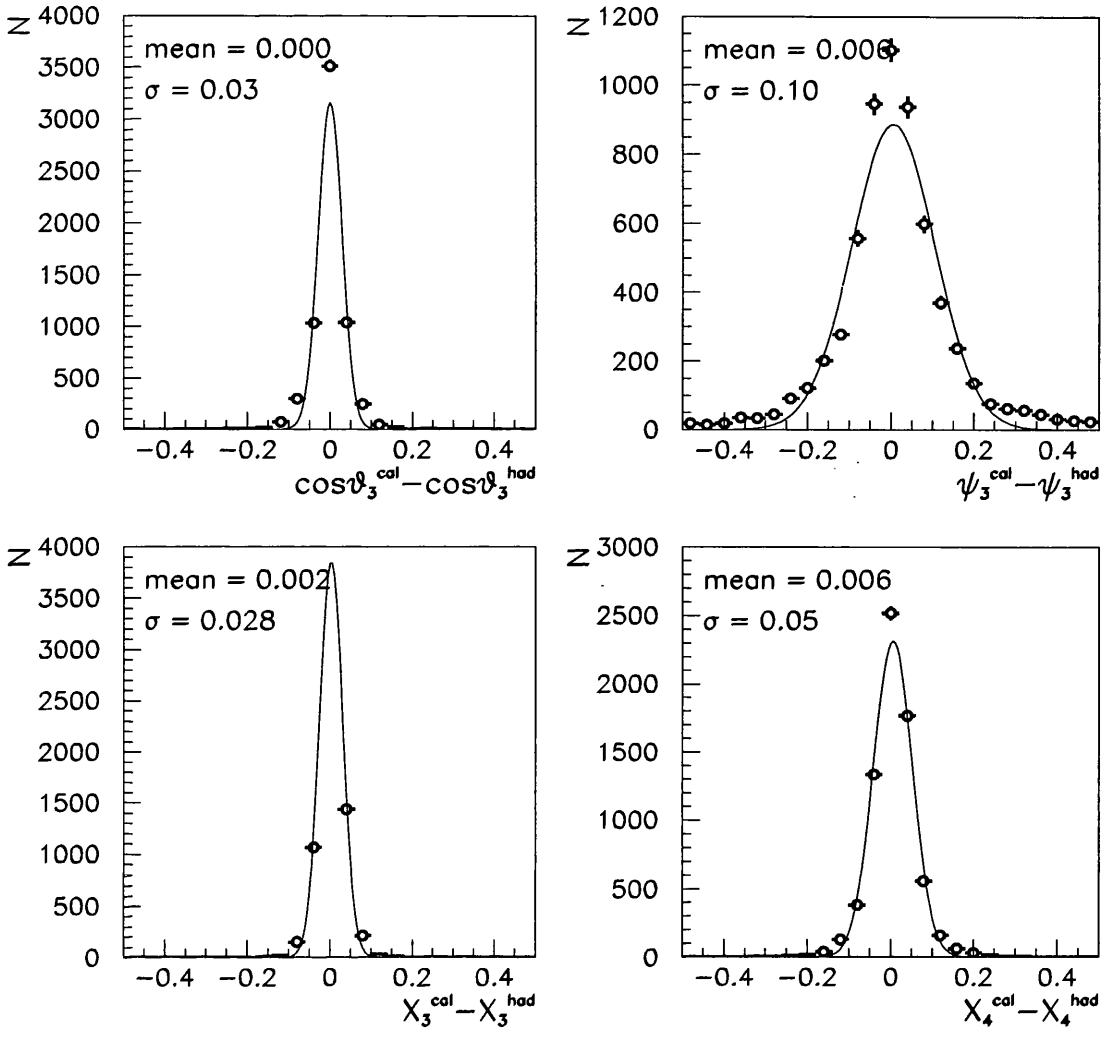

Figure 6.12: Resolutions of angular variables $\cos\theta$ and ψ_3 and energy-sharing variables X_3 and X_4 before E_T correction applied.

6.2 Acceptance correction, efficiencies and purities

There are two stages in obtaining a hadron level measurement which can be compared to theoretical predictions. The previous section, 6.1, illustrated the correction of jet transverse energies and other quantities to give good correspondence between detector and hadron level. The next stage, presented in this section, is to correct for the limited acceptance of the detector to the particular type of events to be measured.

6.2.1 Efficiencies and Purities

It is interesting to observe the effect that different stages of event selection at detector level have on 'true' hadron level PYTHIA three jet events. Figure 6.13 shows the fraction of hadron level events passing the full three jet selection

- $Q^2 < 1$ GeV^2 and $0.2 < y < 0.8$
- two jets with $E_T^{had} > 6$ GeV, a third with $E_T^{had} > 5$ GeV and $\eta < 2.4$ for all three jets
- $M_{3J}^{had} > 50$ GeV, $|\cos\theta_3^{had}| < 0.8$ and $X_3^{had} < 0.95$

which also pass the different levels of online and offline selection which are applied to the events at detector level. The efficiency is shown as a function of M_{3J}^{had}. The bin widths chosen for M_{3J}^{had} reflect the resolution of M_{3J}. The three levels of online selection, (a), (b) and (c), are almost 100% efficient, leading to a cumulative efficiency after the TLT of $\sim$ 95%. The additional offline cleaning cuts, (d), described in section 4.2, are also efficient, reducing the cumulative efficiency to $\sim$ 93%. Application of the three-jet selection given in 6.1.3, (e), reduces the number of hadron level events significantly. The cumulative efficiency drops to 50% for $M_{3J}^{had} = 50$ GeV rising to 75% for $M_{3J}^{had} > 60$ GeV. Finally, requiring that M_{3J}^{had} and M_{3J}^{cor} lie in the same bin, (f), reduces the cumulative efficiency still further to $\sim$ 30% for $M_{3J}^{had} < 80$ GeV and $\sim$ 50% for $M_{3J}^{had} > 80$ GeV. This is known as the bin efficiency.

The bin efficiency, defined as,

$$\text{Bin Efficiency} \equiv \frac{\text{number of events generated and reconstructed in bin(i)}}{\text{number of events generated in bin(i)}}$$

is an interesting quantity to examine since it gives the fraction of 'true' hadron level events which are reconstructed at detector level in the same bin. The higher the efficiency, the greater the fraction of hadron level events which are measured by the experiment in the same bin of the distribution. This minimises the extrapolation of the measurement into unmeasured regions.

The bin purity is defined as

$$\text{Bin Purity} \equiv \frac{\text{number of events generated and reconstructed in bin(i)}}{\text{number of events reconstructed in bin(i)}}$$

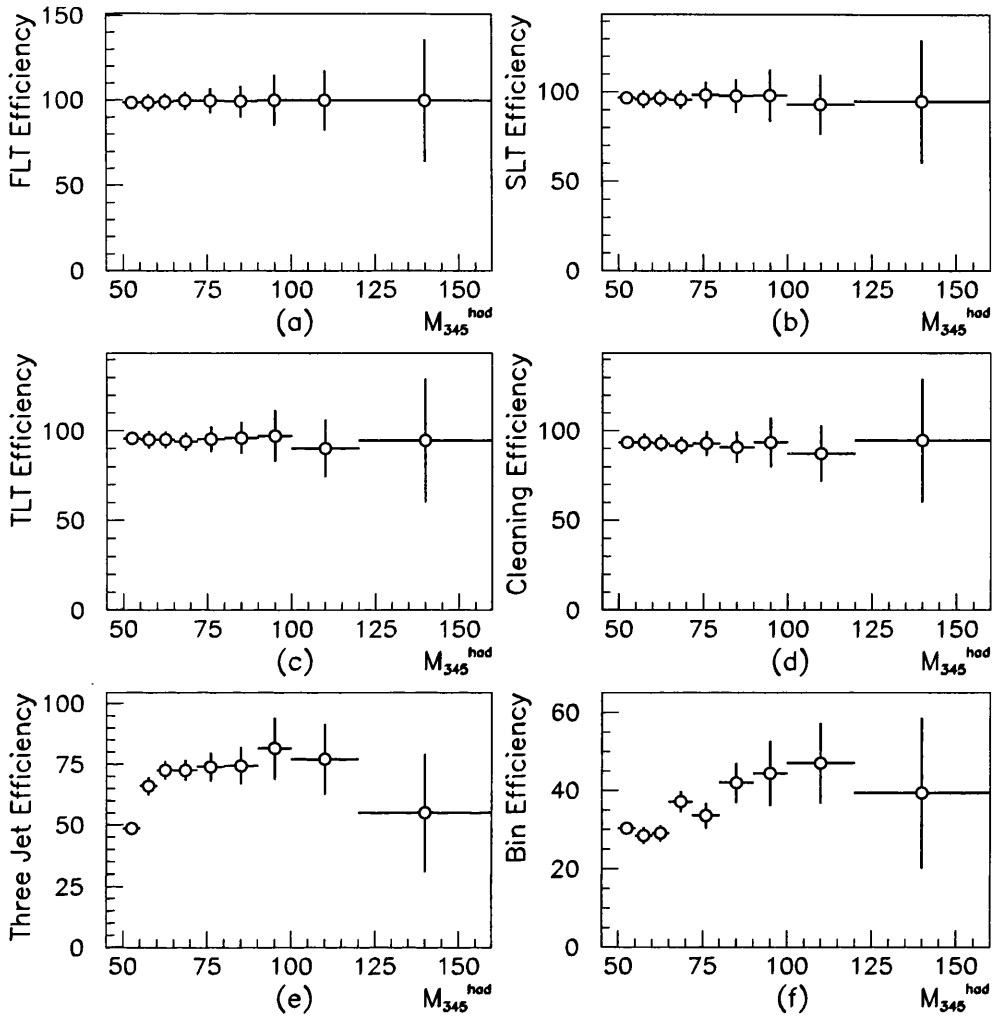

Figure 6.13: Efficiency of different levels of event selection shown for PYTHIA events, i.e. the fraction of hadron level three-jet events which also pass (a) the FLT, (b) the SLT, (c) the TLT, (d) the offline cleaning cuts, (e) the three-jet selection given in 6.1.3 and (f) have M_{3J}^{had} and M_{3J}^{cor} lying in the same bin.

and gives the fraction of the events reconstructed experimentally which actually have a corresponding 'true' hadron level event in the same bin of the distribution. High purities indicate that the contamination of the sample from events migrating from other bins is small. The terms *efficiency* and *purity* will be taken to mean *bin efficiency* and *bin purity* respectively for the rest of this study.

Figure 6.14 shows the efficiency and purity as a function of M_{3J} for events passing the three-jet event selection detailed above. As described previously the efficiency varies

between 30 and 50% being lower at low M_{3J}. The purity is also lower at low M_{3J} and varies between 30 and 50%.

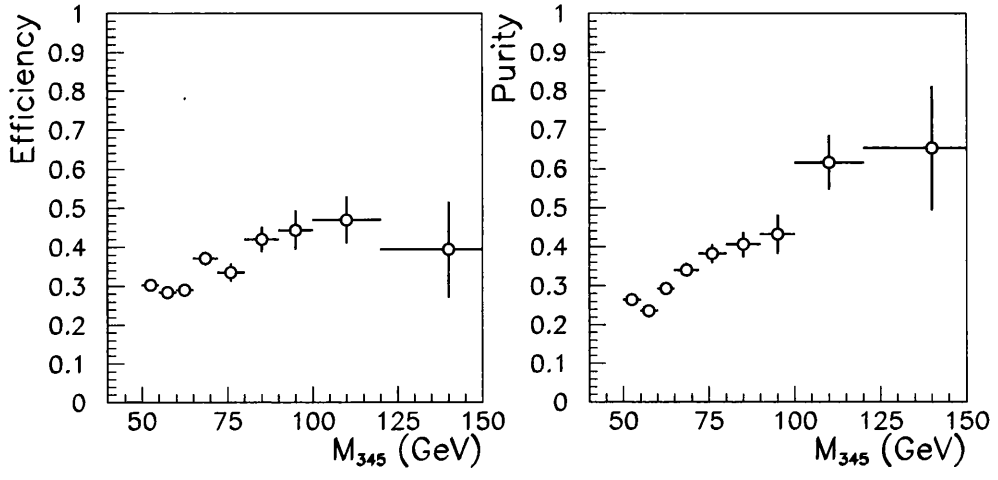

Figure 6.14: Bin efficiency and purity shown for PYTHIA events as a function of M_{3J}.

The efficiency and purity of the $\cos\theta_3$ and ψ_3 distributions are shown in figure 6.15 to be approximately flat in $\cos\theta_3$ and ψ_3 and around 35-40%.

Figure 6.16 shows the efficiency and purity of the X_3 and X_4 distributions. The X_3 efficiency and purity are around 20% in the lowest bin and rise gradually to 40% over the rest of the range. The X_4 efficiency is $\sim$ 30% in the central part of the distribution and 15-20% in the lowest bin and highest two bins. The purity is flat and $\sim$ 30%.

6.2.2 Correction Factors

A measured distribution can be corrected from detector to hadron level by applying the Monte Carlo based bin-by-bin method shown in equation 6.1 provided that the Monte Carlo describes the data and can account for migrations between bins. The correction factor is equivalent to the ratio of purity to efficiency.

Figure 6.17 shows the correction factors which should be applied to the data M_{3J}^{cor}, $\cos\theta_3^{cor}$, ψ_3^{cor}, X_3^{cor} and X_4^{cor} distributions to obtain hadron level quantities. The correction factors for $\cos\theta_3^{cor}$ and ψ_3^{cor} vary between 0.8-1.2 and are reasonably flat as a function of $\cos\theta_3^{cor}$ and ψ_3^{cor}. The correction factors for X_3^{cor} and X_4^{cor} also vary for the most part between 0.8-1.2 except in the lowest bin of X_3^{cor} and the highest bin of

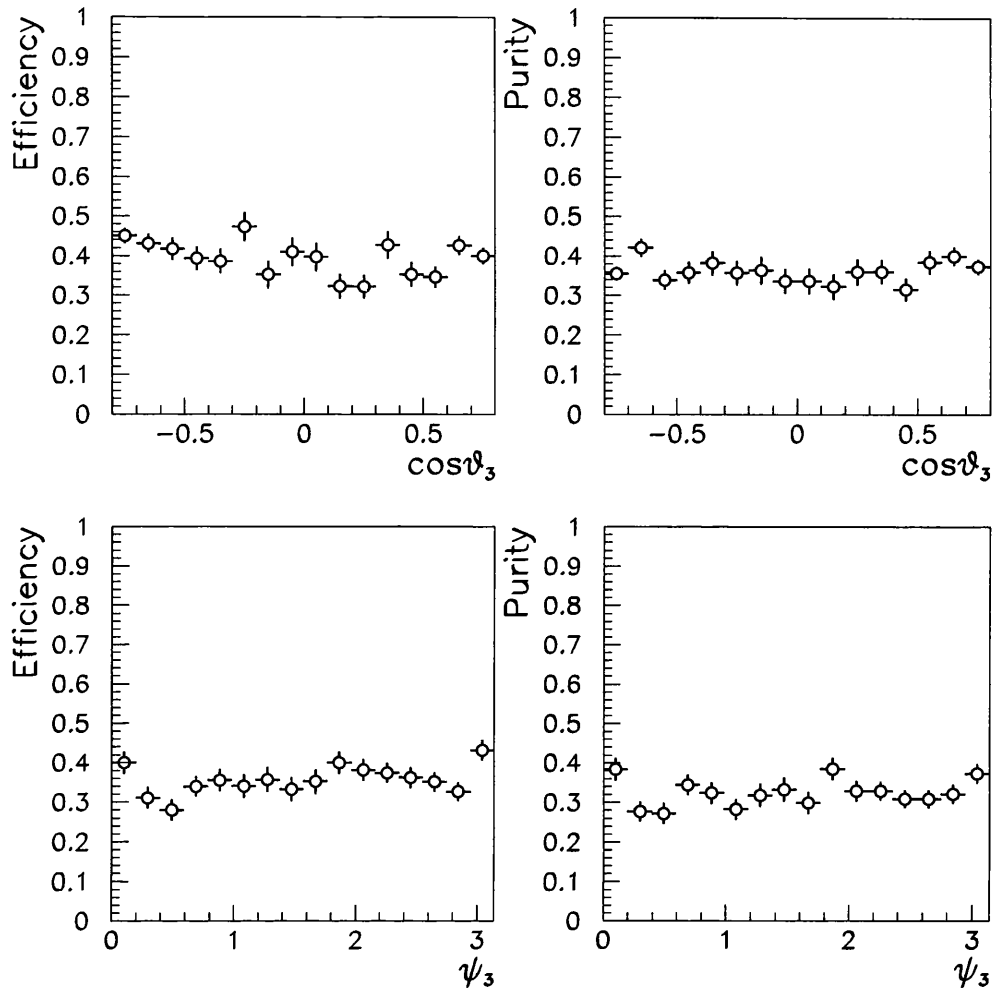

Figure 6.15: Bin efficiency and purity shown for PYTHIA events as a function of $cos\theta_3$ and ψ_3.

X_4^{cor}. The correction factors for M_{3J}^{cor} are also relatively flat and around 1.

6.3 Summary

In summary, it has been shown that it is possible to apply a correction to the transverse energy of detector level jets which compensates for energy losses in the the detector to within 5% thus minimising bin migrations from detector to hadron level. This correction relies on Monte Carlo events and the ZEUS detector simulation. Comparison between the Monte Carlo event generators PYTHIA and HERWIG has shown that the correction method does not depend heavily on the particular model chosen to create

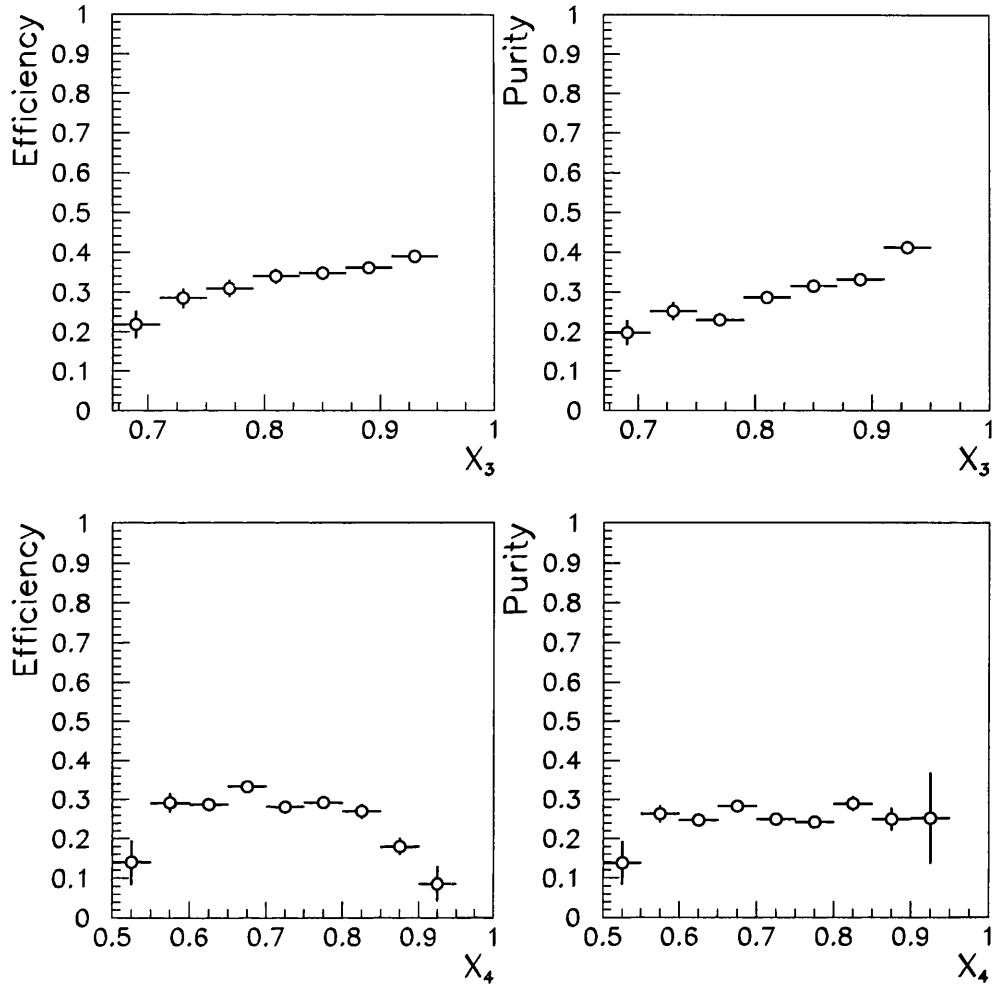

Figure 6.16: Bin efficiency and purity shown for PYTHIA events as a function of X_3 and X_4.

events. Correction method 1 is now applied at all stages in the subsequent analysis with correction method 2 employed as a systematic check.

It has also been shown that there is a good correlation between detector and hadron level for the observables of interest, M_{3J}, $\cos\theta_3$, ψ_3, X_3 and X_4.

Correction factors have been obtained which can correct the measured distributions bin-by-bin for detector acceptance to give hadron level quantities. The data corrected to hadron level are shown in chapter 7 along with details of the systematic checks performed. The corrected data are compared to various hadron and parton level theoretical predictions in chapter 8.

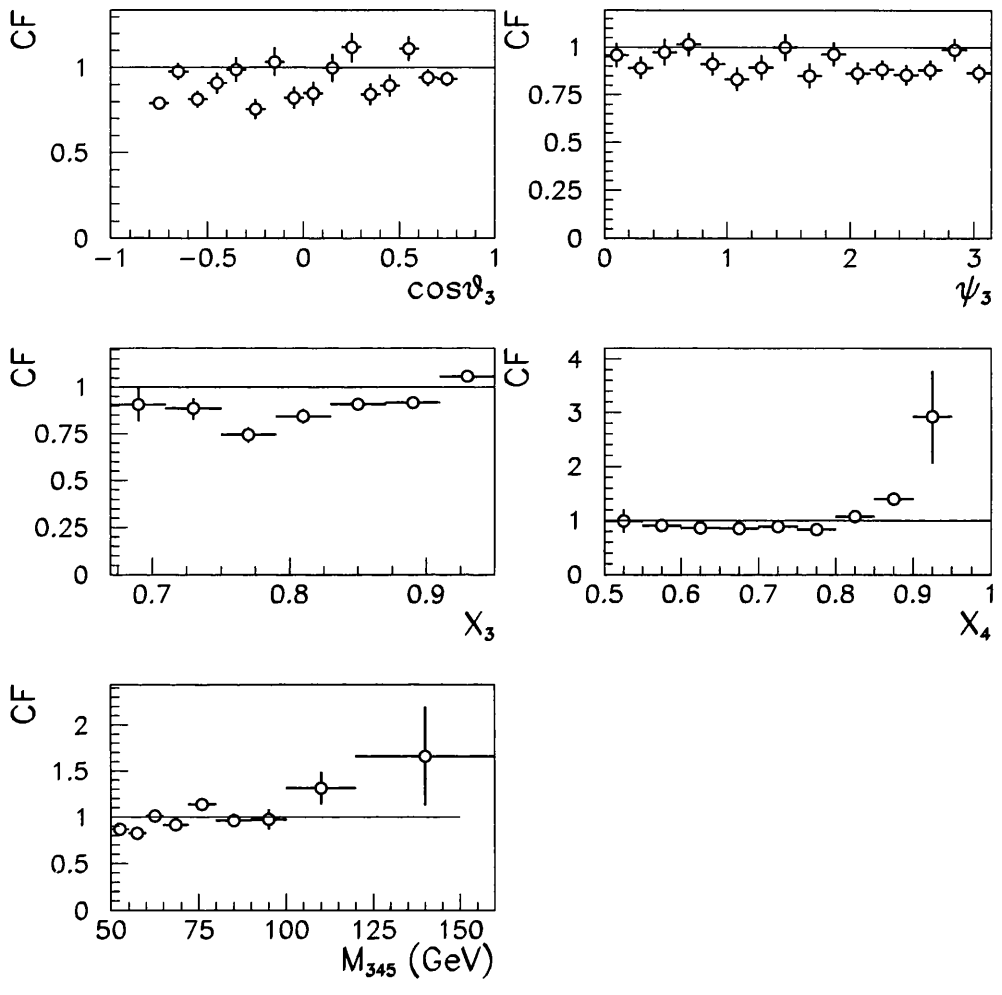

Figure 6.17: Detector to Hadron level correction factors obtained from PYTHIA events.

Chapter 7

Corrected Data and Systematic Checks

7.1 Corrected Data

The corrected data distributions are obtained by applying the correction precedures described in chapter 6 to the measured data. Firstly the transverse energy correction, section 6.1, corrects for energy losses in the detector. Three-jet events are then selected, as stated in section 6.1.3, with

- two jets with $E_T^{cor} > 6$ GeV and a third jet with $E_T^{cor} > 5$ GeV where $\eta < 2.4$
- $M_{3J}^{cor} > 50$ GeV, $|\cos\theta_3^{cor}| < 0.8$ and $X_3^{cor} < 0.95$

These are the criteria used in section 6.2 when calculating the correction for the detector acceptance.

After all the selection cuts 2821 events remain from 16.0 pb^{-1} of data. 425 of these events contain four jets , 56 events have five jets, 3 events have six jets and one event has seven jets. The additional jets in these events have $E_T^{cor} > 5$ GeV.

The background from beam gas and cosmic ray events is negligible. The contamination due to DIS and prompt photon events has been estimated using Monte Carlo events to be $\leq 1\%$ and $\leq 0.1\%$ respectively.

The corrected differential cross section for three-jet production in $bin(i)$ of an observable X is then calculated to be

$$\frac{d\sigma}{dX}(bin(i)) = C(bin(i)) \cdot \frac{number\ of\ events\ in\ bin(i)}{\mathcal{L} \cdot bin\ width} \tag{7.1}$$

where $C(bin(i))$ is the multiplicative factor obtained in section 6.2 to correct for detector acceptance and $\mathcal{L}$ is the integrated luminosity of the data analysed.

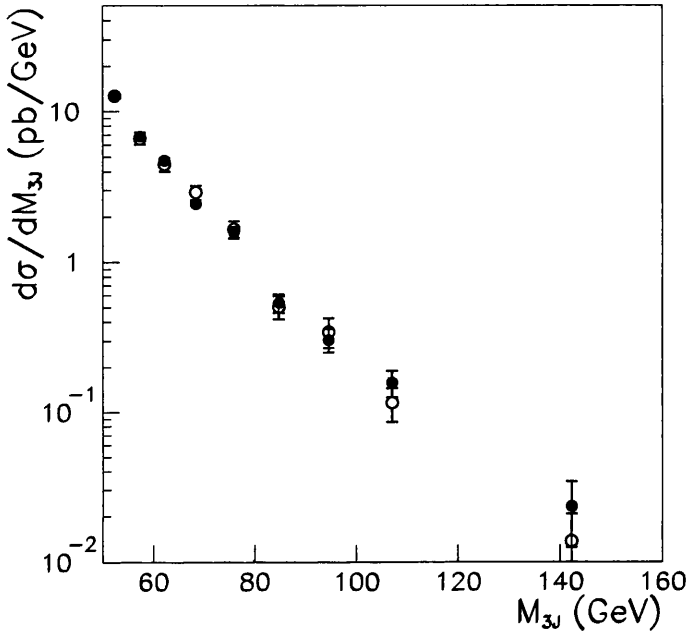

Figure 7.1: The cross section $d\sigma/dM_{3J}$. The corrected ZEUS data are plotted at the mean M_{3J} of the bin and are shown by black dots for the first analysis and by circles for the second analysis. The error bars show the statistical error.

Two independent analyses have been performed: the first was performed by the author and is the subject of this thesis, while the second was performed by Dr L. E. Sinclair. This is conformity with the ZEUS Collaboration rules that all work for publication must be checked in its essential features by a second person.

The differential three-jet cross sections with respect to M_{3J}, $\cos\theta_3$, ψ_3, X_3 and X_4 are shown in figures 7.1 and 7.2. Statistical errors only are shown. The main difference between the two analyses lies in the correction for detector effects. PYTHIA is used to correct for detector acceptance in the first analysis while HERWIG is used for the

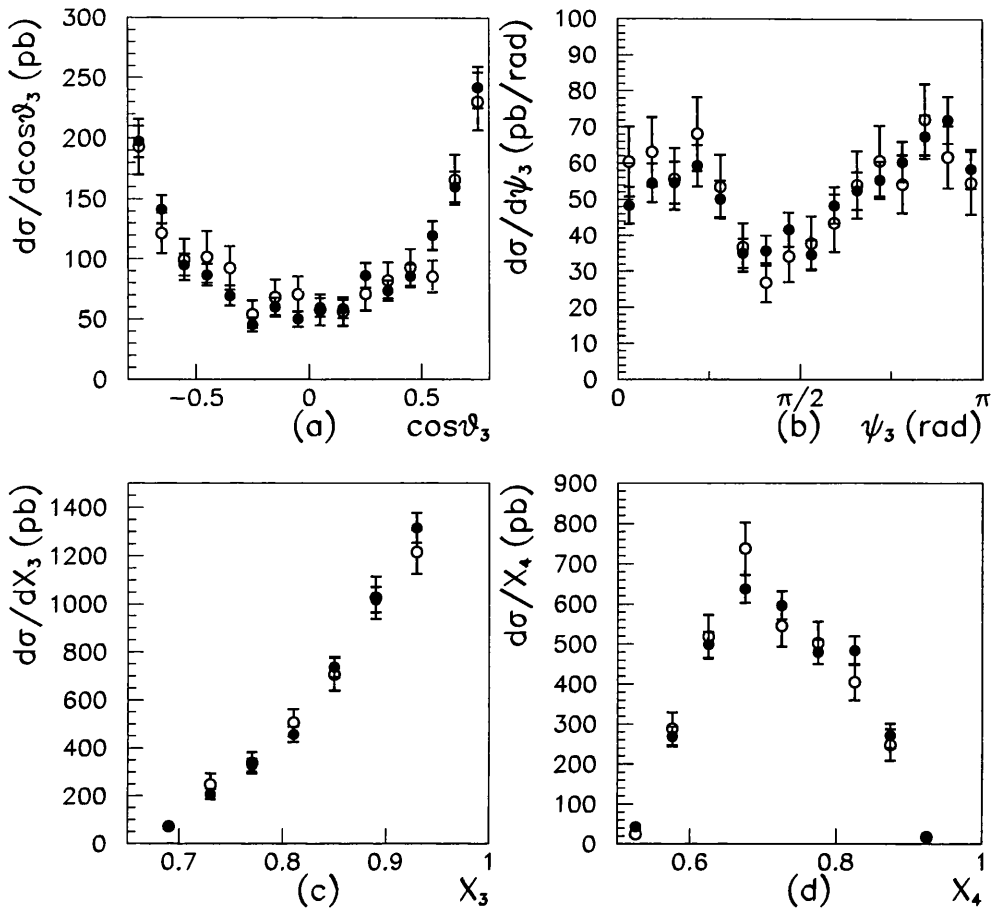

Figure 7.2: The cross sections (a) $d\sigma/d\cos\theta_3$ and (b) $d\sigma/d\psi_3$, (c) $d\sigma/dX_3$ and (d) $d\sigma/dX_4$. The corrected ZEUS data are plotted at the centre of the bin are shown by black dots for the first analysis and open circles for the second analysis. The error bars show the statistical error.

second. The first analysis corrects the transverse energies of the jets with a method that takes into account variations in the energy loss with E_T^{cal} and η (see *correction method 1* in section 6.1) while the second applies a flat correction of $E_T^{cor} = 1.2E_T^{cal}$.

Figure 7.1 shows the cross section $d\sigma/dM_{3J}$ measured by the two analyses while figures 7.2 shows the cross sections $d\sigma/d\cos\theta_3$ and $d\sigma/d\psi_3$ and $d\sigma/dX_3$ and $d\sigma/dX_4$ respectively. Since the correction for detector acceptance is approximately flat in $\cos\theta_3$, ψ_3, X_3 and X_4 the shapes of these distributions are the same as those observed in the raw data in figure 5.14. Figure 7.3 shows the difference in percent in the cross sections measured by the two analyses for $d\sigma/dX_3$, $d\sigma/dX_4$, $d\sigma/d\cos\theta_3$, $d\sigma/d\psi_3$ and $d\sigma/dM_{3J}$.

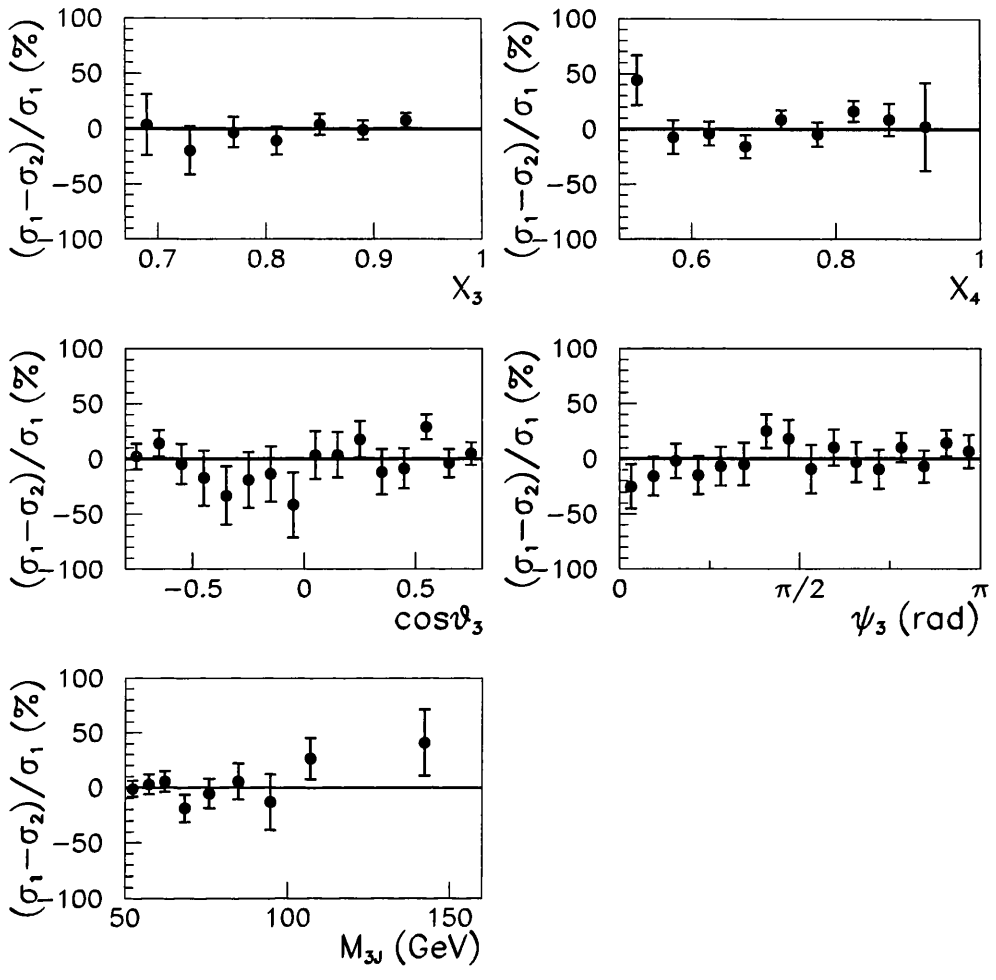

Figure 7.3: The difference between the values of the differential cross sections obtained by the two analyses is shown normalised to the cross section from the first analysis for X_3, X_4, $\cos\theta_3$, ψ_3 and M_{3J}. The errors bars indicate the statistical error.

There is good agreement between the analyses except where PYTHIA and HERWIG differ in their description of the raw data and are expected to produce differences. The $\cos\theta_3$ and ψ_3 distributions shown in figure 5.14 are good examples of this. The effect on the distributions of changing the event selection and correction procedure systematically is detailed in the following section.

In addition, the three-jet cross sections obtained from 1995 and 1996 data individually were compared as a consistency check. Figure 7.4 demonstrates that the 1995 and 1996 cross sections do not differ significantly. The ratio of the cross sections,

$\sigma(95)/\sigma(96)$, is centred on 1 and is approximately flat in M_{3J}, $\cos\theta_3$, ψ_3, X_3 and X_4.

7.2 Systematic Studies

The systematic uncertainty on the measurements was studied by making changes in the selection and correction procedures. The results of this study are shown in figures 7.5 to 7.13 for the data points (shown from left to right) obtained in the following ways

1. Default analysis selection
   - two jets with $E_T^{cor} > 6$ GeV, a third with $E_T^{cor} > 5$ GeV and $\eta < 2.4$
   - $M_{3J} > 50$ GeV, $|\cos\theta_3| < 0.8$ and $X_3 < 0.95$
   - $\langle E_T^{had}/E_T cal\rangle$ *vs* E_T^{cal} (*method 1*) jet transverse energy correction
   - PYTHIA used for acceptance correction
   - GRV photon structure function and CTEQ proton structure function used in PYTHIA
2. Energy scale of the CAL in detector simulation raised by 5%
3. Energy scale of the CAL in detector simulation lowered by 5%
4. E_T^{cor} cut lowered by the width of the E_T resolution so that two jets with $E_T^{cor} > 5.5$ GeV and a third of $E_T^{cor} > 4.5$ GeV were required
5. η cut raised by the width of the η resolution so that $\eta < 2.5$
6. Upper y_{JB} cut raised by width of the resolution to $y_{JB} < 0.7$
7. E_T^{cal} *vs* E_T^{had} jet transverse energy correction used (*method 2*)
8. LAC1 photon structure function [71]
9. MRS(A) proton structure function [72]
10. HERWIG used for acceptance correction
11. M_{3J} cut lowered by the width of the M_{3J} resolution to $M_{3J} > 46$ GeV

12. $\cos\theta_3$ cut raised by the width of the resolution to $|\cos\theta_3| < 0.825$

13. X_3 cut raised by the width of the resolution to $X_3 < 0.975$.

These systematic changes can be grouped into several different categories. Systematics 2 and 3 are designed to show the effect on the cross section of changing the energy scale of the CAL in the detector simulation by $\pm$ 5%, the level of uncertainty on this quantity. Systematics 4-6 and 11-13 show the effect of events migrating into the data sample from outwith the kinematic range of interest. The remaining systematic checks are related to the model dependence of the correction procedure, i.e. changing the event generator used to produce Monte Carlo events from PYTHIA to HERWIG, changing the photon and proton structure function used by PYTHIA and changing the parametrisation of the jet transverse energy correction.

Figure 7.5 shows the percentage difference between each systematic check and the default value of $d\sigma/dM_{3J}$ in each bin of M_{3J}. The numbers on the x-axis refer to the systematic checks detailed previously. Clearly the main effect on the cross section comes from raising(lowering) the CAL energy scale in the detector simulation by 5% (labeled '2' and '3' in figure 7.5) thereby increasing(decreasing) the cross section in each bin, a systematic shift which is completely correlated between bins.

The systematic differences in bins of $\cos\theta_3$ are shown in figure 7.6 for $d\sigma/d\cos\theta_3$. In addition to the energy scale uncertainty, correcting for the detector acceptance with HERWIG rather than PYTHIA events also has a large effect on the cross section. This is due to differences between the PYTHIA and HERWIG $\cos\theta_3$ distributions which affect the correction factors obtained. $d\sigma/d\psi_3$, shown in figure 7.7, also shows signs of sensitivity to the HERWIG correction at low and high ψ_3 where the PYTHIA and HERWIG ψ_3 distributions differ. $d\sigma/dX_3$ demonstrates slight sensitivity to the E_T correction applied to the jets, figure 7.8, while $d\sigma/dX_4$ is also affected by the HERWIG correction, figure 7.9.

The effects of the systematic variations have also been studied for the area normalised distributions. Here the energy scale uncertainties should have a negligible effect since they change only the magnitude of the cross section and not the shape of the distribution.

Figure 7.10 shows systematic variations for $1/\sigma d\sigma/d\cos\theta_3$ in bins of $\cos\theta_3$. As expected the energy scale uncertainty is not now important. On the other hand, differences between the PYTHIA and HERWIG acceptance correction are more noticeable and are in fact the dominant source of systematic uncertainty. The same pattern is observed in figures 7.11 and 7.13 which show the systematic changes for $1/\sigma d\sigma/d\psi_3$ and $1/\sigma d\sigma/dX_4$. Figure 7.12 shows that the shape of the X_3 distribution is slightly sensitive at high and low X_3 to the E_T correction applied to the jets.

In summary, the major uncertainty on the cross section measurement comes from the lack of knowledge of the CAL energy scale. It has however a negligible effect on the shape of the distributions. The use of HERWIG rather than PYTHIA to correct for detector effects is the only other systematic which has a significant effect on the cross section. This effect is generally smaller than that due to the energy scale uncertainty and arises from the differences between the PYTHIA and HERWIG predictions. These differences were observed for the uncorrected data in figure 5.14. The effect of the HERWIG correction on the shape of the area normalised distributions is however the major systematic for the $1/\sigma d\sigma/d\cos\theta_3$, $1/\sigma d\sigma/d\psi_3$ and $1/\sigma d\sigma/dX_4$ measurements. The dependence on the structure functions used in the Monte Carlo models is, in contrast, very small despite the differences between the photon structure functions GRV and LAC1 which have been observed elsewhere [33, 34, 37].

The three-jet cross section is measured as

$$\sigma_{three-jet} = 162.4 \pm 4.1\ (stat.)\ ^{+15.8}_{-5.9}\ (sys.)\ ^{+32.3}_{-24.8}\ (energy\ scale)\ \text{pb}$$

Numerical values for $d\sigma/dM_{3J}$, $d\sigma/d\cos\theta_3$, $d\sigma/d\psi_3$, $d\sigma/dX_3$ and $d\sigma/dX_4$ measurements are given in tables B.1-B.5 in appendix B. Also given are the statistical errors, systematic uncertainties (excluding the energy scale uncertainty) and the energy scale uncertainties. Numerical values for the area normalised distributions are given in tables B.6-B.9 in appendix B along with statistical and systematic errors.

7.3 Comparing Parton and Hadron Level Jets

The data have been corrected to hadron level using hadron and detector level Monte Carlo events to correct for detector effects. LO QCD calculations for three-jet processes

however contain only three partons in the final state, each of which would be associated with a jet. An estimate of the relation between parton and hadron level quantities can be obtained from PYTHIA Monte Carlo events. In each event jets are studied before and after hadronisation, that is jets found respectively from partons from the QCD scatter and parton shower, and from the hadrons. This of course can only be an estimate of the correspondence between the parton level of the theoretical calculations and hadron level since PYTHIA contains only 2→2 QCD matrix elements, although initial and final state radiation are modelled as discussed in section 8.3. The multipartonic final state produced by the parton shower is only an approximation of higher-order calculations.

The three-jet cross sections as a function of M_{3J}, $\cos\theta_3$, ψ_3, X_3 and X_4 for events found with parton and hadron jets are shown in figure 7.14 to be very similar, the ratio σ[hadron jets]/σ[parton jets] being $\sim$ 0.95. The right hand column shows that this ratio is approximately flat for all distributions.

Figure 7.15 demonstrates that there is very little difference between the shapes of the distributions shown by $1/\sigma d\sigma/d\cos\theta_3$, $1/\sigma d\sigma/d\psi_3$, $1/\sigma d\sigma/dX_3$ and $1/\sigma d\sigma/dX_4$ obtained using hadron or parton jets. Again the right hand column shows that the ratio is approximately flat for all distributions.

7.4 Summary

The corrected cross sections $d\sigma/dM_{3J}$, $d\sigma/d\cos\theta_3$, $d\sigma/d\psi_3$, $d\sigma/dX_3$ and $d\sigma/dX_4$ have been shown in section 7.1 for two independent analyses. There is good agreement between the analyses.

The systematic uncertainty in the measurement has been studied in section 7.2. The uncertainty in the CAL energy scale gives rise to a $\pm$ 20-30% uncertainty in the total cross section. The model uncertainty, estimated by performing the correction with both PYTHIA and HERWIG, also a major source of systematic error both for the total cross section and for the area normalised distributions.

Hadronisation effects have been estimated in section 7.3. The ratio of the cross sections σ[hadron jets]/σ[parton jets] was found to be $\sim$ 0.95. The shapes of the

distributions are largely unaffected.

The corrected data will be compared to the predictions of various theoretical models in the following chapter.

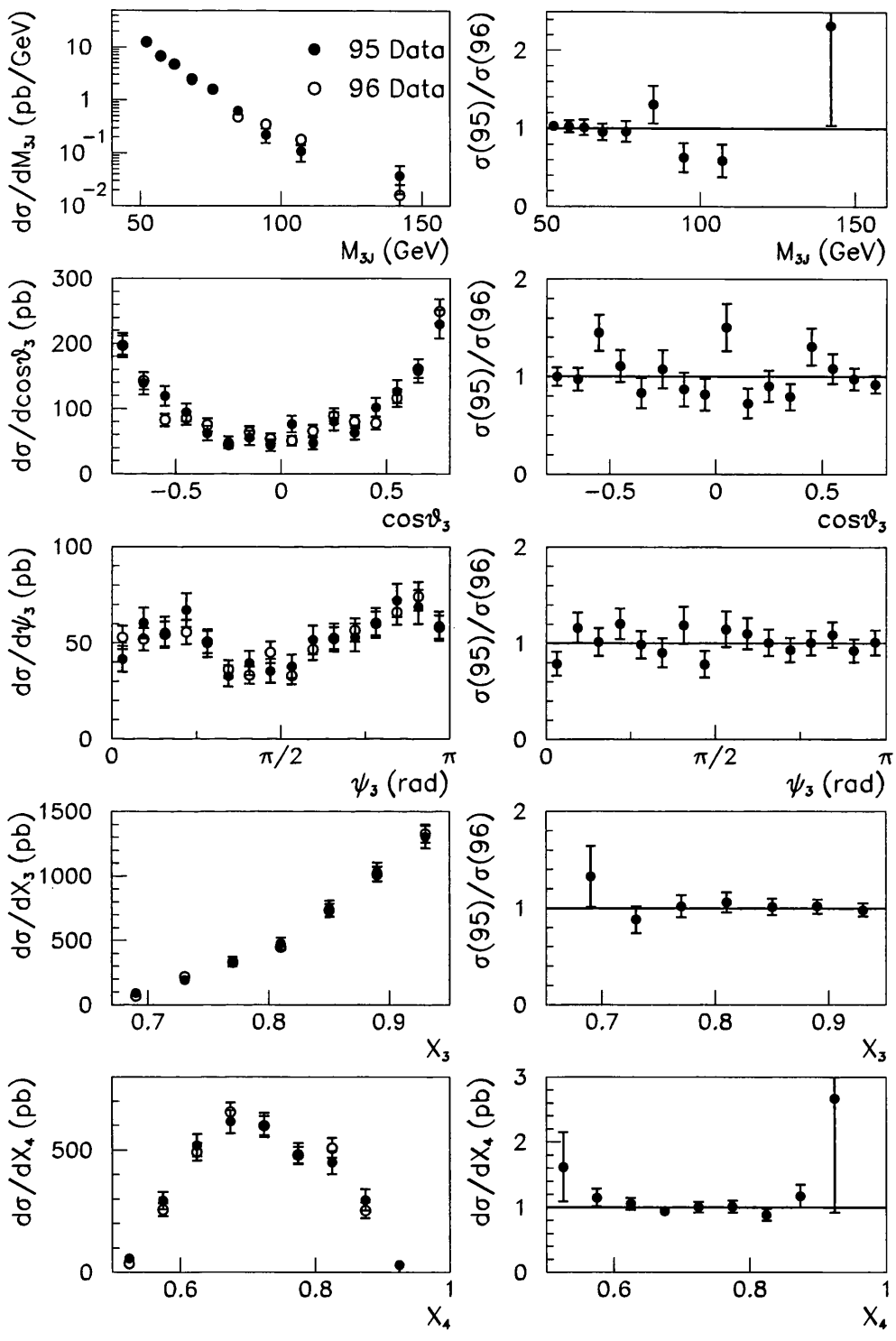

Figure 7.4: The left column shows the differential cross sections in M_{3J}, $\cos\theta_3$, ψ_3, X_3 and X_4 obtained from 1995 and 1996 ZEUS data. The errors bars indicate the statistical error. The right column shows the ratio of the 1995 to the 1996 cross sections. The error bars indicate the contribution to the uncertainty from the statistical error in the 1995 data sample.

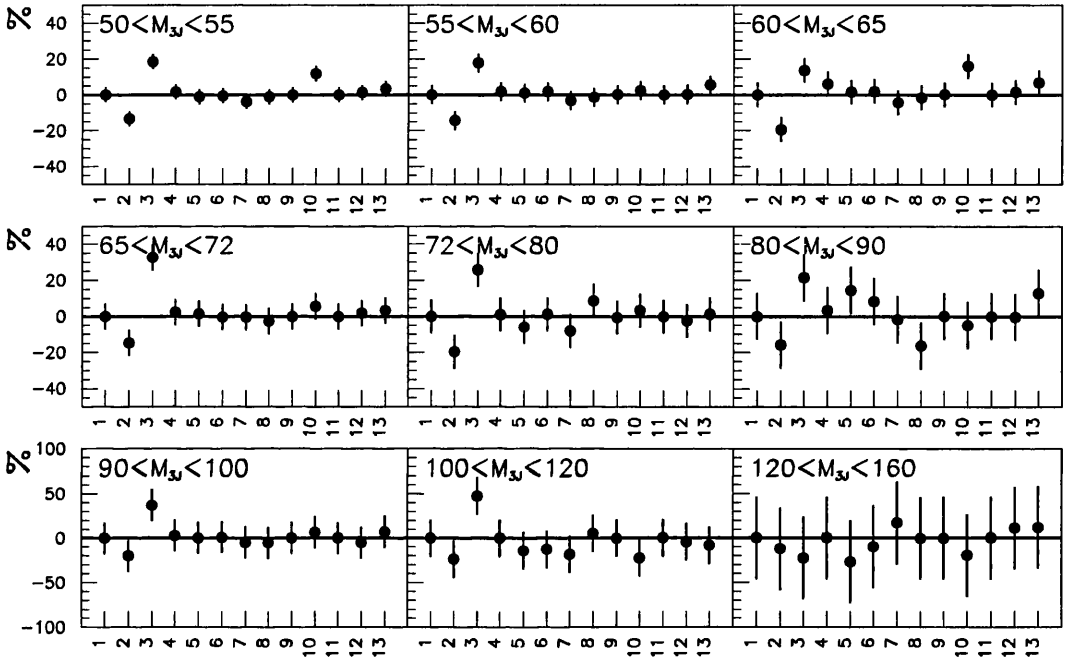

Figure 7.5: Summary of systematic uncertainties for $d\sigma/dM_{3J}$. The difference in percent between the systematic value and the nominal result is shown together with the statistical error from the nominal result. The line at zero refers to the position of the nominal value.

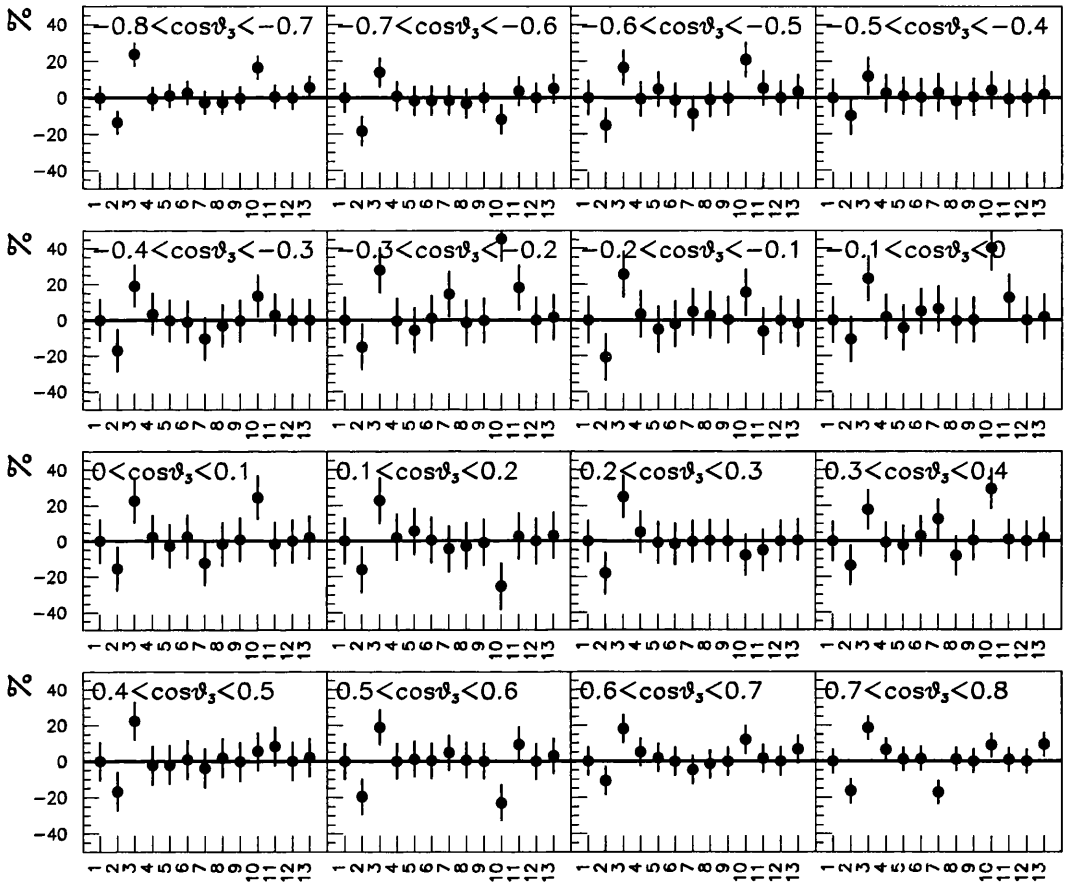

Figure 7.6: Summary of systematic uncertainties for $d\sigma/d\cos\theta_3$. The difference in percent between the systematic value and the nominal result is shown together with the statistical error from the nominal result. The line at zero refers to the position of the nominal value.

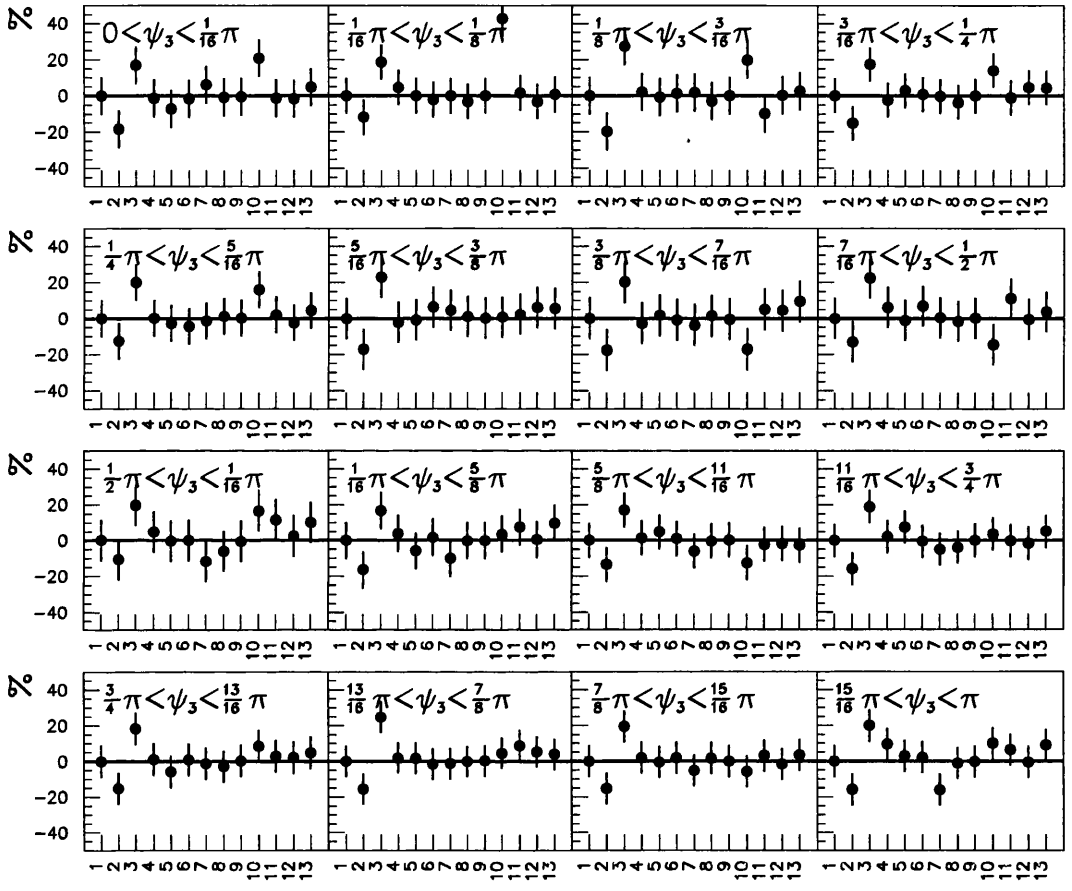

Figure 7.7: Summary of systematic uncertainties for $d\sigma/d\psi_3$. The difference in percent between the systematic value and the nominal result is shown together with the statistical error from the nominal result. The line at zero refers to the position of the nominal value.

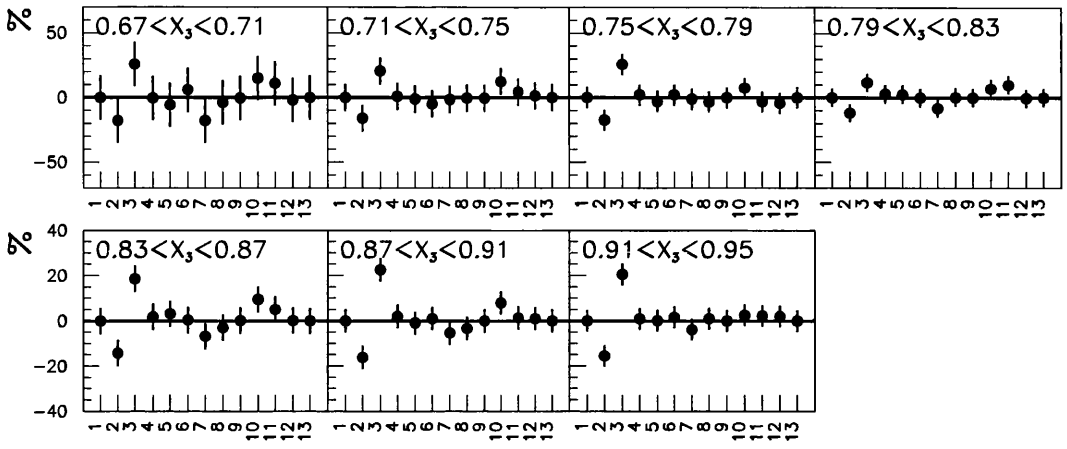

Figure 7.8: Summary of systematic uncertainties for $d\sigma/dX_3$. The difference in percent between the systematic value and the nominal result is shown together with the statistical error from the nominal result. The line at zero refers to the position of the nominal value.

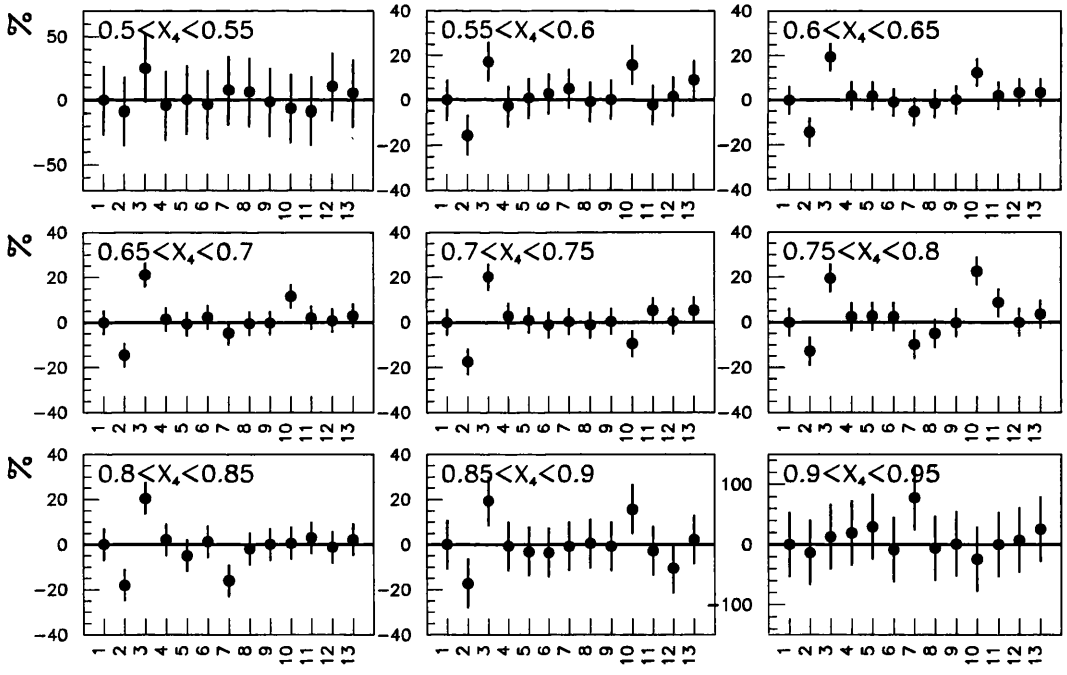

Figure 7.9: Summary of systematic uncertainties for $d\sigma/dX_4$. The difference in percent between the systematic value and the nominal result is shown together with the statistical error from the nominal result. The line at zero refers to the position of the nominal value.

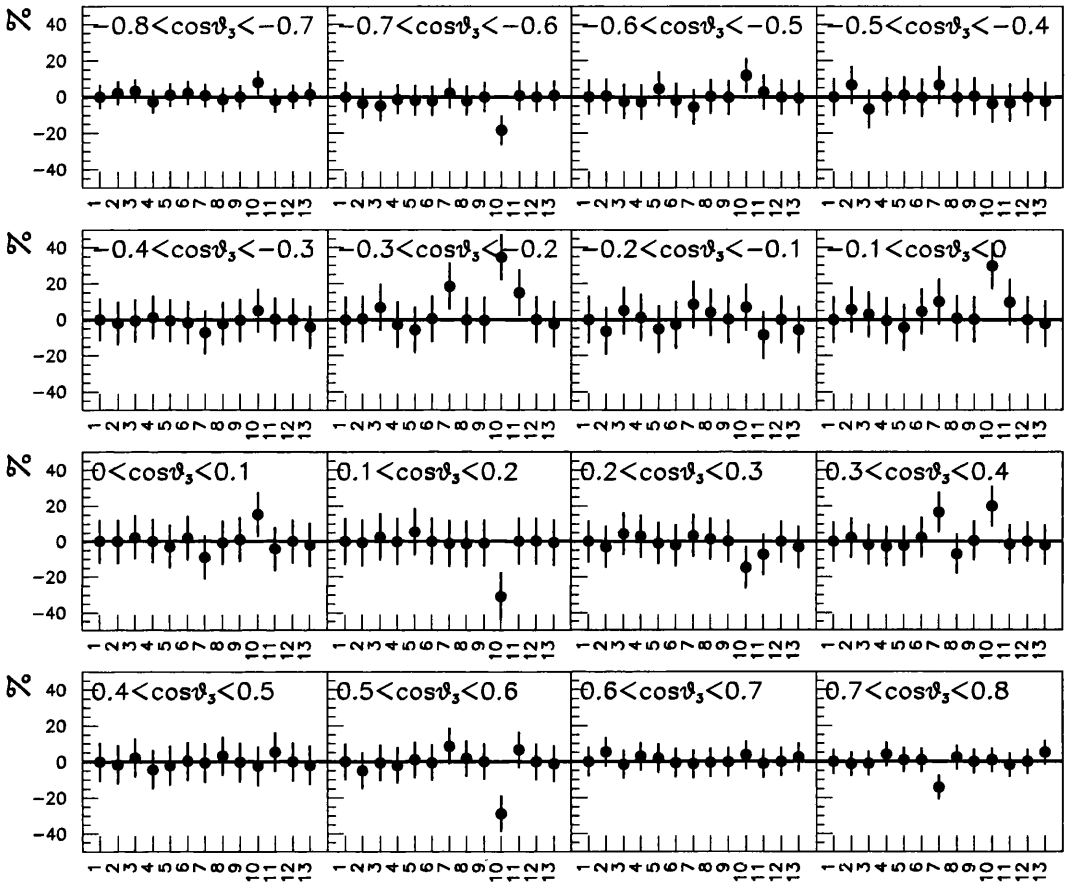

Figure 7.10: Summary of systematic uncertainties for $1/\sigma d\sigma/d\cos\theta_3$. The difference in percent between the systematic value and the nominal result is shown together with the statistical error from the nominal result. The line at zero refers to the position of the nominal value.

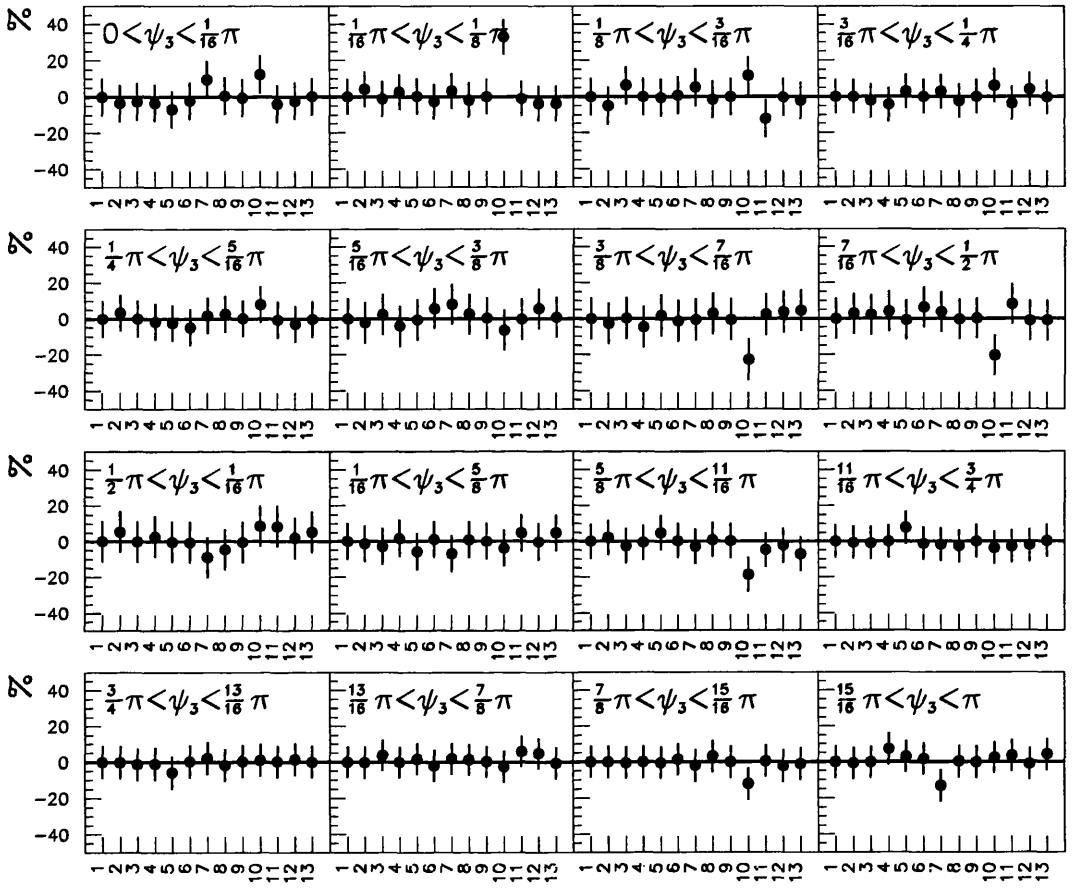

Figure 7.11: Summary of systematic uncertainties for $1/\sigma d\sigma/d\psi_3$. The difference in percent between the systematic value and the nominal result is shown together with the statistical error from the nominal result. The line at zero refers to the position of the nominal value.

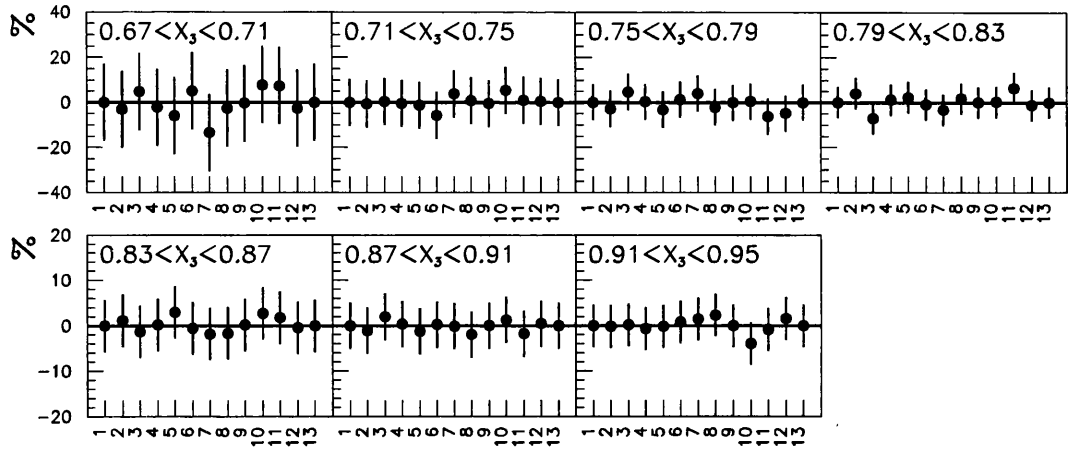

Figure 7.12: Summary of systematic uncertainties for $1/\sigma d\sigma/dX_3$. The difference in percent between the systematic value and the nominal result is shown together with the statistical error from the nominal result. The line at zero refers to the position of the nominal value.

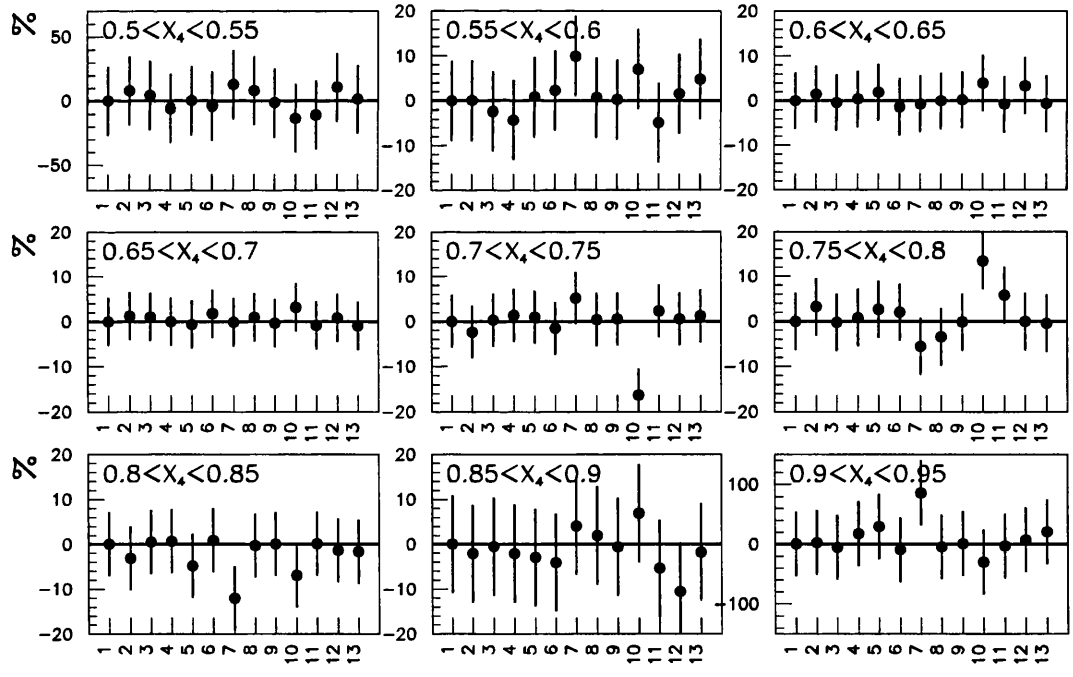

Figure 7.13: Summary of systematic uncertainties for $1/\sigma d\sigma/dX_4$. The difference in percent between the systematic value and the nominal result is shown together with the statistical error from the nominal result. The line at zero refers to the position of the nominal value.

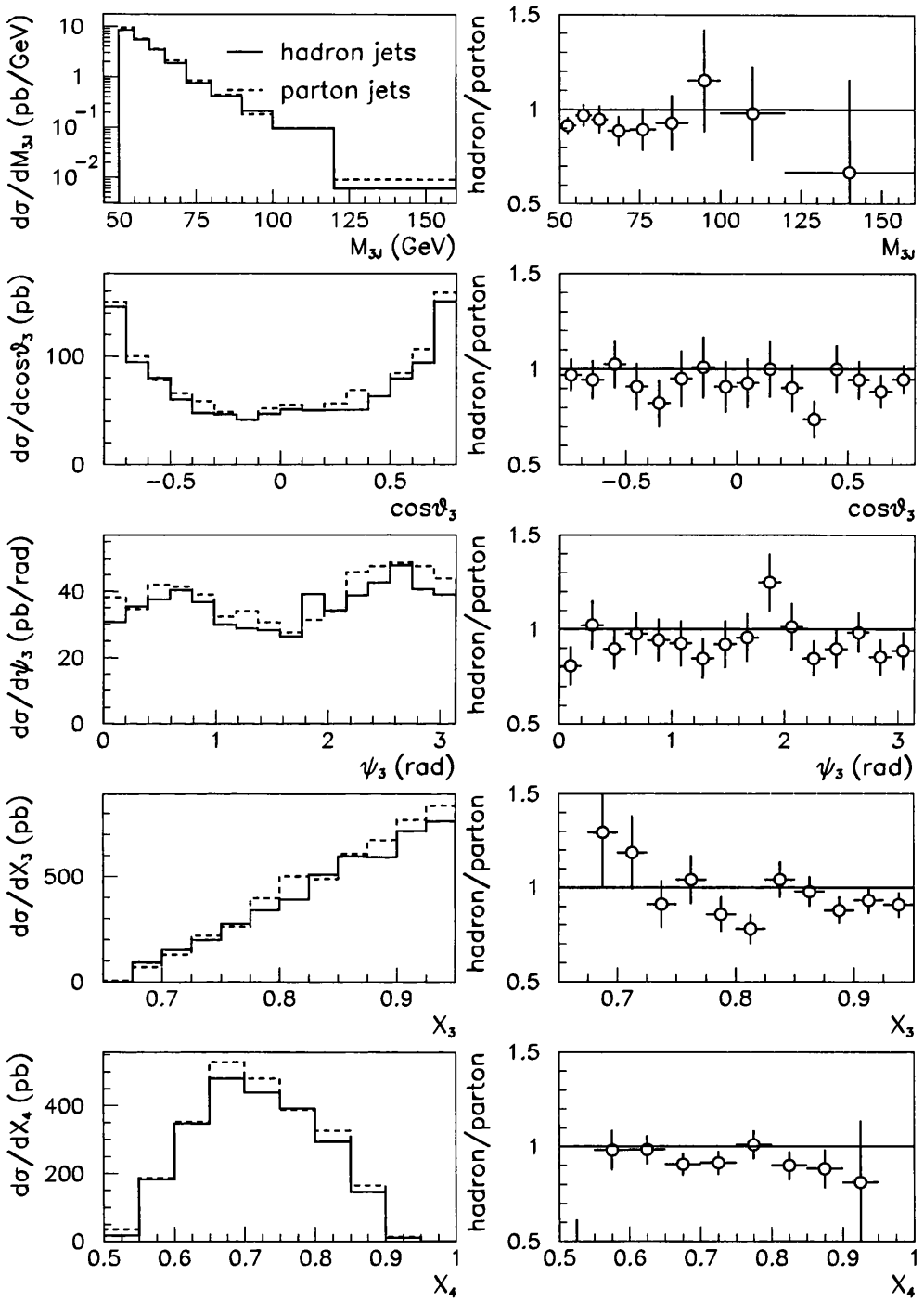

Figure 7.14: The left column shows the three-jet differential cross sections with respect to M_{3J}, $\cos\theta_3$, ψ, X_3 and X_4 for jets of hadrons (solid histogram) and partons (dashed histogram). The right column shows the ratio of the hadron to the parton level three-jet cross sections.

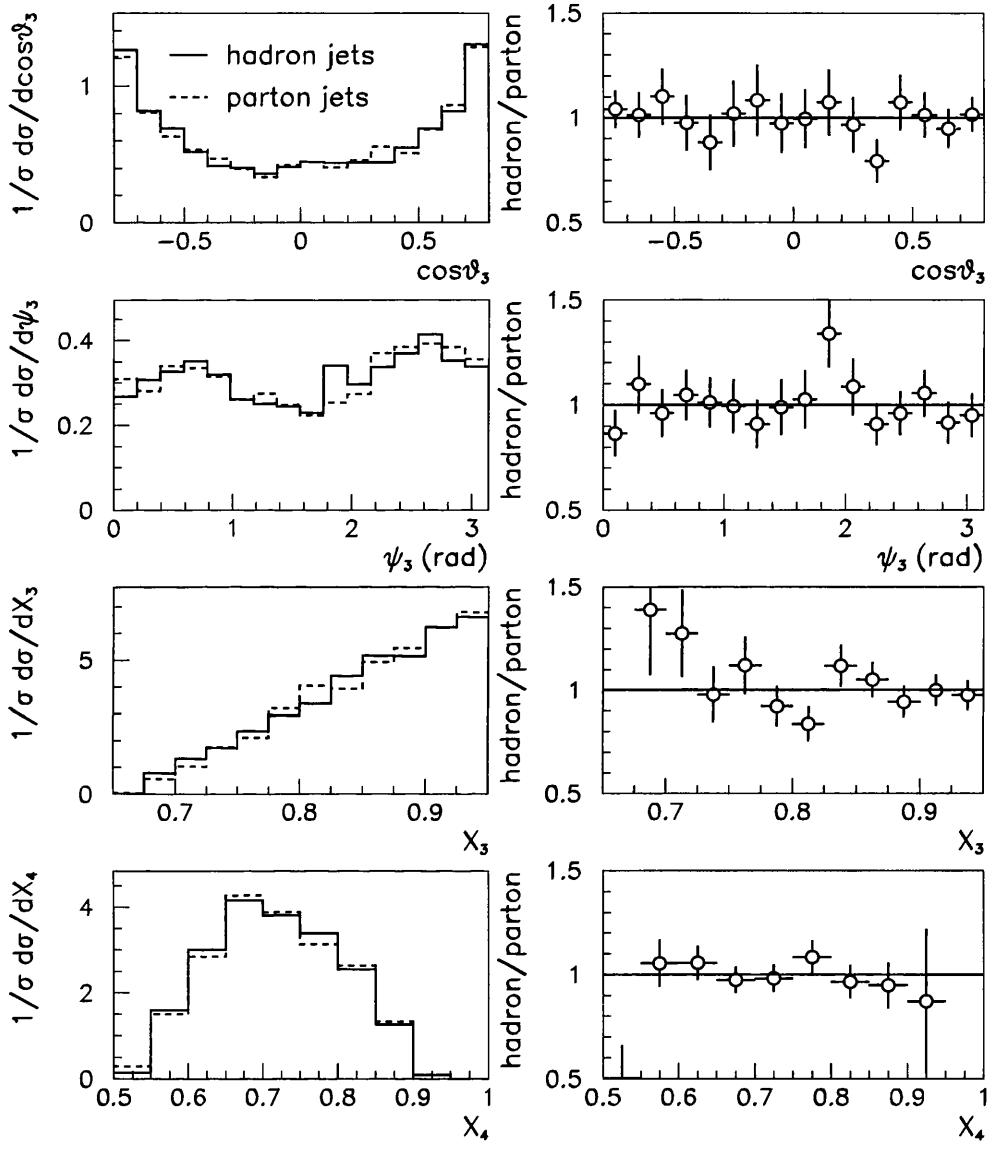

Figure 7.15: The left column shows the area normalised distributions of $\cos\theta_3$, ψ, X_3 and X_4 for jets of hadrons (solid histogram) and partons (dashed histogram). The right column shows the ratio of the hadron to the parton level distributions.

Chapter 8

Interpretation

8.1 $\mathcal{O}(\alpha\alpha_s^2)$ pQCD Calculations and the Parton Shower Model

Theoretical pQCD calculations for photoproduction cross sections at $\mathcal{O}(\alpha\alpha_s^2)$ are available from two groups of authors, Harris & Owens [73] and Klasen [74]. These calculations include $2 \rightarrow 3$ processes as illustrated in figure 1.10. Since three partons are produced in the final state the calculations can be used to describe three-jet production at leading order for the processes currently under consideration. The theoretical uncertainty on the calculation is estimated at $\pm$ 30-40% and is particularly associated with uncertainty in the QCD scale [75].

PYTHIA and HERWIG use the LO matrix elements for $2 \rightarrow 2$ scattering processes while the multiparton final state produced by the parton shower approximates some of the higher-order matrix elements. The event samples compared to the data in this chapter were generated with a minimum p_T of the hard scatter of 8 GeV. Direct and resolved processes were combined according to their relative cross sections.

The measured three-jet differential cross section $d\sigma/dM_{3J}$ is compared to these different models of three-jet production in figure 8.1. The data are peaked at the threshold of 50 GeV and decline exponentially with increasing M_{3J}. Above 90 GeV the statistical errors dominate. The $\mathcal{O}(\alpha\alpha_s^2)$ calculations agree well with the data despite being only LO for this process. Both parton shower models significantly underestimate the cross section for three-jet production, HERWIG more so than PYTHIA.

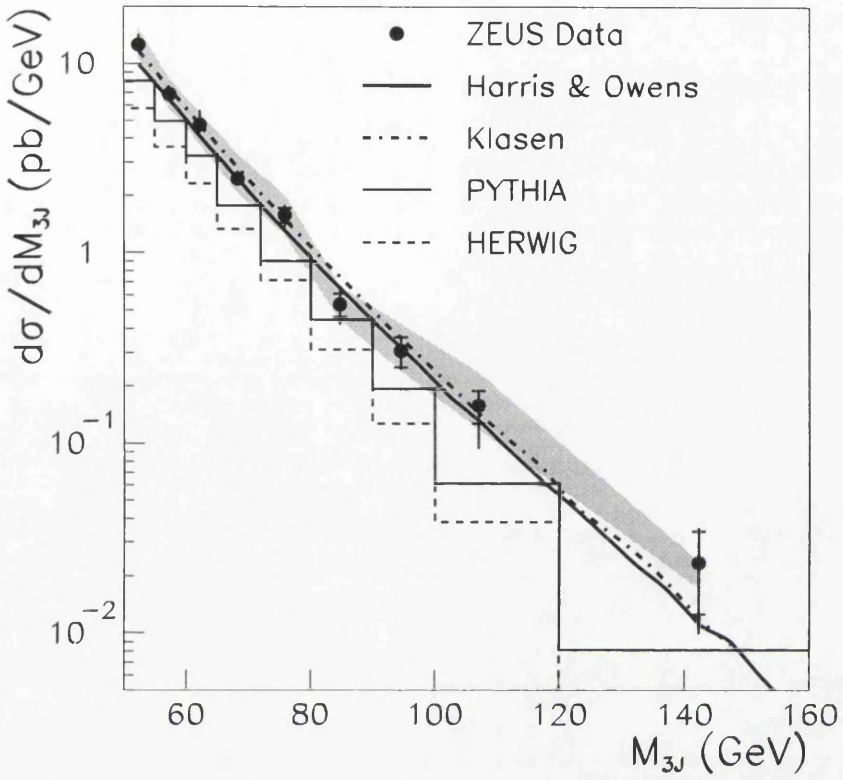

Figure 8.1: The cross section $d\sigma/dM_{3J}$. The corrected ZEUS data are plotted at the mean M_{3J} of the bin and are shown by black dots. The inner error bars show the statistical error while the outer indicate the statistical and systematic errors added in quadrature. The shaded band represents the uncertainty on the measurement due to raising and lowering the CAL energy scale by 5%. Shown in comparison are three-jet cross sections from LO QCD calculations and from PYTHIA and HERWIG.

Figure 8.2 shows the X_3 and X_4 distributions area normalised and compared to $\mathcal{O}(\alpha\alpha_s^2)$, figures 8.2(a) and (b), and to PYTHIA and HERWIG, figures 8.2(c) and (d). In addition to the QCD based calculations the result due to three-parton phase-space alone (fixed matrix element) is shown in figures 8.2(a) and (b).

The X_3 distribution shown in figure 8.2(a) illustrates that the highest energy jet in the three-jet rest frame tends towards taking the maximum amount of available energy. The energy fraction of the second highest energy jet, X_4, can range between 0.5-0.95. The data, shown in figure 8.2(b), are peaked at ~ 0.65 indicating that the third jet also takes a significant fraction of the available energy.

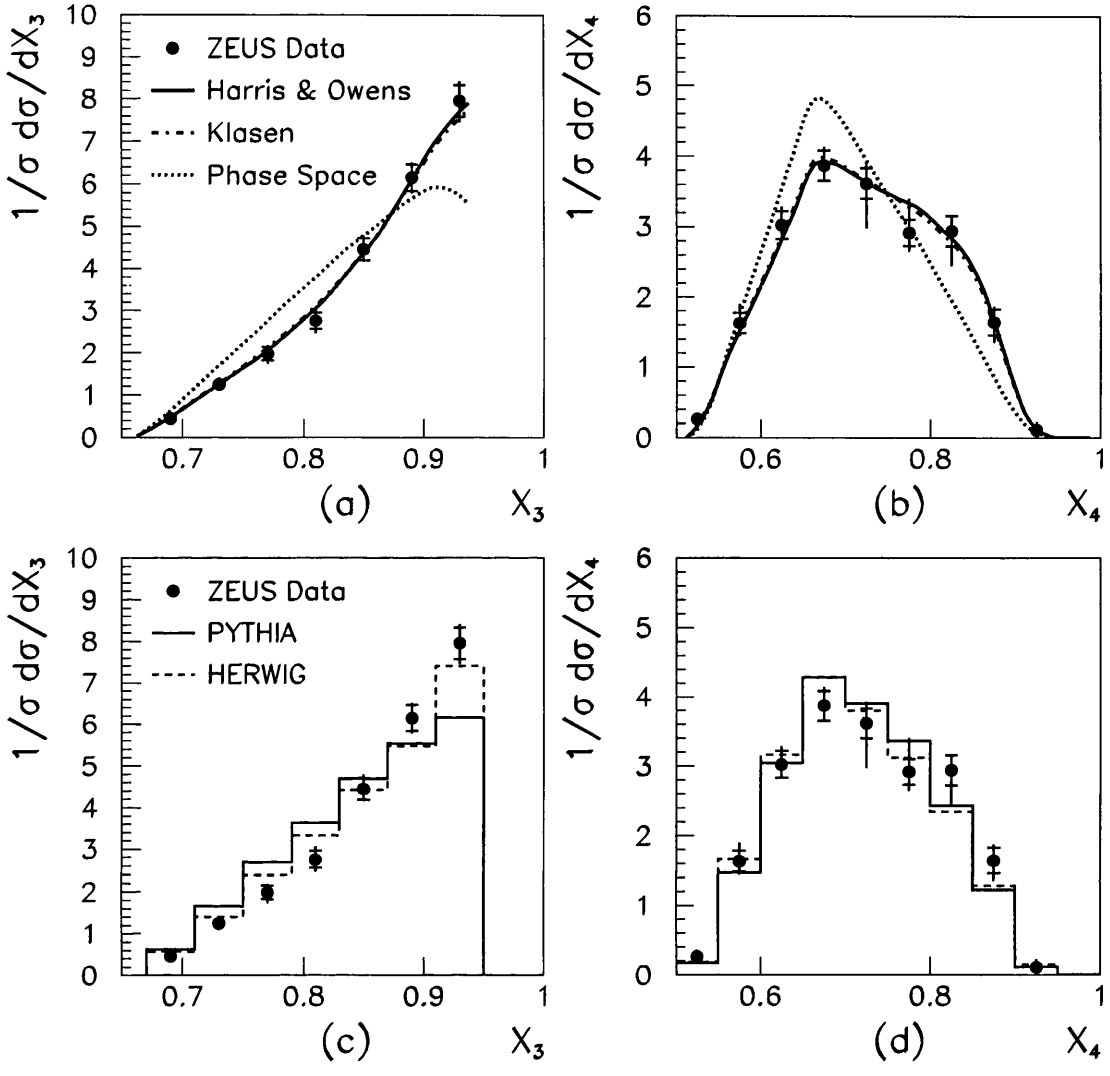

Figure 8.2: Shown are (a) $1/\sigma d\sigma/dX_3$ and (b) $1/\sigma d\sigma/dX_4$ comparing the corrected ZEUS data to $\mathcal{O}(\alpha\alpha_s^2)$ pQCD calculations. Also shown are the PYTHIA and HERWIG predictions in (c) $1/\sigma d\sigma/dX_3$ and (d) $1/\sigma d\sigma/dX_4$. The corrected ZEUS data are plotted at the centre of the bin and are shown by black dots. The inner error bars show the statistical error while the outer indicate the statistical and systematic errors added in quadrature.

There is excellent agreement between the $\mathcal{O}(\alpha\alpha_s^2)$ calculations and the data for both X_3 and X_4 as shown by figures 8.2(a) and (b). Figure 8.2(c) demonstrates that HERWIG also describes X_3 reasonably well while PYTHIA underestimates the amount of events where the highest energy jet takes a large fraction of the available energy. Both PYTHIA and HERWIG underestimate slightly the fraction of events where the second

highest energy jet takes a large share of the available energy, figure 8.2(d). It is clear however that the prediction due to phase space alone is remarkably similar to the QCD based calculations, indicating that the energy-sharing variables are relatively insensitive to the QCD matrix element.

The area-normalised distributions of the angular variables, $\cos\theta_3$ and ψ_3 are shown compared with $\mathcal{O}(\alpha\alpha_s^2)$ calculations, 8.3 (a) and (b), and also to PYTHIA and HERWIG, 8.3 (c) and (d). The result obtained from three-parton phase-space alone is shown in figures 8.3(a) and (b) to be quite different from the QCD based predictions. The shape of the $\cos\theta_3$ and ψ_3 distribution must therefore be sensitive to the QCD matrix element. The phase space prediction for $\cos\theta_3$ is relatively flat, the slight asymmetry arising perhaps from the E_T and angular cuts applied. The data, in contrast, peak sharply at $\cos\theta_3 = \pm\ 0.8$ indicating that the the highest energy jet in the centre-of-mass is likely to be produced at small, rather than large, angles to the beam direction. This indicates that, as in Rutherford scattering, glancing collisions between partons are more likely than head-on-collisions. The $\mathcal{O}(\alpha\alpha_s^2)$ pQCD and parton shower calculations, which take into account the dependence of the distribution on the quark and gluon spins, are in excellent agreement with the data. The success of the parton shower models in describing the data is not overly surprising since $\cos\theta_3$ is determined from the highest energy jet only, has a form similar to $\cos\theta^*$ in dijet events [43] and may not be particularly sensitive to the third jet in the event.

The ψ_3 distribution shows the angle in three-jet centre-of-mass frame between the plane containing the highest energy jet and the beam, and the plane containing the three jets. In contrast to $\cos\theta_3$, ψ_3 has no equivalent for dijet events. Its behaviour is therefore expected to be sensitive to the orientation of the third jet. Figure 8.3(b) demonstrates the suppression of the phase space for three-jet production at $\psi_3 = 0$ or π due to restrictions on the angular separation of jets imposed by the jetfinder and the E_T cut. This can be expected to be a general feature of ψ_3 distributions. Taking this suppression into consideration suggests that the data are peaked at $\psi_3 = 0$ or π, a configuration where the third jet tends to lie relatively close to the plane that contains the highest energy jet and the beam direction in the centre-of-mass. The production of a third jet at large angles to the beam is weaker. Again the $\mathcal{O}(\alpha\alpha_s^2)$

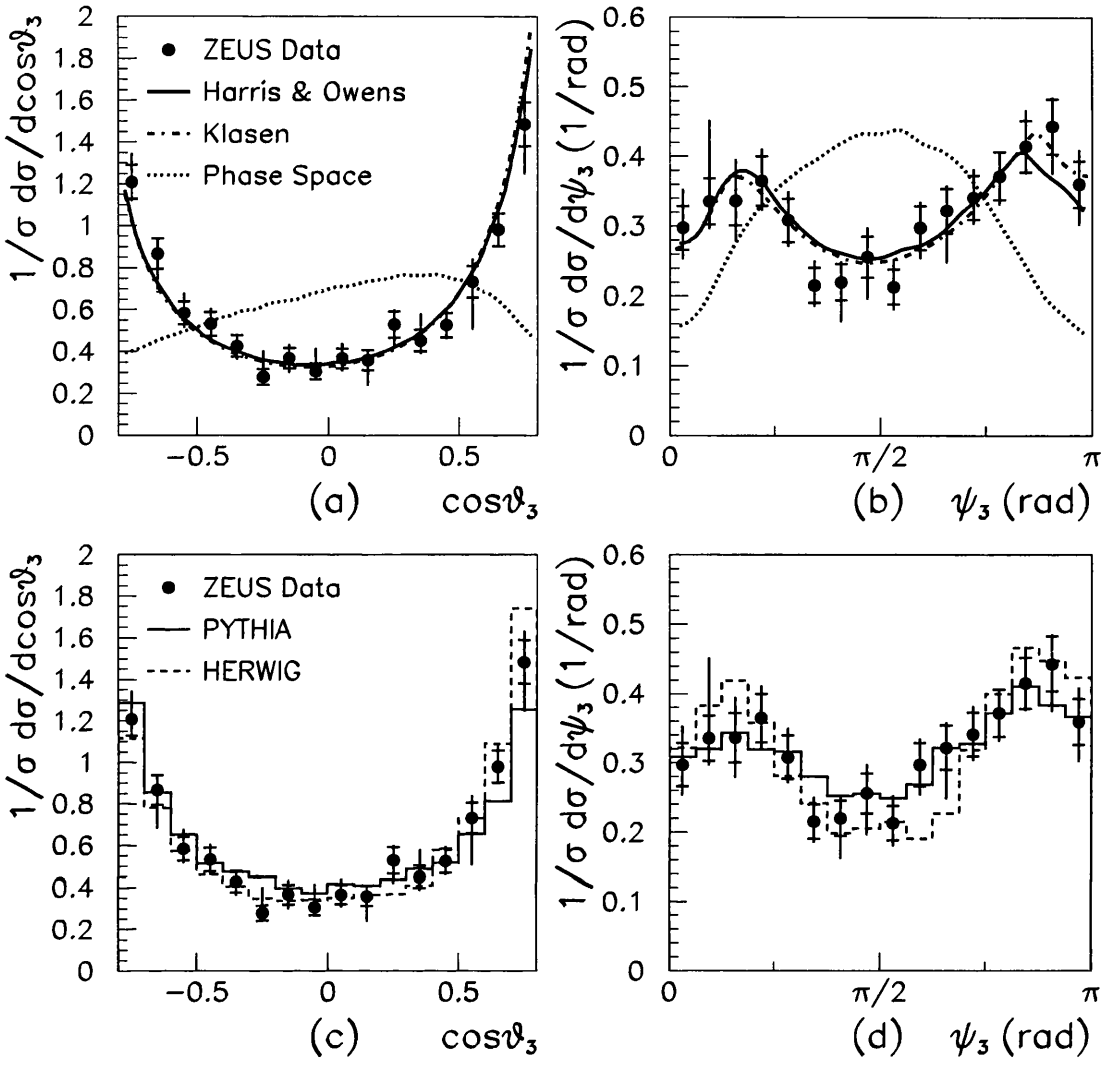

Figure 8.3: Shown are (a) $1/\sigma d\sigma/d\cos\theta_3$ and (b) $1/\sigma d\sigma/d\psi_3$ comparing the corrected ZEUS data to $\mathcal{O}(\alpha\alpha_s^2)$ pQCD calculations. Also shown are the PYTHIA and HERWIG predictions in (c) $1/\sigma d\sigma/d\cos\theta_3$ and (d) $1/\sigma d\sigma/d\psi_3$. The corrected ZEUS data are plotted at the centre of the bin and are shown by black dots. The inner error bars show the statistical error while the outer indicate the statistical and systematic errors added in quadrature.

pQCD calculations provide a good description of the data. It is interesting that the parton shower predictions from PYTHIA and HERWIG are also able to reproduce the data adequately. There appears to be a discrepancy between PYTHIA and HERWIG predictions in figure 8.3(d) with the third jet in HERWIG events more likely to lie close to the beam direction. A more detailed discussion follows in section 8.4.

8.2 Multiparton Interactions

In any interaction involving two hadrons the possibility exists of a secondary hard scatter occuring between the constituent partons of these hadrons. Models of these multiparton interactions (MI) are available in the PYTHIA and HERWIG event generators. Multiparton interactions have been shown to improve the agreement between HERA data and theoretical predictions by increasing the energy flow in events particularly near the proton direction [37, 34, 41].

PYTHIA and HERWIG predictions with and without multiparton interactions are compared with the measured cross sections $d\sigma/dcos\theta_3$ and $d\sigma/d\psi_3$ in figure 8.4 and $d\sigma/dX_3$ and $d\sigma/dX_4$ in figure 8.5. It is clear that the addition of multiparton interactions to either model does not significantly improve the agreement with the data. Indeed the cross sections with and without MI are very similar for PYTHIA and almost identical for HERWIG. It may be concluded that the third jet in our selection of events does not come from an independent hard scatter.

8.3 Initial and Final State Radiation

Within the parton shower model, gluon radiation from partons from the proton and photon involved in the hard scatter is referred to as initial or final state, depending on whether it is radiated from an incoming or outgoing parton. PYTHIA provides the opportunity to study the effects of different classes of radiation by allowing either or both of the initial and final state radiation to be switched off. In the complete calculation, of course, there is interference between the inital and final state diagrams. In figure 8.6 the data are compared to three PYTHIA predictions: the default PYTHIA, PYTHIA with initial state radiation only (ISR) and with final state radiation only (FSR).

It is clearly seen that ISR is the dominant mechanism for producing a third jet within the parton shower model.

The type of three-jet events produced by ISR and FSR is also different. The third jet produced by ISR shows a strong tendency to lie close to the beam direction. This is

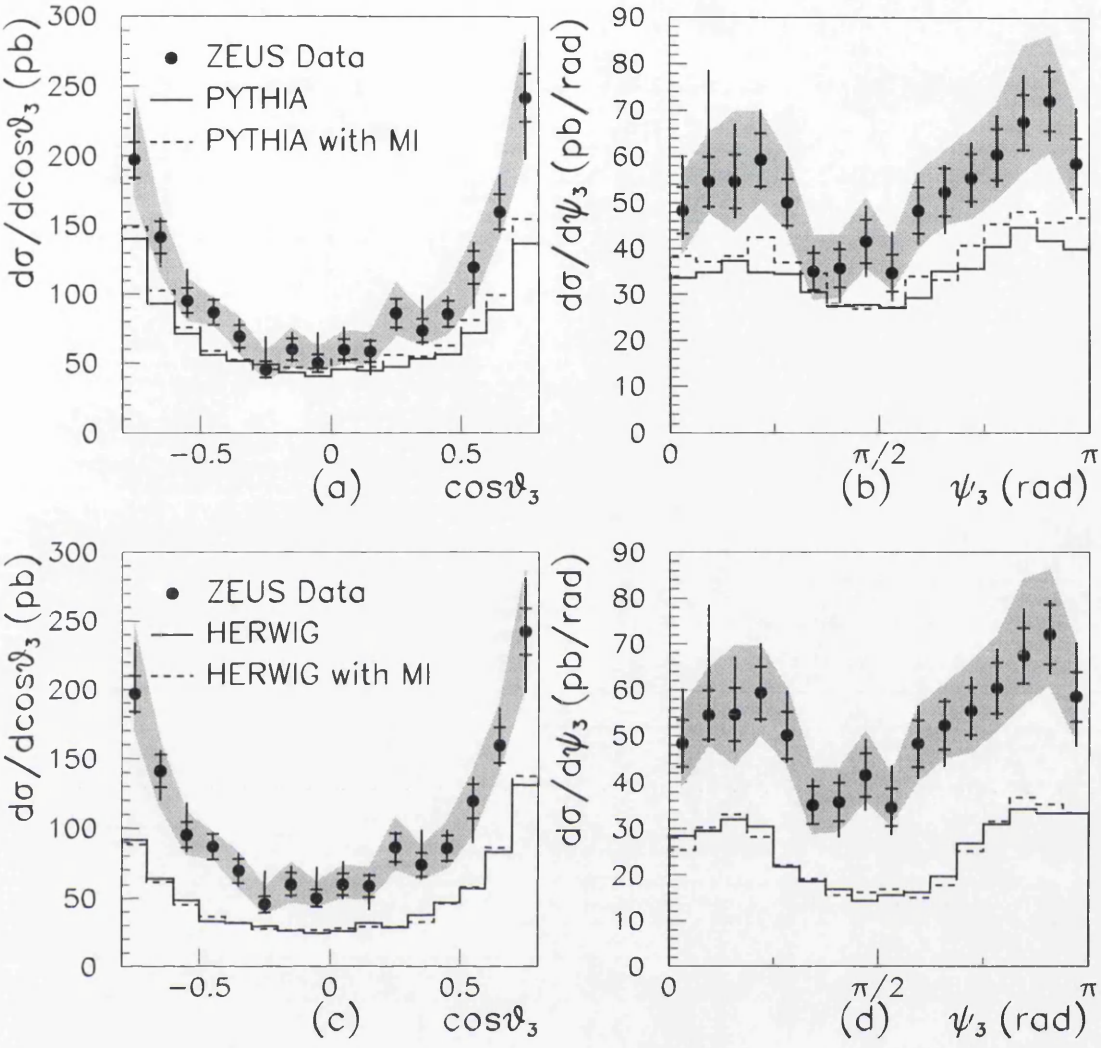

Figure 8.4: $d\sigma/d\cos\theta_3$ and $d\sigma/d\psi_3$. The corrected ZEUS data are plotted at the centre of the bin and are shown by black dots. The inner error bars show the statistical error while the outer indicate the statistical and systematic errors added in quadrature. The shaded band represents the uncertainty on the measurement due to raising and lowering the CAL energy scale by 5%. Shown in comparison are the predictions from PYTHIA and HERWIG with and without multi-parton interactions.

also illustrated in figure 8.7(d) which compares the shapes of the ψ_3 distributions. The angular distribution of the third jet from FSR closely follows that of the phase space prediction shown in figure 8.3(b) implying a more isotropic distribution.

The X_3 and X_4 distributions, figure 8.7(a) and (b), show that when the third jet is

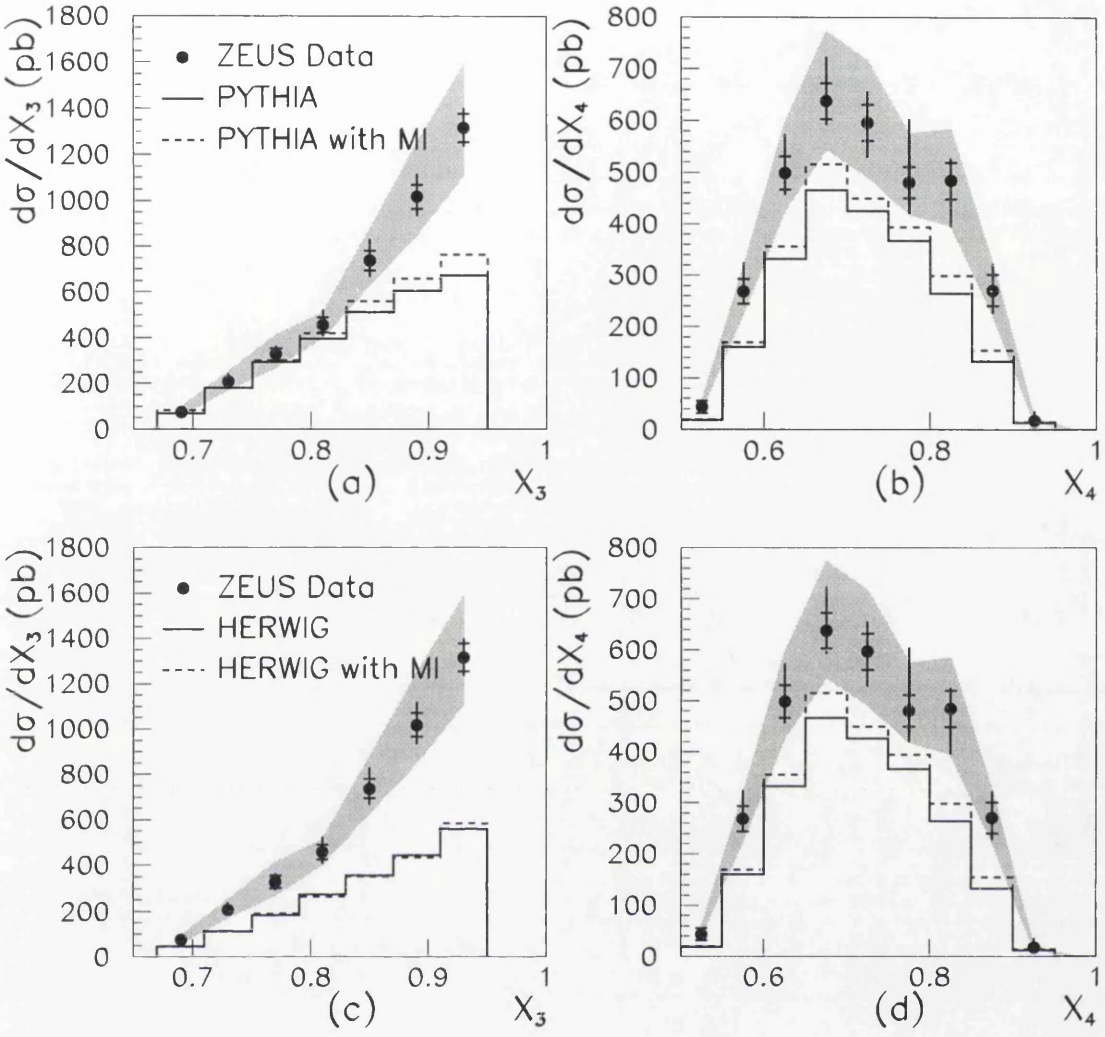

Figure 8.5: $d\sigma/dX_3$ and $d\sigma/dX_4$. The corrected ZEUS data are plotted at the centre of the bin and are shown by black dots. The inner error bars show the statistical error while the outer indicate the statistical and systematic errors added in quadrature. The shaded band represents the uncertainty on the measurement due to raising and lowering the CAL energy scale by 5%. Shown in comparison are the predictions from PYTHIA and HERWIG with and without multi-parton interactions.

produced by FSR the highest two energy jets take relatively larger amounts of energy, leaving less for the third jet, than when ISR produces the third jet. Figure 8.7(c) indicates that the $\cos\theta_3$ distribution is insensitive to the type of parton shower. This would be expected since the highest energy jet comes directly from the hard scatter in the majority of cases and is largely unaffected by the parton showering.

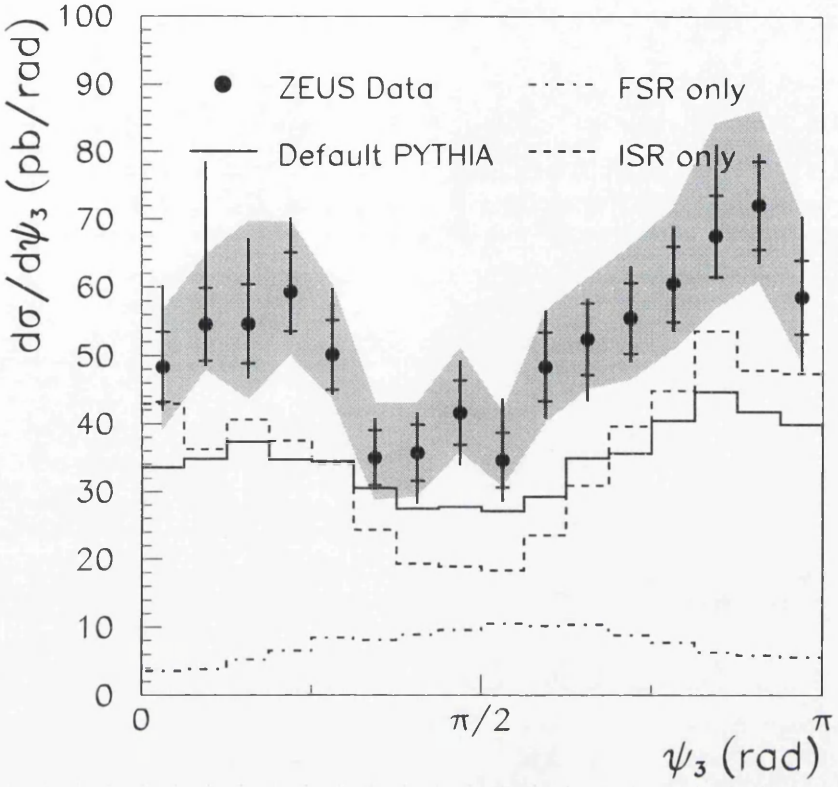

Figure 8.6: $d\sigma/d\psi_3$. The corrected ZEUS data are plotted at the centre of the bin and are shown by black dots. The inner error bars show the statistical error while the outer indicate the statistical and systematic errors added in quadrature. The shaded band represents the uncertainty on the measurement due to raising and lowering the CAL energy scale by 5%. Shown in comparison are the predictions from PYTHIA with and without initial and final state radiation.

In conclusion, comparing the parton shower predictions with the data demonstrates that within the parton shower model the third jet comes from ISR QCD radiation in a large fraction of events. This is particularly clear in the ψ_3 distribution which is sensitive to the orientation of the third jet.

8.4 Colour Coherence

QCD coherence effects arise due to interference of soft gluon radiation amplitudes which results in a restriction of the phase space available for soft gluon emission. The term 'soft' here is relative to the hard scatter. In the parton shower model, as discussed in

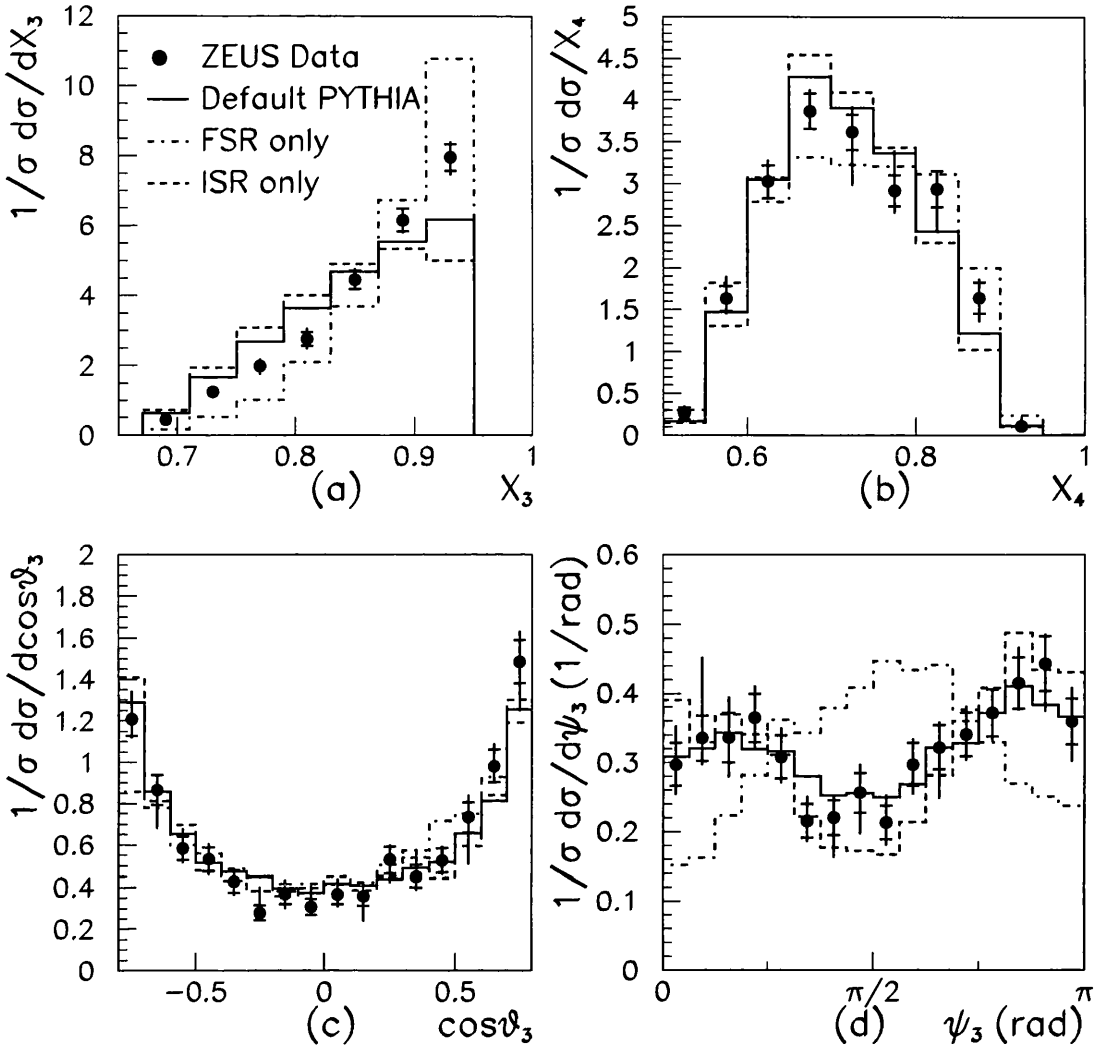

Figure 8.7: (a) $1/\sigma d\sigma/dX_3$, (b) $1/\sigma d\sigma/dX_4$, (c) $1/\sigma d\sigma/dcos\theta_3$ and (d) $1/\sigma d\sigma/d\psi_3$. The corrected ZEUS data are plotted at the centre of the bin and are shown by black dots. The inner error bars show the statistical error while the outer indicate the statistical and systematic errors added in quadrature. Shown in comparison are the predictions from PYTHIA with and without initial and final state radiation.

section 1.3, in addition to the familiar angular ordering effect, the colour flow in an event restricts the angular region into which a parton can be emitted. This approach is implemented in HERWIG. PYTHIA also implements coherence as a restriction on the angular region into which a parton is radiated; however the restrictions can be removed to produce 'incoherent' PYTHIA events. Some degree of coherence is still

present in the incoherent sample due to coherence in the hadronisation process from string fragmentation [27]. The use of jet variables which are relatively insensitive to the hadronisation model used should reduce sensitivity to this.

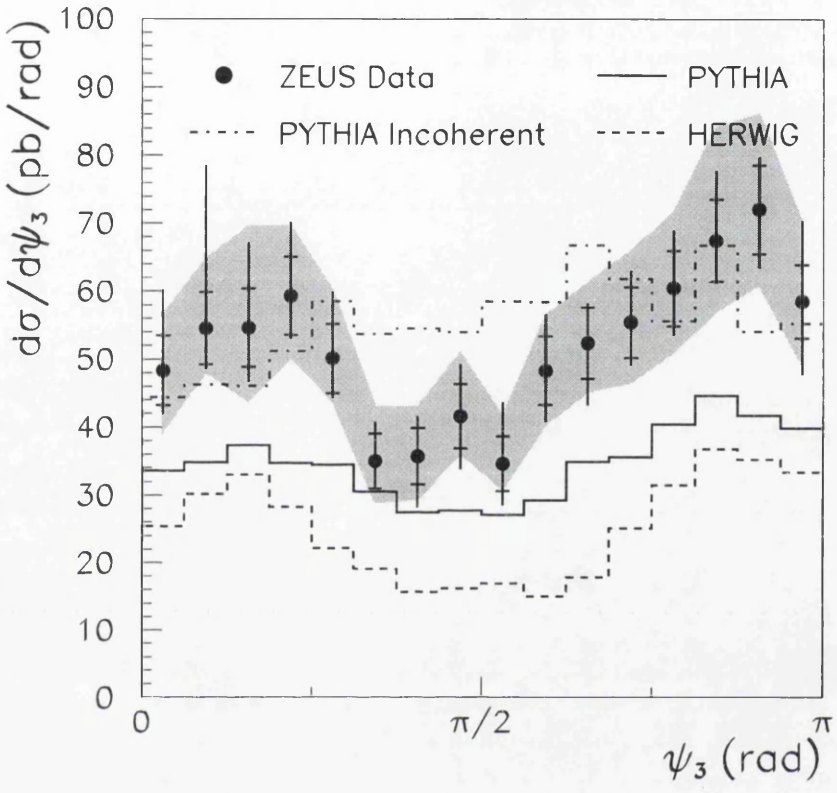

Figure 8.8: $d\sigma/d\psi_3$ compared with the predictions from HERWIG, PYTHIA and PYTHIA without angular ordering. The corrected ZEUS data are plotted at the centre of the bin and are shown by black dots. The inner error bars show the statistical error while the outer indicate the statistical and systematic errors added in quadrature. The shaded band represents the uncertainty on the measurement due to raising and lowering the CAL energy scale by 5%.

Figure 8.8 shows $d\sigma/d\psi_3$ again, comparing the data to three different implementations of colour coherence: HERWIG, PYTHIA and 'incoherent' PYTHIA. Although the incoherent cross section values roughly agree with the data, the uncertainty in the theoretical normalisation means that the agreement in itself cannot be taken as a confirmation of this model. The three-jet cross sections for the models where colour coherence is included in the parton shower are lower than in the incoherent model showing that coherence has reduced the phase space available for three-jet production. This reduction in phase space particularly affects large angle emissions as shown by the

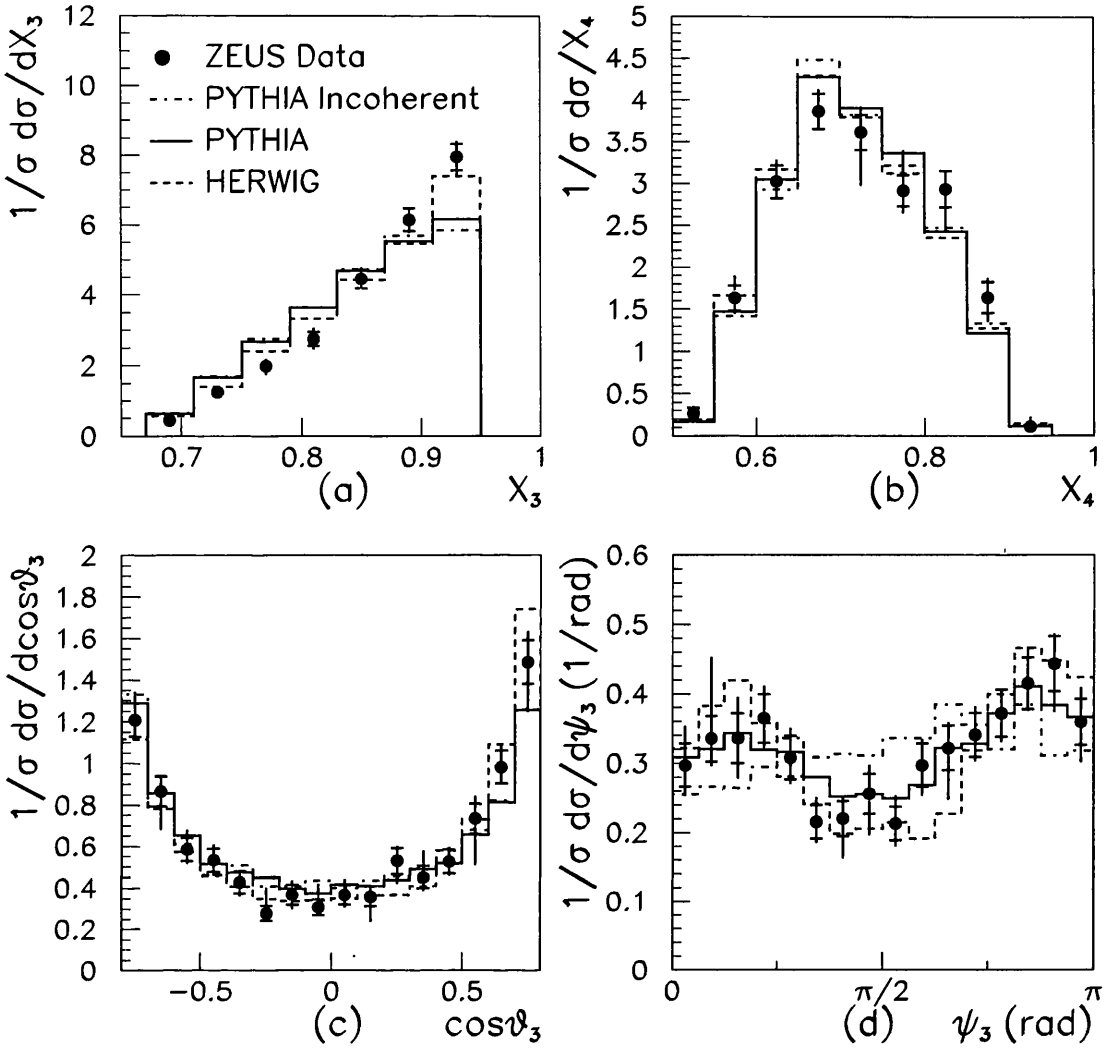

Figure 8.9: $1/\sigma d\sigma/dX_3$, (b) $1/\sigma d\sigma/dX_4$, (c) $1/\sigma d\sigma/dcos\theta_3$ and (d) $1/\sigma d\sigma/d\psi_3$. The corrected ZEUS data are plotted at the centre of the bin and are shown by black dots. The inner error bars show the statistical error while the outer indicate the statistical and systematic errors added in quadrature. The shaded band represents the uncertainty on the measurement due to raising and lowering the CAL energy scale by 5%. Shown in comparison are the predictions from HERWIG, PYTHIA and PYTHIA without angular ordering.

dip in the coherent cross sections at $\psi_3 = \frac{\pi}{2}$ rad. The more restrictive the coherence effects, the more likely the third jet is to lie close to the beam direction ($\psi_3 = 0$ or π rad) since ISR is the dominant mechanism for producing a third jet. Figure 8.9(d) illustrates this clearly; the shape of the HERWIG ψ_3 distribution is peaked towards

$\psi_3 = 0$ and π, while the incoherent PYTHIA prediction is approximately flat and the default PYTHIA prediction lies in between. Only the models which include colour coherence in the parton shower succeed in describing satisfactorily the orientation of the third jet in the data. The data however are not precise enough to discriminate between the models of coherence implemented in PYTHIA and HERWIG. As expected, the variables which are less affected by the parton shower, $\cos\theta_3$, X_3 and X_4, are insensitive to colour coherence effects.

8.5 Summary

The study of three-jet events in photoproduction presented here has enabled a number of features of QCD to be demonstrated. $\mathcal{O}(\alpha\alpha_s^2)$ pQCD calculations from two groups of authors have been shown to provide an excellent description of both the three-jet differential cross section $d\sigma/dM_{3J}$ and the shapes of the angular and energy-sharing observables, $\cos\theta_3$, ψ_3, X_3 and X_4. The X_3 and X_4 distributions closely follow the prediction due to phase space alone but both the $\cos\theta_3$ and ψ_3 distributions prove to be sensitive to the use of the QCD matrix element.

The parton shower model of three-jet production as implemented in PYTHIA and HERWIG also succeeds in describing the shape of the three-jet distributions but underestimates the cross section by 20-40%.

Within the parton shower model the insensitivity to multiparton interactions indicates that the third jet is not the result of an independent hard scatter to any significant extent. A study of the jets produced separately from initial state or final state radiation shows that initial state radiation is responsible for the third jet in most three-jet events while final state radiation has a relatively minor effect with the jet selections employed here. Coherent parton emission is required in the parton shower to provide a satisfactory description of the data.

Chapter 9

Summary

In this analysis the production of three high tranverse energy jets has been measured for the first time for hard photoproduction events. The data were taken from e^+p collisions during the 1995 and 1996 HERA running period and correspond to an integrated luminosity of 16 pb^{-1}.

A clustering type algorithm was employed to find jets and detector corrections were applied to obtain hadron level differential cross sections. The cross section was defined inclusively requiring at least three jets with $\eta < 2.4$, two of which with $E_T > 6$ GeV and a third with $E_T > 5$ GeV. Additional selection criteria of $M_{3J} > 50$ GeV, $|\cos\theta_3| < 0.8$ and $X_3 < 0.95$ permit the study of the angular observables $\cos\theta_3$ and ψ_3 by reducing the effect of the E_T thresholds on these distributions. The energy-sharing variables X_3 and X_4 were also studied.

$\mathcal{O}(\alpha\alpha_s^2)$ pQCD calculations for photoproduction, which are leading order for three-jet production, were compared with the data. Parton shower Monte Carlo event generators such as PYTHIA and HERWIG which employ LO $2 \rightarrow 2$ photoproduction matrix elements but which add to this a separate modelling of initial and final state radiation as part of the parton shower can also approximate multiparton final states. These models can, in addition, provide full hadronisation of the process and allow different aspects of the process to be turned on and off.

The three-jet cross section for events with the above characteristics was measured to be

$$\sigma_{three-jet} = 162.4 \pm 4.1\ (stat.)\ ^{+15.8}_{-5.9}\ (sys.)\ ^{+32.3}_{-24.8}\ (energy\ scale)\ \text{pb}$$

Comparison of the data with the theoretical predictions yielded the following conclusions:

1. The $\mathcal{O}(\alpha\alpha_s^2)$ pQCD calculations were shown to describe the data extremely well, both in absolute cross section and in shape, despite being only LO for three-jet production.

2. The parton shower approach also provided a remarkably good description of the shape of the three-jet distributions but underestimated the total cross section by 20-40%.

3. Within the parton shower model secondary interactions in resolved photoproduction events were shown to have a negligible effect on the three-jet distributions indicating that the third jet is not produced by an independent hard scatter.

4. Also within the parton shower model it was shown that the third jet is produced predominantly by initial state radiation.

5. QCD colour coherence in the parton shower was found to restrict the phase space available for three-jet production. The orientation of the third jet was found to be sensitive to coherence effects; only models which include colour coherence in the parton shower succeed in describing the data satisfactorily.

This first study of three-jet final states in photoproduction has broadened our understanding of QCD at higher orders. It has also provided an important test of the ability of the parton shower extension to fixed order pQCD to reproduce key aspects of multijet final states such as the orientation of jets and the distribution of energy. Multijet final states still have much to tell us and future work promises to reveal further important information on QCD and photon induced processes.

Appendix A

Monte Carlo Event Samples

Monte Carlo events are used to correct measured ZEUS data for detector effects. The total number of these Monte Carlo events which pass the three-jet detector level selection should be considerably greater than the number of data events so that the statistical error in the correction factor is much smaller than the statistical error in the data.

The type of events measured, discussed in section 4.4 has three jets with a relatively low transverse energy threshold, $E_T^{cal} > 5$ GeV for the highest two E_T^{cal} jets, and a high invariant mass, $M_{3J}^{cal} > 45$ GeV. Since the E_T^{cal} distribution of the highest E_T^{cal} jet extends down to only $\sim$ 10 GeV generating events with a $p_{T\,min} = 4$ GeV is completely safe. This however produces many events with low invariant mass which are not required by the analysis. Generating all events with such a low $p_{T\,min}$ would be very inefficient in that of the events generated, few would pass the detector level selection cuts.

This problem can be avoided by generated events with increasing $p_{T\,min}$ values. Four different event samples were generated with the following hadron level selection criteria:

- $p_{T\,min} = 4$ GeV and three jets with $E_{T\,1}^{had} > 5$ GeV, $E_{T\,2}^{had} > 4$ GeV, $E_{T\,3}^{had} > 3$ GeV and $\eta < 3.0$ - *filter 1*

- $p_{T\,min} = 6$ GeV and three jets with $E_{T\,1}^{had} > 7$ GeV, $E_{T\,2}^{had} > 6$ GeV, $E_{T\,3}^{had} > 3$ GeV and $\eta < 3.0$ - *filter 2*

- $p_{T\,min}$ = 8 GeV and three jets with $E_{T\,1}^{had} > 10$ GeV, $E_{T\,2}^{had} > 8$ GeV, $E_{T\,3}^{had} > 3$ GeV and $\eta < 3.0$ - *filter 3*

- $p_{T\,min}$ = 8 GeV, three jets with $E_{T\,1}^{had} > 10$ GeV, $E_{T\,2}^{had} > 8$ GeV, $E_{T\,3}^{had} > 3$ GeV and $\eta < 3.0$ and $M_{3J}^{had} > 60$ GeV - *filter 4*

A small amount of luminosity was generated using filter 1 which was 100% efficient, that is, all events passing the three-jet detector level selection also pass the hadron level filter selection. Since this sample is $\sim$ 100% efficient tighter cuts were used to generate further event samples which increase the available statistics in the high E_T^{had} and M_{3J}^{had} regions, filters 2,3, and 4. Not all detector level three-jet events will pass the hadron level selection of these higher $p_{T\,min}$ filters. The events from all four filters can be combined, however, to reproduce the shape and absolute cross section of filter 1.

Details of the numbers of events generated for each filter and process are shown in tables A.1 for PYTHIA and A.2 and A.3 for HERWIG.

The effectiveness of combining samples of events generated with different selection criteria is demonstrated in figure A.1. Filter 1 has $p_{T\,min}$ = 4 GeV and three relatively low E_T^{had} jets. Filter 4 on the other hand not only has a higher $p_{T\,min}$ (8 GeV) and higher E_T^{had} jets but is also enriched in high M_{3J}^{had} events. Figure A.1(a) shows that the M_{3J}^{had} distribution of the events in these samples is clearly different. Figure A.1(b) shows the three-jet cross section as a function of M_{3J}^{had} for events from filter 1 and also from filters 1 and 4 combined. The combined sample was obtained by reweighting each event according to the cross section and luminosity for the filter selection it passed so that events at high M_{3J}^{had} were given lower weights than those at low M_{3J}^{had}. The validity of this approach is confirmed by the observation that the cross section of the filter 1 events is reproduced closely by the combined sample which also has smaller statistical errors at high M_{3J}^{had}.

The comparison of hadron-level quantities with data corrected to hadron-level is considerably simpler. Since only hadron-level quantities are presented it is not necessary to generate efficiently all detector-level jets. The Monte Carlo samples compared to the data in chapter 8 were thus generated with $p_{T\,min}$ = 8 GeV. Compared to an event sample generated with $p_{T\,min}$ = 4 GeV this represents a reduction in three-jet hadron-level cross section of less than 5 %.

$p_{T\,min}$ (GeV)	$E_{T\,1}^{had}$ (GeV)	$E_{T\,2}^{had}$ (GeV)	$E_{T\,3}^{had}$ (GeV)	M_{3J}^{had} (GeV)	Process	Number of Events $\times 10^{-3}$	Luminosity (pb^{-1})
4.0	5.0	4.0	3.0	0.0	direct	30	6.8
4.0	5.0	4.0	3.0	0.0	resolved	150	6.0
6.0	7.0	6.0	3.0	0.0	direct	40	22.4
6.0	7.0	6.0	3.0	0.0	resolved	70	9.4
8.0	10.0	8.0	3.0	0.0	direct	15	20.0
8.0	10.0	8.0	3.0	0.0	resolved	40	16.6
8.0	10.0	8.0	3.0	60.0	direct	5	34.0
8.0	10.0	8.0	3.0	60.0	resolved	10	23.5

Table A.1: PYTHIA events generated with different filter requirements and simulated for the ZEUS detector in 1996.

$p_{T\,min}$ (GeV)	$E_{T\,1}^{had}$ (GeV)	$E_{T\,2}^{had}$ (GeV)	$E_{T\,3}^{had}$ (GeV)	M_{3J}^{had} (GeV)	Process	Number of Events $\times 10^{-3}$	Luminosity (pb^{-1})
6.0	7.0	6.0	3.0	0.0	direct	20	10.4
6.0	7.0	6.0	3.0	0.0	resolved	60	9.4
8.0	10.0	8.0	3.0	60.0	direct	5	40.8
8.0	10.0	8.0	3.0	60.0	resolved	10	27.3

Table A.2: HERWIG events generated with different filter requirements and simulated for the ZEUS detector in 1995.

$p_{T\,min}$ (GeV)	$E_{T\,1}^{had}$ (GeV)	$E_{T\,2}^{had}$ (GeV)	$E_{T\,3}^{had}$ (GeV)	M_{3J}^{had} (GeV)	Process	Number of Events $\times 10^{-3}$	Luminosity (pb^{-1})
4.0	5.0	4.0	3.0	0.0	direct	30	5.7
4.0	5.0	4.0	3.0	0.0	resolved	100	4.5
6.0	7.0	6.0	3.0	0.0	direct	40	20.8
6.0	7.0	6.0	3.0	0.0	resolved	120	18.8
8.0	10.0	8.0	3.0	60.0	direct	5	41.7
8.0	10.0	8.0	3.0	60.0	resolved	20	53.3

Table A.3: HERWIG events generated with different filter requirements and simulated for the ZEUS detector in 1996.

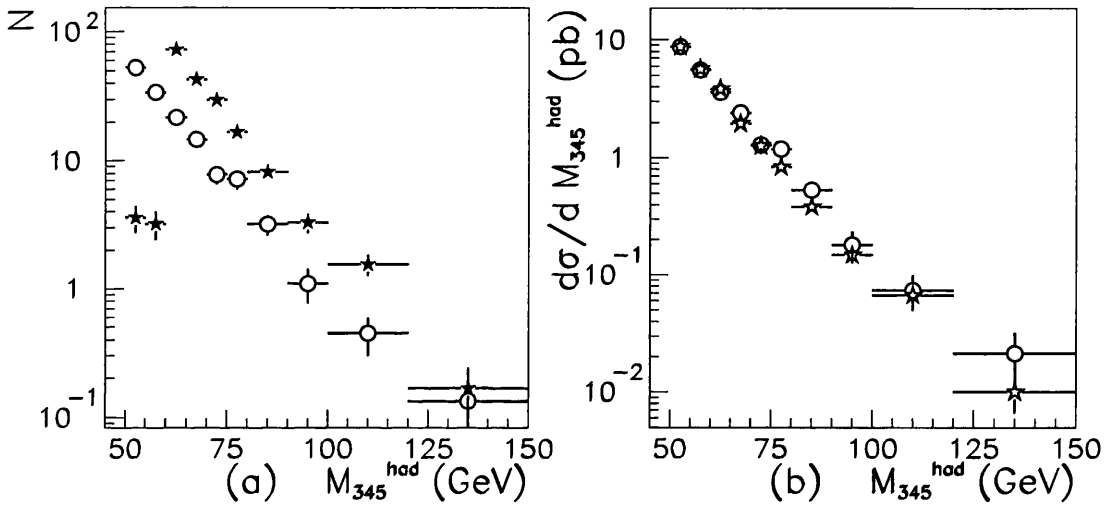

Figure A.1: (a) M_{3J}^{had} distributions for direct and resolved PYTHIA events from filter 1 (open circles) and filter 4 (stars). Total number of events in each sample is shown. (b) $d\sigma/dM_{3J}^{had}$ is shown for filter 1 (open circles) and filters 1 and 4 combined (open stars).

Appendix B

Tables of Data

M_{3J} range	$\langle M_{3J} \rangle$	$\sigma(\pm$ stat. syst. Escale)[pb/GeV]
[50,55]	52.35	$12.57 \pm 0.535\ ^{+1.566}_{-0.511}\ ^{+2.330}_{-1.686}$
[55,60]	57.34	$6.855 \pm 0.364\ ^{+0.443}_{-0.244}\ ^{+1.222}_{-0.987}$
[60,65]	62.18	$4.733 \pm 0.325\ ^{+0.884}_{-0.219}\ ^{+0.649}_{-0.913}$
[65,72]	68.30	$2.455 \pm 0.176\ ^{+0.180}_{-0.072}\ ^{+0.805}_{-0.361}$
[72,80]	75.82	$1.575 \pm 0.142\ ^{+0.151}_{-0.163}\ ^{+0.406}_{-0.308}$
[80,90]	84.73	$0.535 \pm 0.074\ ^{+0.114}_{-0.091}\ ^{+0.115}_{-0.084}$
[90,100]	94.58	$0.305 \pm 0.055\ ^{+0.031}_{-0.027}\ ^{+0.113}_{-0.061}$
[100,120]	107.0	$0.158 \pm 0.031\ ^{+0.009}_{-0.056}\ ^{+0.075}_{-0.038}$
[120,160]	142.3	$0.023 \pm 0.011\ ^{+0.005}_{-0.008}\ ^{+0.000}_{-0.006}$

Table B.1: The measured cross section $d\sigma/dM_{3J}$ with statistical, systematic (excluding the energy scale uncertainty) and energy scale uncertainties.

X_3 range	$\sigma(\pm$ stat. syst. Escale)[pb]	X_3 range	$\sigma(\pm$ stat. syst. Escale)[pb]
[0.67,0.71]	$74.26 \pm 13.0\ ^{+14.4}_{-14.4}\ ^{+19.2}_{-13.3}$	[0.83,0.87]	$736.5 \pm 42.9\ ^{+83.2}_{-55.7}\ ^{+136.}_{-106.}$
[0.71,0.75]	$207.0 \pm 22.1\ ^{+27.3}_{-11.4}\ ^{+42.6}_{-33.0}$	[0.87,0.91]	$1017. \pm 52.5\ ^{+86.0}_{-64.6}\ ^{+229.}_{-165.}$
[0.75,0.79]	$328.0 \pm 26.5\ ^{+25.4}_{-23.4}\ ^{+84.3}_{-58.0}$	[0.91,0.95]	$1315. \pm 62.3\ ^{+58.6}_{-50.7}\ ^{+268.}_{-203.}$
[0.79,0.83]	$456.1 \pm 32.3\ ^{+58.3}_{-38.0}\ ^{+53.2}_{-54.2}$		

Table B.2: The measured cross section $d\sigma/dX_3$ with statistical, systematic (excluding the energy scale uncertainty) and energy scale uncertainties.

X_4 range	$\sigma(\pm$ stat. syst. Escale)[pb]	X_4 range	$\sigma(\pm$ stat. syst. Escale)[pb]
[0.5,0.55]	$43.56 \pm 11.9\ ^{+6.72}_{-5.25}\ ^{+11.0}_{-3.75}$	[0.75,0.8]	$480.5 \pm 30.8\ ^{+120.}_{-52.9}\ ^{+93.6}_{-61.3}$
[0.55,0.6]	$268.5 \pm 24.3\ ^{+51.2}_{-9.98}\ ^{+45.8}_{-41.6}$	[0.8,0.85]	$484.0 \pm 35.6\ ^{+22.0}_{-81.8}\ ^{+98.9}_{-87.5}$
[0.6,0.65]	$498.5 \pm 32.1\ ^{+68.2}_{-27.6}\ ^{+96.4}_{-70.8}$	[0.85,0.9]	$270.5 \pm 30.3\ ^{+42.7}_{-32.2}\ ^{+52.1}_{-46.7}$
[0.65,0.7]	$637.9 \pm 34.9\ ^{+78.6}_{-30.3}\ ^{+134.}_{-92.1}$	[0.9,0.95]	$17.69 \pm 9.55\ ^{+15.9}_{-4.65}\ ^{+2.32}_{-2.38}$
[0.7,0.75]	$596.2 \pm 35.3\ ^{+47.8}_{-57.5}\ ^{+120.}_{-104.}$	[0.95,1.0]	$0.000 \pm 0.00\ ^{+0.00}_{-0.00}\ ^{+0.00}_{-0.00}$

Table B.3: The measured cross section $d\sigma/dX_4$ with statistical, systematic (excluding the energy scale uncertainty) and energy scale uncertainties.

$\cos\theta_3$ range	$\sigma(\pm$ stat. syst. Escale)[pb]	$\cos\theta_3$ range	$\sigma(\pm$ stat. syst. Escale)[pb]
[-0.8,-0.7]	$197.2 \pm 13.0\ ^{+34.9}_{-7.49}\ ^{+46.6}_{-26.8}$	[0.0,0.1]	$59.74 \pm 7.63\ ^{+14.9}_{-7.70}\ ^{+13.5}_{-9.19}$
[-0.7,-0.6]	$141.3 \pm 11.7\ ^{+8.57}_{-17.8}\ ^{+19.6}_{-25.9}$	[0.1,0.2]	$58.56 \pm 7.79\ ^{+4.36}_{-15.2}\ ^{+13.4}_{-9.40}$
[-0.6,-0.5]	$95.31 \pm 9.17\ ^{+21.2}_{-8.64}\ ^{+15.9}_{-14.4}$	[0.2,0.3]	$86.29 \pm 10.3\ ^{+4.58}_{-8.04}\ ^{+21.6}_{-15.5}$
[-0.5,-0.4]	$86.78 \pm 9.14\ ^{+5.28}_{-1.49}\ ^{+10.2}_{-8.56}$	[0.3,0.4]	$73.62 \pm 8.45\ ^{+23.8}_{-6.20}\ ^{+13.1}_{-10.0}$
[-0.4,-0.3]	$69.50 \pm 8.36\ ^{+9.83}_{-7.65}\ ^{+13.2}_{-11.9}$	[0.4,0.5]	$85.68 \pm 9.41\ ^{+8.91}_{-4.23}\ ^{+19.3}_{-14.4}$
[-0.3,-0.2]	$45.44 \pm 5.90\ ^{+23.2}_{-2.65}\ ^{+12.7}_{-6.86}$	[0.5,0.6]	$119.5 \pm 12.0\ ^{+13.2}_{-27.4}\ ^{+22.6}_{-23.4}$
[-0.2,-0.1]	$59.90 \pm 7.89\ ^{+9.99}_{-5.15}\ ^{+15.3}_{-12.5}$	[0.6,0.7]	$159.9 \pm 12.9\ ^{+23.9}_{-8.07}\ ^{+28.9}_{-17.4}$
[-0.1,0.0]	$49.90 \pm 6.38\ ^{+21.5}_{-2.20}\ ^{+11.6}_{-5.38}$	[0.7,0.8]	$242.2 \pm 17.1\ ^{+35.4}_{-41.5}\ ^{+44.9}_{-39.8}$

Table B.4: The measured cross section $d\sigma/d\cos\theta_3$ with statistical, systematic (excluding the energy scale uncertainty) and energy scale uncertainties.

ψ_3 range	$\sigma(\pm$ stat. syst. Escale)[pb/rad]	ψ_3 range	$\sigma(\pm$ stat. syst. Escale)[pb/rad]
$[0,\frac{1}{16}\pi]$	$48.33 \pm 5.10\ ^{+10.7}_{-3.82}\ ^{+8.13}_{-8.86}$	$[\frac{1}{2}\pi,\frac{9}{16}\pi]$	$34.66 \pm 4.04\ ^{+8.04}_{-4.59}\ ^{+6.84}_{-3.66}$
$[\frac{1}{16}\pi,\frac{1}{8}\pi]$	$54.53 \pm 5.33\ ^{+23.5}_{-2.71}\ ^{+10.2}_{-6.41}$	$[\frac{9}{16}\pi,\frac{5}{8}\pi]$	$48.35 \pm 5.04\ ^{+6.45}_{-5.61}\ ^{+8.13}_{-7.92}$
$[\frac{1}{8}\pi,\frac{3}{16}\pi]$	$54.63 \pm 5.78\ ^{+11.1}_{-5.58}\ ^{+15.0}_{-10.8}$	$[\frac{5}{8}\pi,\frac{11}{16}\pi]$	$52.36 \pm 5.21\ ^{+2.68}_{-7.52}\ ^{+8.87}_{-7.05}$
$[\frac{3}{16}\pi,\frac{1}{4}\pi]$	$59.31 \pm 5.73\ ^{+9.21}_{-2.70}\ ^{+10.3}_{-9.02}$	$[\frac{11}{16}\pi,\frac{3}{4}\pi]$	$55.42 \pm 5.15\ ^{+5.57}_{-3.55}\ ^{+10.6}_{-8.75}$
$[\frac{1}{4}\pi,\frac{5}{16}\pi]$	$50.11 \pm 5.07\ ^{+8.35}_{-2.95}\ ^{+10.0}_{-6.25}$	$[\frac{3}{4}\pi,\frac{13}{16}\pi]$	$60.45 \pm 5.57\ ^{+6.44}_{-4.01}\ ^{+11.1}_{-9.30}$
$[\frac{5}{16}\pi,\frac{3}{8}\pi]$	$35.03 \pm 4.06\ ^{+4.02}_{-0.83}\ ^{+8.02}_{-6.02}$	$[\frac{13}{16}\pi,\frac{7}{8}\pi]$	$67.48 \pm 6.01\ ^{+8.30}_{-1.38}\ ^{+16.6}_{-10.4}$
$[\frac{3}{8}\pi,\frac{7}{16}\pi]$	$35.75 \pm 4.17\ ^{+4.14}_{-6.33}\ ^{+7.24}_{-6.29}$	$[\frac{7}{8}\pi,\frac{15}{16}\pi]$	$72.05 \pm 6.49\ ^{+4.18}_{-5.70}\ ^{+14.0}_{-11.0}$
$[\frac{7}{16}\pi,\frac{1}{2}\pi]$	$41.60 \pm 4.72\ ^{+6.13}_{-6.12}\ ^{+9.34}_{-5.40}$	$[\frac{15}{16}\pi,\pi]$	$58.51 \pm 5.40\ ^{+10.6}_{-9.37}\ ^{+11.6}_{-9.31}$

Table B.5: The measured cross section $d\sigma/d\psi_3$ with statistical, systematic (excluding the energy scale uncertainty) and energy scale uncertainties.

X_3 range	$\sigma(\pm$ stat. syst.)[pb]	X_3 range	$\sigma(\pm$ stat. syst.)[pb]
[0.67,0.71]	$0.449 \pm 0.078\ ^{+0.058}_{-0.070}$	[0.83,0.87]	$4.453 \pm 0.259\ ^{+0.198}_{-0.129}$
[0.71,0.75]	$1.251 \pm 0.134\ ^{+0.085}_{-0.076}$	[0.87,0.91]	$6.151 \pm 0.318\ ^{+0.149}_{-0.191}$
[0.75,0.79]	$1.983 \pm 0.160\ ^{+0.125}_{-0.181}$	[0.91,0.95]	$7.954 \pm 0.376\ ^{+0.258}_{-0.330}$
[0.79,0.83]	$2.758 \pm 0.195\ ^{+0.230}_{-0.219}$		

Table B.6: The measured distribution $1/\sigma d\sigma/dX_3$ with statistical and systematic uncertainties.

X_4 range	$\sigma(\pm$ stat. syst.)[pb]	X_4 range	$\sigma(\pm$ stat. syst.)[pb]
[0.5,0.55]	$0.264 \pm 0.072\ ^{+0.055}_{-0.049}$	[0.75,0.8]	$2.915 \pm 0.187\ ^{+0.447}_{-0.191}$
[0.55,0.6]	$1.629 \pm 0.147\ ^{+0.218}_{-0.113}$	[0.8,0.85]	$2.936 \pm 0.216\ ^{+0.036}_{-0.446}$
[0.6,0.65]	$3.024 \pm 0.195\ ^{+0.174}_{-0.059}$	[0.85,0.9]	$1.640 \pm 0.184\ ^{+0.136}_{-0.219}$
[0.65,0.7]	$3.869 \pm 0.212\ ^{+0.158}_{-0.057}$	[0.9,0.95]	$0.107 \pm 0.058\ ^{+0.103}_{-0.034}$
[0.7,0.75]	$3.616 \pm 0.214\ ^{+0.221}_{-0.598}$	[0.95,1.0]	$0.000 \pm 0.00\ ^{+0.00}_{-0.00}$

Table B.7: The measured distribution $1/\sigma d\sigma/dX_4$ with statistical and systematic uncertainties.

$\cos\theta_3$ range	$\sigma(\pm$ stat. syst.)[pb]	$\cos\theta_3$ range	$\sigma(\pm$ stat. syst.)[pb]
[-0.8,-0.7]	$1.209 \pm 0.080\ ^{+0.111}_{-0.044}$	[0.0,0.1]	$0.366 \pm 0.047\ ^{+0.057}_{-0.039}$
[-0.7,-0.6]	$0.866 \pm 0.072\ ^{+0.020}_{-0.171}$	[0.1,0.2]	$0.359 \pm 0.048\ ^{+0.022}_{-0.112}$
[-0.6,-0.5]	$0.584 \pm 0.056\ ^{+0.075}_{-0.041}$	[0.2,0.3]	$0.529 \pm 0.063\ ^{+0.034}_{-0.091}$
[-0.5,-0.4]	$0.532 \pm 0.056\ ^{+0.050}_{-0.045}$	[0.3,0.4]	$0.451 \pm 0.052\ ^{+0.117}_{-0.038}$
[-0.4,-0.3]	$0.426 \pm 0.051\ ^{+0.022}_{-0.039}$	[0.4,0.5]	$0.525 \pm 0.058\ ^{+0.035}_{-0.031}$
[-0.3,-0.2]	$0.279 \pm 0.036\ ^{+0.119}_{-0.019}$	[0.5,0.6]	$0.732 \pm 0.074\ ^{+0.081}_{-0.214}$
[-0.2,-0.1]	$0.367 \pm 0.048\ ^{+0.456}_{-0.050}$	[0.6,0.7]	$0.981 \pm 0.079\ ^{+0.076}_{-0.024}$
[-0.1,0.0]	$0.306 \pm 0.039\ ^{+0.103}_{-0.015}$	[0.7,0.8]	$1.485 \pm 0.105\ ^{+0.105}_{-0.214}$

Table B.8: The measured distribution $1/\sigma d\sigma/d\cos\theta_3$ with statistical and systematic uncertainties.

ψ_3 range	$\sigma(\pm$ stat. syst.)[pb/rad]	ψ_3 range	$\sigma(\pm$ stat. syst.)[pb/rad]
$[0,\frac{1}{16}\pi]$	$0.297 \pm 0.031\ ^{+0.047}_{-0.031}$	$[\frac{1}{2}\pi,\frac{9}{16}\pi]$	$0.213 \pm 0.025\ ^{+0.031}_{-0.022}$
$[\frac{1}{16}\pi,\frac{1}{8}\pi]$	$0.335 \pm 0.033\ ^{+0.112}_{-0.022}$	$[\frac{9}{16}\pi,\frac{5}{8}\pi]$	$0.297 \pm 0.031\ ^{+0.021}_{-0.031}$
$[\frac{1}{8}\pi,\frac{3}{16}\pi]$	$0.336 \pm 0.036\ ^{+0.047}_{-0.045}$	$[\frac{5}{8}\pi,\frac{11}{16}\pi]$	$0.332 \pm 0.032\ ^{+0.018}_{-0.067}$
$[\frac{3}{16}\pi,\frac{1}{4}\pi]$	$0.365 \pm 0.035\ ^{+0.031}_{-0.024}$	$[\frac{11}{16}\pi,\frac{3}{4}\pi]$	$0.341 \pm 0.032\ ^{+0.026}_{-0.021}$
$[\frac{1}{4}\pi,\frac{5}{16}\pi]$	$0.308 \pm 0.031\ ^{+0.028}_{-0.020}$	$[\frac{3}{4}\pi,\frac{13}{16}\pi]$	$0.371 \pm 0.034\ ^{+0.011}_{-0.023}$
$[\frac{5}{16}\pi,\frac{3}{8}\pi]$	$0.215 \pm 0.025\ ^{+0.025}_{-0.017}$	$[\frac{13}{16}\pi,\frac{7}{8}\pi]$	$0.415 \pm 0.037\ ^{+0.037}_{-0.014}$
$[\frac{3}{8}\pi,\frac{7}{16}\pi]$	$0.220 \pm 0.026\ ^{+0.015}_{-0.052}$	$[\frac{7}{8}\pi,\frac{15}{16}\pi]$	$0.443 \pm 0.040\ ^{+0.015}_{-0.056}$
$[\frac{7}{16}\pi,\frac{1}{2}\pi]$	$0.256 \pm 0.029\ ^{+0.031}_{-0.053}$	$[\frac{15}{16}\pi,\pi]$	$0.360 \pm 0.033\ ^{+0.036}_{-0.048}$

Table B.9: The measured distribution $1/\sigma d\sigma/d\psi_3$ with statistical and systematic uncertainties.

Appendix C

Contribution to Future Physics at HERA Workshop

Colour Coherence in Photon Induced Reactions

A. Lebedev[a], L. Sinclair[b], E. Strickland[b], J. Vazdik[a].

[a] P.N.Lebedev Physical Institute, Academy of Sciences of Russia, Leninsky Prospect 53, 117924 Moscow, Russia

[b] Department of Physics and Astronomy, Glasgow University, G12 8QQ Glasgow, Scotland, U.K.

Abstract: Colour coherence in hard photoproduction is considered using the Monte Carlo event generators PYTHIA and HERWIG. Significant effects in the parton shower are found using multijet observables for direct and resolved photon induced reactions. The particle flow in the interjet region of direct processes shows a strong influence of string fragmentation effects.

C.1 Introduction

Colour coherence is an intrinsic property of QCD. Its observation is important in the study of strong interactions and in the search for deviations from the Standard Model [24]. It is interesting to look for colour coherence effects in hard photoproduction processes at the *ep*-collider HERA where large momentum transfers can be achieved and both direct (Fig. C.1(a)) and resolved (Fig. C.1(b)) photon induced events occur. In Section C.2 multijet observables are studied which reveal coherence at the parton

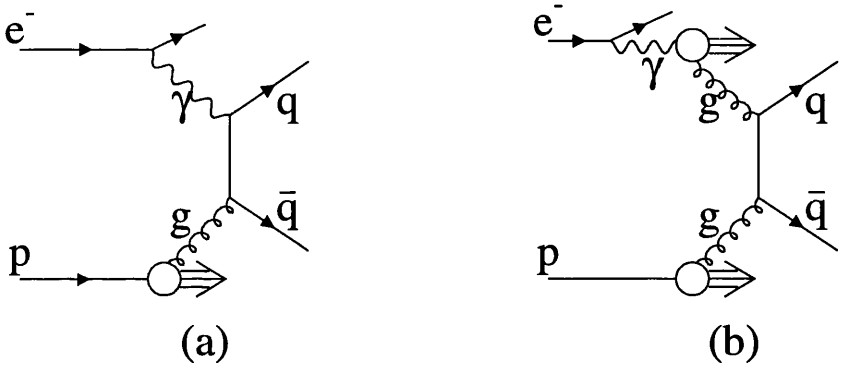

Figure C.1: Examples of (a) direct and (b) resolved photoproduction

shower level for both direct and resolved photoproduction. In Section C.3 consideration of the particle flow in direct photoproduction shows colour coherence effects at the fragmentation stage of hadron production.

C.2 Multijet observables

The effects of colour coherence on the emission pattern of jets in e^+e^- collisions are well known and intuitive. However in hadron–hadron collisions the large number of possible colour flows involved in jet production complicates the identification of variables sensitive to coherence. Here, radiation patterns in γp collisions are studied by considering events where soft radiation is hard enough to form a jet. This reduces the effect of secondary interactions in resolved photoproduction.

The effects arising from different implementations of coherence were studied using 500 pb^{-1} of events generated with PYTHIA 5.7 [63] and HERWIG 5.8 [64]. Direct

and resolved events were generated separately and combined according to their cross sections. Events were generated with a minimum p_T of 20 GeV using the GRV proton and photon structure functions [67]. Two event samples were generated using PYTHIA: the PYTHIA Coherent sample and the PYTHIA Incoherent sample which was obtained by switching off the coherence in the parton shower and the initial-final state coherence. HERWIG represents an alternate implementation of coherent processes. Jets of particles were found using the KTCLUS [61] algorithm in covariant p_T mode with radius equal to 1. Three jet events with at least two jets of transverse energy (E_t^{jet}) satisfying $E_t^{jet} > 30$ GeV and a third jet of $E_t^{jet} > 3$ GeV were selected. The jets are ordered by E_t^{jet} decreasing and referred to as "first", "second" and "third" jet acccordingly in the following. Two scenarios were considered, one to reflect the acceptance in jet pseudorapidity (η^{jet}) of the present ZEUS detector, $|\eta^{jet}| < 2.5$, and one to show the possibilities with an extended acceptance, $|\eta^{jet}| < 4$. In addition the events satisfied $0.2 < y < 0.85$ and $P^2 < 4$ GeV^2, where P^2 is the negative of the four-momentum squared of the photon.

An overall drop in cross section is observed between incoherent and coherent event samples. For example, with a luminosity of 250 pb^{-1} and the standard detector acceptance, $|\eta^{jet}| < 2.5$, 2600 multijet events are predicted by PYTHIA Incoherent, 1728 by PYTHIA Coherent and 1665 events by HERWIG. For comparison in the extended acceptance scenario, $|\eta^{jet}| < 4$, 3012 multijet events are predicted by HERWIG.

The angular distribution of the third jet is also affected. Following [28] the angle α is defined as the azimuthal angle of the third jet about the second jet in the $\eta - \varphi$ plane. Here, however, we use centre-of-mass (c.m.) variables so $\alpha = \arctan(\Delta H/|\Delta\varphi|)$ where $\Delta H = \text{sign}(\eta_2^{cm})(\eta_3 - \eta_2)$ and $\eta_2^{cm} = \eta_2 - 1/2(\eta_2 - \eta_1)$ and $\Delta\varphi = \varphi_3 - \varphi_2$. η_1, η_2 and η_3 refer to the pseudorapidities in the lab frame of the first, second and third jets respectively and positive η is in the direction of the incoming proton. $\Delta\varphi$ is the difference in azimuth (φ) between the second and third jets (in radians). The definition of α is illustrated for a typical event geometry in Fig. C.2(c). The distribution of α as shown in Fig. C.2(a) is broader for coherent events. This is consistent with our understanding that for coherent processes radiation is generally suppressed in regions

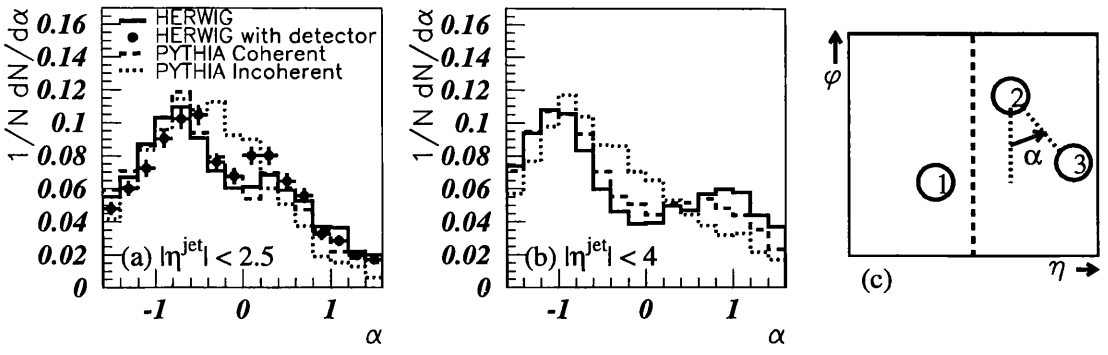

Figure C.2: α distributions (a) with the present acceptance and (b) with extended acceptance. (c) illustrates the definition of α for a typical event geometry. Jets are ordered by E_t^{jet} decreasing.

far from the directions of the incoming coloured partons. In addition, reducing the bias on the distribution by increasing the acceptance from $|\eta^{jet}| < 2.5$ to $|\eta^{jet}| < 4$ produces a more pronounced depletion in the central region for coherent events (Fig. C.2(b)).

Canonical detector effects were simulated by smearing the HERWIG jet quantities with Gaussian distributions of varying widths. A resolution of 20% (10%) was used to smear the E_t^{jet} of jets with $E_t^{jet} < 10$ GeV ($E_t^{jet} \geq 10$ GeV). The width of the difference between generated and detected values of η^{jet} and φ^{jet} was taken to be 0.1. As shown in Fig. C.2(a) such detector effects should not seriously hinder the measurement of α distributions.

The coherent emission of soft radiation does not have a strong effect on the jet profiles of the first and second jets. For instance, in Fig. C.3(a) the transverse energy profile of the second jet is shown. This is the distribution of $\delta\eta_2 = \eta^{part} - \eta_2$, where η^{part} is the η of a particle within one radian of φ of the jet centre, weighted by the transverse energy of the particle, as illustrated in Fig. C.3(c). For this the extended acceptance scenario particles are considered with absolute η up to 5. The profile of the third jet is shown in Fig. C.3(b). The occurrence of two peaks outside the jet core is due to partial overlap in φ of the first or second jet. A strong effect of coherence is apparent; it leads to less energy in the core of the third jet.

One of the anticipated effects of colour coherence is that radiation from an incoming parton should be inhibited in regions far from the initial partons direction. Therefore

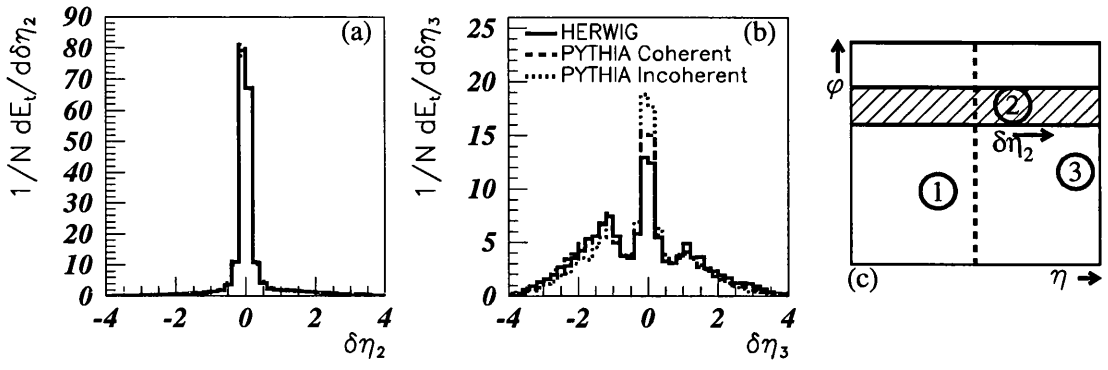

Figure C.3: Jet profiles for (a) the second and (b) the third highest E_t^{jet} jets for the extended acceptance scenario. The definition of the jet profile is illustrated in (c) for the second jet.

in direct photoproduction events, where the single coloured parton in the initial state has positive η, the coherent emission pattern should be at relatively higher η than the incoherent emission. We have selected a subsample of events which is enriched in direct photon events by requiring $x_\gamma > 0.8$ where $x_\gamma = (\sum_{jets} E_t^{jet} e^{-\eta^{jet}})/(2E_\gamma)$. The sum runs only over the two highest E_T^{jet} jets and E_γ is the energy of the incoming photon. The η of the third jet in the c.m. frame, $\eta_3^{cm} = \eta_3 - 1/2(\eta_2 - \eta_1)$, is shown for this selection in Fig. C.4(a). The expected effective enhancement of radiation at large η_3^{cm} can clearly be seen.

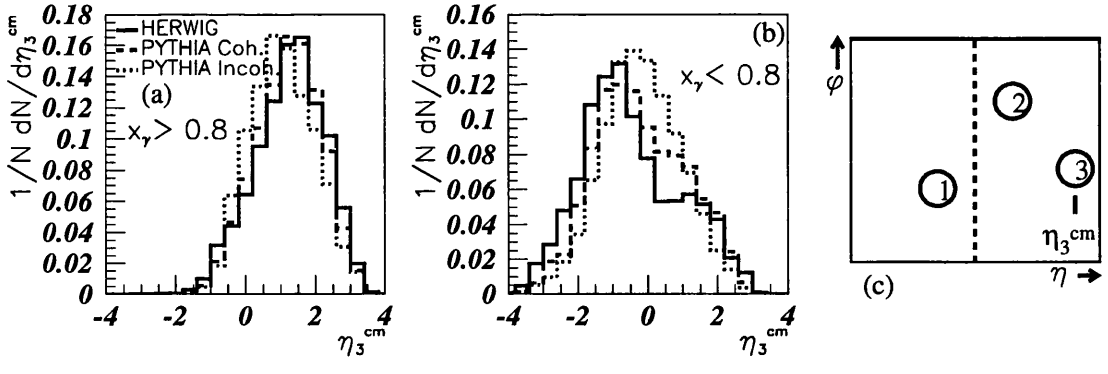

Figure C.4: η_3^{cm} distributions separated by an x_γ cut of 0.8 into (a) direct and (b) resolved samples for the extended acceptance scenario of $|\eta^{jet}| < 4$. In (c) the definition of η_3^{cm} is illustrated.

Resolved events, with incoming coloured partons from both the γ and p directions,

should show an effective enhancement of radiation in coherent processes both at higher positive and at more negative pseudorapidities in comparison to incoherent emission. This effect is evident as shown in Fig. C.4(b). Note that the extended acceptance scenario must be employed in order to see the relative enhancement of radiation at high η in resolved events.

To summarize this section, a high integrated luminosity ($\sim 250\text{pb}^{-1}$) is desirable in order to accumulate statistics in multijet events at high E_t^{jet}. However luminosity upgrades which involve a significant reduction of forward acceptance are not worthwhile for this study. They destroy the sensitivity to colour coherence without significantly improving the statistical uncertainty.

C.3 Interjet string effects in direct photoprocesses

Colour coherence effects which lead to a change in particle flow N distributions in the interjet region should be rather pronounced in the direct photon induced processes such as QED Compton on quark (QEDC), QCD Compton (QCDC) and Photon Gluon Fusion (PGF). These distributions are considered here using the PYTHIA [63] generator with string (SF) or independent parton fragmentation (IF) into hadrons. Using SF is equivalent to taking into account the coherence effects at the hadronization phase of event generation. The flow N depends on the string topology and colour antennae which are different for the three direct processes as shown in Fig. C.5(left).

The calculation at the generator level was done using the GRV proton structure function [67] and minimum p_T equal to 2.0 GeV. The H1 detector simulation was taken into account as well. A jet-cone algorithm [53] with radius equal to 1 was used for the selection of two jets and gamma-jet events with $E_t^{jet\,\text{or}\,\gamma} > 3$ GeV and jet (or final γ) emission angles $25 - 155^o$. This procedure corresponds to the selection of mainly direct processes. The calculated flow of charged particles with $p_t > 0.2$ GeV emitted at angles of less than 20^o to the reaction plane is shown in Fig. C.5(right) as a function of the scale angle Ω. Ω is defined [76] as the ratio of the particle angle θ_h to the angle between partons. $\Omega = 0$ corresponds to the direction of the initial state photon; $\Omega = 1$ – the final state quark; $\Omega = -1$ – the final state γ, gluon or antiquark for QEDC, QCDC or

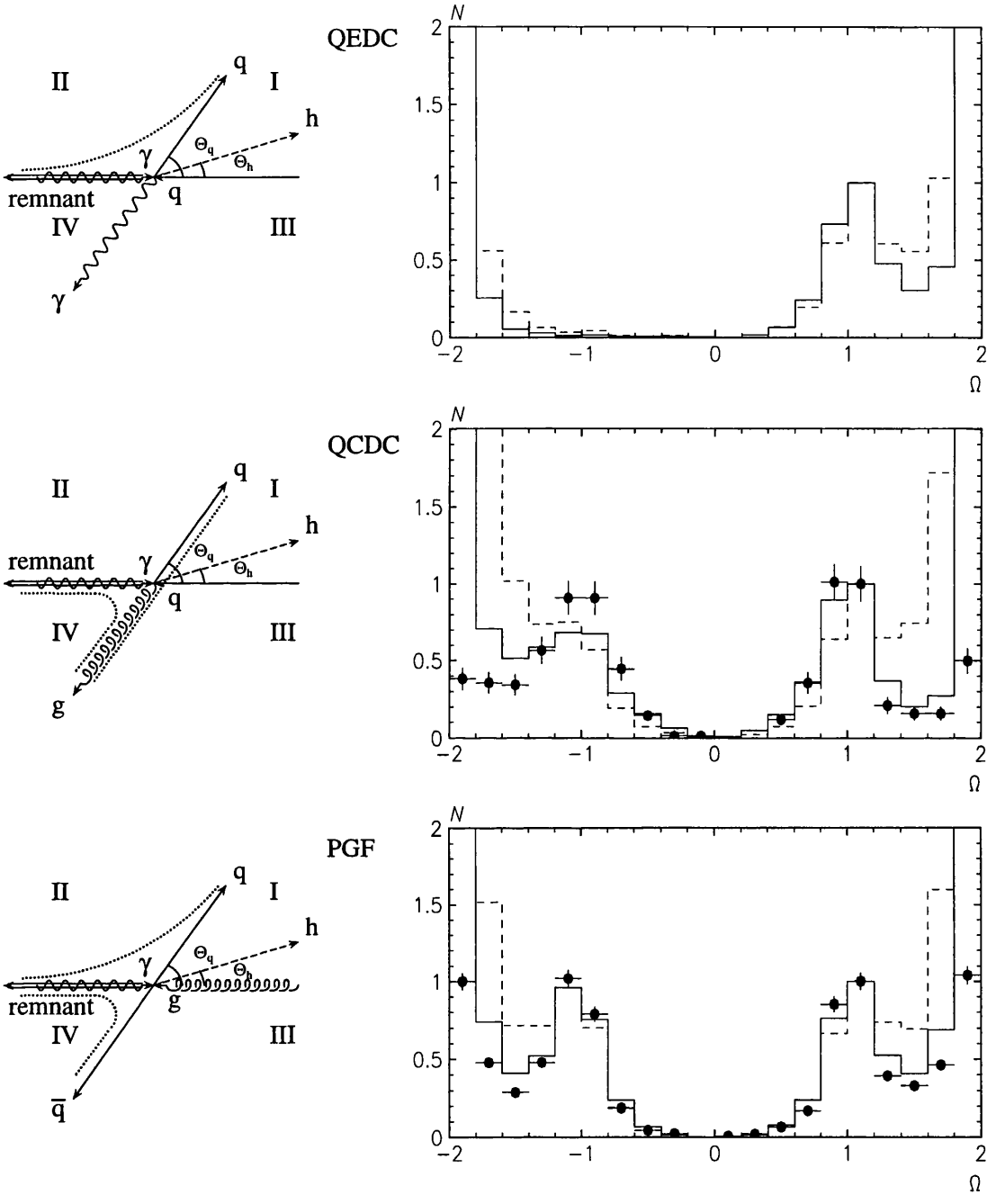

Figure C.5: Left: Topology of direct photoproduction processes in the $\gamma - parton$ c.m. frame. The double line is the proton remnant, dotted - strings. θ_q and θ_h are quark and hadron emission angles. Right: Charged particle flow N normalized to 1 at the quark emission angle vs the scale angle Ω. Solid line - generator level SF, dashed line - generator level IF, dark circle - H1 simulation SF. In the regions I - IV Ω is changing within the limits: $0 \leq \Omega \leq 1$ (I), $1 \leq \Omega \leq 2$ (II), $-1 \leq \Omega \leq 0$ (III), $-2 \leq \Omega \leq -1$ (IV).

PGF respectively; $\Omega = -2$ or 2 – the proton remnant.

It is seen that in the scale angle region between 1 and 2 (region II in Fig. C.5) SF (solid histogram, generator level) and IF (dashed histogram, generator level) give different predictions for N. SF taking into account colour forces leads to a suppression of particle flow which is especially strong for QCDC process. The H1 detector simulation (dark circles, SF) weakly distorts the generator level N distribution except for directions close to remnant proton emission where detector acceptance is rather low. Thus colour coherence effects can be observed at the detector level.

It is interesting to consider ratios of particle flows N for different processes since the ratio is less sensitive to experimental errors. The ratios $R = N(QCDC)/N(QEDC)$, $R^* = N(QCDC)/N(PGF)$ are shown in Fig. C.6. Fig. C.6 displays more clearly the role of colour coherence which leads to drag effects in particle distributions. It is seen that for the case of SF the suppression in N for QCDC is more pronounced than for QEDC and PGF. At $\Omega = 1.7$ the suppression reaches a factor of ~ 3. It has been found that misidentification of quark and gluon jets for QCDC does not change this conclusion.

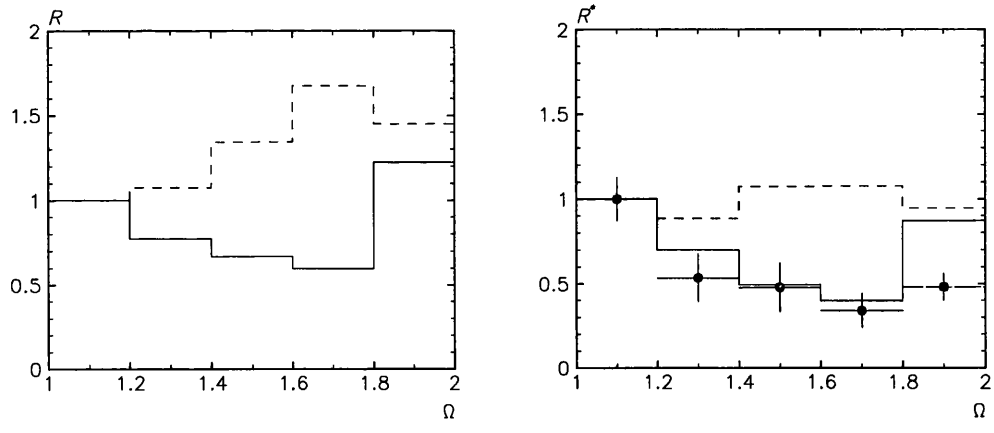

Figure C.6: Ratios R and R^* in the scale angle region $1 < \Omega < 2$. Notations are as in Fig. C.5.

To observe colour coherence at the fragmentation stage of hadron production in direct processes it is necessary to distinguish these processes from resolved photoproduction and to separate QEDC, QCDC and PGF from each other. The jet selection procedure used here enriches the data sample with direct processes. Further enrichment

can be achieved by going to larger $E_t^{jet\,or\,\gamma}$ and by choosing events with x_γ close to 1. Since the direct processes cross section is low we expect $\sim$ 230 QEDC events at the detector level for an integrated luminosity of $\sim$ 100 pb^{-1}. So higher luminosity is needed to study interjet coherence.

C.4 Conclusions

The observation of colour coherence in photoproduction processes is an important challenge, particularly given the unique opportunity at HERA to study direct as well as resolved photon induced reactions. Since the cross sections of multijet events or of prompt photon reactions are small high luminosity *ep*-collisions are necessary for their study. 250 pb^{-1} would appear to be barely sufficient for these studies; however in upgrading to 1000 pb^{-1} it is essential that the forward acceptance should not be reduced.

Appendix D

Contribution to Photon '97 Conference

Paper published in the Proceedings of Photon '97 held in Egmond aan Zee, The Netherlands, 10-15 May 1997, eds A. Buijs and F. Erné, p. 139.

Jet Shapes and Multijet Events in Hard Photoproduction at HERA

E.J. Strickland

(On behalf of the ZEUS collaboration)

Department of Physics and Astronomy, University of Glasgow, Glasgow G12 8QQ, Scotland

Jet shapes and multijet events in quasi-real photon-proton collisions have been studied using the ZEUS detector at HERA. Measured jet shapes are compared to a LO parton shower Monte Carlo prediction, with and without multi-parton interactions, and NLO QCD calculations. The x_γ distribution and 3-jet to 2-jet inclusive production ratio are shown for events with multijet final states.

D.1 Introduction

The study of e^+p collisions at HERA provides many opportunities to study quasi-real photon-proton collisions. At leading order (LO) QCD, the photon can either interact directly with a parton from the proton (direct process) or fluctuate into a hadronic state which acts as a source of partons which scatter off those in the proton (resolved process).

Jets observed experimentally correspond to a reasonable approximation to final state partons, enabling comparison with theoretical calculations to be made. Experimentally, in the case of events with two or more jets, it is possible to define an observable quantity, x_γ^{obs},

$$x_\gamma^{obs} = \sum_{jets} \frac{E_T^{jet} e^{-\eta^{jet}}}{2yE_e} \tag{D.1}$$

which is accessible experimentally, well-defined at higher orders and can be interpreted at lowest order as the fraction of the photon's momentum which goes into the hard scatter.

Two analyses by the ZEUS Collaboration are presented here. The first investigates the internal structure of jets as a means to probe the mechanism responsible for changing a final state parton into an experimentally observed jet; the other studies some features of events with multijet final states.

D.2 Jet Shapes in Hard Photoproduction

Jets are searched for with a cone algorithm with radius $R = 1$ in pseudorapidity[1](η) - azimuth(φ) space and selected with transverse energy, E_T^{jet}, > 14 GeV and -1 < η^{jet} < 2. In this study, pairs of overlapping jets are merged together if the common energy exceeds 75% of the total energy of the lower energy jet. The jet shape, $\psi(r)$, is defined by [58]:

$$\psi(r) = \frac{1}{N_{jets}} \sum_{jets} \frac{E_T(r)}{E_T(R)} \tag{D.2}$$

[1]The pseudorapidity is defined as $\eta = -ln(tan\frac{\theta}{2})$, where the polar angle θ is taken with respect to the proton beam direction.

where R is the radius of the jet defining cone, $E_T(r)$ is the transverse energy within an inner cone of radius r and N_{jets} is the total number of jets in the sample.

Figure D.1 shows reasonable agreement between measured jet shapes and predictions from the LO parton shower Monte Carlo event generator PYTHIA [63] in the region -1 < η^{jet} < 1. In the forward region, however, the data are significantly broader than the predictions. The PYTHIA predictions based on a LO calculation and subsequent fragmentation of single partons using the LUND string model [27] are significantly narrower than the data, indicating that, at the transverse energies studied here, the shape of jets is strongly dictated by parton radiation and cannot be explained by hadronization alone.

The evolution of the jet shape at r=0.5 with η^{jet} and E_T^{jet} is shown in Fig. D.2. The data show that jets become broader as η^{jet} increases, becoming less quark-like and more gluon-like. The addition to PYTHIA of multi-parton interactions (MI), a model which allows more than one interaction between the partons from the proton and photon, improves the agreement with the data in the two high η^{jet} bins. Figure D.2(b) shows that the measured jet shape becomes narrower as E_T^{jet} increases, a possible effect of decreasing α_s.

At LO QCD, a jet is associated with one parton only and therefore has no internal structure. The lowest non-trivial order contribution to the jet shape is given by next-to-leading order (NLO) QCD calculations for the reaction $AB \rightarrow$ jet + X.

Figure D.3 compares the data with NLO QCD calculations of jet shapes [77, 78, 79]. On the theoretical side, an attempt was made to simulate the merging and overlapping procedures of the experimental jet algorithm by introducing at the parton level a parameter R_{SEP} [58] which is related to the separation of two partons in $\eta - \varphi$ space. In the region E_T^{jet} > 17 GeV the jet shapes are reproduced well by the calculations with R_{SEP} = 1.4. The magnitude of the uncertainty in the theoretical expectation is given by the spread of the calculations with R_{SEP} = 1.4 and 2.0.

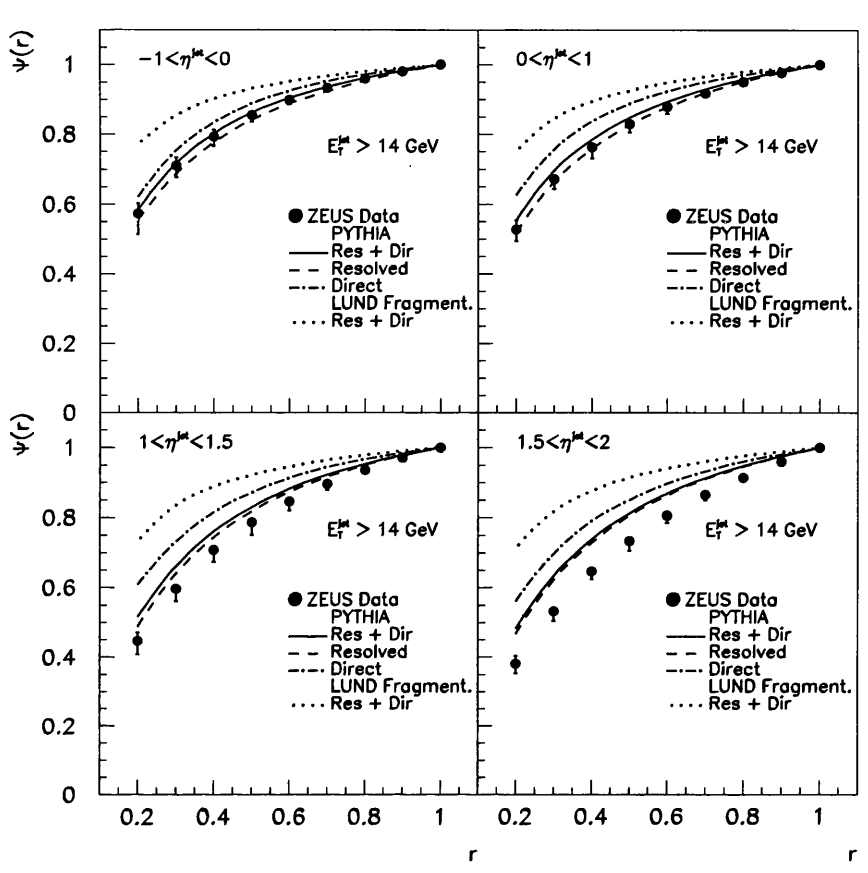

Figure D.1: The measured jet shapes, $\psi(r)$, for jets in the E_T^{jet} range above 14 GeV in different η^{jet} regions are shown and compared to PYTHIA. The predictions of PYTHIA without initial and final state parton radiation are also included ('LUND Fragment').

D.3 Multijet Events in Hard Photoproduction

Dijet studies in hard photoproduction have extensively tested QCD predictions and studies of multijet events would provide a means of testing QCD at higher order. Here, jets are found using the k_T algorithm [61, 62] and events selected with 3 high E_T jets: $E_T^{jet} > 6$ GeV and $\eta^{jet} < 1.5$.

Figure D.4(a) shows the uncorrected x_γ^{obs} distribution defined using the three highest E_T jets in the event. The data are peaked at high x_γ^{obs} with a tail to low values and are in general agreement with PYTHIA predictions. The slight differences at high and

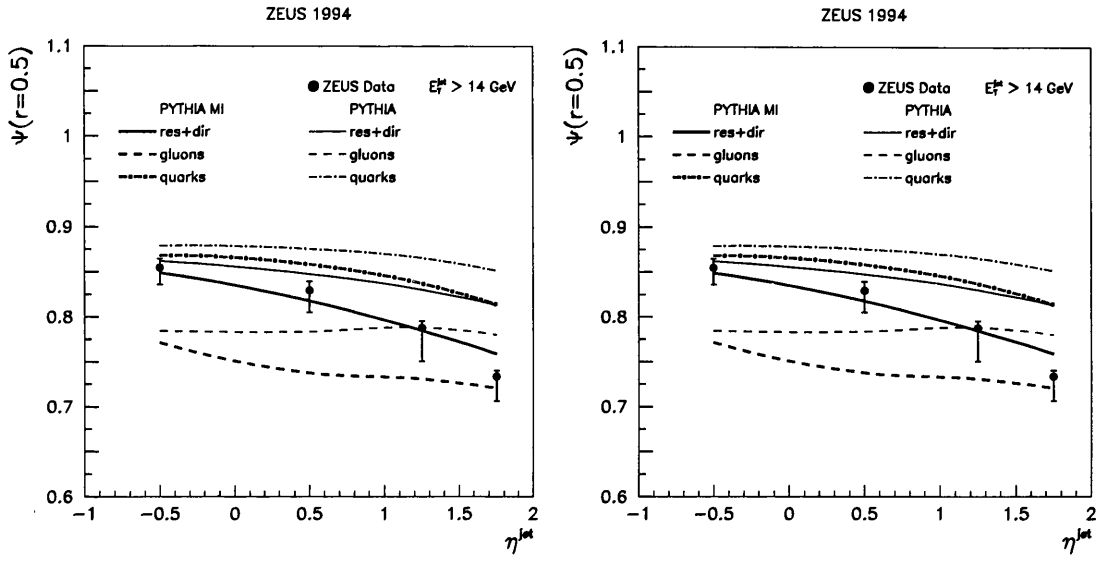

Figure D.2: ψ(r=0.5), left (a), as a function of η^{jet} for jets with $E_T^{jet} > 14$ GeV and compared to predictions from PYTHIA for quark jets only, gluon jets only and all jets (also shown with multi-parton interactions - PYTHIA MI) and right (b), as a function of E_T^{jet} for jets with -1 $< \eta^{jet} < 2$.

low x_γ^{obs} may be due to higher-order processes relevant to 3-jet production which are not included in the Monte Carlo. The low x_γ^{obs} tail shows the need to include resolved processes.

The inclusive 3-jet to 2-jet ratio as a function of $\sum E_T^{jet}$ [80] is shown in Figure D.4(b),

$$\frac{\sigma_3}{\sigma_2} = \frac{\sigma(\gamma p \rightarrow njets + X; n \geq 3)}{\sigma(\gamma p \rightarrow njets + X; n \geq 2)} \tag{D.3}$$

where the sum is over all jets passing the selection cuts. The data rise initially due to the increase in the phase-space available for 3-jet production and then level off. The prediction from PYTHIA is in broad agreement with the data within the large systematic errors.

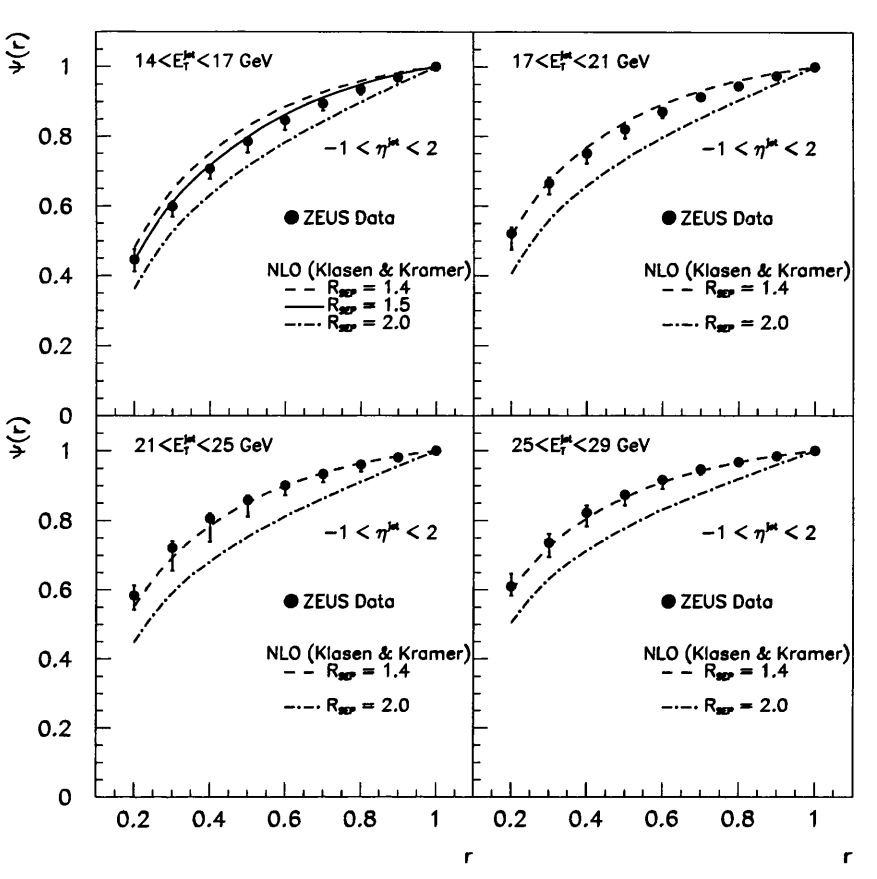

Figure D.3: The measured jet shape, $\psi(r)$, for jets in the range -1 < η^{jet} < 2 in different E_T^{jet} regions. Also shown are the predictions for the jet shapes based upon the NLO QCD calculations by M. Klasen and G. Kramer with various values of R_{SEP}.

D.4 Conclusions

Comparison between data and PYTHIA show that jet shapes in photoproduction are governed strongly by QCD parton radiation. Their description by PYTHIA is improved by the addition of multi-parton interactions. NLO QCD calculations agree with the data using an R_{SEP} parameter of $\approx$ 1.4.

Photoproduced multijet events have been observed. Comparison with a LO parton shower Monte Carlo indicates that both direct and resolved events are needed to describe the x_γ^{obs} distribution. It is hoped that development of a NLO Monte Carlo and

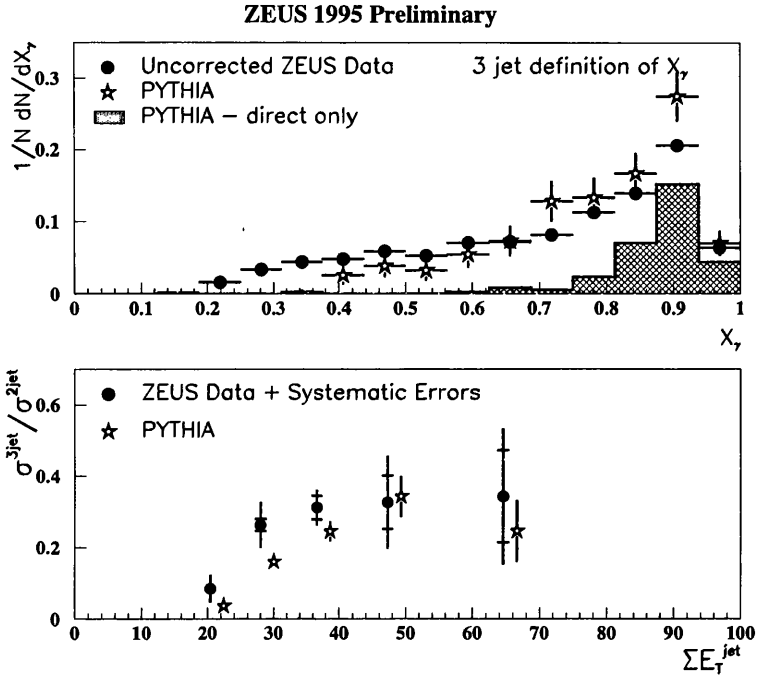

Figure D.4: Shown here are, (a), the x_γ^{obs} distribution with purely statistical errors and (b), the 3 to 2 jet inclusive ratio.

increased statistics will enable further studies to discriminate between the predictions of different models.

References

[1] L. Sinclair for the ZEUS Collaboration, Talk given at the 6^{th} *International Workshop on Deep Inelastic Scattering and QCD (DIS '98), Brussels, Belgium*, 1998, hep-ex/9815010.

[2] L. Sinclair for the ZEUS Collaboration, 'Dynamics of Multijet Production', *XXIX International Conference on High Energy Physics, Vancouver*, 1998, Abstract 800.

[3] A. Lebedev, L. Sinclair, E.Strickland and J. Vazdik, 'Colour Coherence in Photon Induced Reactions', *Proceedings of 1995/96 Workshop Future Physics at HERA*, eds. G. Ingelman, A. De Roeck and R. Klanner, 1996, page 560.

[4] E.Strickland for the ZEUS Collaboration, 'Jet Shapes and Multijet Events in Hard Photoproduction at HERA', *Proceedings of Photon '97, eds. A. Buijs and F. Erné*, World Scientific, 1998, page 139.

[5] F. Halzen and A. D. Martin, *Quarks and Leptons*, John Wiley and Sons, 1984.

[6] E. D. Bloom et al., *Phys. Rev. Lett.* **23**:930, 1969;
M. Breidenbach et al., *Phys. Rev. Lett.* **23**:935, 1969.

[7] M. Gell-Mann, *Phys. Lett.* B8:214, 1964.

[8] G. Zweig, CERN Rep. TH401 and CERN Rep. TH412, 1964.

[9] G. Altarelli, R. Barbieri and F. Caravaglios, Electroweak precison tests: A concise review, hep-ph/9712368, 1997.

[10] ZEUS Collaboration, *Phys. Rev. Lett.* **75**:1006, 1995.

[11] S. Weinberg, *Phys. Rev. Lett.* **19**:1264, 1967;
S. L. Glashow, *Nucl. Phys.* **22**:579, 1961;
A. Salam, 'Weak and electromagnetic interactions', *Proceedings of the Nobel Symposium held in 1968*, 1968.

[12] H. D. Politzer, *Phys. Rev. Lett.* **30**:1346, 1973;
D. J. Gross and F. Wilczek, *Phys. Rev.* D**8**:3633, 1973.

[13] Yu. L. Dokshitzer, D. I. D'Yakonov and S. I. Troyan, *Phys. Rep.* **58**C:271, 1980.

[14] E. Reya, *Phys. Rep.* **69**C:195, 1981;
J. C. Collins, D. E. Soper and G. Sterman, *Nucl. Phys.* B**261**:104, 1985.

[15] V. N. Gribov and L. N. Lipatov, *Sov. J. Nucl. Phys.* **15**:438, 1972;
Yu. L. Dokshitzer, *Sov. Phys. JETP* **46**:641, 1977;
G. Altarelli and G. Parisi, *Nucl. Phys.* B**126**:298, 1977.

[16] ZEUS Collaboration, *Z. Phys.* C**72**:399, 1996;
H1 Collaboration, *Nucl. Phys.* B**439**:471, 1995.

[17] K. Konishi, A. Ukawa and G. Veneziano, *Nucl. Phys.* B**157**:45, 1979.

[18] Y. I. Azimov, Yu. L. Dokshitzer, V. A. Khoze and S. I. Troyan, *Z. Phys.* C**27**:65, 1985.

[19] T. H. Bauer et al., *Rev. Mod. Phys.* **50**:261, 1978;
T. H. Bauer et al., *Rev. Mod. Phys.* **51**:407, 1979.

[20] H. Kolanoski, *Two photon physics at e^+e^- storage rings*, Springer Tracts in Modern Physics, 1984;
Ch. Berger and W. Wagner, *Phys. Rep.* **146**:1, 1987.

[21] J. Vossebeld for the ZEUS Collaboration, Talk given at the *6^{th} International Workshop on Deep Inelastic Scattering and QCD (DIS '98), Brussels, Belgium*, 1998, hep-ex/9805019.

[22] F. Jacquet and A. Blondel, *Proceedings of the study of an ep facility for Europe*, ed. U. Amaldi, 1979, page 391.

[23] T. Sjöstrand, *Phys. Rev.* D**36**:2019, 1987;
G. A. Schuler and T. Sjöstrand, *Nucl. Phys.* B**407**:539, 1993;
J. M. Butterworth and J. R. Forshaw, *J. Phys.*, G**19**:1657, 1993;
J. M. Butterworth et al., CERN-TH-95-82, 1995.

[24] Yu. L. Dokshitzer, V. A. Khoze and S. I. Troyan, *Rev. Mod. Phys.* **60**:373, 1988;
Yu.L.Dokshitzer, V.A.Khoze, A.H.Mueller and S.I.Troyan, *Basics of Perturbative QCD*, Editions Frontieres, Gif/Yvette, 1991.

[25] JADE Collaboration, *Phys. Lett.* B**134**:275, 1984;
JADE Collaboration, *Phys. Lett.* B**157**:340, 1985;
TPC Collaboration, *Z. Phys.* C**28**:31, 1985.

[26] TPC Collaboration, *Phys. Rev. Lett.* **57**:945, 1986;
Mark II Collaboration, *Phys. Rev. Lett.* **57**:1398, 1986.

[27] G. Gustafson, B. Andersson and C. Petersen, *Z. Phys.* C**1**:105, 1979.

[28] CDF Collboration, *Phys. Rev.* D**50**:5562, 1994.

[29] F. Borcherding et al. DØ Collaboration, Talk given at the 9^{th} *Topical Workshop on Proton-Antiproton Collider Physics, Tsukuba, Japan*, FERMILAB-Conf-93/338-E, 1993.

[30] ZEUS Collaboration, *Phys. Lett.* B**322**:287, 1994.

[31] H1 Collaboration, *Phys. Lett.* B**314**:436, 1993.

[32] ZEUS Collaboration, *Phys. Lett.* B**342**:417, 1995.

[33] ZEUS Collaboration, *Phys. Lett.* B**348**:665, 1995.

[34] ZEUS Collaboration, *Eur. Phys. J.* C**1**:109, 1998.

[35] ZEUS Collaboration, *Phys. Lett.* B**413**:201, 1997.

[36] ZEUS Collaboration, *Eur. Phys. J.* C4:591, 1998.

[37] H1 Collaboration, *Nucl. Phys.* B**445**:195, 1995.

[38] H1 Collaboration, *Phys. Lett.* B**415**:418, 1997.

[39] H1 Collaboration, *Eur. Phys. J.* C**1**:97, 1997.

[40] H1 Collaboration, *Z. Phys.* C**70**:17, 1996.

[41] ZEUS Collaboration, *Eur. Phys. J.* C**2**:61, 1998.

[42] S. Geer and T. Asakawa, *Phys. Rev.* D**53**:4793, 1996.

[43] ZEUS Collaboration, *Phys. Lett.* B**384**:401, 1996.

[44] CDF Collaboration, *Phys. Rev. Lett.* **75**:608, 1995;
CDF Collaboration, *Phys. Rev.* D**54**:4221, 1996;
DØ Collaboration, *Phys. Rev.* D**53**:6000, 1996.

[45] ZEUS Collaboration, *The ZEUS Detector Status Report 1989.*

[46] M. Derrick et al., *Nucl. Inst. and Meth.* A**309**:77, 1991;
A. Andersen et al., *Nucl. Inst. and Meth.* A**309**:101, 1991;
A. Bernstein, *Nucl. Inst. and Meth.* A**336**:23, 1993.

[47] D. H. Perkins, *Introduction to High Energy Physics*, Addison-Wesley, 1982.

[48] B. Foster et al., *Nucl. Inst. and Meth.*, Proc. Suppl. B32:181, 1993.

[49] J. Andruszków et al., DESY 92-066, 1992.

[50] G. Wolf, 'HERA Physics', DESY 94-022, 1994.

[51] S. de Jong, PhD thesis, University of Amsterdam, 1990.

[52] G. A. Schuler and H. Spiesberger, 'DJANGO: The Interface for the event generators HERACLES and LEPTO', *Physics at HERA*, eds. W. Buchmüller and G. Ingelman, 1991.

[53] J. Huth et al., 'Towards a Standarization of Jet Definitions', *Proceedings of 1990 Summer Study on High Energy Physics*, ed. E. L. Berger, 1992, page 143, Fermilab-Conf-90/249-E.

[54] G. Sterman and S. Weinberg, *Phys. Rev. Lett.* **39**:1436, 1977.

[55] JADE Collaboration, *Phys. Lett.* B**213**:235, 1988.

[56] CDF Collaboration, *Phys. Rev.* D**45**:1448, 1992.

[57] DØ Collaboration, *Phys. Lett.* B**357**:500, 1995.

[58] S. Ellis, Z. Kunszt and D. Soper, *Phys. Rev. Lett.* **69**:3615, 1992.

[59] J. Butterworth, L. Feld, M. Klasen and G. Kramer, 'Matching Experimental and Theoretical Jet Definitions for Photoproduction at HERA', *Proceedings of 1995/96 Workshop Future Physics at HERA*, eds. G. Ingelman, A. De Roeck, R. Klanner, 1996, page 554.

[60] M. Seymour, 'Jet Shapes in Hadron Collisions: Higher Orders, Resummation and Hadronization', hep-ph/9707338", 1997.

[61] S. Catani, Y. L. Dokshitzer, M. H. Seymour and B. R. Webber, *Nucl. Phys.* B**406**:187, 1993

[62] S. D. Ellis and D. E. Soper, *Phys. Rev.* D**48**:3160, 1993.

[63] H.-U. Bengtsson and T. Sjöstrand, *Computer Physics Commun.* **46**:43, 1987;
T. Sjöstrand, *Computer Physics Commun.* **82**:74, 1994.

[64] G.Marchesini et al., *Computer Physics Commun.* **67**:465, 1992.

[65] T. Sjöstrand, *Computer Physics Commun.* **39**:347, 1986;
H.-U. Bengtsson and T. Sjöstrand, *Computer Physics Commun.* **43**:367, 1987.

[66] R. Brun et al., CERN DD/EE84-1, 1987.

[67] M. Glück, E. Reya and A. Vogt, *Phys. Rev.* D**46**:1973, 1992.

[68] CTEQ Collaboration, MSUHEP-41024.

[69] ZEUS Collaboration, *Proceedings of the International Europhysics Conference on HEP*,1995.

[70] ZEUS Collaboration, *Phys. Lett.* B**354**:163, 1995.

[71] H. Abramowicz, K. Charchula and A. Levy, *Phys. Lett.* B**269**:458, 1991.

[72] A.D. Martin, R.G. Roberts and W.J. Stirling, *Phys. Rev.* D**50**:6734, 1994.

[73] B. W. Harris and J. F. Owens, *Phys. Rev.* D**56**:4007, 1997.

[74] M. Klasen, T. Kleinwort and G. Kramer, hep-ph/9712256, 1997.

[75] M. Klasen, hep-ph/9808223, 1998.

[76] V.A.Khoze, A.I.Lebedev, J.A.Vazdik, *Mod. Phys. Lett.* A**9**:1665, 1994.

[77] G. Kramer and S. G. Salesch, *Phys. Lett.* B**317**:218, 1993.

[78] G. Kramer and S. G. Salesch, *Phys. Lett.* B**333**:519, 1994.

[79] M. Klasen and G. Kramer, DESY-97-002, 1997.

[80] E. Gallas, FERMILAB-CONF-96-304-EF, 1996.